A study of the structure of the Belgian crust by Moho determination and local seismic tomography

Els Sichien

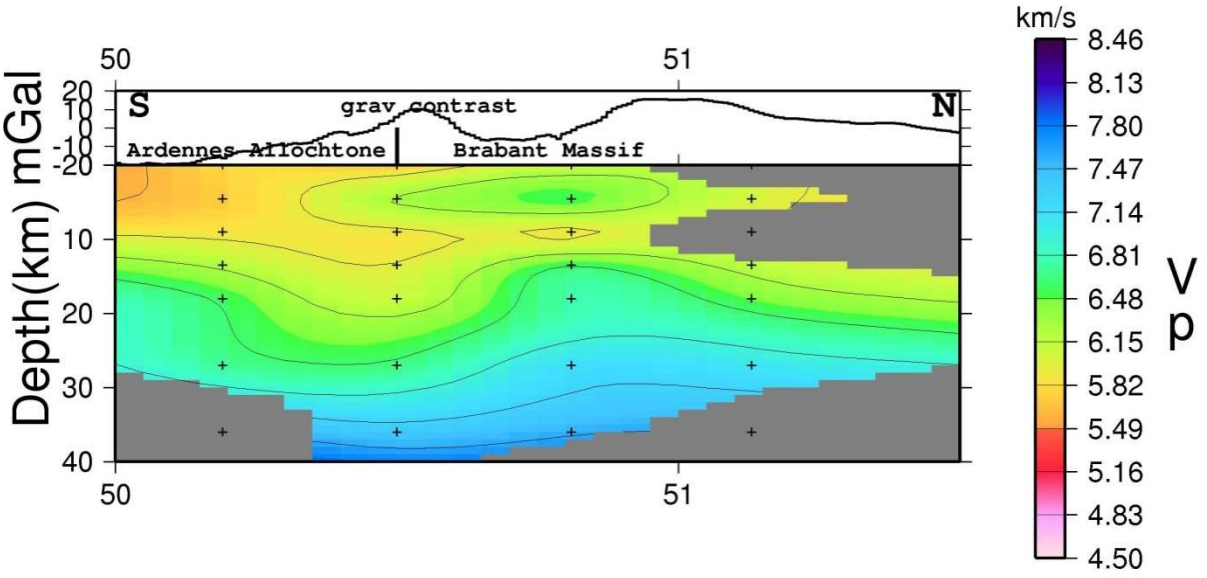

Academic year 2009-2010
Thesis submitted for the degree of Doctor of Science, Geology
Promoter: Prof. Dr. Jean Pierre Henriet
Co-promoter: Dr. Thierry Camelbeeck

UNIVERSITEIT GENT

A study of the structure of the Belgian crust by Moho determination and local seismic tomography

Els Sichien

This research was financially supported by the Institute for the promotion and Innovation through Science and Technology in Flanders (IWT-Vlaanderen).

To refer to this thesis:

Sichien, E., 2010. A study of the Belgian crust by Moho determination and local seismic tomography, PhD thesis, Ghent University, Belgium.

In Dutch: Een studie van de Belgische korst door Moho diepte determinatie en het uitvoeren van een okale seismische tomografie, Doctoraatsthesis, Universiteit Gent, België.

Front cover:

"Tomographic result along a profile crossing the sharp gravimetric contrast"

The figure shows the result of the local seismic tomography along a profile crossing the gravimetric contrast. Above the tomographic results, the Bouguer gravity measurements along the profile are shown, as well as the position of the main geological features along this profile

UNIVERSITEIT GENT

A STUDY OF THE STRUCTURE OF THE BELGIAN CRUST BY MOHO DEPTH DETERMINATION AND LOCAL SEISMIC TOMOGRAPHY

Een studie van de structuur van de Belgische korst door Moho diepte determinatie en het uitvoeren van een lokale seismische tomografie

Els Sichien

Academic year 2009-2010

Thesis submitted for the degree of Doctor of Science, Geology

Promoter: Prof. Dr. Jean Pierre Henriet
co-promoter: Dr. Thierry Camelbeeck

Faculteit Wetenschappen RCMG ROB IWT

Members of the reading committee:

Prof. Dr. J.-P. Henriet (Ghent University, Belgium): promoter
Dr. T. Camelbeeck (ROB, Belgium): co-promoter
Dr. T. Monfret (Géosciences Azur, France)
Prof. Dr. Granet (l'Institut de Physique du Globe, France)

Members of the examination committee:

Prof. Dr. P. Jacobs (Ghent University, Belgium): chairman
Prof. Dr. J.-P.Henriet (Ghent University, Belgium): promoter
Dr. T. Camelbeeck (ROB, Belgium): co-promoter
Dr. T. Monfret (Géosciences Azur, France)
Prof. Dr. Granet (l'Institut de Physique du Globe, France)
Prof. Dr. M. De Batist (Ghent University, Belgium)
Prof. Dr. J. Verniers (Ghent University, Belgium)
Prof. Dr. K. Vanneste (guest professor Ghent University, Belgium)

Voorwoord

Langs deze weg zou ik iedereen willen bedanken die de laatste 4,5 jaar heeft bijgedragen tot het realiseren van deze thesis.

In de eerste plaats mijn promotor Prof. Dr. Jean-Pierre Henriet om mij de kans te bieden de DEA "Dynamique de la lithosphère, des Marges océaniques aux chaïnes de Montagnes" te volgen en zo kennis te maken met de wereld van de seismische tomografie en om nadien de promotor van deze thesis te willen zijn. Verder wil ik hem ook graag bedanken voor de vele uren die hij aan het nalezen en verbeteren van dit werk heeft gespendeerd.

Je voudrais aussi remercier mon co-promoteur, Dr. Thierry Camelbeeck, non seulement pour la proposition du sujet, mais aussi pour le temps précieux qu'il a consacré à la lecture de cette thèse. Bien qu'il m'ait laissé trouver mon propre chemin, je pouvais toujours compter sur lui quand je me trouvais dans une impasse. Nos discussions et ses explications éclairantes m'ont beaucoup aidé.

Heel wat mensen hebben mij ook geholpen om meer kennis te vergaren omtrent de verschillende aspecten van mijn werk. Dr. Tony Monfret, merci d'avoir mis votre confiance en moi, la géologue belge ne maîtrisant pas très bien le français, pour le travail de mémoire du DEA. Tony, j'ai énormément apprécié que vous ayez guidé mes premiers pas dans le monde de la tomographie sismique et, de cette façon, de m'avoir donné l'opportunité de débarquer dans cette grande aventure! Merci aussi pour votre présence permanente durant cette thèse, pour votre aide face aux problèmes tomographiques et pour les discussions multiples par mail. Merci aussi de m'avoir accueillie chez vous, à Biot, pour la rédaction de l'article! Vous m'avez appris presque tout ce que je sais sur la tomo! Merci beaucoup!

Dr. Michel Everaerts, merci pour les discussions sur la géologie profonde de la Belgique, les interprétations et modélisations des données gravimétriques et magnétiques.Verder wil ik ook graag Dr. Michiel Dusar bedanken voor het ter beschikking stellen van verschillende originele seismische reflectieprofielen en Willem Versteeg voor het becijferen van de gebruikte frequentiebanden op verschillende van deze profielen en dus voor het bepalen van de maximale diepte waarop informatie kon worden bekomen langsheen deze profielen. I would also like to thank the many scientists I met on several national and international meetings, their comments and discussions gave me a lot of insight in my work.

Verder wil ik ook de collega's in Brussel bedanken, niet alleen voor de vele verjaardags- en andere feestjes, maar ook voor de hulp allerhande. William, bedankt om mij in te wijden in de geheimen van de Sterrenwacht, zeker deze van de administratie, alsook in de wondere wereld van het picken van arrival times en het programmeren in fortran. Bedankt ook om bij wiskundige problemen even mee te redeneren! Koen Verbeeck, mijn appreciatie voor de vele geologische discussies, de hulp bij het aanmaken van verschillende figuren, het nalezen van dit hele manuscript, om mij met Map info te leren werken en zo veel meer. Mijn dank ook voor de dagelijkse quote die steevast een glimlach op mijn gezicht toverde. Bedankt ook aan Dr. Kris Vanneste voor de geanimeerde discussies en het nalezen van verschillende hoofdstukken van deze thesis. Al je tips en correcties werden in acht genomen. Henri Martin et Fréderic De Vos, merci beaucoup de m'avoir aidé lors de tous les

problèmes informatiques! Tous mes remerciements à Dr. Fabienne Collin pour les discussions sur la tomographie, pour les explications du fonctionnement du programme Inver3D et pour la guidance dans le labyrinthe du code de ce programme. Merci aussi pour la relecture du chapitre sur la tomographie et pour vos commentaires et corrections, ils m'ont beaucoup aidé.

Verder wil ik ook graag de Kampioenen van judoclub Berlare bedanken om mij elke zaterdag even mijn frustraties te laten vergeten en mij te tonen dat hoe moeilijk ook, je nooit mag opgeven, want geluk is te vinden in de kleine dingen. Dank ook aan Ronny en de andere judoka's om mij tijdens de soms zware trainingen de mogelijkheid te bieden even mijn zinnen te verzetten en mijn frustraties letterlijk van mij af te werpen. Een speciaal woordje van dank ook aan Katrien De Saedelaere voor het prachtig inscannen van de Birps profielen, op mijn eentje was het mij nooit gelukt!

Mama, papa, Lies en Jolien, bedankt om steeds in mij te blijven geloven en om mij op te peppen wanneer ik het even niet meer zag zitten, om toch te proberen te begrijpen waar ik nu juist mee bezig was! Jolien, bedankt om tijdens je laatste vakantiejob vele uren te spenderen aan het corrigeren van de soms pietluttige details aan mijn figuren en mijn gezaag hieromtrent te aanhoren. Sorry voor de keren dat ik mijn geduld verloor! Lies, bedankt om de lastige passages samen met mij na te lezen en te herwerken. Zonder jullie had ik het niet gekund!

Stefan, mijn doktoraat heeft een hele tijd van mijn leven ingenomen en alhoewel je deze moeilijke materie niet volledig begreep en niet altijd snapte waarom ik daar nu juist zoveel tijd moest insteken, heb je mij toch altijd gesteund! Bedankt voor alles!!

Overmere, Oktober 2009

Els

Table of Contents

List of Figures

List of Tables

List of Abbreviations

ART	Algebraic Reconstruction Technique
CAB	The upper limit of the velocity model determined by Calbini (2003)
CAL	Velocity model determined by Calbini (2003)
CAL04	The earthquake relocation programme used the velocity model determined by Calbini (2003) and an initial depth of 4 km
CAO	The lower limit of the velocity model determined by Calbini (2003)
DWS	Derivative Weight Sum
GG1	Gravimetric Gradient 1
JFR	Juan Fernandez Ridge
MEU	Seismic station at Meuville
MGCR	Mid-German Cristalline Rise
Moho	Discontinuity of Mohorovicic
P	Longitudinal or primary seismic wave
Pg	Direct longitudinal or primary seismic wave
PiP	Longitudinal or primary seismic wave reflected on a discontinuity (not Mohorovicic)
Pn	Longitudinal or primary seismic wave (head wave) refracted on the discontinuity of Mohorovicic
PmP	Longitudinal or primary seismic wave reflected on the discontinuity of Mohorovicic
RMS	Root Mean Square
Rob	Seismic station at Robertville
ROB	Royal Observatory of Belgium
RVG	Roer Valley Graben
S	Transverse or secondary seismic wave
SH	Horizontally polarized transverse wave
SKQ	Seismic station at Steenkerque
SmS	Transverse or secondary seismic wave reflected on the discontinuity of Mohorovicic

STD	Velocity model determined by Ahorner (1984)
STD04	The earthquake relocation programme using the velocity model determined by Ahorner (1984) and an initial depth of 4 km
STD10	The earthquake relocation programme using the velocity model determined by Ahorner (1984) and an initial depth of 10 km
SV	Vertically polarized transverse wave
Tp	Arrival time for the longitudinal or primary seismic wave
Ts	Arrival time for the transverse or secondary seismic wave
TWT	Two-way travel time
UCC	Seismic station at Uccle
Vp	Velocity of the longitudinal or primary seismic wave
Vs	Velocity of the transverse or secondary seismic wave
ZEV	Seismic station at Zevekote

Introduction

The complexity of the crust

The Belgian territory, situated at the northern edge of the Variscan Orogeny (Late Devonian-Late Carboniferous Figure I- 1), has known a complex deformation history. It is composed of several Caledonian Inliers, like the Brabant Massif (Figure I-2 E) and the Ardennes inliers (Rocroi, Stavelot and Condroz inlier (Figure I-2 E)), and the Ardennes Allochthon. The Ardennes Inliers and the Brabant Massif have been deformed during the Caledonian Orogeny (Ordovician-Early Devonian Figure I- 1), when Avalonia collided with Baltica and Laurentia (Figure I-2A-B). The former were deformed during the Ardennian phase, while the latter was deformed during the later Brabant phase. After an episode of extension and deposition, the Ardennes Devonian and Carboniferous sediments were deformed by the Variscan Orogeny (Carboniferous-Permian Figure I- 1) (when Laurussia collided with Gondwana to form Pangaea (Figure I-2 C)). The Rhenohercynian zone (Figure I-2F) of the Variscan deformation, to which the Ardennes sedimentary basins belong, acted as a "thin-skinned fold and thrust belt". It was displaced several kilometers northward along the Midi-overthrust and pushed over the southeastern edge of the Brabant Massif. During the Alpine Orogeny (Paleogene-Neogene Figure I- 1), the Belgian territory was quite stable and has not known a lot of deformation, except in the north-eastern extremity, where the Roer Valley Graben (Figure I-2E-D) (part of the Rhine Graben) opened as part of the European Cenozoic Rift System during the late Oligocene (Figure I-2D). This complex deformation history is reflected in the complexity of the European crust. When the propagation velocities of the different seismic waves are determined, distinct crustal blocks differing in their internal seismic velocity structure can be assigned to geologically defined terrains of the Caledonian and Variscan Orogeny. The average crustal thickness is around 28-30 km, except underneath the Rhine Graben where the crust thins to 25-26 km and underneath the Rhenish Massif, where the Moho is as deep as 37 km. Towards the Alps, the crust even thickens progressively to a depth of 60 km underneath the central Alps.

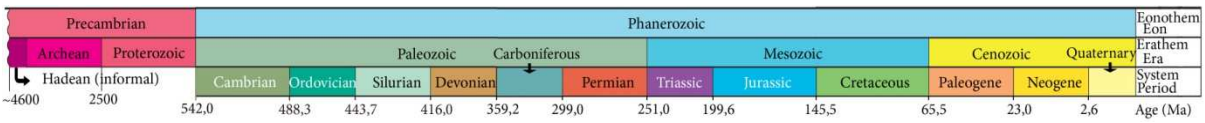

Figure I- 1: Geological Time Table (International Commission on Stratigraphy, 2009)

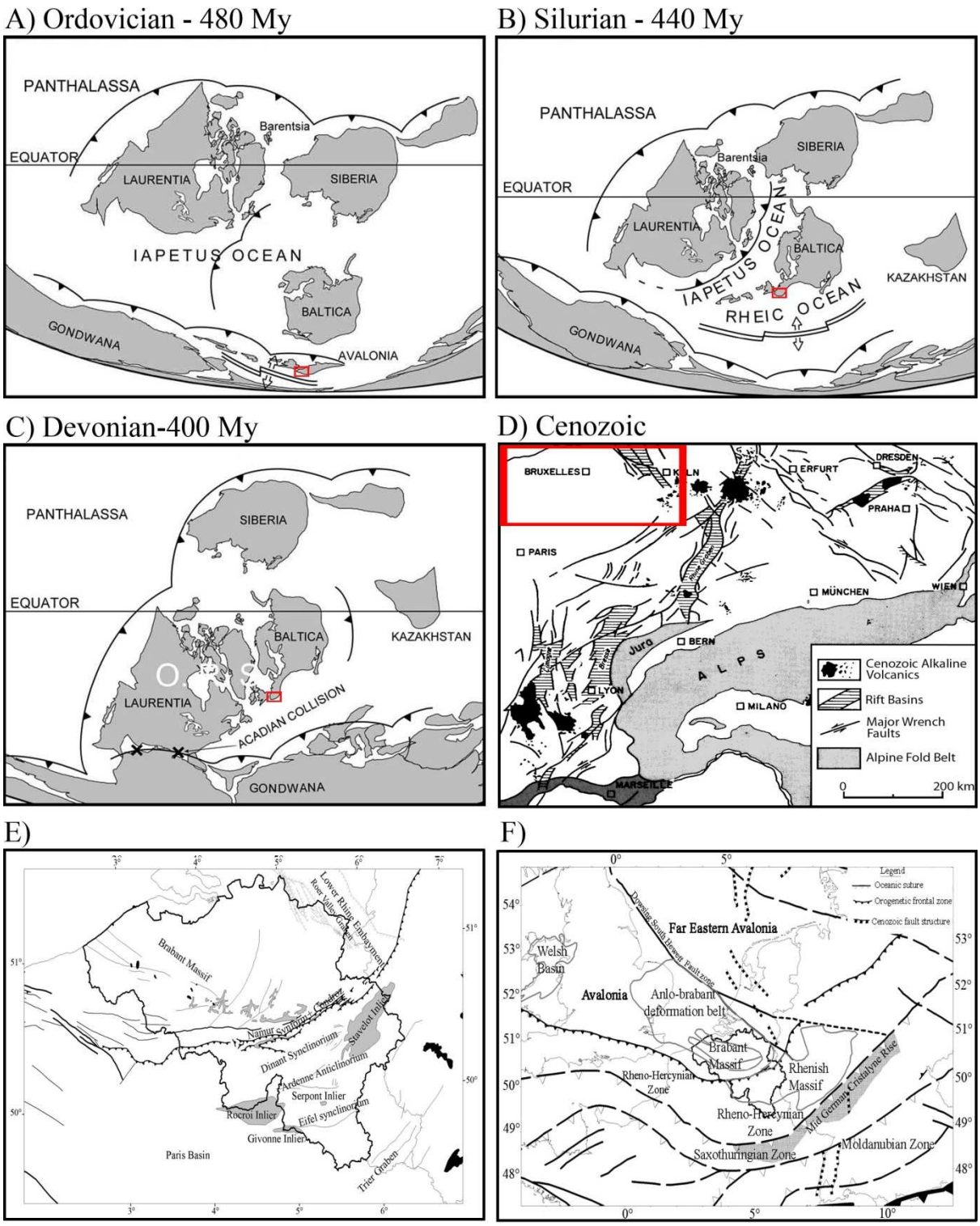

Figure I-2: Schematic maps showing the position of the continents through time as well as a schematic geological map of both Belgium and Central Europe.

Red Box indicates studied region. (A) Position of the different Continents during the Ordovician, (B) Silurian and (C) Devonian (from www.scotese.com). (D) Structural elements of the Cenozoic Rift System of Western and Central Europe (Modified after Brousse & Bellon, 1983 and Coulon, 1992). (E) Schematic geological map of Belgium. Grey zones = Pre Variscan sediments and Black zones = magmatic rocks. Also indicated: Major faults in gray and black and political borders. See Figure 2.1 on page 28 for larger version. (F) Basement tectonic sketch map of NW Europe showing the different continents and zones of the Variscan Orogeny (redrawn from Verniers *et al.*, 2002). See Figure 2.2 on page 29 for larger version.

Even now, the crust is still deforming under a geodynamic stress field, induced by the opening of the Atlantic Ocean and the northward movement of Africa. This is evidenced by the intraplate earthquakes that strike Europe, especially in the Rhine Graben (including the Roer Valley Graben), southern Norway, western France, etc. How the different regions of Europe react to this stress field, heavily depends on its former geological evolution. Heterogeneities are often inherited from earlier basin geometries, which themselves are influenced by pre-existing structural trends in the basement, underlining the importance of structural heritage. For instance, the emplacement of the European Cenozoic Rift System (Figure I-2 D), which extends from the Dutch North Sea to the western Mediterranean, involved the reactivation of Permo-Carboniferous shear systems. It is important to better understand the structures that are or can be reactivated in the present field, so their influence on human life can be evaluated. This is one of the objectives of the Topo-Europe project (Cloetingh *et al.*, 2007), in which the influence of the lithospheric and lower crustal structure on the topography and other superficial structures is studied. Before a similar study can be performed on the Belgian territory, the lower crustal and upper mantle structures have to be very well known. Because this is not the case, yet, the current knowledge will be extended by determining the Moho depth and performing a local seismic tomography in this study.

Present knowledge of the crustal structure

In Belgium not much is known about the extension of the different crustal structures in depth, especially into the middle and lower crust. Geophysical tools are important to study the geological structure of Belgium, because apart from a few outcrops the structures are mostly covered by a thick package of Permian to Quaternary sediments. Until now, only seismic profiles and gravimetric and magnetic data gave some insights. All these methods have some restrictions. The reflection and refraction seismic profiles did not give much information on the middle and lower crust, because neither reflectors nor refracting horizons can be seen at these depths and because they only allow a 2D view. Gravimetric data have a tendency to highlight superficial anomalies, which does not make it the best tool to study the deeper crust. Magnetic data are equally sensitive to both deep and superficial causal bodies, but only show the structure of magnetic objects. Where significant magnetic contrasts are lacking, no information can be obtained.

In the seventies and eighties several deep reflection and refraction seismic profiles were shot in Belgium and the surrounding countries (Bouckaert *et al*., 1988; Matte and Hirn, 1988; Dekorp research group, 1991; Klemperer and Hobbs, 1991) (Figure I-3). On these profiles, the Brabant Massif is characterised by an unreflective middle and lower crust below which the Moho could not be observed. The sediment cover of the Brabant Massif is visible, as well as the Midi overthrust. Further away from the Brabant Massif several crustal structures become visible and the Moho depth could be determined. In the east, the Moho deepens towards the Brabant Massif from 8 s TWT to 10 s TWT (two way travel time), as seen along the DEKORP profile. In the south, the Moho deepens from about 10 s TWT near the Brabant Massif to approximately 13 s TWT slightly north of the Bray fault zone along the ECORS profile. In the North Sea, the Moho depth could be determined north and south of the Brabant Massif, but not underneath it. The Moho discontinuity corresponds to a

reflector at 10 s TWT on both sides of the massif. Unreflective crust underneath the Ardennes Allochthon was interpreted as the Brabant Massif that extends this far.

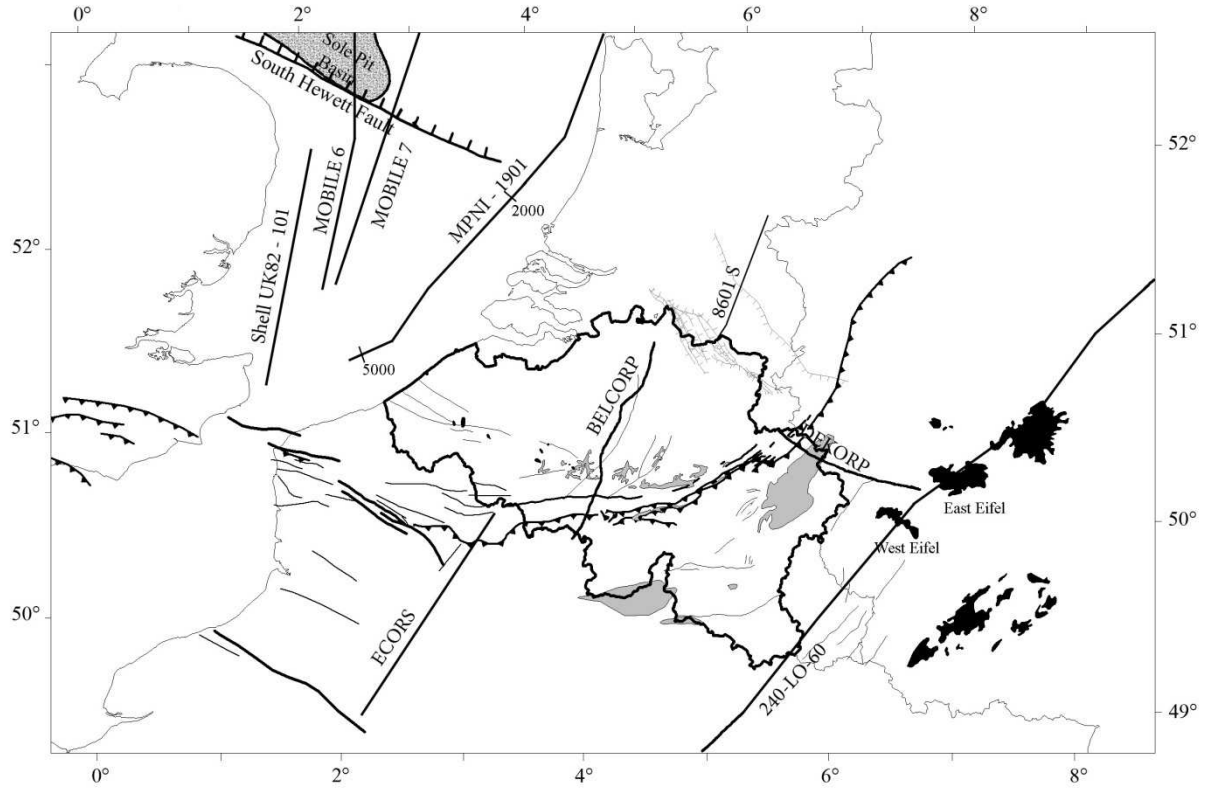

Figure I-3: Position of the different seismic profiles shot in and around the Belgian territory. Grey zones = Pre Variscan sediments and Black zones = magmatic rocks, dark grey zone: Sole Pit Basin. Major Fault lines are also indicated in black and grey as well as the political borders.

Gravity and magnetic data (Figure I-4 and Figure I-5) however do show that there is a huge difference between the crust in the north and the south of Belgium (Chacksfield, 1993; Everaerts, 2000; De Vos *et al*., 1992; Oulidi, 1998 and Mansy *et al*., 1999). In the north the crust has high gravity values, explained by the dense ($\rho > 2.70$) Cambrian-Silurian sediments of the Brabant Massif, whereas in the south, the crust is characterised by low gravity values, explained by the presence of light ($2.64 < \rho > 2.70$) Devonian and Carboniferous sediments. In fact, the entire lower crust has to be composed of a light material to fully explain this negative anomaly (Everaerts, 2000). This sharp transition is either explained by a rapid southward plunge of the Brabant Massif or by a structural separation of the entire crust between the Brabant Massif and the Ardennes Allochthon (Everaerts, 2000).Although Everaerts (2000) modelled this gradient with solely superficial origins, namely the presence of the Mons Basin and the gradual plunge of the Brabant Massif towards the south. Furthermore, the northern positive anomaly of the Brabant Massif is disrupted by a negative anomaly, which has been interpreted as an Ordovician batholith or a Precambrian intrusive body that has blocked the deformation of the Brabant Massif during the Brabant phase. Underneath the Campine area to the north the positive anomaly reaches its highest values. These values cannot be explained by the (light) sediments that fill the basin, but might be explained by an uplift of the boundary of the middle-lower crust or by a Moho high underneath the Campine basin (Oulidi, 1998).

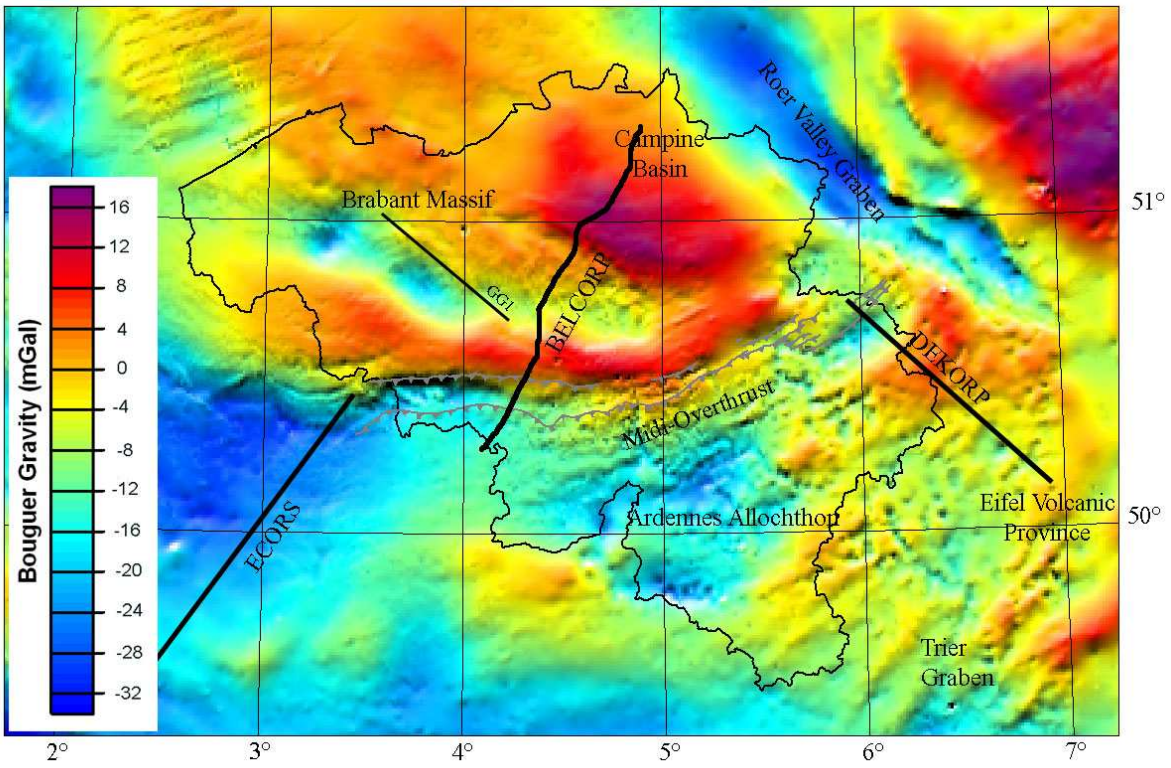

Figure I-4: The Gravity Bouguer Anomaly map of the Region
The location of the most important tectonic structures and positions of important seismic reflection profiles are shown.
The back line represents the Belgian border.
Bouguer gravity anomaly data: Royal Observatory of Belgium

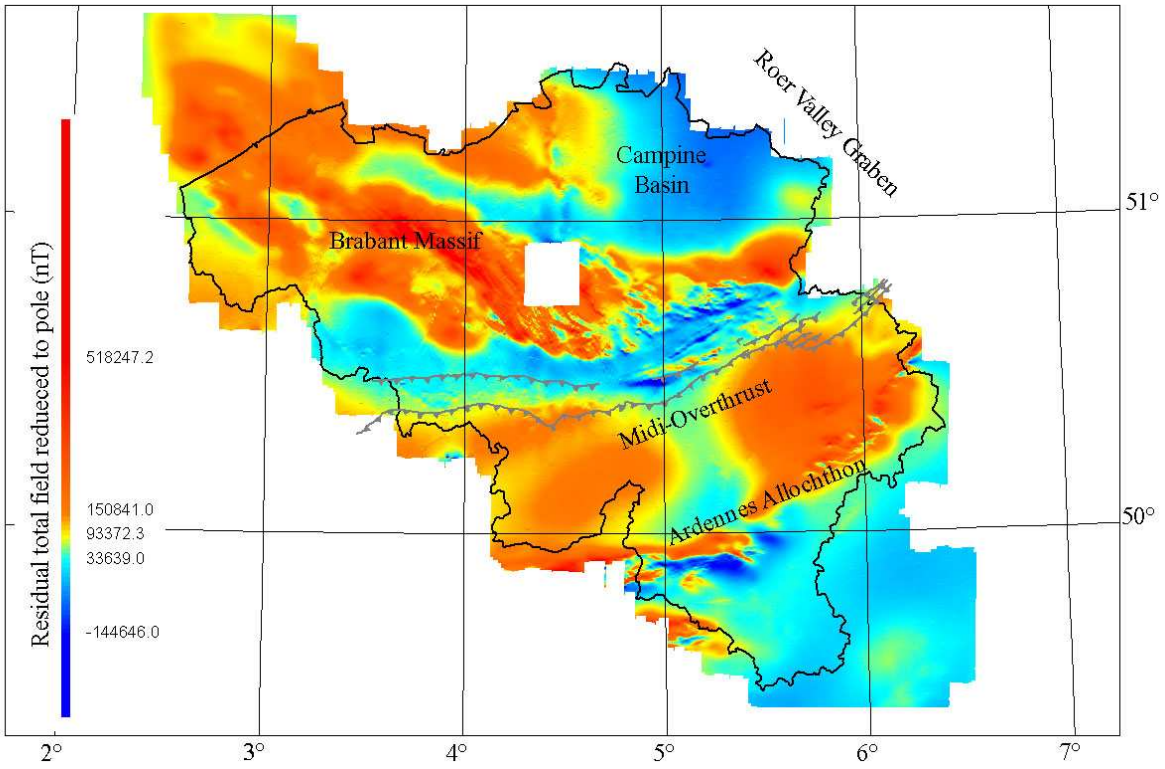

Figure I-5: Aeromagnetic anomaly map reduced to the pole
The location of the most important tectonic structures are shown.
Magnetic field reduced to the pole data: Royal Belgian Institute of Natural Sciences, Belgian Geological Survey.

Not only gravimetric data show a difference in the crust between the north and south of Belgium. Magnetic data show a magnetic deep crust underneath the Ardennes Allochthon and a non-magnetic deep crust underneath the Brabant Massif. The deep magnetic sediments of the Ardennes Allochthon are interpreted as Neoproterozoic crust (Chacksfield, 1993; Everaerts, 2000; Sintubin & Everaerts, 2000). The superficial magnetic features all correspond to magnetic Palaeozoic sediments of the different massifs.

Objectives and methodology

The general aim of this thesis is to improve our understanding of the structure of the Belgian crust, especially the lower and middle crust. This will be achieved by using a local seismic tomography. Because it is important that the initial model, used to start the tomographic inversion, corresponds well to reality, the Moho depth (or the crustal thickness) is determined first. The thickness of the crust is determined according to a self-developed method (see Chapter 3) that uses the arrival times of P- and S-waves from local earthquakes. These waves do not only contain information on the velocity structure of the crust but also on the Moho depth. This will provide a first estimate of the crustal thickness underneath Belgium, especially underneath the Brabant Massif. It is clear that to determine accurate Moho depths and tomographic results, the used earthquakes have to be very well constrained in space and time. The most accurately located local earthquakes registered by the seismic network of the Royal Observatory of Belgium between 1985 and 2007 are used. To expand the region where the Moho depth can be determined, mine-induced earthquakes in Germany and North Sea explosions are added to the dataset. The earthquakes and explosions are relocated with the programme hypo2000, a programme developed by the Royal Observatory of Belgium, based on hypo71. Afterwards they are classified according to the location error. Only the best-located earthquakes and explosions are used in further steps.

After the classification of the earthquakes and the determination of the Moho depth, the local seismic tomography can finally be performed. In this tomographie, the three-dimensional P-wave velocity distribution (Vp) and the three-dimensional Vp/Vs-ratio structure will be determined with the use of two tomographic programmes , namely SIMULPS (Evans *et al.*, 1994) and INVER3D (Collin, 1998). SIMULPS is a well-known programme that already has been used in several tomographic studies all over the world. INVER3D, however, is a programme developed at the Royal Observatory of Belgium, that has not been used for an extensive three-dimensional tomography yet. The results and procedures of both programmes will be compared because they use different approaches during the tomography inversion.

Finally, the results of this tomography will be compared to the seismic, magnetic and gravimetric data for a better understanding. It might explain why the crust is so different between the north and south of the country and why the middle and lower crust is unreflective on the seismic profiles. The tomographic results and the Moho depth determination might also indicate whether the positive gravimetric anomaly underneath the Campine Basin is caused by a shallower Moho or not.

Main results and structure of the thesis

The first chapter gives an overview of the basic theory needed to be able to understand the methods used in this study. It explains the wave propagation, the ray theory, the theory of the hodochrones and the seismic phases in the crust and upper mantle. A short overview of the seismic methods used in this study to investigate the crustal structure, as well as in older studies, the results of which are presented in chapter 2, is also given. The methods discussed are seismic reflection, wide angle reflection and refraction studies, surface wave analysis, seismic tomography and receiver function analysis.

In chapter 2, a synthesis is presented of the major geological units of the region under study: the Brabant Massif, the Ardennes Allochthon, the Roer Valley Graben, the Eifel Volcanic Province. Per geological unit, a short overview of the superficial geology is given, followed by a complete overview of the middle/lower crust and upper mantle studies. The gravimetric and magnetic data are discussed at the end of this chapter.

Chapter 3 discusses the state of the data set, why the data set is relocated, the method used to relocate this data set and the evaluation of this relocation.

The fourth chapter explains the method used to determine the Moho depth, followed by the representation and interpretation of the results. For the first time, the Moho depth has been determined underneath the onshore Brabant Massif. A double reflection can also be seen underneath the Eifel Volcanic Province. The best frequency band to visualise the Moho depth has also been evaluated.

In the last chapter, the theory behind seismic tomography will be discussed first, followed by the explanation of the method used. At the end of the chapter, the results are presented and interpreted. The superficial geological structures can also be observed in the velocity structure of the first 4.5 km. The batholith determined on the gravimetric data cannot be seen in the seismic velocity structure. Lower crust velocities are detected in the middle crust underneath the Eifel Volcanic Province, offering an explanation for the double reflection determined at the same place with the Moho depth determination.

Chapter 1 Seismic methods and crustal structure

1.1 Theory of wave propagation

In an elastic homogeneous isotropic medium, when a wave propagates away from a source, the relation between stresses and displacements is given by the homogeneous equation of motion, which includes no body force (Stein & Wysession, 2002):

$$\sigma_{ij,j}(x,t) = \rho \frac{\partial^2 u_i(x,t)}{\partial t^2} \tag{1.1}$$

This equation can be entirely resolved in terms of displacement because the stress is related to the strain, by the Hooke law.

So when equation (1.1) is solved for the x component of a Cartesian coordinate system:

$$\frac{\partial \sigma_{xx}(x,t)}{\partial x} + \frac{\partial \sigma_{xy}(x,t)}{\partial y} + \frac{\partial \sigma_{xz}(x,t)}{\partial z} = \rho \frac{\partial^2 u_i(x,t)}{\partial t^2} \tag{1.2}$$

The derivatives of the stress components are deduced from the strains in terms of displacement:

$$\sigma_{xx} = \lambda\theta + 2\mu \frac{\partial u_x}{\partial x} \tag{1.3}$$

$$\sigma_{xy} = \mu\left(\frac{\partial u_x}{\partial y} + \frac{\partial u_y}{\partial x}\right) \tag{1.4}$$

$$\sigma_{xz} = \mu\left(\frac{\partial u_x}{\partial z} + \frac{\partial u_z}{\partial x}\right) \tag{1.5}$$

Finally this equation becomes:

$$\rho \frac{\partial^2 u_x}{\partial t^2} = (\lambda + \mu)\frac{\partial \theta}{\partial x} + \mu \nabla^2 u_x \tag{1.6}$$

where θ represents the cubic dilatation ($\nabla \bar{u}$); u_x represents the x component of the displacement vector $\bar{u}$, t represents time and ρ represents density. The Lamé constants λ and μ are independent when the medium is isotropic and homogeneous. μ is called the shear modulus or rigidity and represents the resistance of the material against shear.

Similar equations can be obtained when equation (1.1) is resolved for the y and z component. The three components can be combined into a single vector equation:

$$\rho \frac{\partial^2 u(x,t)}{\partial t^2} = (\lambda + \mu)\frac{\partial \theta}{\partial x} + \mu \nabla^2 u(x,t) \tag{1.7}$$

The theorem of the Helmholtz decomposition gives the solution of the equation as a sum of two potentials: a scalar potential ϕ and a vector potential ψ (Aki & Richards, 1980):

$$\bar{u}(x,t) = \bar{\nabla}\emptyset(x,t) + \bar{\nabla} \times \bar{\psi}(x,t) \tag{1.8}$$

with the following vector entities:

$$\begin{cases} \bar{\nabla} \times \bar{\nabla}\emptyset = 0 \\ \bar{\nabla} \cdot (\bar{\nabla} \times \bar{\psi}) = 0 \end{cases} \tag{1.9}$$

This finally gives:

$$\nabla\left((\lambda + 2\mu)\nabla^2\emptyset - \rho\frac{\partial^2\emptyset}{\partial t^2}\right) + \bar{\nabla} \times (\mu\nabla^2\bar{\psi}\rho\frac{\partial^2\bar{\Psi}}{\partial t^2}) = 0 \tag{1.10}$$

This results in the following conditions:

$$\begin{cases} \nabla^2\emptyset - \dfrac{\rho}{\lambda + 2\mu}\dfrac{\partial^2\emptyset}{\partial t^2} = 0 \\ \nabla^2\bar{\psi} - \dfrac{\rho}{\mu}\dfrac{\partial^2\bar{\psi}}{\partial t^2} = 0 \end{cases} \tag{1.11}$$

These two equations have the same form as the equation for a classical wave:

$$\frac{\partial^2\bar{\psi}}{\partial t^2} = \mathrm{v}^2\,\nabla^2\bar{\psi} \tag{1.12}$$

where v represents the propagation velocity.

1.1.1 P-waves

The first part of equation (1.11) represents the transmission of a dilatation in an elastic medium with a velocity:

$$v_P = \sqrt{\frac{\lambda + 2\mu}{\rho}} \tag{1.13}$$

It describes a wave that propagates in a way creating zones of dilatation and compression. The vibration of the particles is parallel to the axis of propagation. They are called longitudinal or primary (P) waves because they arrive first at the surface, due to their larger propagation velocity.

1.1.2 S-waves

The second part of equation (1.11) explains the propagation of the shear waves ($\overline{\nabla} \times \bar{u}$). The velocity of propagation equals:

$$v_S = \sqrt{\frac{\mu}{\rho}} \tag{1.14}$$

In the case of the S-waves, particles oscillate in a plane perpendicular to the axis of propagation of the wave. They are called transverse, torsion or secondary waves; because they are slower than P-waves they; arrive second at the surface. Because no shear mode exists in liquids, S-waves do not propagate in this medium.

1.2 The ray theory

The solution of the P- and S-waves in equation (1.11) gives us the position of the wave front. The wave front is the group of points that move in the same way at the same moment, forming a three-dimensional surface. The ray is defined as the normal of the wave front; its direction is thus identical to the direction of propagation of the waves. In this paragraph the travel time along rays will be calculated.

This equation can be seen as an approximation of the wave equation after applying the high-frequency approximation and is called eikonal equation. Its inverse is called the “refraction index”, denoted as n. The ray is one of the solutions of this equation.

$$(\frac{\partial W(\bar{x})}{\partial x})^2 + (\frac{\partial W(\bar{x})}{\partial y})^2 + (\frac{\partial W(\bar{x})}{\partial z})^2 = \frac{c_0^2}{c^2(\bar{x})} \tag{1.15}$$

where c_0 is the real velocity of the wave and c_x is the apparent velocity of the wave in the x-direction.

Because the earth fulfils these conditions, the solution is a good approximation of reality.

The solution of this equation is given by W(x,y,z). This function represents a three-dimensional surface and a ray normal to this wave front. For any given W, at any given instant, all the points of this surface W have the same phase, but not necessarily the same amplitude.

This ray travels through a circular arc with length s, during a time t. We call $\frac{dx}{ds}$, $\frac{dy}{ds}$, $\frac{dz}{ds}$, the direction cosines of the ray.

They need to satisfy:

$$(\frac{dx}{ds})^2 + (\frac{dy}{ds})^2 + (\frac{dz}{ds})^2 = 1 \tag{1.16}$$

Moreover, because the gradient of a function is the normal of this function, we obtain:

$$\nabla W(\bar{x}) \propto s \tag{1.17}$$

The direction cosines of the ray are thus proportional to each of the gradient components of the function defining the wave front.

The equation (1.16) becomes:

$$(a\frac{\partial W(\bar{x})}{\partial x})^2 + (a\frac{\partial W(\bar{x})}{\partial y})^2 + (a\frac{\partial W(\bar{x})}{\partial z})^2 = 1 \tag{1.18}$$

where a, the proportionality factor, equals:

$$\frac{c(\bar{x})}{c_0} \tag{1.19}$$

This is the eikonal equation.

The normal equations are found from the equations (1.16), (1.18):

$$n\frac{dx}{ds} = \frac{\partial W(\bar{x})}{\partial x} \tag{1.20}$$

$$n\frac{dy}{ds} = \frac{\partial W(\bar{x})}{\partial y} \tag{1.21}$$

$$n\frac{dz}{ds} = \frac{\partial W(\bar{x})}{\partial z} \tag{1.22}$$

The variation of this equation along the ray is given by:

$$\begin{aligned}\frac{d}{ds}\left(n\frac{dx}{ds}\right) = \frac{d}{ds}\left(\frac{\partial W(\bar{x})}{\partial x}\right) = \frac{\partial}{\partial x}\left[\frac{\partial W(\bar{x})}{\partial x}\frac{dx}{ds} + \frac{\partial W(\bar{x})}{\partial y}\frac{dy}{ds} + \frac{\partial W(\bar{x})}{\partial z}\frac{dz}{ds}\right] \\ = \frac{\partial}{\partial x}\left\{n\left[\left(\frac{dx}{ds}\right)^2 + \left(\frac{dy}{ds}\right)^2 + \left(\frac{dz}{ds}\right)^2\right]\right\} = \frac{\partial n}{\partial x}\end{aligned} \tag{1.23}$$

This gives the equation of the trajectory of the ray:

$$\frac{d}{ds}\left(n\frac{dx_i}{ds}\right) = \frac{\partial n}{\partial x_i} \qquad \text{i=1,3} \tag{1.24}$$

This is a differential equation of second order for which the two principal conditions are:

- The direction of the ray in a reference point is given by: $\left(\frac{\partial \bar{x}}{\partial s}\right)_{s_0}$

- The position of the reference point is s_0

In a horizontally stratified half space (Figure 1.1), we see that:

$$\begin{cases} \frac{dx}{ds} = \sin(\theta) \\ \frac{dz}{ds} = \cos(\theta) \end{cases} \quad (1.25)$$

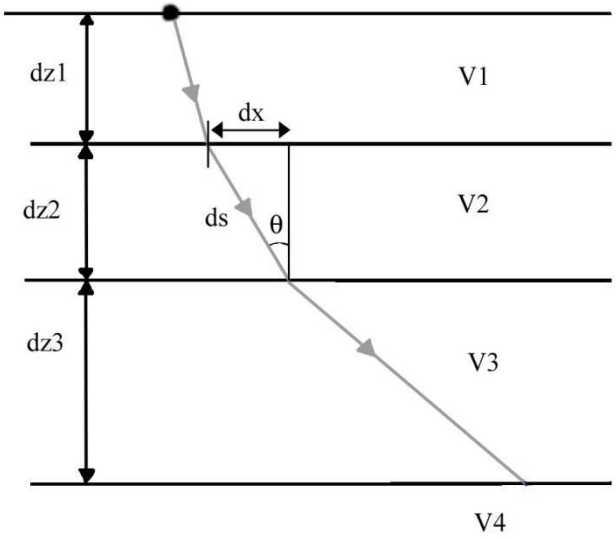

Figure 1.1: Wave propagation in a layered half space
V1 < V2 < V3 < V4: the seismic velocity for respectively layer 1,2,3 and 4; dz1, dz2 and dz3: thickness of the different layers; θ: the incidence angle of the ray and can be easily determined from the ray path length (ds) and the horizontal distance travelled in a layer (dx).

The angle θ measures the inclination of the ray to the vertical and is called the incidence angle. The two preceding relations allow us to derive Snell's law:

$$n\frac{dx}{ds} = \frac{\sin(\theta)}{c(z)} = p \quad (1.26)$$

where p is called the ray parameter. It varies between 0 and $\frac{1}{c_{zmax}}$. 0 corresponds to an angle θ of 0° (the ray is horizontal) and $\frac{1}{c}$ corresponds to an incidence angle of 90° (the ray is vertical). The ray parameter is constant along the entire trajectory of the ray, from the source until the earth's surface (for instance).

We can thus remark that when the propagation velocity of the P-waves increases with depth, the ray gets more and more curved upward.

$$\frac{di}{ds} = \sin(\theta)\frac{c}{c^2}\frac{dc}{dz} = p\frac{dc}{dz} \tag{1.27}$$

If we consider that the propagation velocities in the earth's interior increase, not in a continuous way, but discontinuously, we can consider that, like optical rays, the seismic rays are refracted on virtual and real interfaces between different layers, characterised by different propagation velocities.

1.3 Hodochrones for a stratified horizontal half space

How and when a ray hits the surface will be calculated for a velocity model in which the seismic velocity increases in a continuous way (Figure 1.2) with depth as is the general tendency in the earth's crust.

In paragraph 1.2, the ray parameter and the following relation were determined:

$$n\frac{dx}{ds} = \frac{\sin(\theta)}{c(z)} = p \tag{1.28}$$

$$\begin{cases} \dfrac{dx}{ds} = \sin(\theta) \\ \dfrac{dz}{ds} = \cos(\theta) \end{cases} \tag{1.29}$$

From these relations, it can be determined that for an infinitesimal horizontal distance dx, the ray path ds and the travel time dt can be deduced:

$$dx = ds\ \sin\theta = \frac{dz}{\cos\theta}cp = \frac{cp}{\sqrt{1-c^2p^2}}dz \tag{1.30}$$

$$ds = \frac{dz}{\sqrt{1-c^2p^2}}$$

$$dt = \frac{ds}{c} \tag{1.31}$$

So when the receiver is at the same depth of the source, the horizontal distance and propagation time are given by:

$$X = 2\int_0^Z \frac{cp}{\sqrt{1-c^2p^2}}dz \tag{1.32}$$

$$T = 2\int_0^Z \frac{dz}{c\sqrt{1-c^2p^2}} = 2\int_0^Z \frac{dz}{c^2\sqrt{\frac{1}{c^2}-p^2}} \tag{1.33}$$

In a time-distance graph, the relation between the arrival time and horizontal distance between the source and receiver is given by the following formula:

$$T = pX + 2\int_0^Z \sqrt{\frac{1}{c^2}-p^2}\,dz \; = pX + \tau_p \tag{1.34}$$

which is the equation of a straight line with the ray parameter as the slope and τ_p as the intersection of the straight line and the time axis.

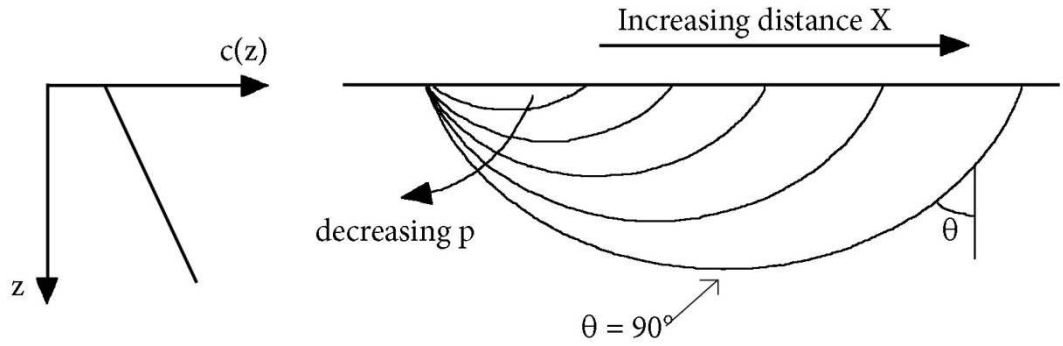

Figure 1.2: Ray path geometry in a velocity model with a constant increase.
Velocity model with a constant increase in velocity with depth (on the left) and the corresponding geometry of rays passing through this velocity model (on the right). z: depth; c(z): velocity: p: ray parameter and θ: incidence angle

In fact, the earth's crust is more complicated than could be described by a simple, constant increase in velocity. It can occur that there are layers in which the velocity increases faster than the surrounding velocities, or layers with lower velocity can be involved. In the first case, when the rays hit the zone in which the velocity increases faster, rays arrive at the surface faster and a zone with triple arrival times appears (Figure 1.3). In the second case, when the rays hit the zone with lower velocity, they arrive at a larger distance from the source, leaving a zone where no rays hit the surface, also called a shadow zone (Figure 1.4).

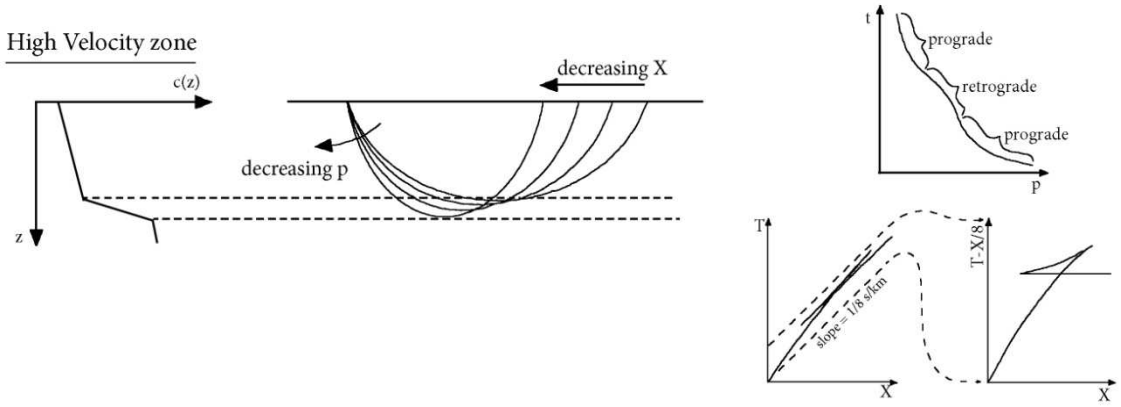

Figure 1.3: Ray path geometry in a velocity model with high-velocity layer.
Velocity model with a layer in which the velocity increases faster (on the left) and the corresponding geometry of rays passing through this velocity model (in the middle). On the right hand side, the corresponding time-distance graph. z: depth; c(z): velocity: p: ray parameter, T: time and X: distance

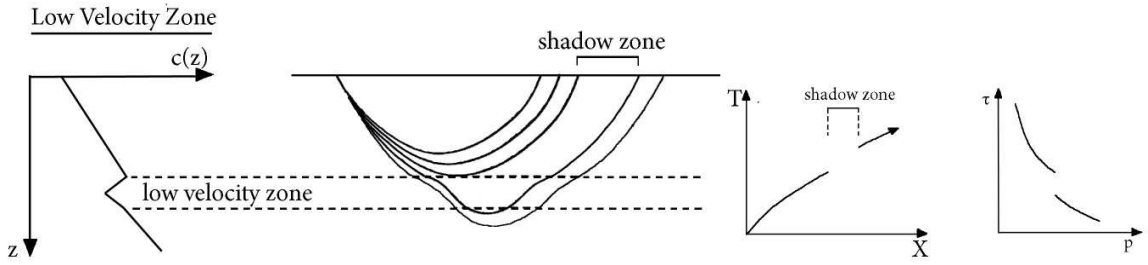

Figure 1.4: Ray path geometry in a velocity model with a low-velocity layer.
Velocity model with a layer with lower velocity (on the left) and the corresponding geometry of rays passing through this velocity model (in the middle). On the right hand side, the corresponding time-distance graph. z: depth; c(z): velocity: p: ray parameter, T: time and X: distance

1.4 Seismic phases related to the crust and upper mantle

The earth's crust is not just composed of a gradual continuous velocity increase or decrease. In some cases, there are horizons along which a high velocity contrast can be deduced. So, they act as discontinuities. Then, three waves can be detected, namely the direct (Pg), the refracted (Pn) and the reflected (PmP, the on the Moho reflected P-wave) wave (Figure 1.5). The arrival times of these waves are given respectively by the formulas (1.35), (1.36)and (1.37):

$$t(X)_g = \frac{\sqrt{X^2 + Z^2}}{v_0} \tag{1.35}$$

$$t(\nabla)_n = \frac{\nabla}{v_1} + 2h_0 \sqrt{\frac{v_1 + v_0}{v_1 - v_0}} \tag{1.36}$$

$$t(\nabla)_m = \frac{\sqrt{\nabla^2 + (2h_0 - z)^2}}{v_0} \tag{1.37}$$

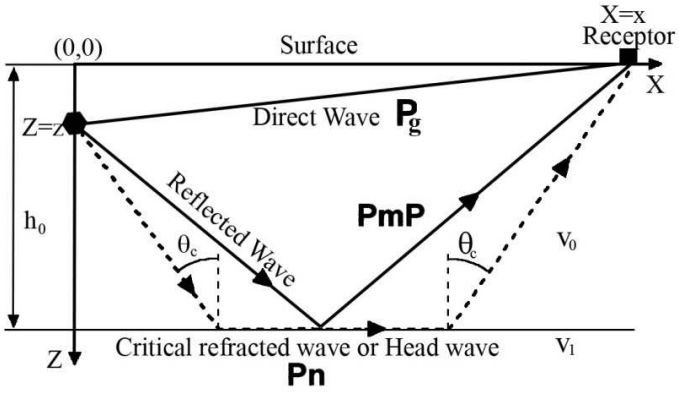

Figure 1.5: Three basic ray paths for a layer over a halfspace model.
As can be seen in this graph, the direct and reflected rays travel within the layer, whereas the head wave ray path also includes a segment just below the interface and thus travels faster, because V_1 is a higher velocity then V_0. h_0 is the depth of the layer, θ_c the critical incidence angle, z the depth of the source and x the horizontal distance between the receptor and the source. After: Stein & Wysession, 2002.

These formulas can be plotted as a travel time versus distance plot (Figure 1.6), which shows that, because the velocity v_1 is higher than the velocity v_0, the travel time curve of the direct wave has a higher slope and starts at the origin (Figure 1.6), whereas the refracted wave has a lower slope but a nonzero intercept. The head wave does not exist at small distances, because the critical angle has to be attained before the head waves exist. The distance at which the refracted wave occurs for the first time is called the critical distance. Because the velocity is higher in the layer below, it is easy to see that after a certain distance the refracted wave arrives before the direct wave. This point is called the cross-over distance. This distance depends on the velocities of the two layers and the thickness of the top layer. This distance is found by $t(\nabla)_g = t(\nabla)_n$ or:

$$\nabla_d = 2h_0 \sqrt{\frac{v_1 + v_0}{v_1 - v_0}} \tag{1.38}$$

So from these travel time distance plots (Figure 1.7), the velocity structure at depth can be determined. The slopes of the different branches of the plot determine the velocity of the different layers, the cross-over distance determines the depth of the layer or alternatively, the intersection of the refracted wave with the zero distance (intercept-time).

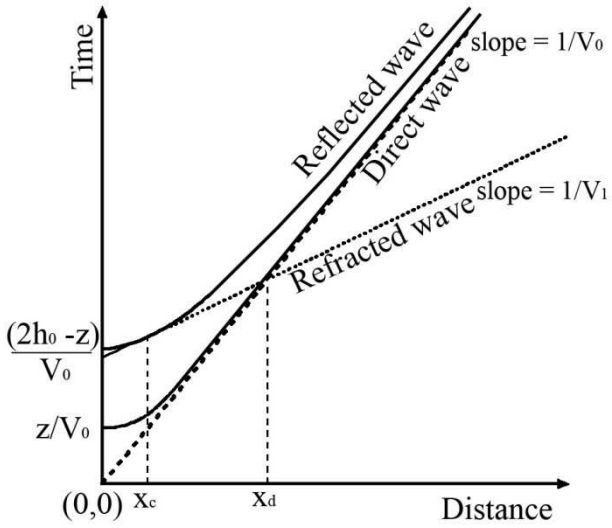

Figure 1.6: Travel time versus distance plot for three ray paths in Figure 1.5.
The direct wave is the first arrival for receivers closer than the cross-over distance Xd. Beyond Xd the refracted wave arrives first. The refracted wave only exists beyond the critical distance Xc. Z: depth of the source, h_0: thickness of the layer, $V_0 < V_1$: velocity of the waves traveling respectively through layer 0 and 1. After: Stein & Wysession, 2002.

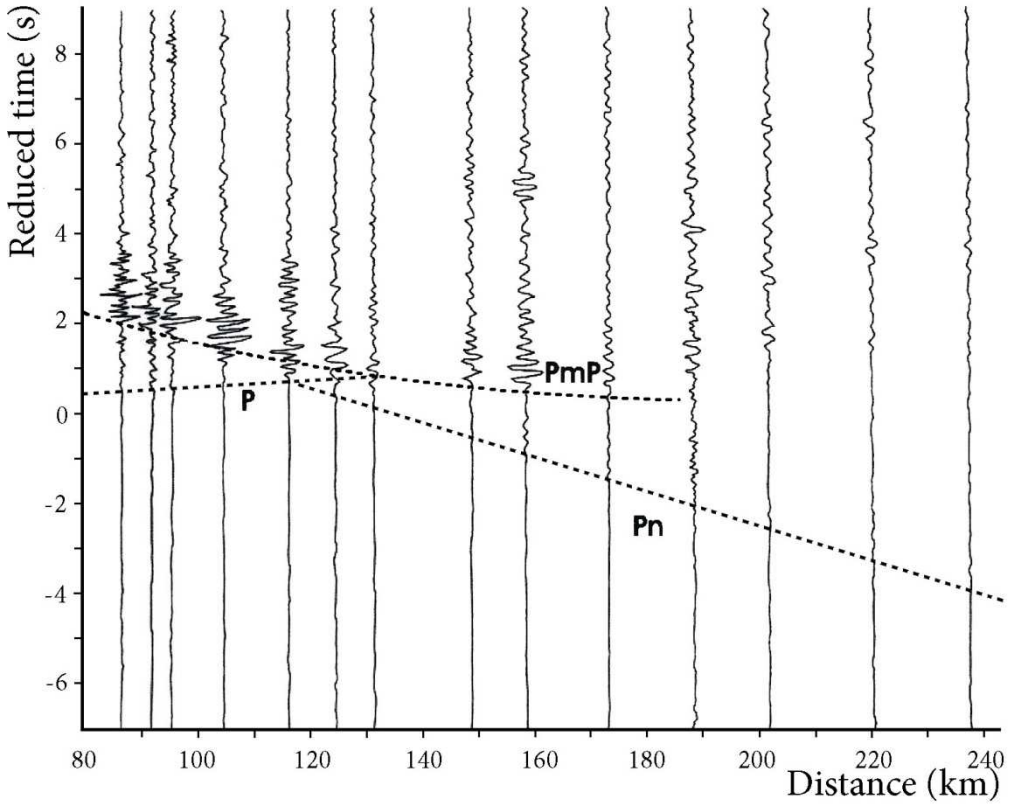

Figure 1.7: Travel time versus distance plot for the three ray paths in Figure 1.5 deducted from real seismograms in a reduced time-distance plot.
The direct wave is the first arrival for receivers closer than the cross-over distance Xd. Beyond Xd the refracted wave arrives first. The refracted wave only exist beyond the critical distance Xc. In a reduced time graph, the arrival time of the different waves are diminished by the distance between the source and the receiver divided by a chosen velocity (6 km/s in this graph) After: Stein & Wysession, 2002.

1.5 Seismic methods to investigate the crustal structure

In this paragraph several seismic methods that have been used to study the crustal and mantle structure are described. They all use to some extent the above explained theory and have been used in one or more studies of the Belgian and surrounding regions crust.

1.5.1 Seismic reflection

Seismic reflection studies enable us to study the crustal structure using observed arrivals of seismic waves, reflected on interfaces in the crust, where the acoustic impedance changes. The resolution obtained by this method makes it the main method used by oil exploration to map subsurface sedimentary structures. It has also increasingly been used to obtain information on the fine structures within the crust and the crust-mantle boundary.

In seismic reflection studies, one assumes that there is a stack of horizontal layers in the crust and mantle, each with a distinct acoustic impedance. Dipping layers, faults, etc can be included in the

model. Normal incident P-waves from a surface energy source are reflected on a surface and can be recorded by geophones close to the source.

On land, explosions can be used as a source as well as a gas exploder (a gas mixture explodes in a chamber that has a movable bottom plate resting on the ground) or a vibroseis (in which a steel plate is pressed to the ground and vibrated in increasing frequency (5-60 Hz) for several seconds). The signals are recorded by a set of geophones placed at certain distances from one another and from the source. At sea, airguns (in which a bubble of very-high-pressurized air is released into the water) are mostly used as sources. Both the source and the receivers (a cable with several hydrophones) are towed behind a vessel and the signal is continuously registered.

The disadvantage of this method is that because the P-waves are reflected at almost normal incidence, they are a lot smaller in amplitude than wide angle reflections or refractions, and they are therefore more difficult to recognize than wide angle reflections. As they are more likely to be obscured by background noise, sophisticated averaging techniques have to be used to detect near vertical reflections at depth. A way to improve the signal to noise ratio is to average the signals from nearby receivers to enhance reflections and reduce the background noise. This averaging is called stacking. A common-midpoint stacking combines all the traces that have the same midpoint (Figure 1.8). In order to be able to stack these traces, one must correct them for their different travel times due to different offsets. This correction is called normal-moveout correction and is given by:

$$\Delta t_{NMO} = \frac{x^2}{2v_0^2 t_0} \tag{1.39}$$

for a one layer case, with t_0 the vertical two way travel time, x the offset between the source and the receiver and v_0 the velocity of the first layer.

The calculated value has to be subtracted from all the traces so that the signals line up. After which they can be averaged out. All these processes result in a profile with distance in the x-direction and two-way travel time in the y-direction (Figure 1.9) on which reflections at different layers can be seen, and the geometry of these layers can be followed along the profile.

Several seismic reflection profiles both on land (BELCORP, ECORS and DEKORP profiles) and at sea (BIRPS profiles, MPNI-9101 profile) were shot in and around the Belgian territory. The BELCORP and DEKORP profile were shot using vibroseis with a frequency bandwidth of 12-48 Hz. The ECORS reflection profile has been shot using explosions, the geophones only registered from a frequency of 10 Hz, so lower frequencies were lost. For the profiles shot at sea, the MOBIL campaign used less airguns with a lower volume than the campaign that shot the MPNI profile. So, it is possible that on the MOBIL profiles no Moho reflections are seen underneath the Brabant Massif due to the frequency range and penetration depth attained with the type and amount of airguns used, whereas on the MPNI profile some Moho reflections can appear.

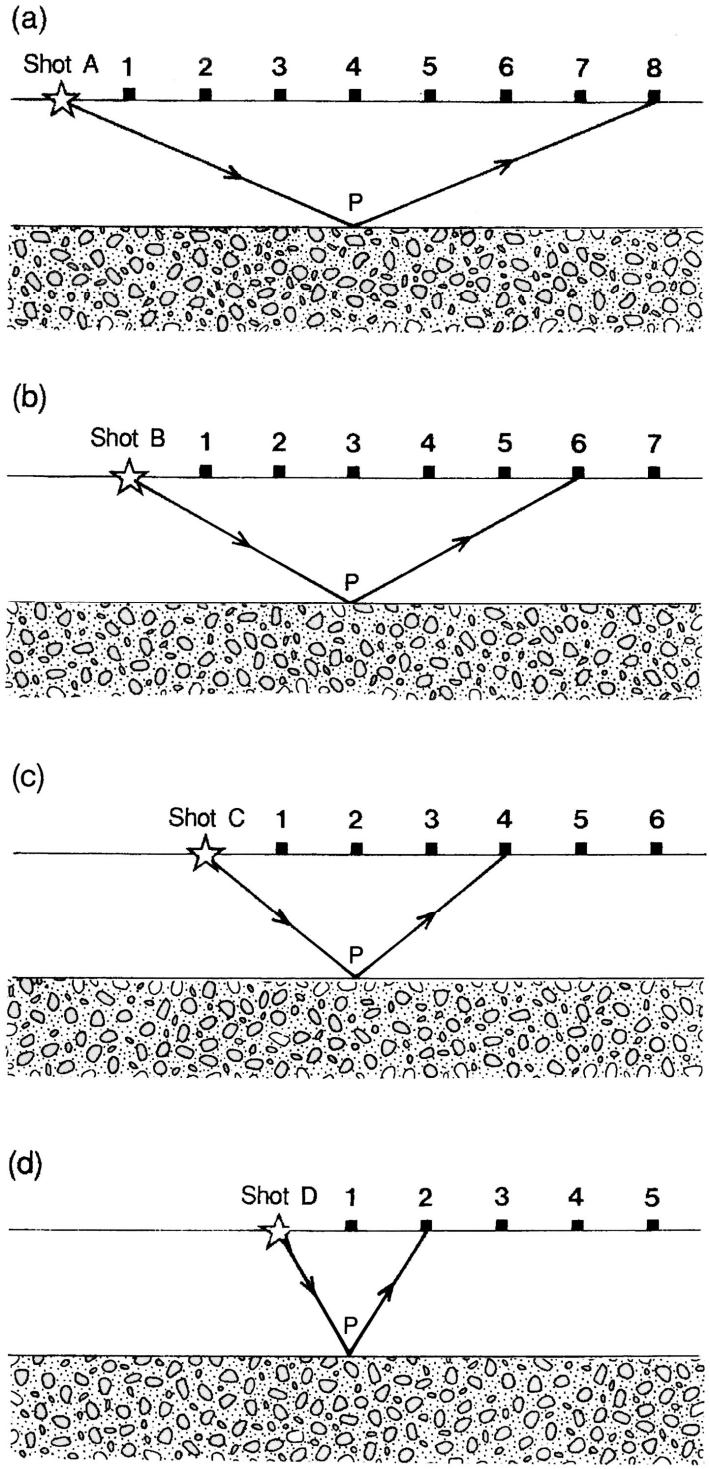

Figure 1.8: Schematic representation of common midpoint stacking.
In this example, 8 geophones (squares) record each shot (star). In (a), shot A is fired and a reflection from a particular point P on the reflector (the interface between two layers) is recorded by geophone 8. In (b), all the geophones and the shotpoint have been moved one step to the right and the reflection in the same point P is now registered by geophone 6. In (c) and (d), the geophones and shotpoints have again been moved to the right and this time, the reflection in the same point P is registered by geophone 4 and 2 respectively. After: Fowler, 2005.

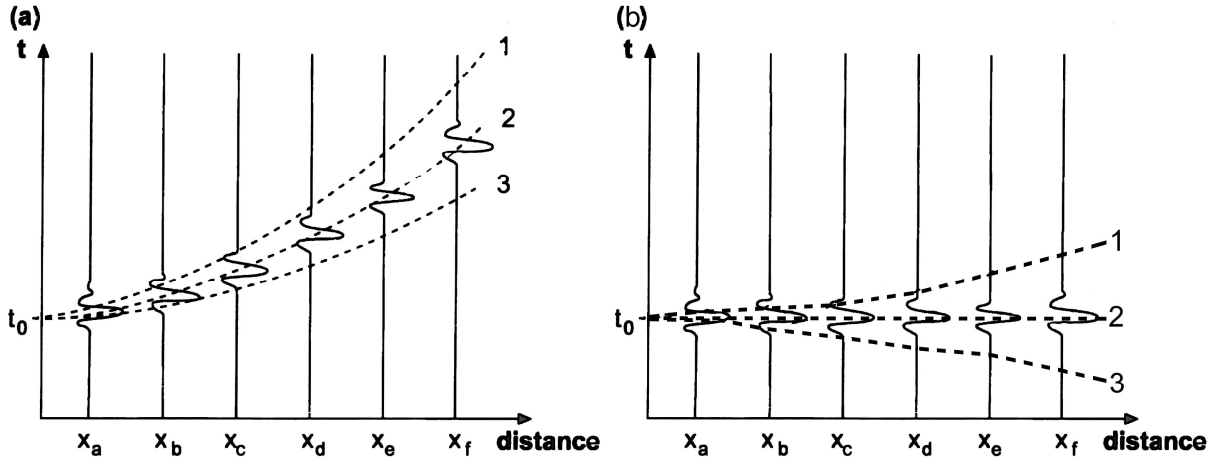

Figure 1.9: Schematic representation of the Nmo-correction.
(a) Reflections from an interface, recorded at distances xa, xb, xc, xd, xe and xf. Three travel time curves (1, 2 and 3) are shown for two-way-normal-incidence time t0 and increasing values of velocity. Clearly curve 2 is the best fit to the reflections. To stack the traces, the NMO time-correction for curve 2 is subtracted (b) from each trace so that the reflections line up with a constant arrival time t0. Then, the traces can be added to yield a final trace with increased signal-to-noise ratio. After: Fowler, 2005. (b) The same reflections from an interface, recorded at distances xa, xb, xc, xd, xe and xf after NMO-correction for curve 2 and ready for stacking.

1.5.2 Wide angle reflection and refraction

Refraction seismic studies are very straightforward. They allow obtaining the evolution of the propagation of P-waves (Vp) in function of depth directly from identifying travel-time branches, measuring their slopes, cross-overs and amplitude behaviour along the branches as is discussed in the previous paragraph 1.3. They can be related to one-or two dimensional models of the primary layers of the crust.

Wide-angle reflection studies use wide angles of incidence (close to the critical angle) because they graze along the discontinuities and they are primarily sensitive to velocity changes and not to changes in density. The P-waves constrain the P-velocity contrast only, the S-waves, the S-velocity discontinuity.

In this study, the problem with these hodochrones is that the Pn-wave of earthquakes is mostly not very energetic, making it difficult to determine the cross-over distance correctly. Second problem is the fact that earthquakes have an irregular occurrence both in location and time and therefore, the receivers are not always positioned in an exact profile as is needed for the hodochrones.

1.5.3 Surface wave analysis

As the title mentions, this technique focuses on seismic waves that travel along the surface. These waves are dispersive, this means that their propagation velocity differs with frequency. On top of that, their penetration depth decreases when frequency increases. For a superficial source, like a quarry blast, these waves are amongst the most energetic and their dispersivity can be used to determine the variation with depth of the S-wave velocity.

The first step in the method consists in calculating the dispersion curve that links the velocity with the frequency. This curve can be determined for either the group velocity or for the phase velocity. A variety of numeric techniques have been proposed in the last 20 years to calculate and interpret the dispersion curves. An overview is given by Officer (1974), Stein & Wysession (2003) and Fowler (2005). Once the curves are determined, they are inversed so that a stratified Vs-structure can be found. Because this is a non-linear problem, the solution can only be found by an iterative procedure. An advantage of this method is that one only needs a small number of seismic stations. In the short period domain (periods lower than one second), the method allows to study the first few kilometers of the crust. In the long period domain (periods of several seconds to several hundreds of seconds), surface waves are used to determine the structure of the lower crust and mantle.

The Belgian seismic network is only equipped with 7 broadband stations, so only partial information can be obtained of the mantle from a surface wave analysis. More information can be obtained in the short period domain as most Belgian seismic stations are short period seismometers. A similar study was performed by Jongmans & Camelbeeck (1994) on the Stavelot Inlier.

1.5.4 Seismic tomography

Another technique that is often used to study the lower and middle crust is a local seismic tomography. With this technique, the velocity structure in the crust is determined in a three-dimensional way from arrival times of seismic waves recorded by seismic stations (Figure 1.10). It uses the same approach as a X-ray CT-scan used in medical practice, but it was developed separately from it in the beginning, it was only later on, at the end of the seventies and eighties that some cross-over between both techniques occurred (Lee & Pereyra, 1993).

The goal of a local earthquake tomography is to improve the estimates of the model parameters (hypocenters and velocity structure) by perturbing them in order to minimize the misfit between the calculated and the observed arrival times. This generally requires an iterative procedure, because the hypocenter locations are inherently coupled to the velocity structure in equation (1.40) can lead to significant non-linearity (See chapter 5 paragraph 5.2.4). Various estimates of the solution quality are also desired, such as the matrix of resolution and uncertainty, as well as improvement in data fit and uniqueness of the final solution.

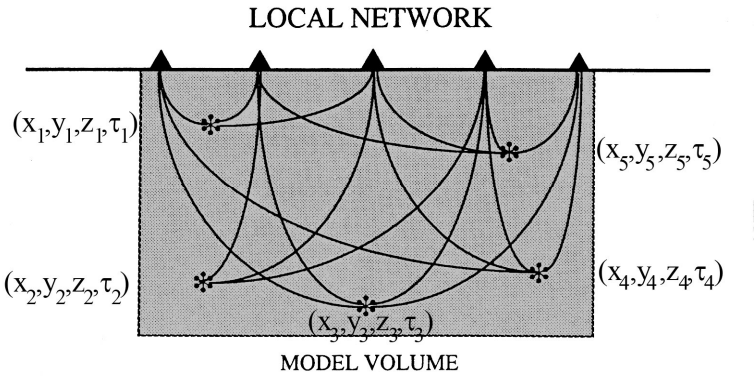

Figure 1.10: Schematic representation of a local earthquake tomography problem.
A seismic network (triangles) covers the area of geologic interest, and earthquake sources (flowers) are distributed within the model volume. The lines represent the ray paths between the earthquake sources and the stations. After: Thurber, 1993.

The body wave travel time T_{ij} from an earthquake i to a station j is expressed using the ray theory (see paragraph 1.3) as a path integral:

$$T_{ij} = \int_{source}^{receiver} uds \tag{1.40}$$

where u=u(x,y,z) is the slowness field (reciprocal of velocity) at location (x,y,z) and ds is the element of path length in a small volume around x,y,z. The actual observations are the arrival times t_{ij} of the different seismic phases, which can be expressed as:

$$t_{ij} = \tau_i + T_{ij} \tag{1.41}$$

where τ_i is the origin time. In fact, the only known elements in this problem are the receiver locations and the arrival times (that suffer some uncertainty). The source coordinates (x_i, y_i, z_i), the origin time (τ_i), the ray path and the slowness field are all unknown and the objective is to determine them.

When a set of arrival times t_{ij}^{obs} measured at a network of stations (times of first P- and /or S-waves) is known, the calculated arrival times t_{ij}^{cal} are determined from equations (1.40) and (1.41) using trial hypocenters and arrival times and an initial model of the seismic velocity structure. The differences between the observed and calculated arrival times are the residuals r_{ij}.

$$r_{ij} = t_{ij}^{obs} - t_{ij}^{cal} \tag{1.42}$$

The residuals can be related to the increment of the hypocenter location, earthquake origin time, and the velocity structure parameters that will minimize the difference between t_{ij}^{obs} and t_{ij}^{cal} by a linear approximation:

$$r_{ij} = \sum_{k=1}^{3} \frac{\partial T_{ij}}{\partial x_k} \Delta x_k + \Delta\tau_i + \int_{source}^{receiver} \delta u \, ds \tag{1.43}$$

It should be noted that the lack of information on the hypocenter location parameters is also setting the limits of the integration of the last term in the equation. Equation (1.43) is of the same form for the P- and S-arrival time data. The hypocenter partial derivatives $\frac{\partial T_{ij}}{\partial x_k}$ are proportional to the components of the ray vector, times the seismic slowness at the source point (Thurber, 1986):

$$\frac{\partial T_{ij}}{\partial x_k} = -\frac{1}{V}\left(\frac{dx_k}{ds}\right)_{source} \tag{1.44}$$

Furthermore, if any finite parameterization of the velocity structure is adopted, then equation (1.43) can be written as:

$$r_{ij} = \sum_{k=1}^{3} \frac{\partial T_{ij}}{\partial x_k}\,\Delta x_k + \Delta\tau_i + \sum_{l=1}^{L} \frac{\partial T_{ij}}{\partial m_l}\Delta m_l \tag{1.45}$$

where m_l represents the L parameters of the velocity model. The velocity model partial derivatives $\frac{\partial T_{ij}}{\partial m_l}$ are essentially line integrals along the ray path reflecting the relative influence of each model parameter on a given travel time.

1.5.5 Receiver function analysis

Receiver function analysis uses the recordings from teleseismic earthquakes (distance between epicenter and station is more than 1000 km) to confirm gross crustal and upper mantle boundaries. It is called “receiver function” because the position of the boundaries is determined for every “receiver” or every seismic station. Where several receivers are positioned in a study area, crustal thickness maps can be drawn. It uses P- to S-conversions at these boundaries that arrive after the direct P-wave, most strongly on the horizontal components (Figure 1.11). These P- to S-conversion arrivals are much more visible on the longitudinal component of a seismogram (horizontal component) than on the vertical component. By deconvolving the longitudinal component, the obscuring effects from the source function and the instrument response can be eliminated, leaving a signal that is composed of primarily S-wave conversions below the station. These traces can be inverted towards a model of the shear velocity layering in the crust. These arrival times are then migrated into a 3D subsurface to study the depth of the interfaces.

A receiver function analysis does not provide any information on the absolute velocity structure at the contrasts. It only provides information on the depth of the interfaces and only of the interfaces that have a high enough velocity contrast to form P- to S-conversions like the Moho, the 410 km and the 660 km discontinuity in the mantle. This method is thus mostly used to study the upper mantle structure and besides information on the Moho depth, does not provide a lot of information on the crustal structure. Budweg *et al.* (2006) performed a receiver function analysis on the teleseismic earthquakes registered during the Eifel plume project.

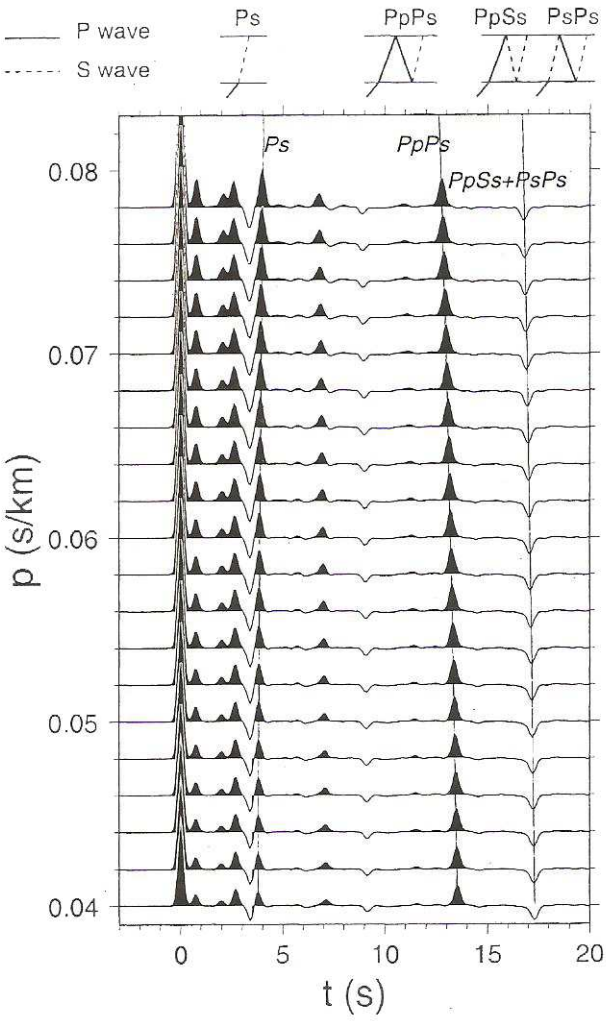

Figure 1.11: Radial receiver function showing the Moho converted phase Ps and the multiples PpPs, PpSs and PsPs. Their ray paths are illustrated at the top. After: Zhu & Kanamori, 2000.

Chapter 2 Geological background - the contribution of geophysics to the knowledge of the crustal structure in Belgium and surrounding regions

2.1 Introduction

The complex geological history of Belgium and its surrounding region resulted in several geological structures (Figure 2.1). The Brabant Massif in the northwest of Belgium is a Caledonian Massif (Verniers *et al.*, 2002) that is covered by a Permian to Quaternary sediment cover that thickens towards the north and south. It can only be studied in a few outcrops in the valleys of some small rivers like the Dendre, Sennette, Samme and Dyle at its southern border. The Brabant Massif is limited in the northeast by a Cenozoic structure namely the Roer Valley Graben. This graben is characterised by a thick sediment cover that has deposited in the graben and is one of the regions with the highest seismic activity (cfr. Roermond Earthquake, 1992 (Camelbeeck *et al.*, 1994)). To the southeast, the Condroz inlier and the Namur "synclinorium" separate the Brabant Massif from the Ardennes Allochthon. Both the thrust and the allochthon are Variscan structures. The internal structure of the Ardennes Allochthon is rather complex and it is composed of several synclinoria and anticlinoria (Figure 2.1). Some Caledonian Inliers (Stavelot, Rocroi, Serpont and Givonne) are exposed in this region. To the east of the Ardennes Allochthon, another Cenozoic structure is situated, namely the Eifel Volcanic Province. Underneath this region, a mantle plume is suspected (Budweg *et al.*, 2006). This chapter will give an overview of the geological history of these different structures. Both the upper crust geology and the knowledge of structures in depth will be discussed.

2.2 Brabant Massif

The Brabant Massif is of early Palaeozoic age and was part of a micro-plate, called Avalonia (Figure 2.2), which extends to the Rhenish Massif in Germany in the east and to the Welsh Basin in Wales in the west (Verniers *et al.*, 2002). The lower Palaeozoic inliers (Stavelot, Rocroi, Serpont and Givonne) located in the Ardennes Allochthon and the Condroz inlier (Figure 2.1) are also part of Avalonia. All these structures have known a similar deformation history but they correspond to slightly different phases in the collision of Avalonia with Baltica and Laurentia during the Brabantian and Ardennian deformation phases.

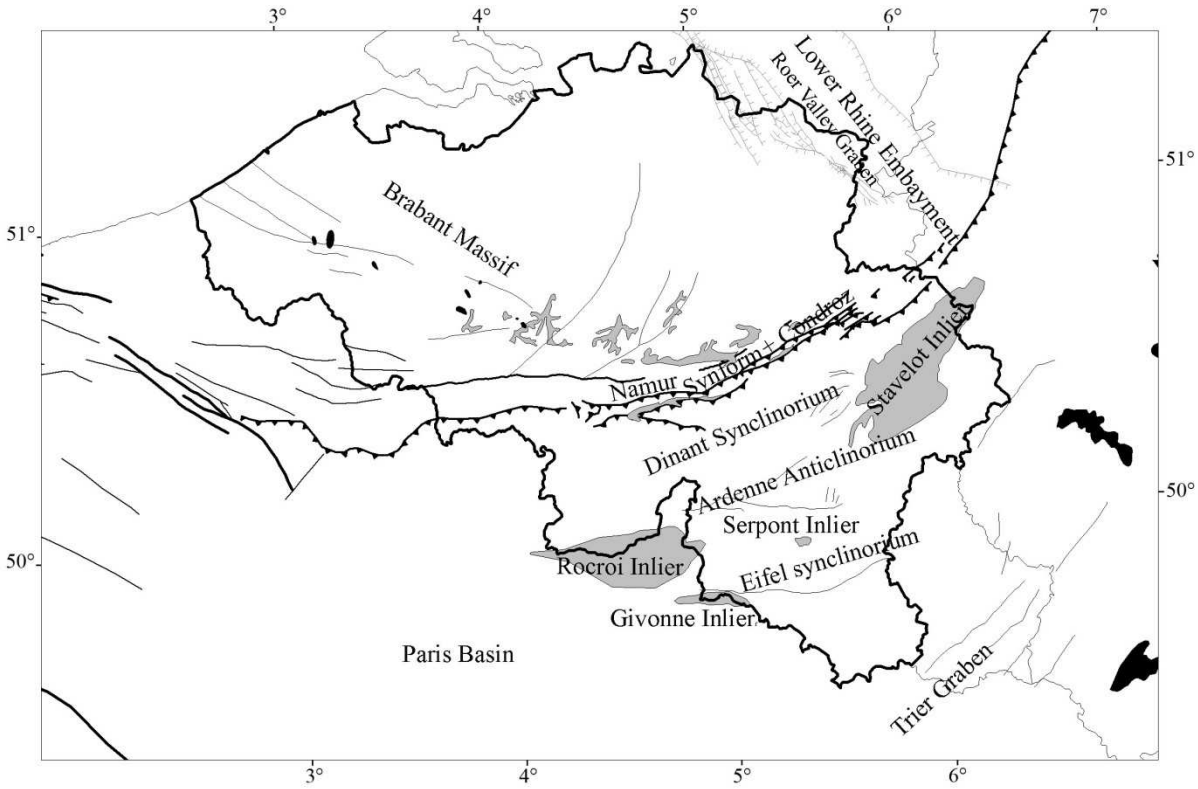

Figure 2.1: Schematic map showing the different tectonic structures of Belgium.
Grey zones = Pre Variscan sediments and Black zones = magmatic rocks. Major Fault lines are also indicated in black and grey as well as the political borders.

During the early Cambrian, a rift formed along the Anglo-Brabant-Ardennes area soon after or during the Neoproterozoic Panafrican Orogeny (Murphy *et al.*, 1999). This structure has played an important role in the later deformation history. Avalonia is considered to be Gondwana-derived as are several other small continents. One of them called Far Eastern Avalonia was situated slightly to the north, with a small ocean in between both continents (Verniers *et al.*, 2002). During Caradoc-Ashgill, subduction magmatism was initiated and turbidites were generated in a tectonically instable region. When Avalonia docked with Baltica, in the late Caradoc or early Ashgill, an anticlockwise rotation started provoking subduction of the oceanic crust between Avalonia and Far Eastern Avalonia, giving rise to calc-alkaline subduction magmatism in the Brabant Massif. This volcanism ended in the Brabant Massif in the early Llandovery, possibly because the oceanic crust had completely subducted. Continuing rotation created the Silurian foreland basin and the long-lived Wenlock to early Eifelian shortening and inversion of the central steep belt of the Brabant Massif. Some areas were shielded from deformation such as the southwestern Brabant Shelf and the Condroz Shelf, possibly because they were situated on top of a Neoproterozoic basement, or a more rigid low density body at depth (see paragraph 2.6 of this chapter). The end of rotation by Eifelian time determined the Brabantian deformation.

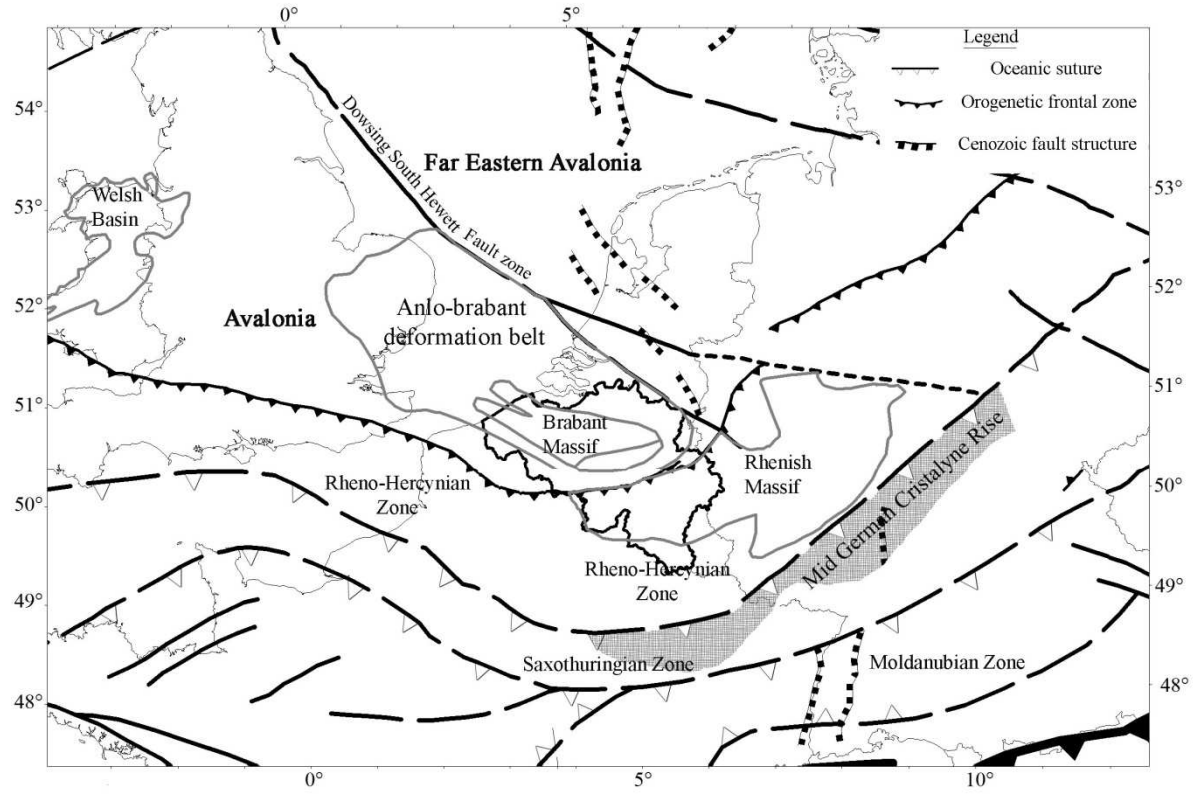

Figure 2.2: Basement tectonic sketch map of NW Europe (redrawn from Verniers *et al.,* 2002). Political borders are indicated in light grey, Belgian borders in black.

2.2.1 Surface Geology

Verniers *et al*. (2002) gives a thorough review of the geological history of the Brabant Massif. A summary is provided in this paragraph. Three megasequences (Vanguestaine, 1992) can be determined in the Brabant Massif: Megacycle 1 with lower Cambrian to Tremadocian units, megacycle 2 with Arenig to Caradoc units and megacycle 3 with Ashgill to Silurian units. The base of megasequence 1 on a supposed Neoproterozoic crystalline craton is not observed. The presence of this craton however is inferred from inclusions in xenoliths in the upper Ordovician magmatic rocks, from lithic fragments with a predominance of metavolcanic rocks in the lower Cambrian sediments (Vander Auwera & André, 1985; André, 1991) and from the presence of colourless euhedral zircons which were formed during a magmatectonic event dated as latest Proterozoic (U-Pb data from 530-600 Ma; Von Hoegen *et al.*, 1990) in the Blanmont formation. Megasequence 1 contains earliest Cambrian to early Tremadocian, often thick terrigenous and deep sea sediments with greywacke, sandstone and thick sequences of pelagic to hemipelagic mudstone. Coarse-grained sediments occur only in the basal part of the sequence and become finer towards the upper member. At the top of megasequence 1, a substantial hiatus occurs from the lower Tremadocian to the upper part of the middle Arenig (estimated hiatus of about 12 Ma, Verniers *et al.*, 2001). The sediments point to an environment deeper than the shelf.

The terrigenous shallow shelf sediments of megasequence 2 are much thinner than those of megasequence 1. The dark grey mudstone records a rapidly subsiding shelf. Only at the top of

megasequence 2, a drastic change in environment occurs, with sedimentation of turbiditic sequences in a deeper environment.

The transition from megasequence 2 to 3 shows a drastic change from deep water to shelf with a short hiatus in time, less than 1 Ma (Verniers *et al*., 2001). At the bottom muddy sandstone with bioclasts deposited on a shelf evolved to an anoxic dark grey graptolitic mudstone, which is followed by many volcanic and metavolcanic sedimentary rocks deposited on a shallow shelf. From the mid Llandovery two distinct basinal areas developed. In the southwestern Brabant Massif a deep shelf environment persisted while in the north and central Brabant shelf, a turbiditic regime was present on a slope or in a deep basin.

Magmatism

In the Brabant Massif there were three periods of volcanism between the Cambrian and the mid Devonian: two minor ones intercalated in the lower Cambrian and in the lower Tremadocian of megasequence 1. A third major period at the top of megasequence 2, lingering into the base of megasequence 3, dated from mid Caradoc to late Llandovery in the Brabant Massif and continuing into the early Wenlock in the Condroz Inlier.

The interstratified magmatic rocks of Cambrian age have not been studied in detail because their interpretation is made difficult by their interstratified position and the epizonal metamorphic grade. The occurrence of these volcanic rocks might be important, because they could indicate magmatic activity before or during the rifting episode that caused Avalonia to drift away from Gondwana. The late Ordovician to early Silurian magmatism is however well documented in the Brabant Massif. It occurs south of the main axis of the Brabant Massif and is clearly calc-alkaline and probably caused by subduction of oceanic lithosphere beneath the Avalonia microcontinent (André *et al.*, 1986, Van Grootel *et al.*, 1997). It is mostly dacitic in composition with some rhyolites and rare andesitic and basaltic rocks, observed as inclusions within the more felsic rocks. In the Brabant Massif, the volcanic rocks are mostly ash-flow tuffs and volcanic breccias, but also some lava flows and several associated subvolcanic sills or neck-like bodies. Most original structures were lost in the magma because of secondary low temperature paragenesis during the expulsion (André & Deutsch, 1986) and the metamorphism associated with the early Devonian to Eifelian deformation (André *et al*., 1981). Dating of the volcano-sediments shows a peak in magmatic activity in the lower Ashgill.

Tectonometamorphic evolution

The Brabant Massif is characterised by an overall NW-SE structural grain (Debacker, 2001) curving into a more ENE-WNW direction (Debacker, 2001) in the east. The massif shows an apparently symmetrical disposition with a Cambrian core flanked on both sides by Ordovician-Silurian strata. Weakly metamorphosed and deformed lower Paleozoic metasediments are unconformably overlain by undeformed diagenetic Givetian deposits (Legrand, 1967; De Vos *et al.*, 1993; Debacker *et al.*, 1999; Verniers *et al*., 2002). The deformation is characterised by the cogenetic development of folds and cleavage. There is evidence for only one deformation event.

2.2.2 Middle and lower crust

Several geophysical studies (such as seismic profiles and gravimetric and magnetic studies) have been performed in the past to reveal the structure of the middle and lower crust underneath the Brabant Massif. Several seismic profiles, like the BELCORP (Bouckaert *et al*., 1988), ECORS (Matte & Hirn, 1988), BIRPS (Klemperer S. & Hobbs R., 1991) and MPNI-9101 (Rijckers *et al.,* 1993) have been shot on- and offshore at the edges of or over the Brabant Massif (Figure I-3). The information obtained from these profiles is discussed here.

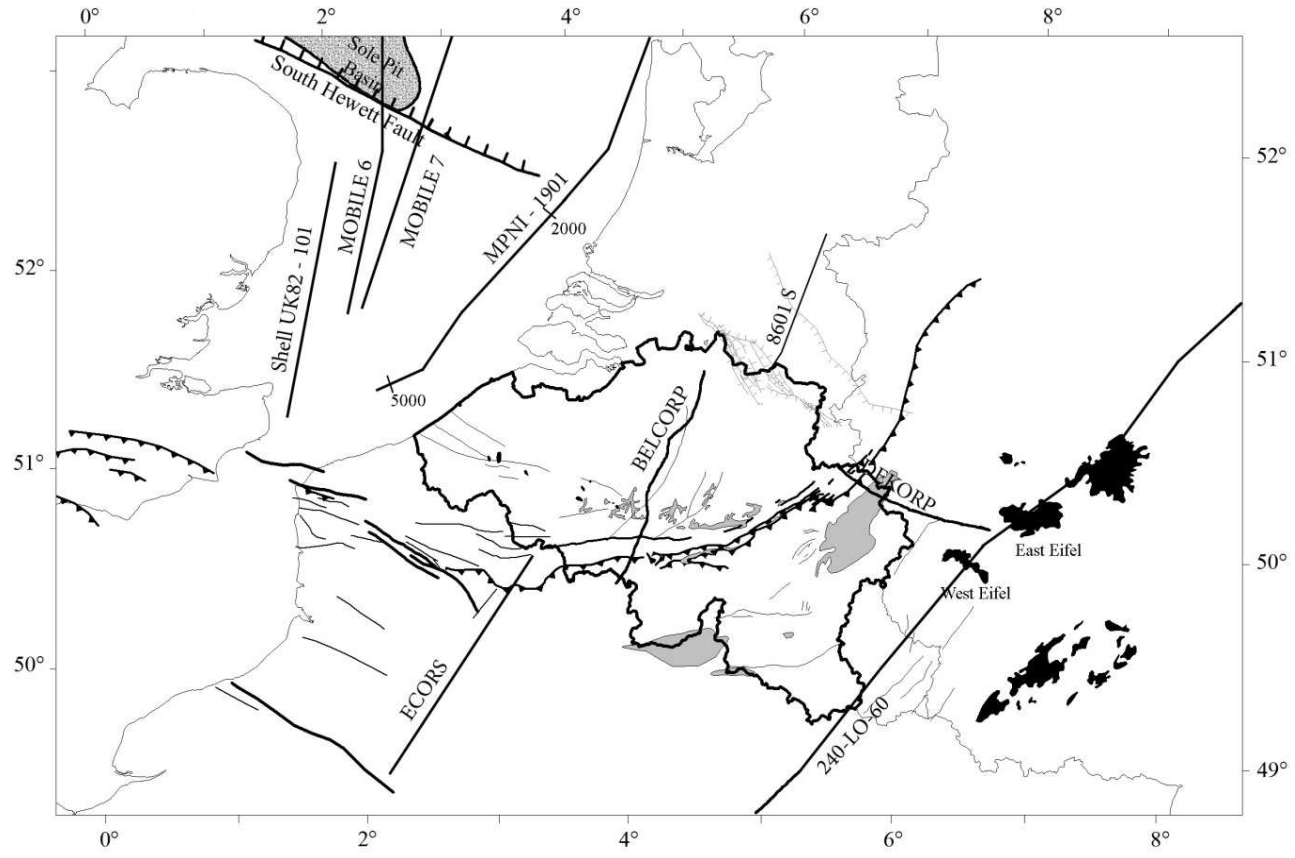

Figure 2.3: Position of the different seismic profiles shot in and around the Belgian territory. Grey zones = Pre Variscan sediments and Black zones = magmatic rocks, dark grey zone: Sole Pit Basin. Major Fault lines are also indicated in black and grey as well as the political borders.

2.2.2.1BELCORP Profile

In 1984, the Begian Geological Survey shot the BELCORP profile (Figure I-3). This profile is related to several other profiles (ECORS, DEKORP) in the region, because they were shot in the framework of the International Lithosphere Project and the European Geotraverse (Bouckaert *et al.,*1988). The BELCORP profile was shot directly over the Brabant Massif (from Turnhout in the north to Jeumont in the south) and should have been able to determine its middle and lower crustal structure. Unfortunately, the lower and middle crust on this profile (Figure 2.4) seems to be unreflective. The only clear reflections are the sediments (from the lower Devonian onward) that cover the Brabant Massif (Figure 2.4). At the location of the Brabant Massif, no strong reflection can be followed over long distances. One can

(after intensive filtering) see some short reflections that can be grouped into zones with similar dip (Figure 2.5). The origin of these short reflections is not clear. Bouckaert *et al.*(1988) interpreted these reflections as alternations of different lithologies from which the longer reflections have been degraded by recrystallization of the rocks. So, they represent the remnants of former larger structures. Bouckaert *et al.* (1988) also tried to determine the Moho depth along the profile. Unfortunately, the normally expected highly reflective lower crust underlain by a transparent mantle is not visible. If they take the lowest limit of the short dipping reflectors as the Moho, it should be located at 12 s TWT in the south and at 14 s TWT in the north. This corresponds with a Moho depth of about 40-50 km. This result has to be interpreted with caution because it is not sure that the observed reflections (or the absence of them) correspond to the Moho at all.

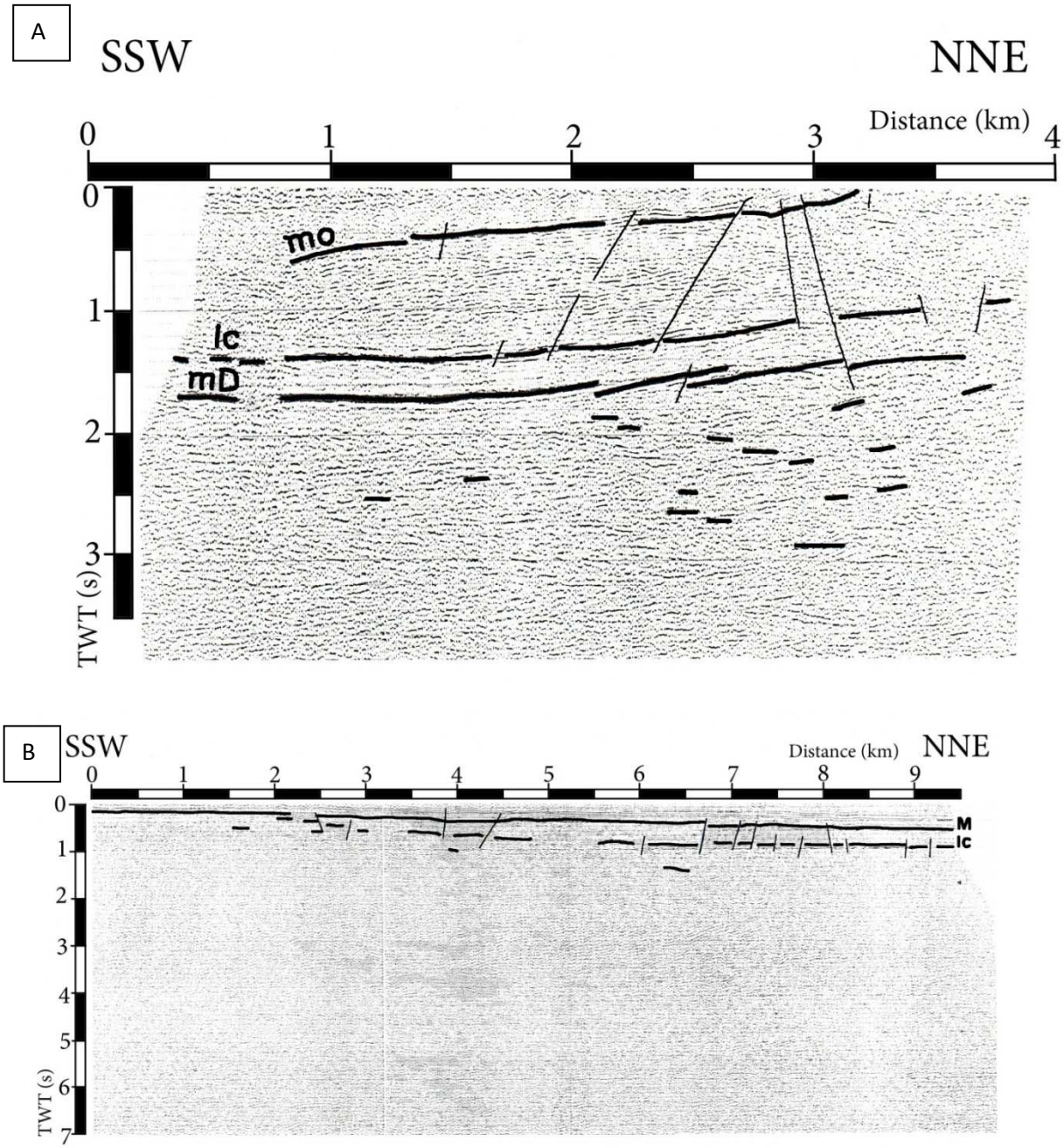

Figure 2.4: The southern and northern edges of the Belcorp profile showing the unreflective lower crust and the sediment cover.
A: the southern part of the profile and B: the northern part of the profile. mo: Midi overthrust; lc: lower Carboniferous; mD: mid Devonian; M: base of the Cretaceous (redrawn from Bouckaert *et al.*, 1988).

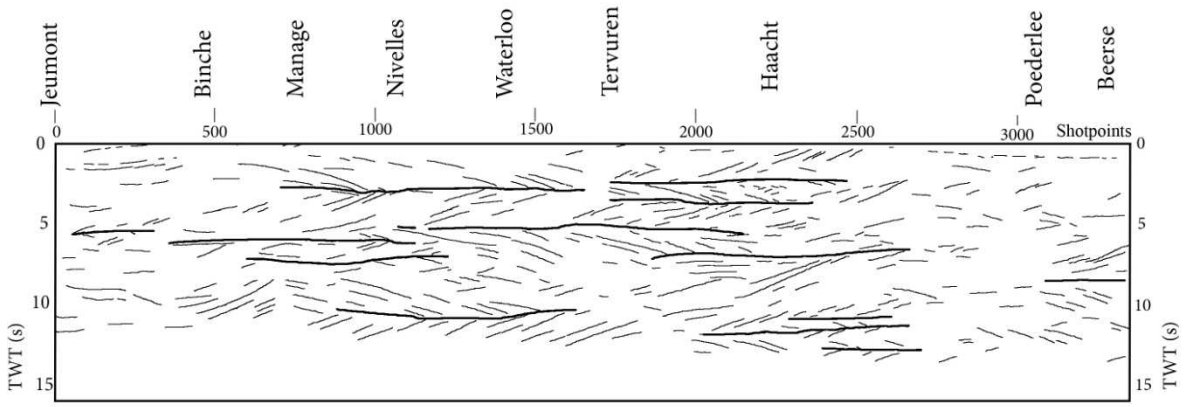

Figure 2.5: Interpretation of the filtered Belcorp profile.
The short dipping reflectors along the profile and the boundaries traced between the different dip-trends. Redrawn from Bouckaert *et al*., 1988.

2.2.2.2ECORS profile

The ECORS profile (Matte & Hirn, 1988) was also shot in the framework of the deep seismic reflection profiling project "International Lithosphere Project". Along the ECORS profile (seen on Figure I-3 and Figure 2.6) both wide angle and vertical profiles were shot. It is composed of several profiles stretching from Epinoy in the north to La Rochelle in the south. For this study, only the northern part of the northernmost profile was important because it crosses the Midi overthrust and should therefore show some reflections in the Brabant Massif. On this profile, the Midi overthrust can be followed at 5-7 km of a depth (Figure 2.6). The Brabant Massif is again seen as an unreflective block on the vertical reflection profile, so no Moho can be determined. On the wide-angle reflection profile, however, the Moho is detectable by a low frequency signal. It appears roughly parallel to the Dinant Nappe and dips southward from a depth of 30 km below the Midi overthrust to 40 km, 100 km further south. Just north of the Bray fault, the Moho can be visualised by strong gently north dipping reflections (Figure 2.6). This is very different compared to the Moho underneath the Brabant Massif, that is not visible on vertical reflection profiles. No continuity can be seen between the south dipping Moho from the north and the north dipping Moho from the south (Figure 2.6).

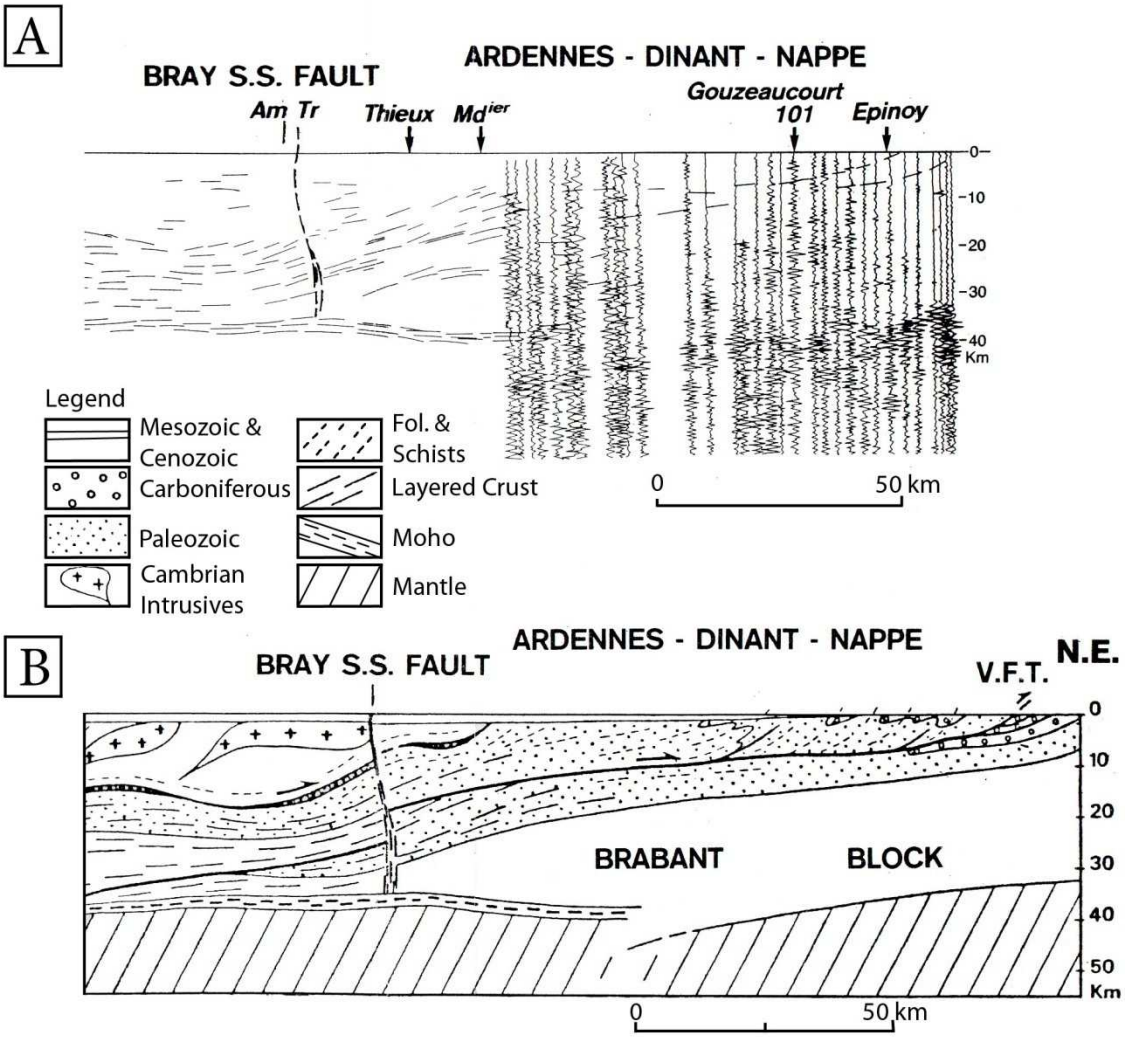

Figure 2.6: The northern part of the ECORS profile.
A: the vertical and wide angle reflection data used in the profile. B: the interpretation of the seismic data. Redrawn from Matte and Hirn (1988).

2.2.2.3 BIRPS profiles

Several profiles have been shot around the British Islands during the BIRPS project (Klemperer S. & Hobbs R., 1991; Blundell, 1990). For this study, only the MOBIL 6, 7 and SHELL (UK82-101) profiles are of interest, because they cross the Brabant Massif (Figure I-3). The MOBIL 6 profile crosses the Sole Pit inversion structure and the South Hewett fault zone (Figure 2.7). The MOBIL 7 profile is situated only slightly to the east of the MOBIL 6 profile and thus shows similar structures. The SHELL (UK82-101) profile (Figure 2.8) is situated more to the south crossing the South Hewett shelf and the Brabant Massif. On the MOBIL 6 and 7 profiles, the sediment cover (containing Permian to Quaternary sediments and structures) thins towards the south and is accompanied by a change in reflectivity of the lower crust (Blundell *et al.*, 1991). From km 0 to km 50 (horizontal distance), a normal "layered lower crust" can be seen below the sole Pit structure and the south Hewett Shelf at 7.5 to 12.5 s TWT (Klemperer S. & Hobbs R., 1991). Toward the south, the lower crust reflections become weaker and a Moho reflection cannot be determined. Weak dipping reflections can be determined beneath normal

Moho depths (15 s TWT). South of km 60, bright reflections can be seen in the middle crust (between 3 to 7 s TWT) and are interpreted as being shear zones formed by differential stretching between the upper and lower crust (Reston & Blundell, 1987). Because similar reflections can be seen on the SHELL (UK82-101) profile, further south than the basins edges, they might have a much older origin, possibly from the Caledonian or even Cadomian Orogeny. The transition between the reflective lower crust underneath the North Sea basin and the unreflective crust underneath the Brabant Massif is also seen south and north of the massif on other profiles (Matte & Hirn; 1988 and Remmelts & Duin, 1990). Its unreflectiveness cannot be explained by the age and stability of the Brabant Massif, because underneath the Baltic shield, a Moho reflection can be followed and this shield is stable for more than 1800 Ma instead of the 500 Ma of the Brabant Massif.

The SHELL (UK82-101) profile (Figure I-3 and Figure 2.8) begins south of the edge of the South Hewett Shelf and crosses the Brabant Massif (Klemperer S. & Hobbs R., 1991). In the north, only 0.5 s TWT (or approximately 1.5 km) of upper Cretaceous to Quaternary sediments directly overly the Carboniferous or older strata of the Brabant Massif. Similar to the MOBIL 6 and 7 profiles, south dipping mid crustal reflections can be seen on this profile, they can also be observed further south but the dip seems to be opposite. This indicates that the north dipping mid crustal reflections are not formed by the extension of the North Sea basin, but their origin might be found in the Cadomian or Caledonian Orogeny. It is thus not impossible that the south dipping northern mid crustal reflections have the same origin. In this case they might be reactivated during the extension of the North Sea basin. On this profile, Moho reflections can also be seen at the extreme northern and southern edges of the profile.

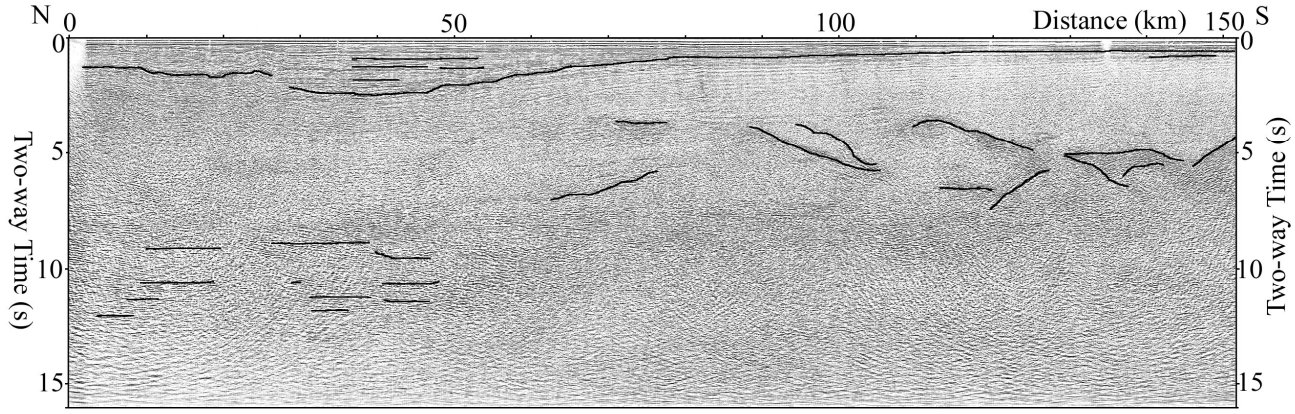

Figure 2.7: The MOBIL 6 profile. Modified from Klemperer & Hobbs (1991).

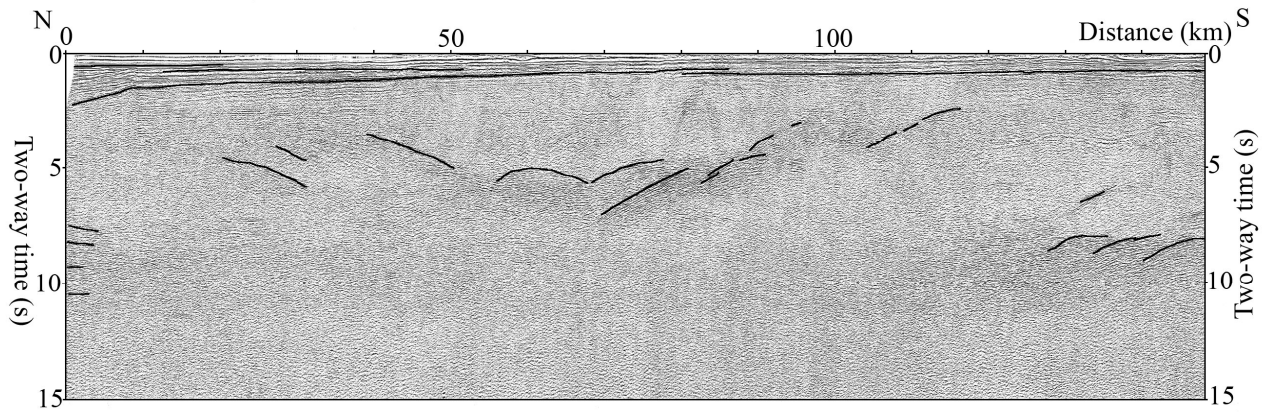

Figure 2.8: The SHELL profile. Modified from Klemperer & Hobbs (1991).

2.2.2.4 MPNI-9101 profile

In 1991, a deep seismic line, MPNI 9101 (Figure I-3) was recorded in the southern North Sea by the Geological survey of the Netherlands and Belgium (Rijckers *et al.*, 1993). On this profile, a reflective lower crust was visible underneath the Brabant Massif (Figure 2.9), unlike the other profiles. Two bands of reflections can be seen at 8 s TWT and 12 s TWT underneath the Brabant Massif. Rijckers *et al.* (1993) interpreted the 12 s TWT as the reflection at the Moho, which decreases from 12 s TWT to 10 s TWT to the north. After depth conversion, this gives a depth of 38 km underneath the Brabant Massif and 31 km further north. The middle crust underneath the Brabant Massif appears to be unreflective; no dipping reflectors like on the MOBIL profiles Blundell *et al*. (1991) can be seen. Why all these reflections can be seen underneath the Brabant Massif on this profile and not on others is not clear. No explanation is provided by Rijckers *et al.* (1993).

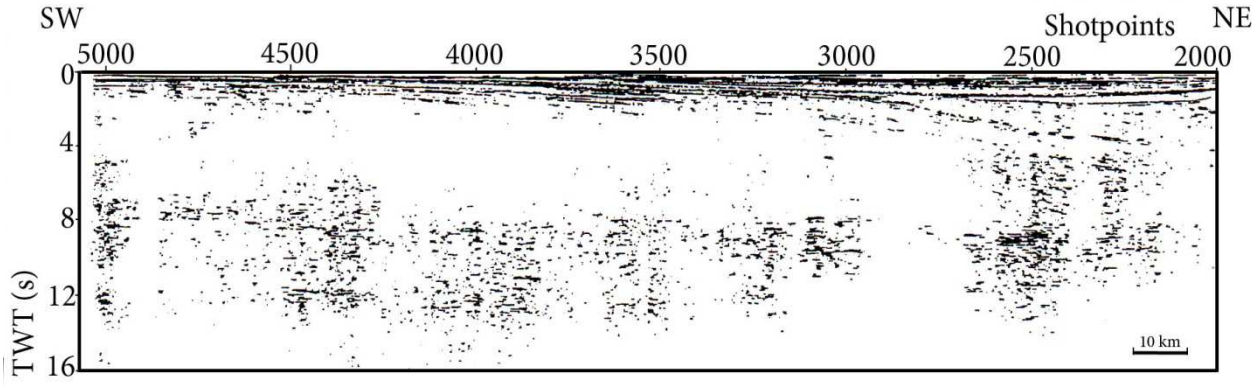

Figure 2.9: Coherency filtered stack of the southern part of MPNI-9101 (shotpoints 2000-5000). Redrawn from Rijckers *et al*. (1993).

2.2.2.5 Other attempts to determine the Moho and/or the velocity structure underneath the Brabant Massif

Sourriau (1979) determined the velocity structure of the upper mantle beneath the Paris Basin and the Benelux. She found two velocity anomalies (lower than expected velocities) one lays underneath the Eifel Volcanic Province, and is linked to a Moho uplift due to volcanic activity. The other anomaly is situated northeast of Brussels and corresponds to the gravimetric high of the Campine region (see paragraph 2.6.1). Sourriau (1979) explained this anomaly by a Moho uplift to 20 km of depth underneath this region.

De Vuyst (1967) determined the Moho depth underneath Belgium when studying the magnetic anomalies. He found a Moho depth of 20 km underneath the Brabant Massif and up to 60 km underneath the Ardennes Allochthon.

The results of the gravimetric and magnetic data for the Brabant Massif are discussed in paragraph 2.6 of this chapter.

2.3 Ardennes Allochthon

The Ardennes Allochthon is composed of several tectonic structures (Figure 2.10) from north to south: the Dinant Synclinorium, the Ardennes Anticlinorium, the Caledonian Inliers (Stavelot, Serpont and Rocroi), the Neufchâteau-Eifel synclinorium and the Givonne Inlier in an anticlinorium further to the south. The Condroz inlier and the Namur "synclinorium" separate the Brabant Massif from the Ardennes Allochthon.

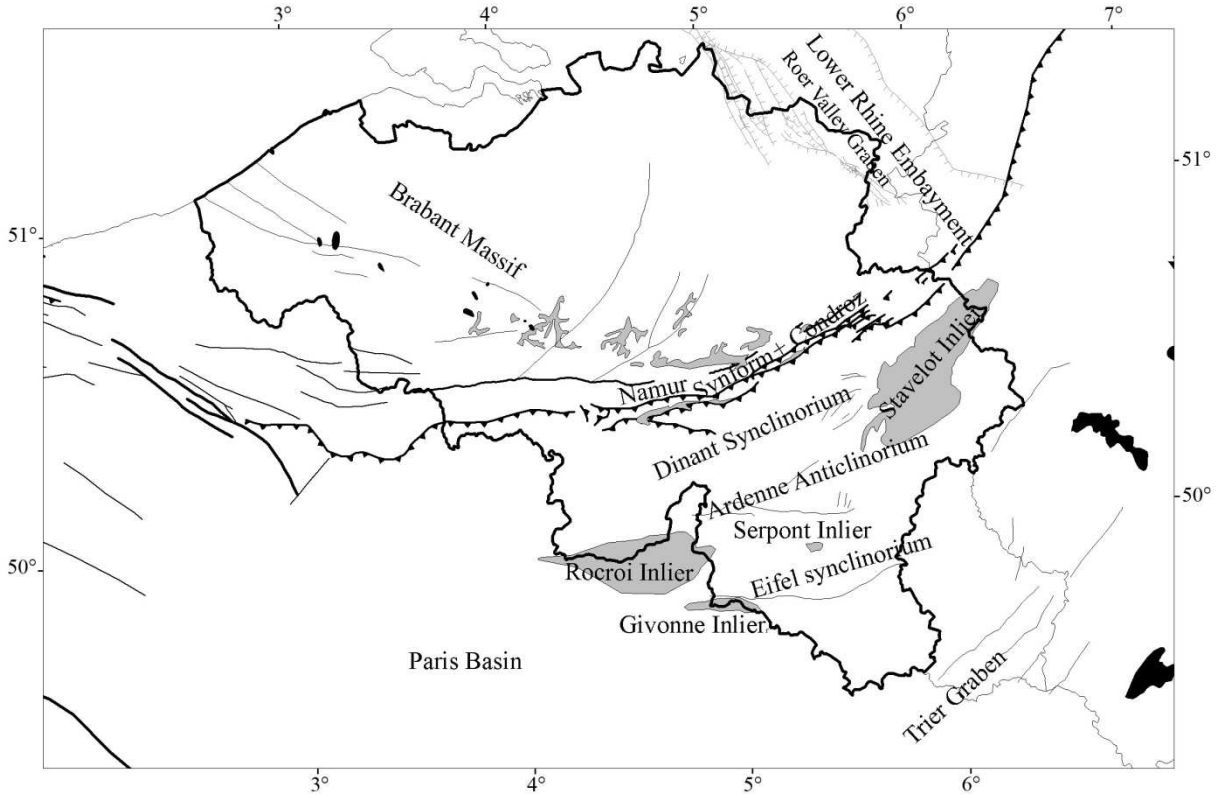

Figure 2.10: Schematic map showing the different tectonic structures of Belgium.
Grey zones = Pre Variscan sediments and Black zones = magmatic rocks. Major Fault lines are also indicated in black and grey as well as the political borders.

2.3.1 Surface Geology

First the geological history of the Caledonian Inliers positioned in the Ardennes Allochthon and the Condroz inlier are described. Then, the geology of the other parts of the Ardennes Allochthon is discussed.

2.3.1.1Caledonian Inliers

The Caledonian Inliers in the Ardennes Allochthon have known a similar tectonic history as the Brabant Massif. Their tectonic history is described in paragraph 2.2. Verniers *et al.* (2002) also provides a thorough review of the Caledonian history of the Ardennes inliers. The following paragraph is a summary.

Sedimentation in the Caledonian Inliers

Only the upper part of megasequence 1 as described in the Brabant Massif (Figure 2.10) is found in the Condroz Inlier (Verniers *et al.*, 2002). Here, this sequence is composed of low-density distal turbidites, identical in facies to the same formation in the Brabant Massif (Verniers *et al.*, 2001; 2002). The unconformity at the top of megasequence 1 is well constrained, with a hiatus from the early Tremadocian to Llanvirn. Megasequence 2 begins with a conglomerate followed by a graptolitic mudstone. After a hiatus, micaceous siltstones are deposited and covered by calcareous mudstone sediments, after another time gap. All the sediments deposited in the Condroz Inlier suggest that the inlier was located in a deep shelf environment (Verniers *et al.*, 2002).

In the four Ardennes inliers, only the two larger ones (Stavelot and Rocroi (Figure 2.10)) contain megasequence 1 and 2. The minor ones (Givonne and Serpont (Figure 2.10)) only contain parts of megasequence 1. Megasequence 3 is absent due to the deformation of the inliers during the Ardennian tectonic phase, which occured when megasequence 3 was deposited in the Brabant Massif (Michot, 1980). After the erosion of the deformation belt, the Rocroi, Serpont and Givonne inliers were covered by Pridoli and Lochkovian sediments, whereas the Stavelot Inlier was covered by Lochkovian strata. At the base of the Stavelot Inlier, near-shore to intertidal shallow shelf deposits are found on an inferred Neoproterozoic crust (Von Hoegen *et al.*, 1990) and later a more open and deep shelf. Higher up, coarse turbiditic facies alternates with mudstone-siltstone dominated siliciclastics, deposited as turbidites on the lower slope/upper fan region of a submarine fan-valley system (Van Hoegen *et al*. 1985; Geukens, 1999; Verniers *et al.*,2001). During the Tremadocian, Bouma-type turbidites are followed by low-density turbidites and this period ends with sandstone deposits on a platform. All sediments are deposited in a deep environment. A gap of a certain duration separates megasequence 1 from megasequence 2 (Vanguestaine, 1992), after which a drastic change in environment can be seen from a shallow platform to a probably deep water environment with mudstone-siltstone dominated siliciclastics and turbiditic levels. In the Rocroi inlier a similar megasequence 1 is present, but apparently less thick than in the Stavelot Inlier. Megasequence 2 is only partly preserved here.

Tectonometamorphic evolution of the Caledonian Inliers

The overall architecture of the inliers is very similar, with a predominantly east-west trending structural grain and strongly north-verging fold trains. The dominant pervasive cleavage is south-dipping. The overall structure of the inliers is that of a north-verging overturned-antiform with a marked difference between the southern and northern unconformity (south: weakly south dipping; north: subvertical to overturned). Along the southern unconformity, epizonal and mesozonal metamorphism occurs (Verniers *et al.*, 2002) .

The Rocroi Inlier has an overall east-west trending structural grain. Its internal structure consists of two narrow antiformal areas, composed of lower Cambrian units, separated by a very broad synformal

area, composed of middle to upper Cambrian units and some middle Ordovician (Verniers *et al.*, 2002). The Stavelot Inlier is situated close to the Variscan thrust front and some of the thrusts that crosscut the inlier are part of the Variscan thrust front. The inlier itself consists of two distinct lithostructural domains, separated by the Xhoris-Monschau thrust (Fielitz, 1992; Sintubin, 1994; Verniers *et al.*, 2002). The southern domain is characterised by two dome-like structures, composed of lower Cambrian. The overall internal grain is east-west trending, comparable to the other inliers. The northern domain is characterised by a number of Variscan thrust sheets in the footwall of the Xhoris-Monschau thrust. The overall structural grain has a NE-SW trend (N60°E) which coincides with the structural grain outside the inlier. Superposed on the border zone between both domains is a post-Variscan graben structure. The infill is considered to be of Permian age. The exact determination of the Caledonian tectonometamorphic event in the Ardennes Allochthon is obscured by the Variscan tectonometamorphic event (Verniers *et al.*, 2002).

2.3.1.2Devonian and Carboniferous history of the other parts of the Ardennes Allochthon

The Devonian and Carboniferous are a transition period between two tectonometamorphic events: namely the Caledonian and the Variscan Orogeny. The Variscan Orogeny is in fact a composition of several tectonometamorphic domains, namely the Moravo-Silesian, Moldanubian, Saxo-Thuringian, the Mid-German Crystalline Rise (MGCR) and the Rhenohercynian zone (Figure 2.11). The Ardennes Allochthon is a part of the Rhenohercynian zone and can be interpreted as a passive margin during the Devonian and the Dinantian. A rift opening can only explain the differences in Devonian sediments in Belgium. During the Variscan Orogeny a passage from a dilatation regime to a compressive regime explains the folding and shortening. This change in tectonic environment is due to the collision of the Rhenohercynian and the MGCR zone. The deformation has propagated in the Rhenohercynian basin along a mid-crustal décollement level, carrying the Condroz, the Dinant synclinorium and the Ardennes to the north. The limit of the translated zone is given by the Midi fault in Belgium and the Eifel-Aachen fault in Germany. The junction between both faults is not very clear. The amount of displacement of the Ardennes Allochthon has long been under discussion (Adams & Vandenberghe, 1999; Oncken *et al.*, 2000).

During the early Devonian essentially sandstone and slates are deposited in both continental and marine environment. They are mostly found in the Dinant and Neufchâteau synclinoria (Goemare *et al.*, 2006 ; Goemare & Dejonghe, 2005). During the middle Devonian a radical transgressive regime is installed and the terrigene facies are replaced by organoclastic sediments and the first constructed carbonates. The transgressive phase that started in the Eifelian attains its maximum during the late Devonian covering the entire Brabant Massif and even the Campine Basin. During this period, sedimentation evolves to calcareous-detrital sediments. The Dinantian is characterised by sedimentation of marine carbonates, whereas the Namurian comprises terrigenous sediments of near-coastal origin. During the Westphalian, paralic sediments contain numerous veins of coal, they are sometimes interrupted by short marine incursions. The metamorphism in the Devonian and Carboniferous sediments is depending on the area pre- and/or synorogenic (Fielits & Mansy, 1999).

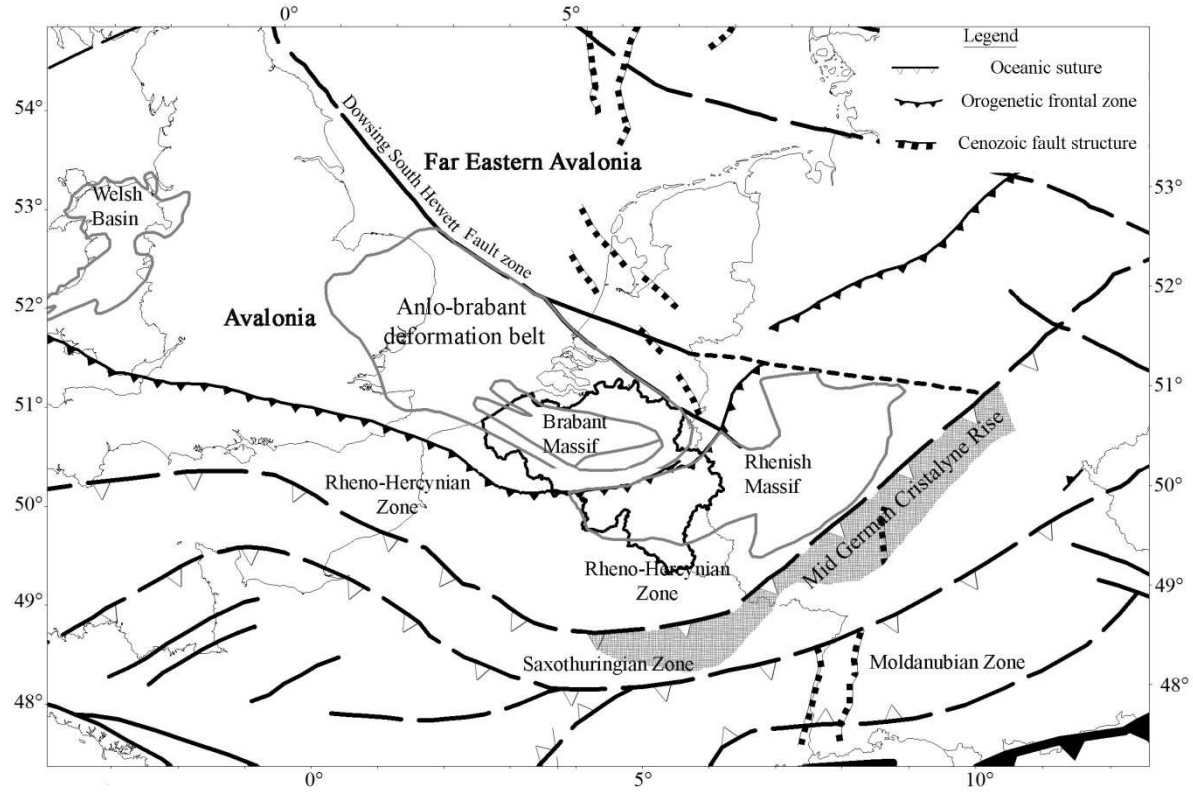

Figure 2.11: Basement tectonic sketch map of NW Europe (redrawn from Verniers *et al.,* 2002). Political borders are indicated in light grey.

In the Belgian Lorraine (Figure 2.12), only the upper series of the Triassic, namely the Keuper and Rhaetian can be observed. The Keuper sediments were deposited during a transgression that covers the southeast corner of the Ardennes basement. These sediments have a clayey-sandy (locally even conglomeratic) composition of fluviatile origin at their base, followed by red and gray marls. During the Rhaetian, soft sandstones and marls and black clay are deposited alternately and represent a lagoon origin. Only the Lias and lower Dogger crop out in the Lorraine Belge and represent a series of transgressions and regressions. The Lias is represented by an alternation of siliciclastic and limestone facies. The end of the Lias and the beginning of the Dogger is characterised by the epi-orogenetic uplift of the Brabant basement. Two to three km of Carboniferous sediments and an unknown amount of lower Palaeozoic rocks are exposed to erosion during this period.

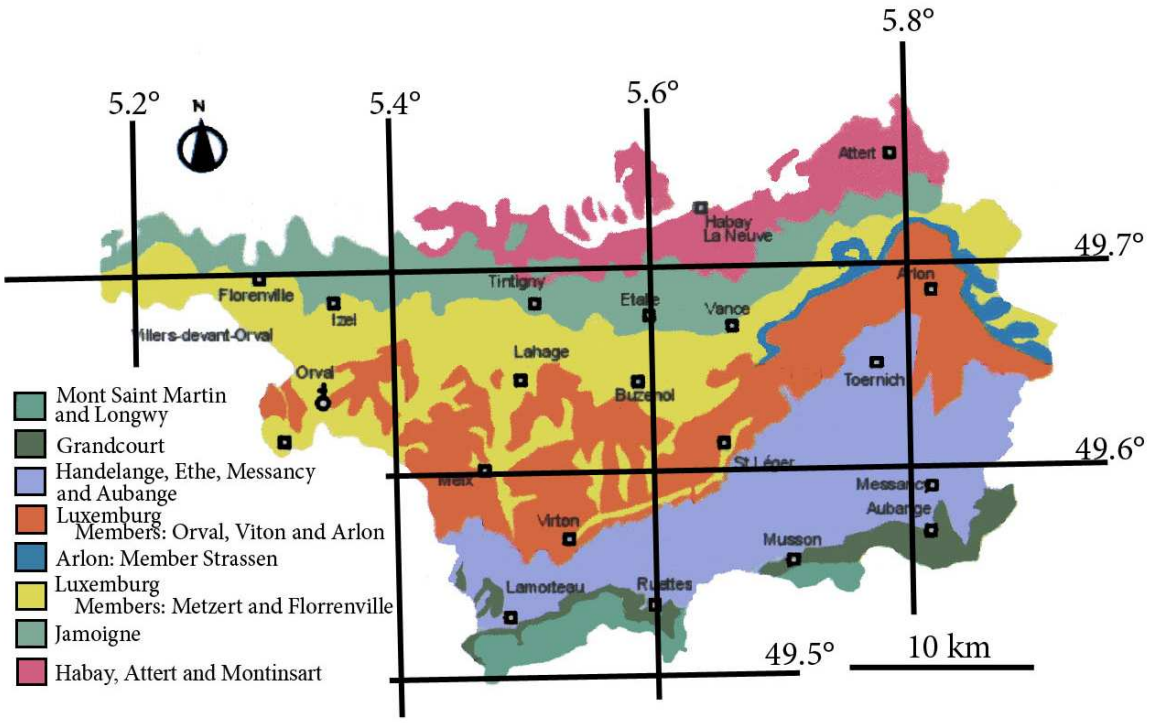

Figure 2.12: Geological map of the Belgian Lorraine. Redrawn from Boulvain *et al.*, 2001.

2.3.2 Middle and lower crust

Several geophysical studies (such as seismic profiles, gravimetric and magnetic studies) have been performed in the past to reveal the structure of the middle and lower crust underneath the Ardennes Allochthon and the Rhenish Massif. Not only a seismic profile (DEKORP (DEKORP Research Group, 1991)) has been shot in the region, also a seismic velocity study of the crust has been performed (Jongmans and Camelbeeck, 1994)

2.3.2.1DEKORP Profile

The DEKORP profiles (Figure I-3, DEKORP Research Group, 1991) were shot in the same framework of the "International Lithosphere Project" and the "European Geotraverse" as the earlier mentioned BELCORP and ECORS profiles. For this study, only DEKORP 1 and only part 1A is important. Profile 1A runs from the Variscan Foreland in Belgium across the Midi overthrust over the Stavelot Inlier across the axial depression of the Eifel North-South zone to the city of Adenau. Its azimuth is WNW-ESE. In the north-western part of the profile, only a few reflections can be distinguished in the upper crust, probably originating from the Devonian/Carboniferous sediment cover of the Brabant Massif (1 on Figure 2.13). Below the Stavelot Inlier, a strong reflection from 1.2 to 1.3 s TWT (2) is dipping south-eastward with an angle of about 10° and can be followed for 20 km. This reflection transforms into a series of shorter reflections further to the south (3), which represents the detachment of the Midi overthrust. Below the southern end of the Stavelot Inlier, the Midi overthrust becomes steeper and its character changes to a wide band of narrow parallel reflections between 1.5 and 3.2 s TWT (4). This

zone corresponds to a metamorphic zone at the surface. Between km 40 to 55 horizontal distance, the Midi reflection becomes a ramp like structure, which can be followed down to 4.4-5.0 s TWT (5-6). For the next 25 km, steep reflections mark the continuation of the Midi thrust (7). At the end of the profile, less distinctive reflections (8) mark the Midi thrust that forms a ramp between the Eifel North-South zone and the Stavelot Inlier. Reflections at Moho level are almost horizontal (9) underneath the Eifel North-South Zone at 9-10 s TWT. Near Adenau, the reflection of the Midi overthrust merges with the Moho reflections (10). The deepest band of reflections at Moho level dips to the northwest towards the Brabant Massif. It is found at 10 s TWT (11) below the Eifel North-South Zone and goes up to 9 s TWT (12) near Adenau and even up to 8 s TWT (13) at the ESE end of the profile. Near Stavelot, the Moho is overlain by a wedge-shaped zone without clear reflections (14).

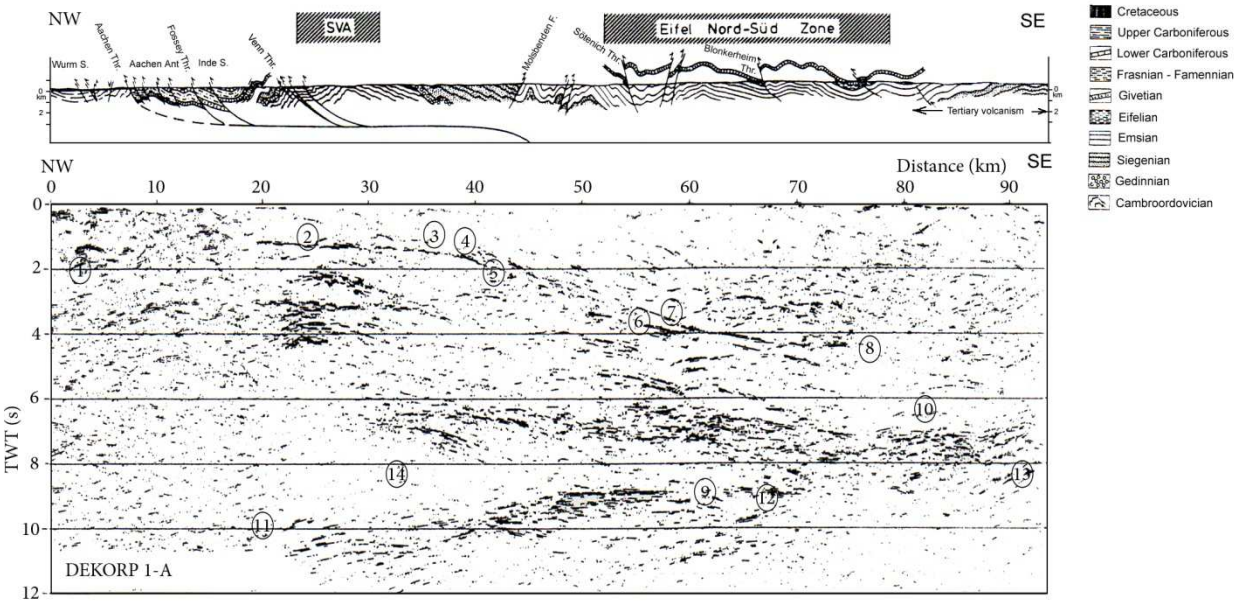

Figure 2.13: Automatic line drawing of the final stack of profile BELCORP/DEKORP 1A with geological cross-section. SVA: Stavelot-Venn Anticline. Redrawn from DEKORP Research Group (1991).

2.3.2.2Velocity structure under the Stavelot Inlier

Jongmans and Camelbeeck (1994) have analyzed the seismic signal of quarry blasts registered by some stations of the seismic network of Belgium. They used two methods to study the upper crustal structure of the Stavelot Inlier, namely seismic refraction and the inversion of surface waves to be able to study the Vp- and Vs-velocity in the upper 5-6 km of the crust along two profiles (Figure 2.14 A). On Figure 2.14 B, one can see that the hodochrones of both profiles are slightly curved, indicating a progressive increase of Vp. Furthermore, they are both very different. Figure 2.14 C indicates that the velocity along profile 2, parallel to the structures, is a lot faster than the velocities along profile 1, crossing the structures (5.5 to 6.3 km/s and 4.6-5.7 km/s respectively). A similar trend can be observed for the surface waves (profile 1: 2.2 to 3.2 km/s whereas profile 2: 2.5 to 3.5 km/s). So, they found that the Stavelot Inlier is anisotropous with lower Vp- and Vs-velocities in a NNW-SSE direction.

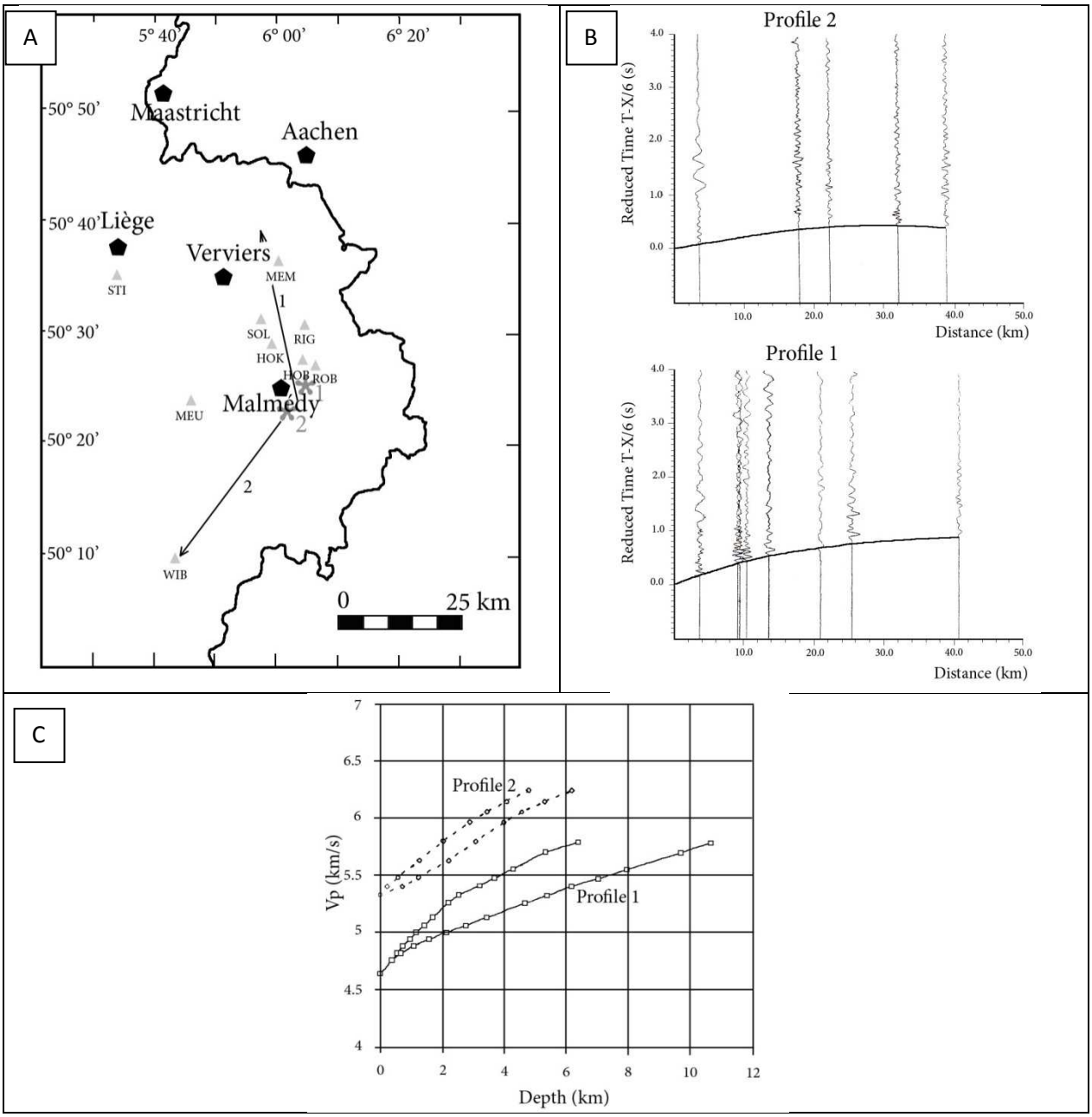

Figure 2.14: Results of the Surface wave analysis performed by Jongmans & Camelbeeck (1994).
A: Map with the location of the stations (triangles) used in the study, the location of the quarries (flowers) (1 : The Quarry of Waimes and 2: the quarry of Bellevaux-Ligneuville) and the position of the profiles. B. Signals and hodochrone for the P-wave for both profiles. C. Evolution of the velocity of the P-wave with depth. Redrawn from Jongmans & Camelbeeck (1994).

More information on the deep structure of the Ardennes Allochthon can be obtained from the gravimetric and magmatic data (see, paragraph 2.6 of this chapter).

2.4 Roer Valley Graben

The Roer Valley Graben (RVG) forms part of the northwestern branch of the Lower Rhine Rift System and stretches from Euskirchen in Germany to ‘s Hertogenbosch in the Netherlands. It also covers the northeastern part of Belgium (Figure 2.15). It is the most prominent Cenozoic feature in the Netherlands and Belgium, filled with more than 2000 m of Cenozoic deposits. It is a region with a high

level of seismicity known from historical times onward (Alexandre 1985). Deep-seated fault zones, still active under the influence of the present day stress field, frequently generate tectonic earthquakes (cfr. Roermond earthquake, 1992 (Camelbeeck *et al.*, 1994)). The Roer Valley Graben can be divided into a number of tectonic subunits (Figure 2.15)(Geluk *et al.*, 1994). From northeast to southwest: the Krefeld block that borders the subsiding area; the Venlo, Peel and Köln block, a zone of intermediate subsidence; the Roer Valley Graben and the Erft block, the zone of strongest subsidence, the Eastern and Western Campine blocks of intermediate subsidence. The subsiding area is delimited by the Brabant Massif, the Ardennes Allochthon and the Eifel in the southwest and by the Rhenish Massif in the east. The Roer Valley Graben is an asymmetric NW-SE trending structure, bordered by a series of antithetic faults to the Peel fault at the southwestern margin (the Feldbiss, Neeroeteren and Heerlerheide Faults).

2.4.1 Surface Geology

The oldest deposits found in the Roer Graben are the Carboniferous Westphalian A, B and C deposits. By regional geological knowledge, these are underlain by Namurian and Dinantian sediments (Delmer, 1963; Geluk *et al.*, 1994). In the Campine Basin Westphalian D deposits also occur, indicating that during the Westphalian, controlling fault patterns existed. The patterns show that the fault system had a similar orientation as the Cenozoic Roer Valley Graben. The Westphalian displacement along the Peel fault cannot be determined from seismic profiles. Deformation of the Carboniferous deposits north of the Variscan front was limited to block-faulting and tilting of the strata. A thick Permian-Triassic-Jurassic sequence unconformably overlies the Carboniferous sediments. Outside and at the edges of the graben, this sequence may be strongly reduced or even removed by middle Jurassic to Cretaceous erosion, related to the Kimmerian tectonic phase. upper Cretaceous sediments then overlie Carboniferous sediments. During the Permian, the entire graben acted as a fault-bounded plateau where subsidence is similar over the entire graben. During the Triassic, the subsidence becomes not fault-bounded and the erosion of these layers is not due to Triassic erosion, but to the erosion inflicted by the Kimmerian tectonic phase. This Kimmerian tectonic phase covers the time span between the middle Jurassic and the late Cretaceous. During this phase, erosion persisted and was associated with the uplift of the Brabant and Rhenish Massifs. During this period (sub-Hercyninan phase), a tectonic inversion of the graben occurred. This means that Jurassic Basins became uplifted and subject to erosion, whereas previously high areas subsided. Faults active during the Kimmerian phase acted as reverse faults during the inversion. At the start of the Cenozoic, minor differences in thickness of sediments over the graben suggest a tectonic quiescence in the area. During the late Paleocene and the Eocene, a regional hiatus occurs; it increases in stratigraphic range towards the southeast on the graben shoulders and towards the graben centre. Since the Oligocene, sedimentation resumed in a mild tensional regime, throws on individual faults are no larger than 20m (Demyttenaere, 1989). The late Oligocene marked a dramatic change; from this time onward, the strongest subsidence took place in the Roer Valley Graben (Demyttenaere, 1989; Geluk, 1990; Geluk *et al*., 1994). The rapid subsidence of the graben was accompanied by the tilting of the Eastern Campine Block. During the Miocene, Pliocene and Quaternary, sedimentation became more and more restricted to the Roer Valley Graben, although elsewhere sedimentation occurred at a lower rate.

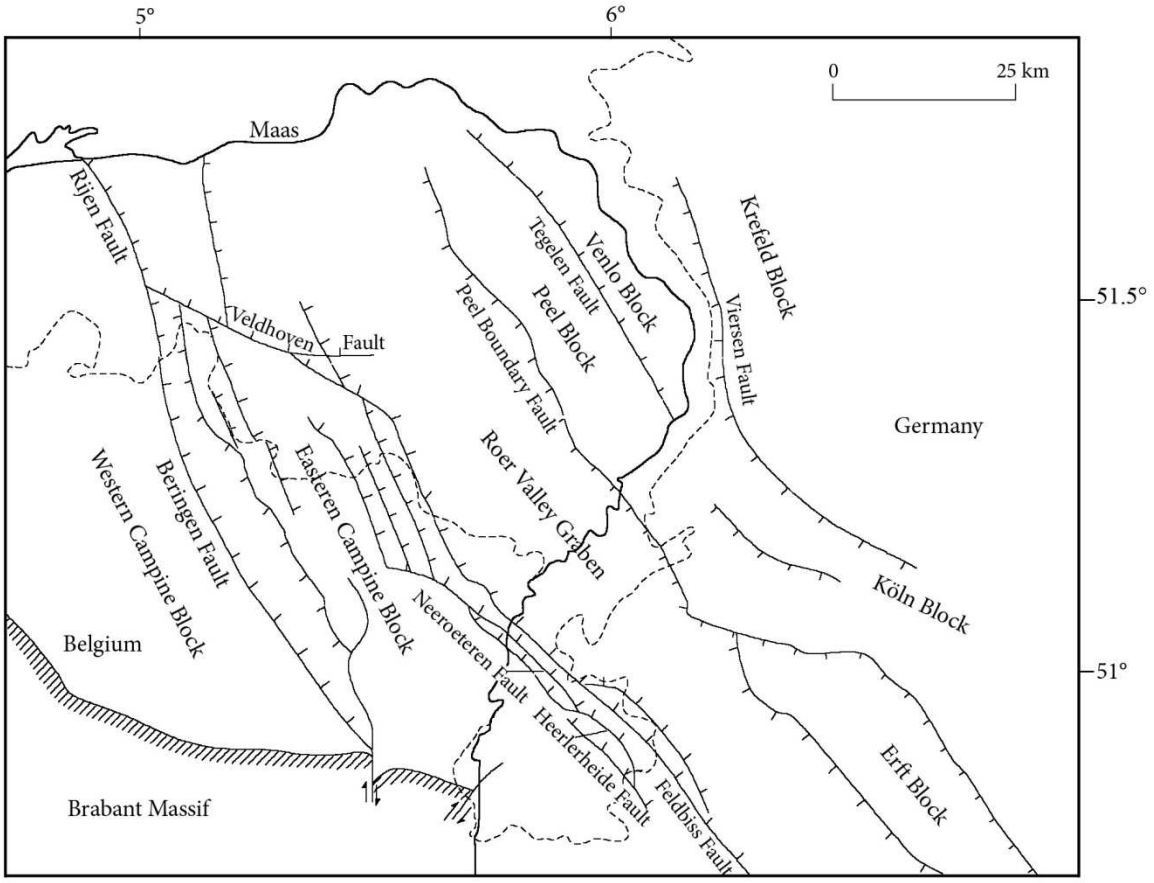

Figure 2.15: Structural framework of the Roer Valley Graben, showing the main blocks and main faults at the base of the Tertiary.
Redrawn from Geluk *et al.*, (1994).

2.4.2 Middle and lower crust

In 1986 and 1987, nearly 540 km of onshore seismic lines have been shot in The Netherlands to study the deep crust (Remmelts & Duin, 1990). For this study, the southern part of line 8601 is important (Figure 2.16). On this profile, the crust becomes less reflective towards the Roer Valley Graben. Where reflectors appear, they form thin bundles of 1-1.3 s TWT thickness. The poor lower crustal reflectivity may be possibly related to the presence of the Brabant Massif. The upper crust appears to be transparent over its entire line, however the sediment infill of the Roer Valley Graben is visible. The faults that bound this graben cannot be followed below the graben. So, the Peel Boundary Fault cannot be traced deeper than the base of the Carboniferous at a depth of 7-8 km. Although not very clear, there is an indication for the Moho depth underneath the graben at 10-11 s TWT or 27 km of depth. Thus according to the authors, there is a distinct uplift of the Moho from an average depth of 30 km beneath the graben flanks to a depth of 27 km below the graben, although this is not visible on their figures (cfr. Figure 2.16).

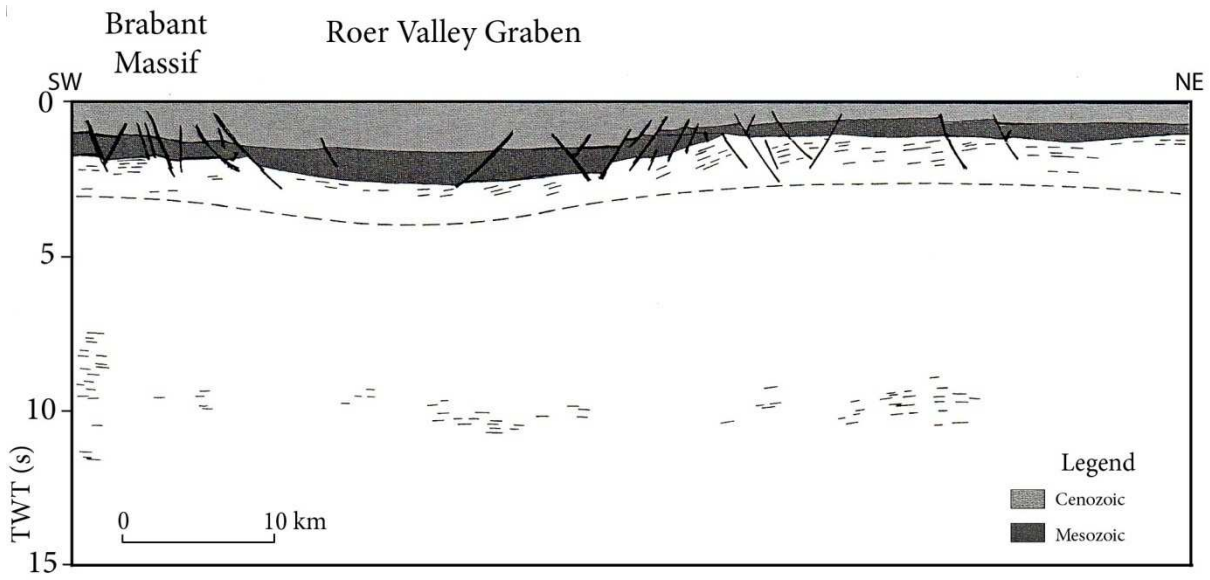

Figure 2.16: Line Drawing of line 8601.
The Dashed line is the top of the Basement. Redrawn from Remmelts & Duin (1990).

2.5 Eifel Volcanic Province

The Eifel Volcanic Province is part of the Rhenish Massif. It has known several volcanic episodes in the Cretaceous (~108 My), Tertiary (45 to 18 My) and a last episode about 600 to 700 ky ago where two volcanic fields started to evolve in the West and in the East Eifel (Lippolt, 1983). The most recent volcanic activity was about 11 000 years ago (Brauer *et al.*, 1999). Presently, a high flux of different magmatic gases and increased rates of mantle-derived gases are still observed (Griesshaber *et al.*, 1992). This intraplate magmatism has been attributed to a major European hotspot in the past (Duncan *et al.*, 1972).

2.5.1 Surface geology (Illies et al., 1979)

The Quaternary volcanism of the Eifel volcanic region is one of the youngest volcanism of Central Europe and contains two volcanic fields. It is located west of the Rhine River and north of the Mosel River. The East Eifel and West Eifel Volcanic Fields are 25 km apart and separated by areas of Tertiary volcanism. The West-Eifel region is composed of 220 eruptive centers; the east Eifel is composed of circa 70 centers. The volume of erupted material and the number of volcanoes increase towards the center of both fields. The chemical composition of rocks from both fields is moderately potassic alkali basalt with basanite being dominant in the East Eifel and nephelinites, melitite nephelinites and leucitites in the West Eifel. This volcanism is situated in the Rhenish Massif, an uplifted plateau that is composed of a thick series of slates, greywackes, quartzites, limestones and locally volcanics of mainly Devonian and lower Carboniferous age. These strata are part of the Rhenohercynian zone of the Variscan Mountain Belt and were strongly deformed and metamorphosed during the Variscan Orogeny. During the Mesozoic and the Cenozoic, the Rhenish Massif has known a history of uplifts.

The first phase was during the late Carboniferous and early Permian. Then early Permian and Mesozoic seas flooded the massif, except for its central part that stayed above sea level. Wide-spread dominantly basaltic eruptions pierced the massif during the late Eocene, Oligocene and Miocene. From the late Pliocene, the whole massif was subjected to a regional uplift at varying rates, which was associated with wide-spread Quaternary volcanism as is found in the Eifel volcanic zone. Both the volcanism and uplift of the massif can be explained by a mantle plume positioned underneath the Eifel Volcanic Province.

2.5.2 Mantle plume characteristics

In 1971 Morgan argued that hotspots are caused by upwelling of hot buoyant mantle material from deep seated sources. Nowadays, a mantle plume is thought to ascend from a thermal boundary layer (like the core mantle boundary) as soon as the density and viscosity contrast rises above that of the surrounding material (Figure 2.17). The rising diaper develops a more or less broad plume head due to resistance of the overlying mantle, whereas the upwelling material underneath this head is concentrated to a small channel. If the rising plume hits an obstacle or its buoyancy diminishes, the hot material spreads laterally and forms a broad mushroom-like plume head. A mantle plume cannot be observed directly, only its consequences like volcanism, heat flow, uplift and gravity anomalies can directly be observed (Ritter 2005).

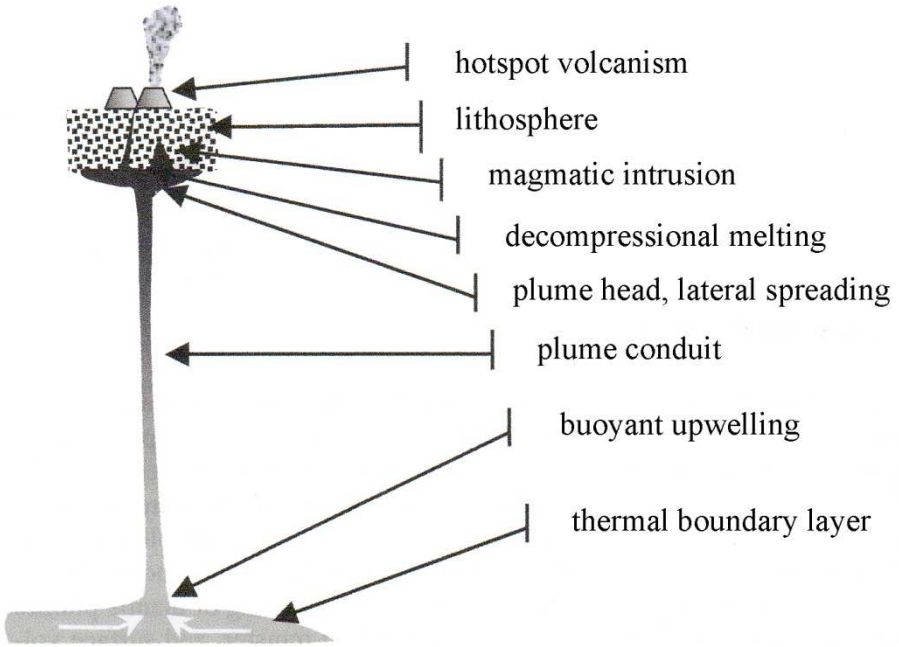

Figure 2.17: Schematic sketch of a buoyant mantle plume that is upwelling from a thermal boundary layer. Redrawn from Ritter, 2005.

2.5.2.1General characteristics of a mantle plume

One of the most important characteristics is the linear volcanic track on moving lithospheric plates. This means that an apparent linear, age-progressive distribution of volcanic features can be distinguished near the plume location (Figure 2.18). This is caused by the overriding plate moving with respect to the plume source (f.i. the Hawaiian-Emperor seamount chain). The oldest volcanic features are farest away from the plume head in the direction of movement of the overriding plate (Morgan, 1971).

Secondly, the volcanic rocks of mantle plumes often show anomalous high $^{3}He/^{4}He$ ratios in comparison to volcanic rocks from other origins, due to their deep origin. The crust and upper mantle are depleted in ^{3}He because, part of the ^{3}He is lost into space and ^{4}He is enriched by the natural decay of U and Th. Volcanic rocks of mantle plumes are also enriched in iron (Fe) and titanium (Ti).

There are also geophysical anomalies associated with hot spots and plumes, namely thermal, seismic and gravimetric anomalies. The thermal anomaly is already indicated in the word hotspot and is seen in the high heat flows measured at the surface and the excess volcanism. These thermal anomalies together with the more fluid magma of the mantle plumes produce anomalies in seismic velocities of the mantle. In a warmer fluid body with lower density than the surrounding mantle, lower seismic velocities can be measured. Mantle plumes are also accompanied by a dynamic uplift of the surface (Burov & Guillou-Frottier, 2005) resulting in positive geoid anomalies over the plume locations.

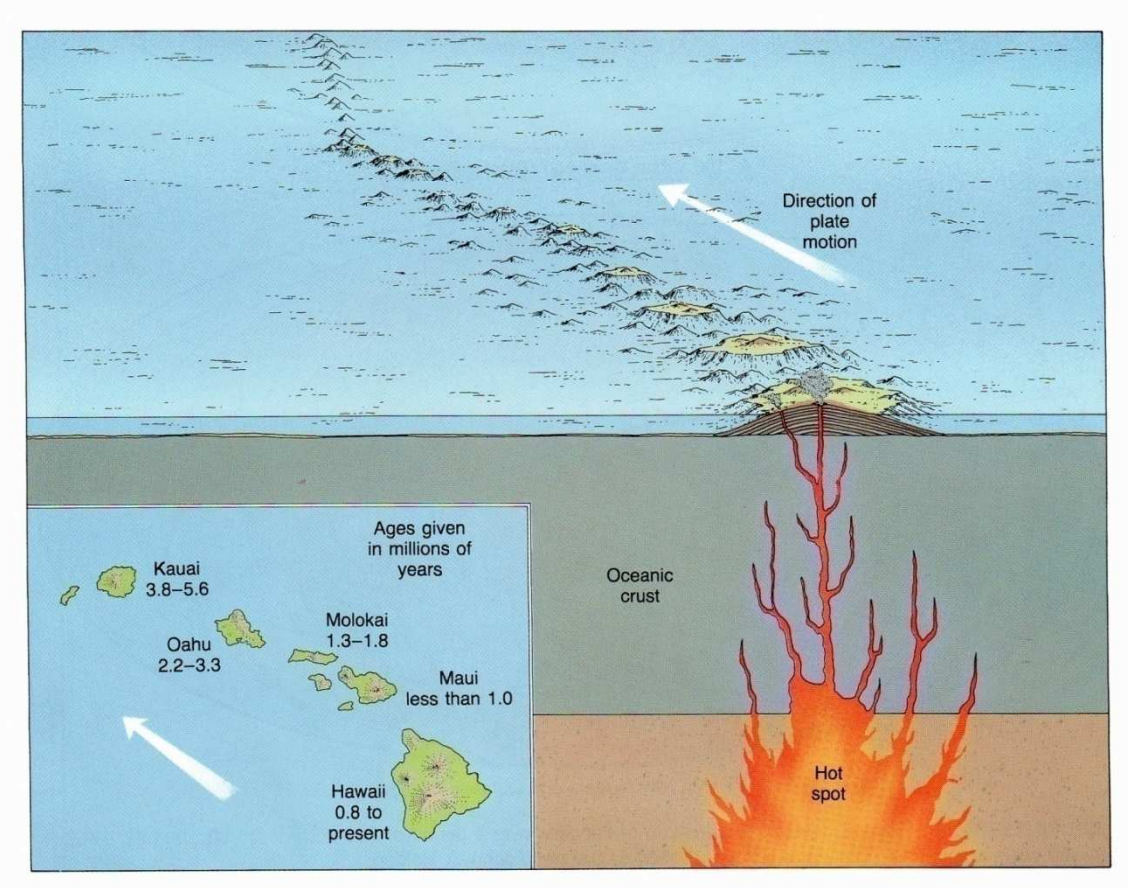

Figure 2.18: The chain of islands and seamounts that extend from Hawaii to the Aleutian trench. Radiometric dating of the Hawaiian Islands shows that the volcanic activity decreases in age toward the island of Hawaii. Redrawn from Lutgens & Tarbuck,1982.

2.5.2.2Do these characteristics apply to the Eifel Volcanic Province?

According to Ritter (2005) and Budweg *et al.* (2006) the uplift of the Rhenish Massif and the high heat flux measured in the Eifel Volcanic Province is caused by a mini-mantle plume. This mini-mantle plume is also characterised by a low seismic velocity anomaly has been demonstrated with a teleseismic tomography (Ritter,2005; Budweg *et al.,*2006). Even the geochemical content of the volcanic rocks and the temperature history of the deformed mantle xenoliths in these rocks favour a deep-seated origin (Seck & Wedepohl, 1983). Budweg *et al.* (2006) modeled a Moho uplift underneath the Eifel Volcanic Province and interpreted it as a sign of the mini-mantle plume. Unfortunately, the seismic velocity anomaly can only be followed to the transition zone at 410 to 650 km of depth. Ritter (2005) argues that the Eifel mini-plume might originate at this depth, but this zone is not a thermal boundary. So for a mantle plume to develop at this depth, somehow, a thermal boundary should be added to this boundary. Ritter (2005) proposed a deep-seated larger mantle plume that rose from the core/mantle boundary, but can only pass the transition zone through several mini-plumes.

Meyer and Foulger (2007) propose another origin for the Eifel Volcanic Province because according to them, the mantle plume model has to be altered too much to explain the volcanism. Several criteria for a mantle plume are indeed not fulfilled.

There is no linear volcanic track in the Eifel Volcanic Province and the volcanism stays at the same place even though the crust has moved more than 1000 km to the north since the volcanism started. A second problem is the fact that the uplift of the Rhenish Massif coincides with the volcanism whereas in the case of a mantle plume the uplift precedes the volcanism. A third problem is the geochemical content of the volcanic rocks. First of all no high $^{3}He/^{4}He$ anomaly can be distinguished. Secondly, in a mantle plume setting an evolution of tholeiitic and andesitic mantle through time and space would be expected, whereas in the Eifel Volcanic Province, different magmas erupt more or less simultaneously. The origin of the observed heat flux can also be debated because a similar heat flux is observed underneath the Rhine Graben. A fourth problem is the size. Even when including the Vogelsberg volcanism, the volcanic region does not reach the surface of 50 000 to 100 000 km² that seems to be typical for other mantle plumes or hot spots (Meyer and Foulger, 2007). Therefore, they propose that the Eifel Volcanic Province is caused by an upper mantle convection cell originated from the subduction of European lower crust and lithosphere in the Alpine Orogeny.

2.5.3 Middle and lower crust

Several studies have been performed in the region. In the seventies a lot of different seismic profiles were shot (Mechie *et al.*, 1983; Meissner *et al.,* 1976; Giese, 1983) and a receiver function analysis was performed by Budweg *et al.* in 2006.

2.5.3.1Seismic profiles

In 1979, the Rhenish Massif Seismic Refraction Experiment has been designed to investigate the structure of the crust and the uppermost mantle of the Rhenish Massif (Mechie *et al.*, 1983). Along the 600 km long 240-LO-60 profile (Figure I-3) and along several shorter perpendicular profiles; shots were performed at several points. Along this profile, a Pg-phase can be distinguished at a velocity higher than 6.0 km/s (Figure 2.19). Furthermore, an intracrustal reflection can be traced along most of the profile and on all the shorter crossing profiles. A lateral variation especially at the crust mantle boundary is also evidenced. For most of the profile, the crust-mantle boundary is either a first order discontinuity or a thin transition zone (< 1 km) at approximately 30 km of depth. Between the Ardennes and the Eifel, however, there is a 6-12 km transition zone before a velocity of 8.1 km/s is reached at 36 km of depth. On the crossing profiles there is usually a 3 km transition zone between crust and mantle.

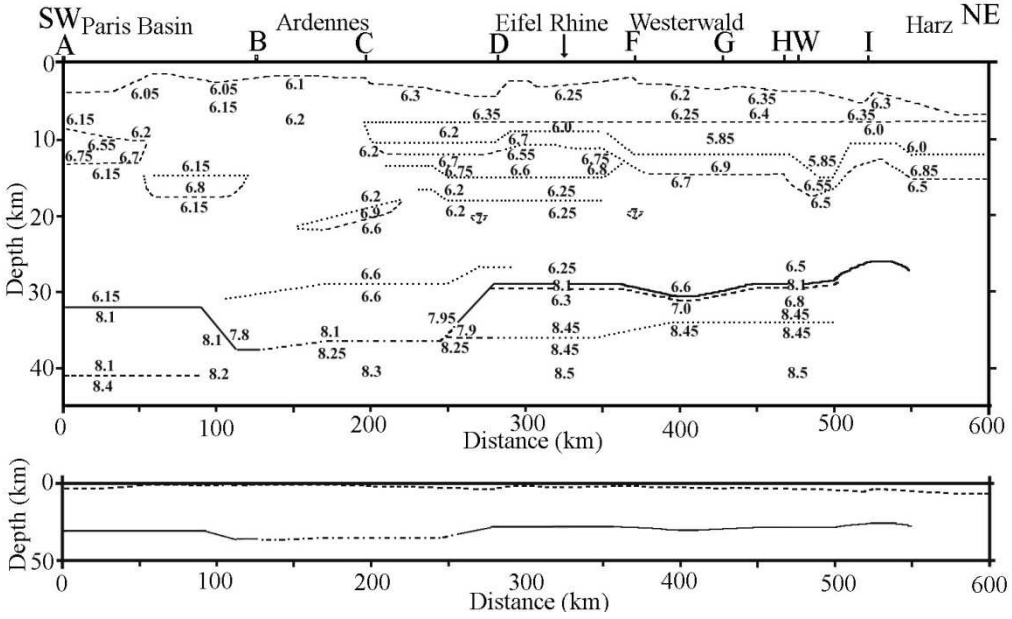

Figure 2.19: Two-dimensional cross-section (top with vertical exaggeration 5:1; middle without vertical exaggeration) for the P-wave velocity structure beneath the main profile 240-LO-60.
Legend : __ Moho as discontinuity with a seismic velocity contrast of > 0.2 km/s; -.- Moho as discontinuity with a seismic velocity contrast of ≤ 0.2 km/s; ---- other discontinuity with a seismic velocity contrast of > 0.2 km/s; ..... another discontinuity with a seismic velocity contrast of ≤ 0.2 km/s. Redrawn from Mechie *et al.*, 1983.

Mooney en Prodehl (1978) reinterpreted seismic profiles shot in the seventies (Figure 2.20). They distinguished four phases on three types of profiles: On type I profiles (see Figure 2.21) PmP-, Pg- and Pn-phases can be distinguished, on type II profiles (Figure 2.22) all the phases of type I profiles and an additional type PiP-phase can be distinguished, on type III profiles (see Figure 2.23) only PiP-, Pg- and Pn-phases are visible. The type I profiles are characterised by a homogeneous crust with velocities from 6.3 to 6.6 km/s. A thin mantle transition of about 1 km thickness within which the velocity increases rapidly up to about 7.7 km/s. On type II profiles the PmP can be weaker or stronger than the PiP. The profiles with strong PmP have an intermediate reflector at 15 km of depth where the velocity increases to 6.0 - 6.4 km/s. Where the PmP-reflector is less visible, the PiP-reflector is located at 20 km

depth. For the type III profiles, the velocity increases rapidly from 6.0 to 7.3 km/s at 23-24 km of depth and then increases gradually to 8.0 km/s at 27-28 km of depth.

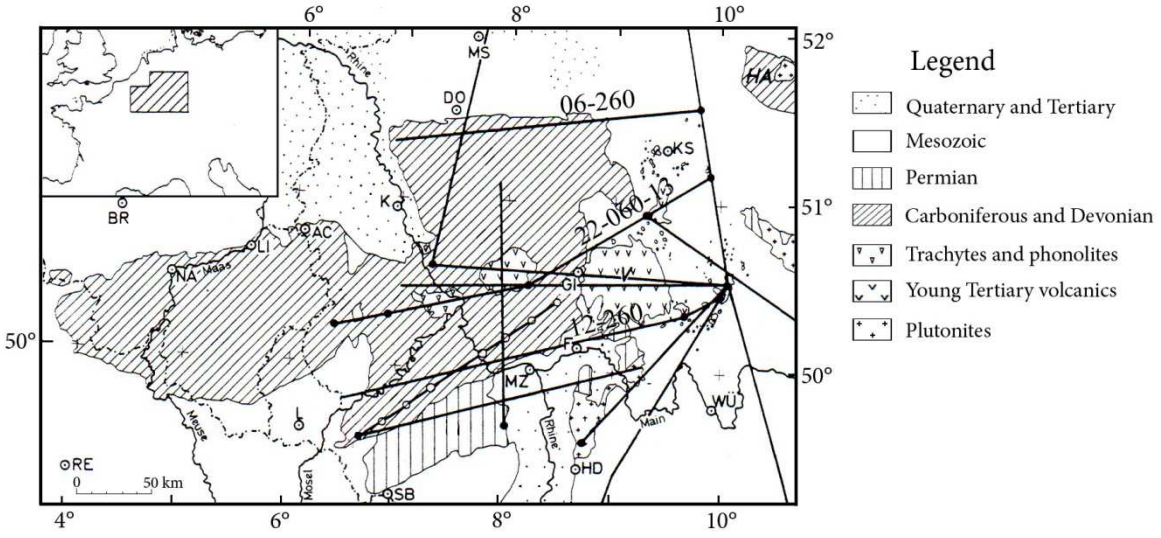

Figure 2.20: Location of the seismic refraction profiles on a generalized geologic map of the Rhenohercynian zone and adjacent areas.
® Cities: AC: Aachen, DO: Dortmund, LI: Liège, KS: Kassel, L: Luxemburg, F: Frankfurt, BR: Brussels, K: Köln, GI: Giessen, SB: Saarbrücken, HD: Heidelberg, NA: Namur, MS: Münster, MZ: Mainz, WÜ: Würzburg, RE: Reims. Redrawn from Mooney & Prodehl, 1978.

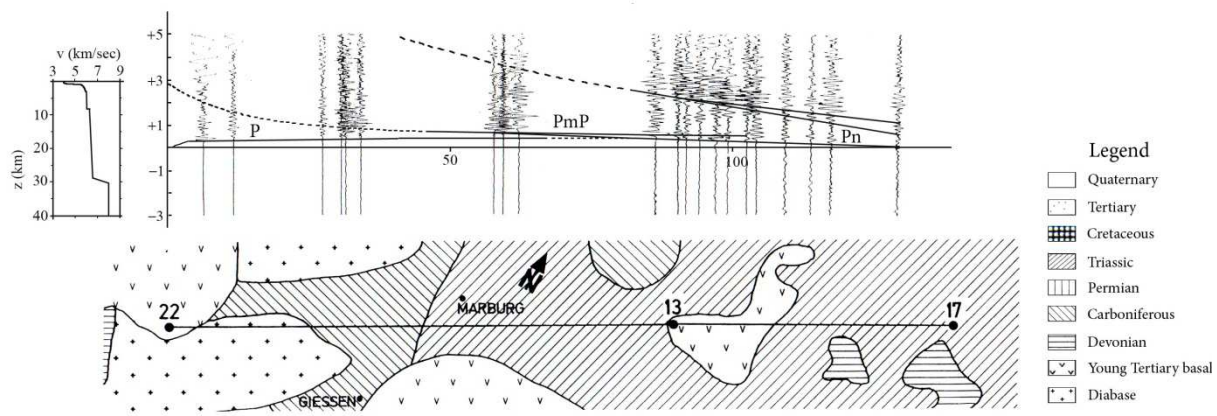

Figure 2.21: An example of the type I profiles (Profile 22-060-13).
Top: record section with theoretical traveltime curves corresponding to the indicated velocity-depth function (top left). The broken lines represent sub-critical reflections. Bottom: geological sketch of the area where the profile was shot. Redrawn from Mooney & Prodehl, 1978.

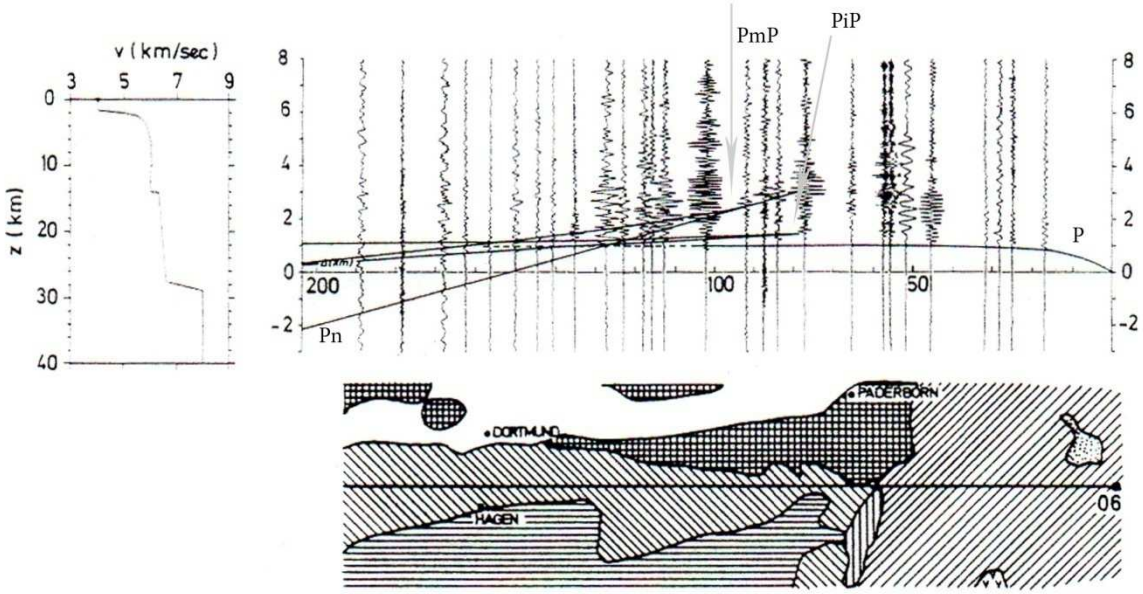

Figure 2.22: An example of the type II profiles (Profile 06-260).
For further information see Figure 2.21. Redrawn from Mooney & Prodehl, 1978.

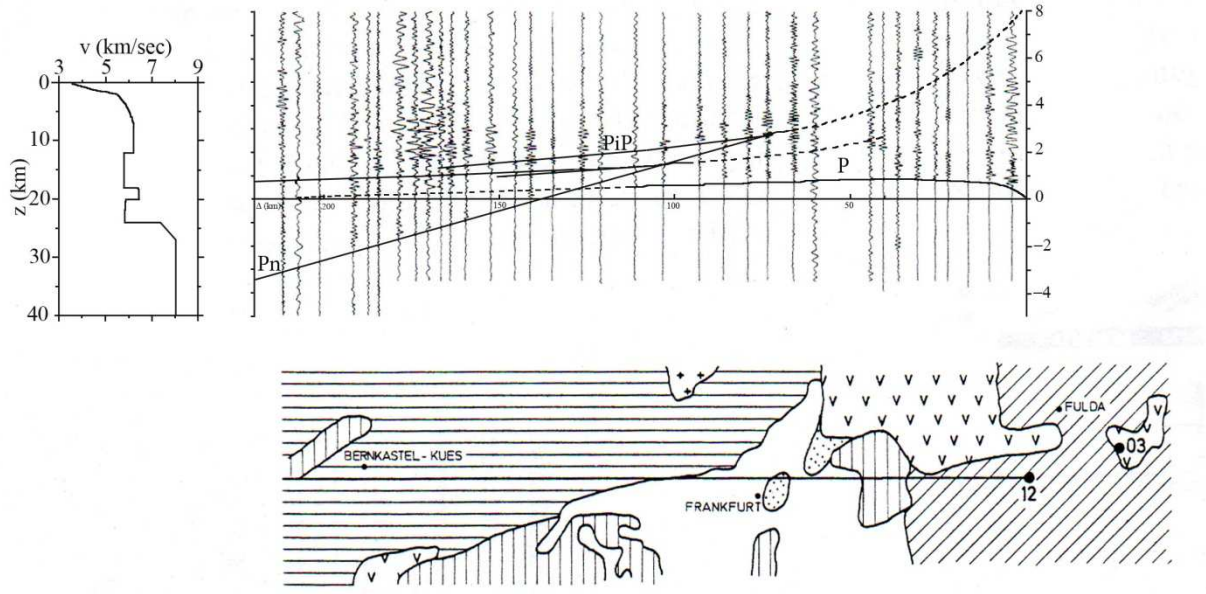

Figure 2.23: An example of the type III profiles (Profile 12-260).
For further information see Figure 2.21. Redrawn from Mooney & Prodehl, 1978.

Giese (1983) used refraction data taken from Giese *et al.* (1976), Mooney and Prodehl (1978) and Mechie *et al.* (1983) to study the crustal structure along two crustal sections (Figure 2.24). One of these sections is located from Aachen to the Palatinate Forest. Along this section (line AA' seen on Figure 2.24), the average crustal thickness is about 30 km. In the Mossel depression however, a 10 km broad transition zone between the crust and the mantle is seen. Both in the Saxothuringian zone and the south of the Rhenohercynian zone, intracrustal reflections are dipping from north to south at about 12 to 14 km of depth. Between this intracrustal reflection and the crust/mantle boundary, a low velocity zone can be distinguished. In the north of the Rhenohercynian zone, no clear mid-crustal

reflections can be distinguished. Giese interpreted the intracrustal reflection seen along this crustal section at 10-20 km as being lower crust and/or parts of an older crust/mantle transition thrusted into the middle crust.

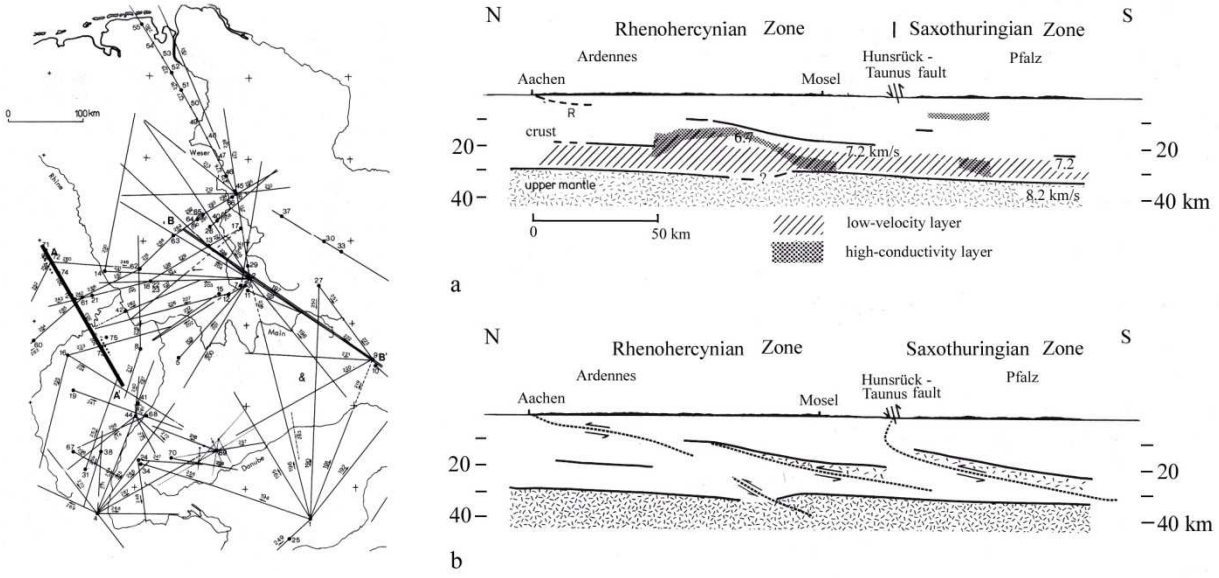

Figure 2.24: Interpretation of the profile studied by Giese, 1983.
Left: Network of crustal seimic-refraction and reflection profiles in western Germany. The thick black line AA' represents the position of the crustal section described on the right. Right: A. Interpretation of the crustal section shown on the map on the left. The hatched zone indicates the presence of a low-velocity layer in the crust. The Densely dashed signature shows were magnetotelluric soundings detected high electrical conductivity. B. Simplified tectonic interpretation of the section. Redrawn from Giese, 1983.

Receiver function analysis

Budweg *et al*. (2006) performed a receiver function analysis to study the mantle structure beneath the Eifel. A receiver function analysis uses P- and S-wave conversions at different surfaces in the crust and mantle from teleseismic earthquakes (earthquakes which occur more than 1000 km away from the station). It is called receiver function because the depth of the different surfaces is determined for every receiver separately. They used data from 96 teleseismic events recorded by 242 seismic stations . Underneath the Eifel, the Moho is situated at approximately 30 km, with a Moho uplift of approximately 2 km underneath the Eifel Volcanic Fields and toward the west it deepens to 32 km underneath the Ardennes Allochthon (Figure 2.25). Because this study focused more on the velocity structure in the lithosphere, not much can be said about the velocity structure in the crust.

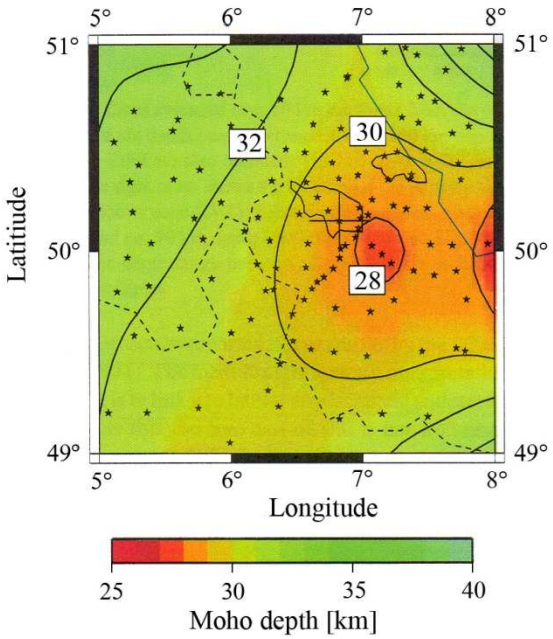

Figure 2.25: Moho depth as colour code and contour lines under the Eifel Volcanic Fields determined from receiver functions.
The stars indicate the seismic stations and the dashed lines are the political borders. Redrawn from Budweg *et al*., 2006.

2.6 Gravimetric and Magnetic data

As mentioned in several previous paragraphs, information can also be obtained from gravimetric and magnetic data. Both the Bouguer gravity anomaly map and the magnetic field reduced to the pole map will be discussed in this paragraph.

2.6.1 Gravimetric map

The Bouguer gravity anomaly map of Belgium (Figure I-4), shows a strong gravity contrast between the northern and southern part of Belgium. The entire northern area corresponds to a gravity high, with the exception of a negative anomaly in its central-western part. This gravity high corresponds approximately to the position of the Brabant Massif and can be explained by the dense Cambrian to Silurian sediments of this massif (Everaerts 2000, Chacksfield, 1993). The southern part of Belgium corresponds to a gravity low separated from the gravity high by a sharp gradient close to the position of the Bordière fault and the Midi overthrust. In this zone, two centers with even lower gravity anomalies can be distinguished. These can be explained by the presence of lighter Devonian-Carboniferous sediments that compose the crust in this place.

The sharp transition zone between the gravity high and low is more accentuated in the southeast and south than to the west of the ECORS-profile. Three explanations are possible to explain this sharp gradient: either it is an important crustal boundary or the Brabant Massif plunges a lot faster in the south and southeast than in the west (Everaerts 2000). Everaerts (2000) modeled this gradient and was able to explain it by solely superficial origins, namely the presence of the Mons Basin south of the

gradient and the gradual sinking of the Brabant Massif towards the south. In the northeast, this transition has a NW-SE direction and it corresponds to the southern end of the Roer Valley Graben (Feldbiss fault). Here, the 2000 m loose sediment infill of the graben can explain the low gravity values east of the transition.

In the gravity high, two distinct anomalies can be seen. The first is the clear gravity low, where the second is situated underneath and to the southwest of the Campine region with very high gravity values. The gravity low is elongated in a west-northwest direction in its western part and in an approximately east-west direction in the eastern part. It follows the structural grain of the Brabant Massif. In fact, the negative anomaly is composed of two main centers of negative values (-34 mgal). Several lineaments can be distinguished on the Bouguer anomaly gravity map. Some of them correspond to known faults, others are suspected to be unknown faults. This negative anomaly has been modelled and corresponds to a steep-sided probably fault bounded body with a low density of 2.63 g/cm^3 (Everaerts *et al.*, 1996) positioned at a minimum depth of 2.5 km. This body has first been interpreted as a granitic body of Ordovician age, correlated with the magmatic rocks found at the surface of this age. But this has proven very unlikely because the Ordovician magmatic rocks found at the surface have an intermediate composition (andesitic to dacitic) (André 1991, Verniers *et al.*, 2002; Sintubin & Everaerts, 2002) of higher density than the granitic body and cannot have evolved from a granitic magma. Therefore, a second magmatic episode has to be considered. Variscan granites cannot explain the anomaly due to the close kinematic relationships between the body and the Silurian-early Devonian age. Therefore, this body is interpreted as a Neoproterozoic crustal body of granitic composition (Sintubin & Everaerts, 2002). This explanation is also favoured by the geochemical characteristics of the terrigene sediments of Cambrian-Ordovician age (VanderAuwera and André 1985; André, 1991).

The high gravity values found underneath the Campine region can only be explained by a feature at depth. Oulidi (1998) modeled this anomaly and found that it can either be explained by the expulsion of lower crust material in the upper crust by an overthrust or by an uplift of the Moho discontinuity that reaches its maximum underneath the Roer Valley Graben, but already starts underneath the Campine region.

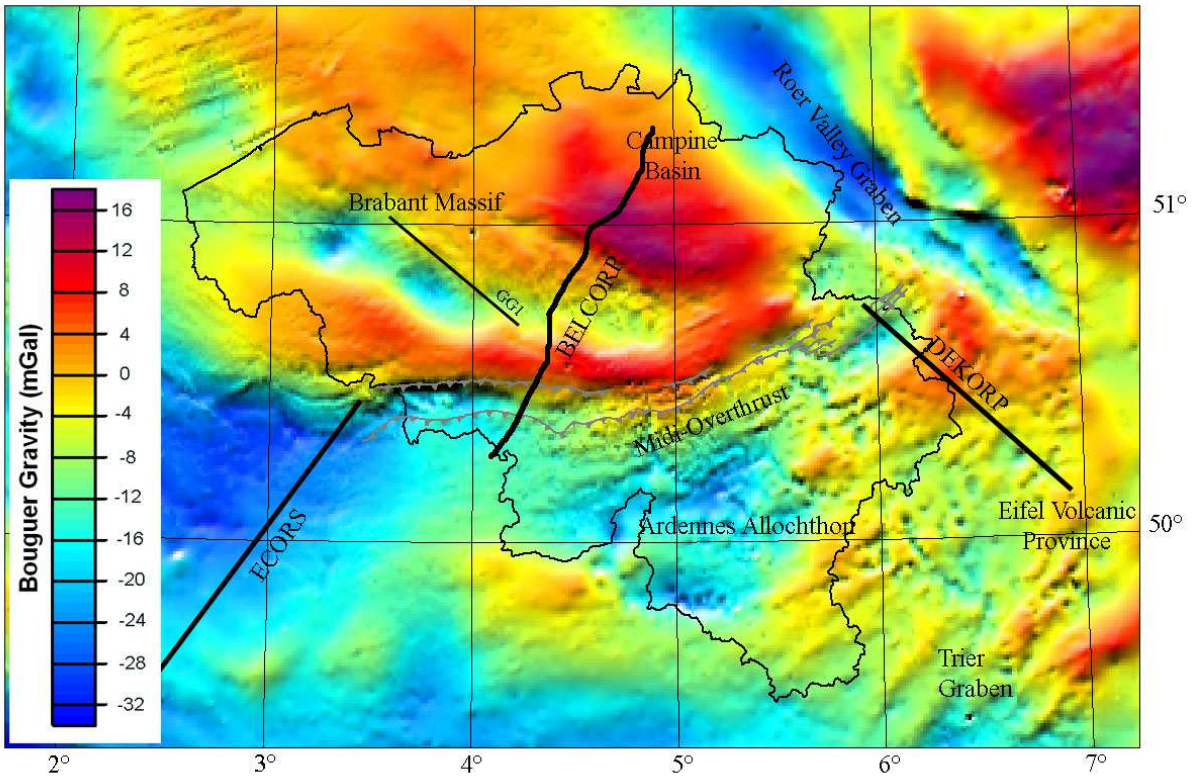

Figure 2.26: The Gravity Bouguer Anomaly map of the Region with the location of the most important tectonic structures and positions of important seismic reflection profiles. The back line represents the Belgian border. Bouguer gravity anomaly data: Royal Observatory of Belgium

2.6.2 Magnetic map

Information cannot only be obtained from gravimetric data but also from magnetic data (Figure I-5). On the magnetic map reduced to the pole, one can see two different domains: one corresponding to the Brabant Massif and one to the Ardennes Allochthon. The positive magnetic anomaly of the Brabant Massif corresponds to the heart of the massif. This anomaly is actually composed of several superimposed high frequency (short wavelength) anomalies. In fact, between Gent and Perwez a succession of parallel northwest-southeast oriental ridges can be seen. The anomaly is prolongated in a discontinuous way in the North sea to the North. In the south; it is very steep and corresponds to the northern border of the negative gravimetric anomaly and the GG1 gravimetric gradient (Figure I-4) and corresponds to the position of the Asquempont fault. The magnetic positive anomaly in the Brabant Massif corresponds to the magnetic sediments of the Tubize Formation (Chacksfield *et al.*, 1993). The Campine region is characterised by a large negative zone, whereas in the Antwerp region a slight positive anomaly is seen (Everaerts, 2000).

In the Ardennes Allochthon, high frequency anomalies correspond to the position of the Rocroi and Stavelot Inlier. Underneath these Stavelot anomalies, a low frequency anomaly can also be distinguished and can be associated to a second low frequency anomaly slightly to the west but with lower amplitude. Both anomalies have been modeled as deep-seated Precambrian blocks (Chacksfield *et al.*, 1993), that have been displaced compared to one another by the proposed Antwerp-Saint Hubert fault (Paproth, Dreesen & Thorez, 1986).

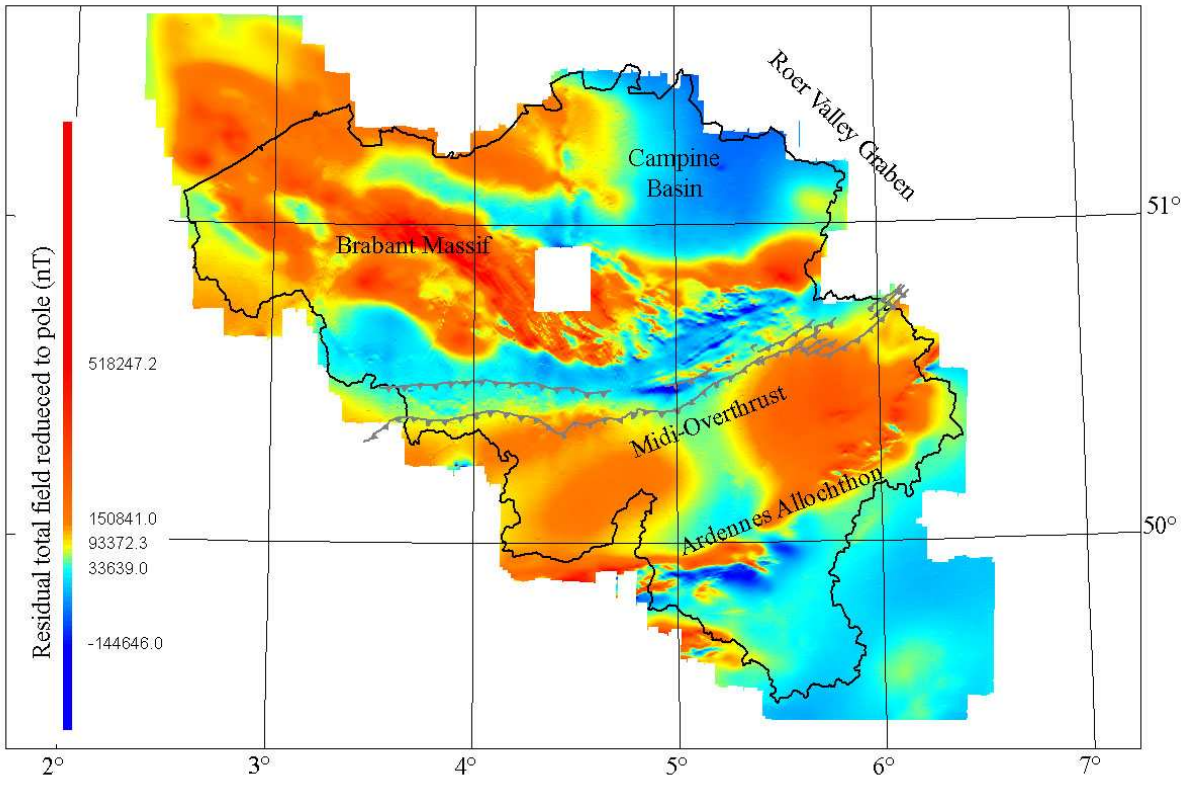

Figure 2.27: Aeromagnetic anomaly map reduced to the pole with the location of the most important tectonic structures. The black line represents the Belgian border.
Magnetic field reduced to the pole data: Royal Belgian Institute of Natural Sciences, Belgian Geological Survey.

Chapter 3 The dataset and the preliminary crustal model

3.1 Introduction

In the framework of this study, waveforms from the Belgian seismic network were used. This seismic network is composed of 24 permanent stations (Figure 3.1). The emplacement of these stations was based on the following criteria (Camelbeeck, 1994):

1. In theory, the distance between the stations must not be greater than three times the largest depths of the earthquakes to assess the earthquake focal depth in the studied area.

2. The level of noise will be reduced if the station is placed on solid rock instead of on unconsolidated rocks.

3. The installation and maintenance costs are elements that need to be considered when choosing a site.

Besides the permanent network, the Royal Observatory of Belgium (ROB) also possesses some mobile stations that can be installed quickly around epicenters or can be placed in profile when important quarry blasts are notified. Certain mobile stations are placed so that they interpolate the permanent network. Most stations are equipped with three-component short period (signal > 1 Hz) seismometers (Mark-Product and Lennartz), some with a three-component broadband (signal between 0.01 Hz and 50 Hz) seismometer (Güralp, CMG-40, CMG-3E or GMC-3T).

Earthquakes are not only located using data from the Belgian network but also with arrival times from stations in neighbouring networks, like the Bennsberg seismic network. The data from this network will also be used to perform the local tomography, because the seismograms themselves registered at the stations of this network are not provided (just the measured arrival times of P- and S-waves), no PmP- or SmS-waves can be determined and therefore these stations cannot be used to determine the Moho depth.

To be able to determine the Moho depth and to perform the local seismic tomography, the sources of seismic energy used include three different kinds of events:

- Local earthquakes in Belgium and surrounding regions
- Induced earthquakes by mining activity in Germany
- Artificial explosions in the southern North Sea

Only the local earthquakes will be used in the tomographic inversion due to homogeneity reasons (see Chapter 5 paragraph 5.4.1), whereas all three types of events are used to determine the Moho depth. Because the majority of the local earthquakes happens in the east or north-east of Belgium and because most of the stations are placed in the southern part of the country, it is only possible to determine the Moho depth underneath the Ardennes Allochthon. To be able to determine the Moho depth at more places, the German mine-induced earthquakes and the North Sea explosions were added to the dataset.

The mine-induced earthquakes should provide information on the south east of the Belgian territory and the Grand Duchy of Luxemburg. These mine-induced earthquakes were originally only located using the Bennsberg data, which results in not very well located events. Therefore they were relocated, after adding the arrivals of these events at the Belgian stations. When these events are located, the depth can be fixed at 1 km, because the mines that induce these earthquakes are not much deeper than that.

The North Sea explosions were added to the dataset, so that information on the Brabant Massif can be attained. These explosions are performed by both the Royal Navy of Belgium and that of The Netherlands in the framework of the destruction of bombs from the Second World War left in the North Sea. Both navies provide the time of defusing and the location of the bombs. Because they are situated at the edge of the Belgian seismic network, it is very difficult to locate them to a better degree with the seismic arrival times only. Therefore, the coordinates provided by the Navy are used. Only the exact time (seconds) has to be deduced from the arrival times of the explosions at the different stations.

The local earthquakes were also relocated because the earthquake database of the Royal Observatory of Belgium lacks a classification that allows selecting the well-located earthquakes, and for several of the same earthquakes different locations were given in the database. Because only well-located earthquakes can be used to determine the Moho depth and the local seismic tomography, all the earthquakes were relocated before proceeding with the Moho determination and the local seismic tomography. For this relocation the programme mknorm2000 was used. This programme has been developed by H. Martin at the Royal Observatory of Belgium and is based on the programme Hypo71 (Lee & Lahr, 1975). In comparison with Hypo71, this programme can use two different models for P- and S-waves. Thus, the Vp/Vs-ratio can change from layer to layer, whereas in the original hypo71 programme a constant Vp/Vs-ratio is required. However, the layer thicknesses still have to be the same for the P- and S-velocity models. To evaluate the sensitivity of the calculated locations in function of the geometry of the network, the programme Mknorm2000 performs 500 different locations of each earthquake. This is done by adding an aleatory increment according to a normal distribution with a σ of 0.05 s for P-waves and 0.1 s for S-waves to the P- and S-arrivals, which are considered as mean of the normal distribution. The values are considered as the standard deviation of the uncertainties in the seismic phases measurements.

The chosen location is the mean of the 500 solutions, and the spatial distribution of the whole solution set is used to determine the location uncertainty at a 0.95 confidence level.

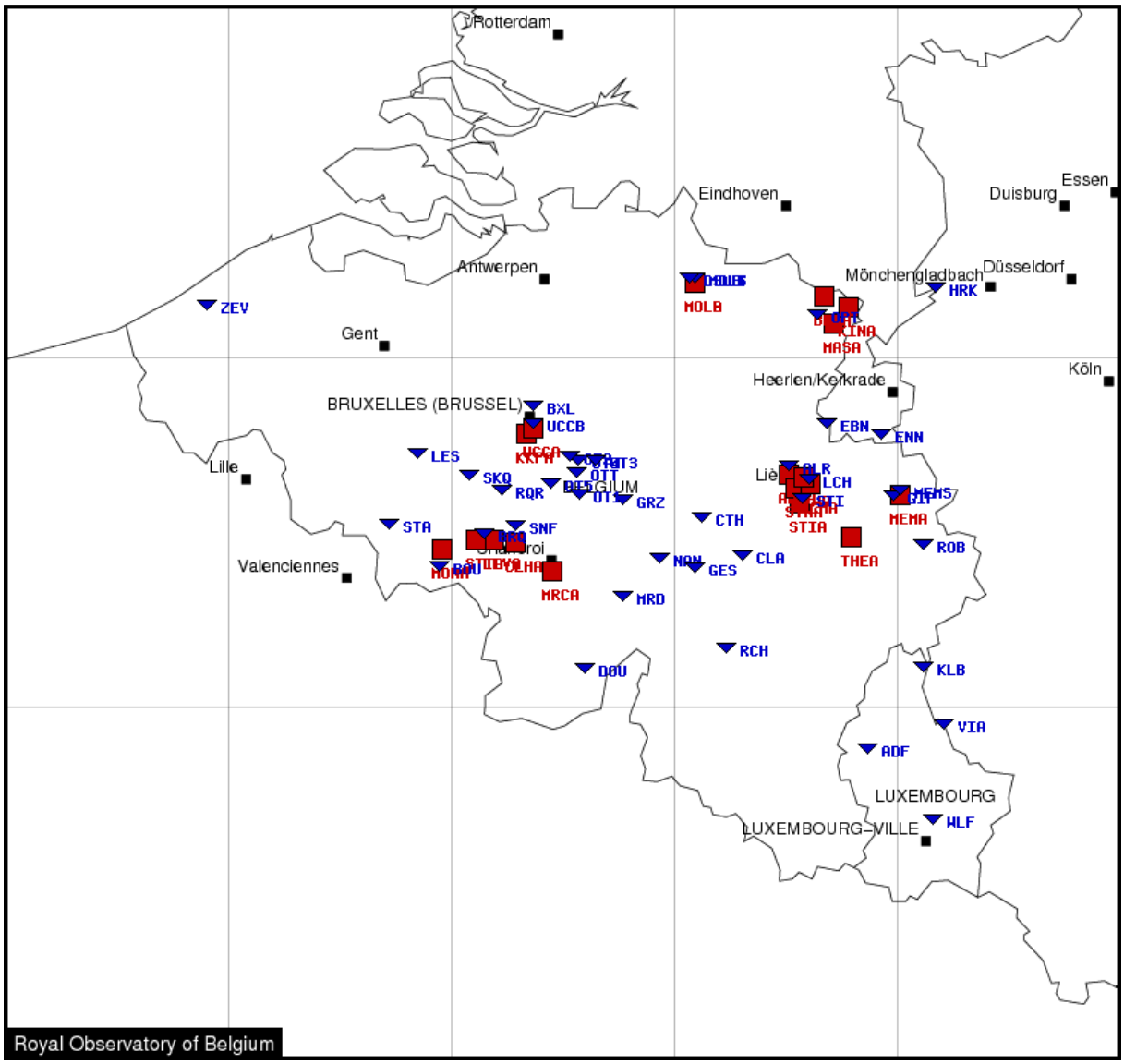

Figure 3.1: Map showing the stations of the Belgian seismic network of the Royal Observatory. The blue triangles represent the permanent and mobile seismic stations, the red squares represent the seismic accelerometers. Black lines represent the political borders.

3.2 Crustal velocity models used in earthquake location

Several one dimensional seismic velocity models of the crust have been deduced in the past to locate earthquakes. The two most important velocity models are one derived by Ahorner & Pelzing (1984) and one by Calbini (2003).

The STD model by Ahorner & Pelzing (1984) is derived from earthquakes located in the eastern Lower Rhine Embayment and then adapted to fit the arrival times of the Liège earthquake on November 8, 1983 and its greatest aftershocks (Table 3-1).

Calbini (2003) determined a new velocity model CAL (Table 3-1) using the programme Velest (Kissling *et al.*, 1994; Husen *et al.*, 2000), a programme that relocates earthquakes and is capable of determining a one dimensional velocity model of the crust at the same time. She also used

earthquakes located in the Lower Rhine Embayment, but these earthquakes were located by the Belgian seismic network, which includes a lot more stations than when Ahorner & Pelzing (1984) determined his model (the Belgian seismic network has only been developed from 1985 onwards), so a lot more arrival times could be used in this study.

The STD model (Ahorner & Pelzing, 1984) consists of 7 layers (see Table 3-1), the CAL model (Calbini, 2003) of 9 layers (Table 3-1). In both models the Moho depth is taken at 32.5 km.

STD			CAL		
Vp (km/s)	Depth (km)	Vs (km/s)	Vp (km/s)	Depth(km)	Vs (km/s)
5	0,0	2,976	5 ± 0.45	0,0	2,98 ± 0.29
5,5	1,0	3,274	5,37 ± 0.48	1,0	3,44 ± 0.18
5,8	2,0	3,452	5,98 ± 0.18	2,0	3,45 ± 0.12
6	3,0	3,571	6,0 ± 0.18	3,0	3,47 ± 0,05
6,25	12,0	3,720	6,10 ± 0.18	8,0	3,54 ± 0.08
6,5	19,0	3,869	6,17 ± 0.12	12,0	3,61 ± 0.07
8,07	32,5	4,804	6,5 ± 0.20	19,0	3,71 ± 0.09
			7,5 ± 0.23	30,0	4,04 ± 0.32
			7,71 ± 0.15	32,5	4,46 ± 0.17

Table 3-1 : Velocity models STD (Ahorner & Pelzing, 1984) and CAL (Calbini, 2003). Both models are a representation of the velocity structure of the crust of North-West Europe.

3.3 Earthquake relocation

3.3.1 Theory

An earthquake is determined by its origin time (t) and its hypocenter location (x,y,z). The x and y coordinates are the coordinates of the epicenter location (t.i. the location of the normal projection of the hypocenter on the earth's surface), and z represents the depth underneath the earth's surface at which the earthquake occurred.

Different methods can be used to locate an earthquake. The method used depends on the position and density of the seismic stations. In this paragraph only the method used in this study to relocate the earthquakes registered by the Belgian seismic network will be explained (Aki & Richards, 1980; Camelbeeck, 1994).

The arrival time of the seismic waves registered at a certain station i depends on the origin time t of the earthquake and the travel time $T(x,x_i)$ along the ray path connecting the earthquake to the station at the surface:

$$\tau_i^{\omega}=t+T^{\omega}(x,x_i) + \varepsilon_i^{\omega} \quad (3.1)$$

Where τ_i^{ω} is the arrival time of the wave ω measured on the seismogram, t is the origin time of the earthquake, $T^{\omega}(x,x_i)$ is the travel time for the wave ω along the path between the coordinates of the earthquake (x) and the station (x_i), and ε_i^{ω} is the uncertainty on the measurement of the arrival time.

The best estimation of the origin time (t) and the hypocenter (x) are looked for. When the velocity structure is known, the solution can be found by resolving the following equation:

$$\tau=A(m) \quad (3.2)$$

Where τ is the data vector containing the arrival times measured in the station, and m is an assumed model vector composed of the origin time of the earthquake and its location.

$$m=(x,y,z,t) \quad (3.3)$$

The calculation is complicated by the fact that the travel time of the wave along the ray is not known precisely. It can however be approximated from a simple idealized spatial velocity model, that somewhat resembles the real velocity structure, but can never completely represent it. The travel time function is a non-linear function in x and x_i.

In this inverse method, an approximated origin time (t*) and location (x*,y*,z*) are chosen. From these approximated parameters, a theoretical arrival time T in the station i is calculated (Lee & Stewart, 1989).

$$T_i(x^*,y^*,z^*,t^*) =t_i(x^*,y^*,z^*) + t^* \quad \text{for i=1,…,n} \quad (3.4)$$

The residual in time in the station i (V_i) is determined by the difference between the calculated arrival time and the observed arrival time.

$$V_i(x^*,y^*,z^*,t^*)= \tau_i^{\omega} - T_i(x^*,y^*,z^*,t^*) \quad \text{for i=1,…,n} \quad (3.5)$$

Linearising the problem, the equation above can be re-written as:

$$V_i - \varepsilon_i = \frac{\delta T_i}{\delta x}\Delta x + \frac{\delta T_i}{\delta y}\Delta y + \frac{\delta T_i}{\delta z}\Delta z + \Delta t \quad (3.6)$$

With $\frac{\delta T_i}{\delta x}$, $\frac{\delta T_i}{\delta y}$, $\frac{\delta T_i}{\delta z}$ the partial derivatives of the travel time from the coordinates of the hypocenter to the station i.

Δt, Δx, Δy and Δz are the adjustments needed for the origin time and the hypocenter of the earthquake.

In matrix form:

$$A\,\delta x = T \qquad (3.7)$$

Where A is the matrix of the partial derivatives, δx is the adjustment vector (Δt, Δx, Δy, Δz) and T is the residual vector.

Because the problem is not linear, the solution can only be found by an iterative procedure, where with every iteration, the difference between the calculated and the observed arrival time $\Sigma_k V_k^2$ is minimized.

Mknorm2000 uses the coordinates of the station with the lowest arrival time as the initial coordinates of the earthquake in the iteration together with a chosen focal depth. As mentioned in the introduction, the earthquakes are located in a chosen velocity model.

3.3.2 Parameter determination

3.3.2.1Model determination tests

When locating earthquakes, the degree of accuracy attainable for locating hypocenters is mainly determined by the geometrical configuration of the network, the adequacy of the assumed crustal model and the precision of the P- and S-wave arrival time picking. It is important to know the influence of these different parameters. Therefore several tests have been performed with the earthquakes of 1985 and 1998.

Three trial focal depths (4, 10 and 25 km) and two velocity models (CAL and STD) were compared.

In a first phase, the earthquakes were located using the two velocity models and the three initial trial depths. The purpose of this test was to see whether the different models converge to the same solution (= probably the correct solution). The results were plotted in latitude-longitude, longitude-depth and latitude-depth diagrams to see the differences in solutions between the different model-depths. Wadati-plots (or tp-ts versus tp diagrams (Wadati, 1933)) were also constructed. In an ideal Wadati-plot the best-fitting line should pass through the origin. The deviation of the best-fitting line at the origin gives an indication of the accuracy of the locations (Figure 3.3). From these wadati-plots, the origin time of the earthquake was corrected and then a T^2-Δ^2 plot was made. Out of this plot the focal depth was recalculated and compared with the solutions obtained for each earthquake.

In the latitude-longitude, longitude-depth and latitude-depth diagrams the coherence between the different models was studied. These diagrams showed that the locations given by the models STD04 and STD10 (velocity model STD and initial trial depths of respectively 4 and 10 km) differ more than 2 km in latitude-longitude and more than 5km in depth from the locations given by the other models for respectively 6/12 and 4/12 of the relocated earthquakes (Figure 3.2). For two earthquakes, the CAL04 model showed a deviation. For three out of twelve earthquakes, all the locations for the different models were coherent (Figure 3.2). These graphs also show that in some cases the location of the earthquakes is very well resolved for one combination of velocity model and initial depth, but the location is very different from the results of the other combinations (Figure 3.2 middle column). Therefore, the model has to be chosen very carefully, to avoid “false” well-located earthquakes.

The Wadati-plots (Figure 3.3) also indicate that the CAL-models show less deviation from the origin than the STD-plots (except for three out of twelve earthquakes).

The depths calculated from the T^2-Δ^2 plots show the same tendencies as the depths determined by the location with the different models. Due to the large error bars on the calculated depths no other conclusions can be drawn.

After these tests the CAL model was selected as best-fitting velocity model.

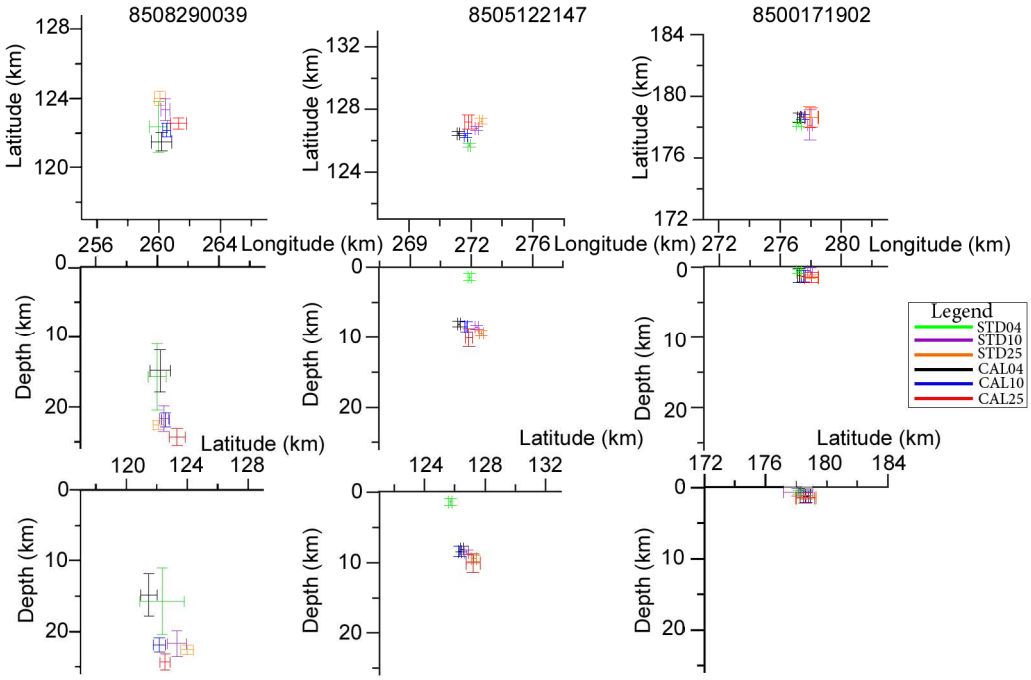

Figure 3.2: Above: Latitude-longitude (Lambert coordinates), middle: longitude-depth (Lambert coordinates) and below: latitude-depth graphs for the earthquakes: 19850829 at 00:39 (left); 19850512 at 21:47 (middle) and 19850817 at 19:02 (right)
For the earthquake locations determined in the standard (STD) and Calbini (CAL) velocity models for respectively three initial depths (4, 10 and 25 km).

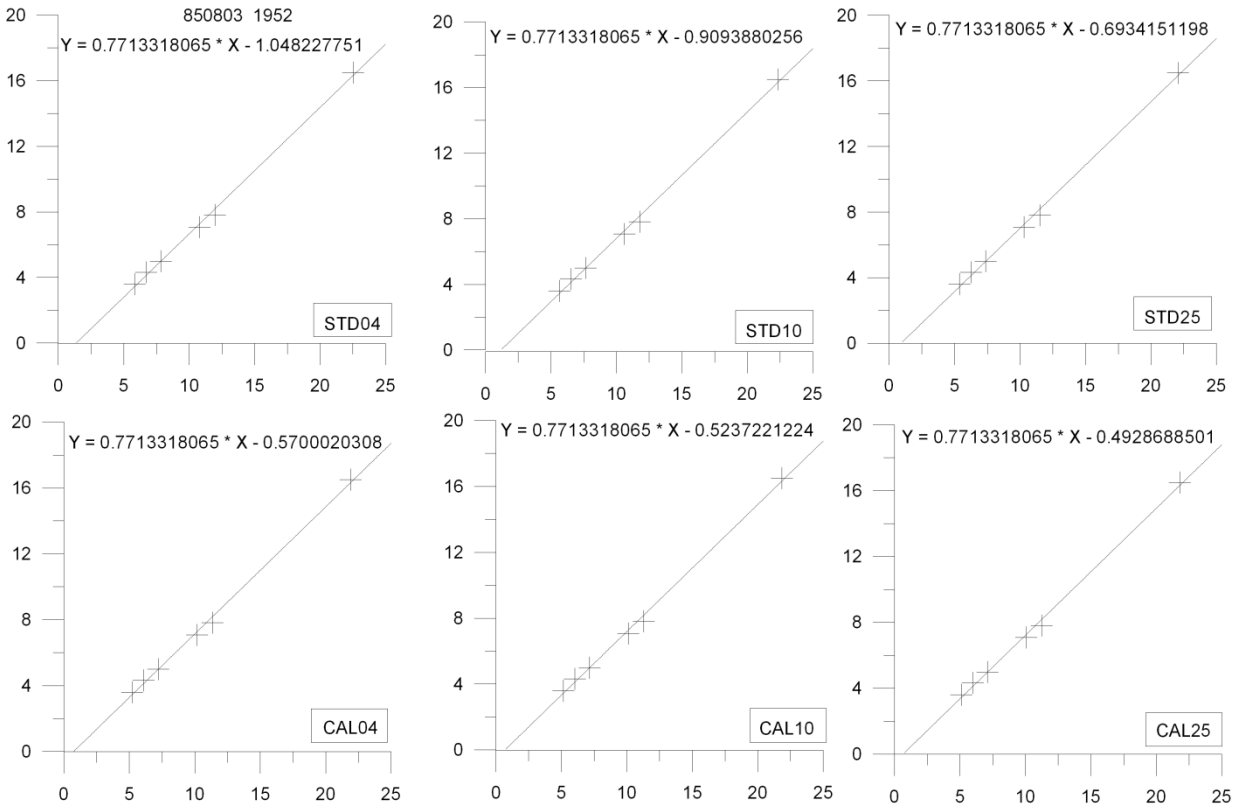

Figure 3.3: Wadati-plots for the different relocations for the earthquake of 17/08/1985 at 19:02. As can be seen in the figure is the slope of the trendline the same in all plots. This is so, because it only depends on the measured ts and tp. The only variable over the different plots is the calculated origin time of the earthquake that has been substracted from tp (x-axis). The closer the intersect with the y-axis is to the origin, the better the location.

In a second phase the uncertainty limits (1σ) of the CAL (Calbini, 2003) model were tested (Table 3-2). The 1998 earthquakes were relocated using three different initial trial depths and the CAL-model and its lower (CAO) and upper limit (CAB) (Table 3-2), so that the influence of the CAL-model could be investigated. In the original CAB model low-velocity layers appear. Because the programme mknorm2000 cannot locate earthquakes with such low-velocity layers, further changes had to be made to the CAB-model. For the well-located earthquakes the lower limit (CAO) and the CAL model were very close (Figure 3.4). The CAB model showed more differences. This might be explained by the fact that the original CAB model needed to be changed because of the occurrence of low velocity layers. In the end no selection was made between the initial trial depths or limits of the CAL model. In the end, all three models and all three initial depths for the relocation of the earthquakes were used. These graphs also show that for some combinations of model-initial depth, the earthquake is very well located, but for the other combinations, the location is very different or not very well located. Therefore the final model and initial depth have to be carefully chosen.

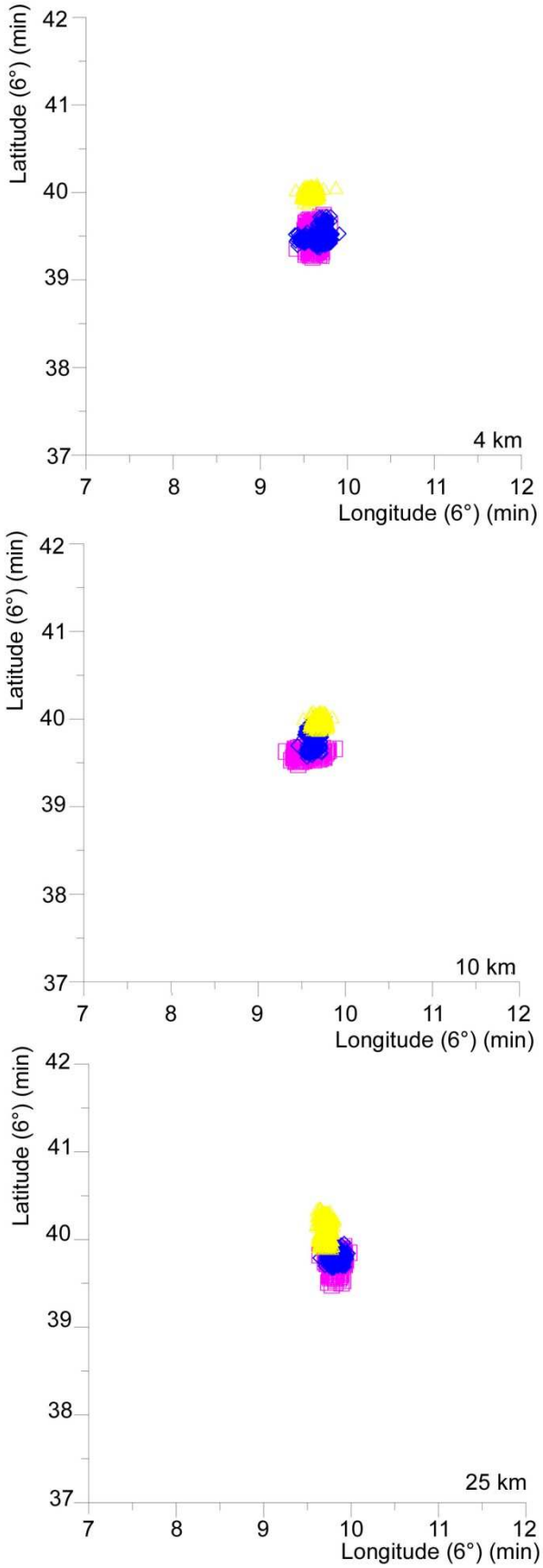

Figure 3.4: Different locations for the earthquake of 6/04/1998 at 07:20.
The upper, middle and lower charts give the locations starting respectively from the initial depths 4, 10 and 25 km. The yellow triangles show the 500 iterations for the CAB model, the red squares the 500 iterations for the CAO model and the blue diamonds the 500 iterations for the CAL model.

CAO			CAL			CAB (adapted)			CAB (original)		
Vp (km/s)	Depth (km)	Vs (km/s)	Vp (km/s)	Depth (km)	Vs (km/s)	Vp (km/s)	Depth (km)	Vs (km/s)	Vp (km/s)	Depth (km)	Vs (km/s)
4,55	0,0	2,68	5	0,0	2,98	5,45	0,0	3,28	5,45	0,0	3,28
4,89	1,0	3,27	5,37	1,0	3,44	5,85	1,0	3,58	5,85	1,0	3,76
5,8	2,0	3,35	5,98	2,0	3,45	6,16	2,0	3,59	6,16	2,0	3,55
5,82	3,0	3,44	6,0	3,0	3,47	6,18	3,0	3,60	6,18	3,0	3,52
5,92	8,0	3,47	6,10	8,0	3,54	6,28	8,0	3,61	6,28	8,0	3,62
6,05	12,0	3,54	6,17	12,0	3,61	6,29	12,0	3,68	6,29	12,0	3,68
6,31	19,0	3,64	6,5	19,0	3,71	6,70	19,0	3,78	6,70	19,0	3,78
7,28	30,0	3,76	7,5	30,0	4,04	7,73	30,0	4,32	7,73	30,0	4,32
7,56	32,5	4,28	7,71	32,5	4,46	7,86	32,5	4,64	7,86	32,5	4,64

Table 3-2 Velocity model CAL with its upper and lower standard deviation limits (CAO and CAB)

3.3.2.2Conclusions

All the earthquakes were located using the CAO, CAL and CAB models and the three initial trial depths. In this way, “false” well located earthquakes can be eliminated as well as possible. The average of the 4500 iterations (500 for each model and initial trial depth, see above) was taken as best fit and final solution. Out of all these iterations 2σ limits were calculated for both the three spatial coordinates (x,y,z) and the origin time.

3.3.3 Seismic events relocation

In the end, 793 earthquakes were relocated. From these earthquakes, the square root of the sum of the squares of the 2σ of the different coordinates was taken. When this root was less than two, the earthquakes were considered to be well located. This way, 36 earthquakes were very well located ($2\sigma < 2$), 104 well located ($2 < 2\sigma < 4$) and 653 less well located ($4 < 2\sigma$). For the tomographic study and the Moho determination, only the 140 very-well and well-located earthquakes were used (Table 3-3 and Figure 3.5).

The first results of the mknorm2000 programme showed several bugs in the determination of the uncertainties on the localization. When the time uncertainty is calculated, the programme only takes into account the seconds and not the minutes. These bugs were corrected afterwards.

When the results of the relocation are compared with the traditionally determined earthquakes in the database, the results of this study are overall better located than the locations given in the database. Of the 32 well-located earthquakes that can be compared: 29 are better constrained in latitude and longitude whereas 19 are better constrained in depth. In some cases (20011112 at 00h13 or 20030323 at 22h23) however, the latitude-longitude or the depth are less well determined. In other cases (like the 20040719 at 01h40 earthquake the uncertainty in the database is: 3.50 km latitude-longitude and 10.32 km in depth), the earthquakes are localized much better than before. As mentioned in the paragraph 3.3.2, some earthquakes, like 20010217 at 00h54 that are very well determined in the database (1.32 km latitude-longitude and 1.64 km depth) are not very well determined in this study (12.64 km in latitude-longitude and 7.14 km in depth). For these earthquakes, there is a great influence of the model-initial depth on the location. For some model-initial depth couples, the earthquake will be very well determined, but when the locations of the different model initial depth couples are compared to one another they are very different. These are the “false” well-located earthquakes mentioned in paragraph 3.3.2. This trend can also be seen in the well-located earthquakes. For all 13 earthquakes where the depth is less well constrained in this inversion, the 2σ of the original locations is at less than 2.5 km, so very well constrained. In this study 2σ now varies between 2.4 and 3.7 km.

For the Moho determination induced earthquakes in Germany and explosions in the North Sea were also used. The German induced earthquakes were located for the three velocity models but keeping the depth fixed at 1 km. This is needed because the earthquakes are mine-induced and these mines are not much deeper than 1 km. For the North Sea explosions, the locations provided by the navies of both the Netherlands and Belgium were used, because these locations are more accurate than any calculated location. The exact origin time of these explosions was determined. This was done by determining the arrival time from the P- and S-waves in the different stations and recalculating the origin times of the explosions from these arrival times and the distances between the stations and the explosion location. The locations and arrival times of both German induced earthquakes and North Sea explosions can be seen in Figure 3.5 and respectively in Table 3-4 and Table 3-5. Because these earthquakes and explosions were specifically measured and located for this study, they cannot be compared to old locations in the database.

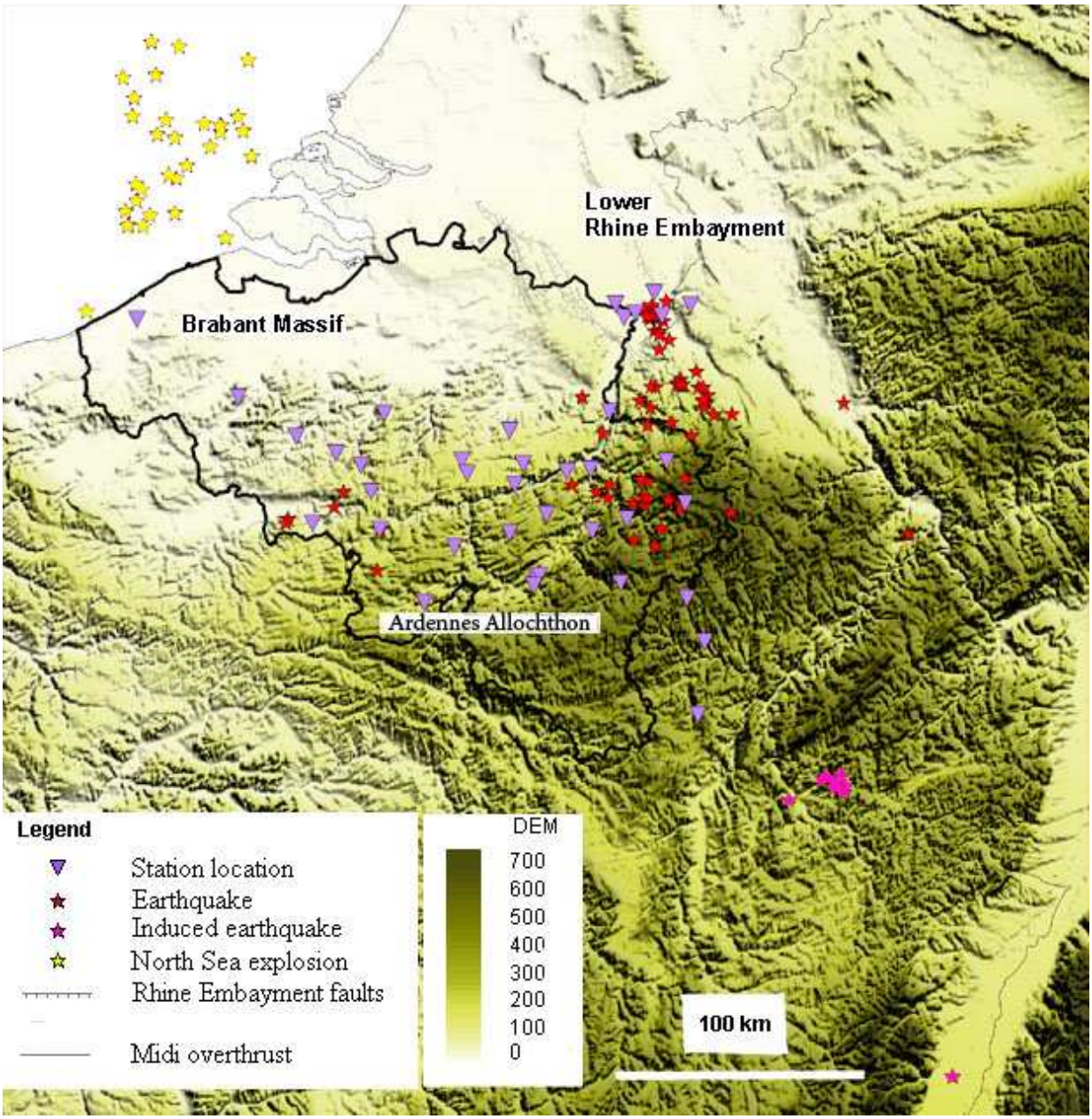

Figure 3.5: Map with the localizations of the earthquakes (red stars), Explosions in the North Sea (yellow stars) and German mine-induced earthquakes (pink stars) used in this study.

date	hour	sec	2σ	Old sec	Old 2σ	latitude (km)		2σ	Old latitude (km)		longitude (km)		2σ	Old longitude (km)		2σ hor	Old 2σ hor	depth (km)	2σ	Old depth (km)	Old 2σ
1985/08/20	1454	6,59	0,74	06	?	50	31,33	1,28	50	25.8	5	48,17	1,4	5	48,00	1.90	?	21,16	3,36	20,8	?
1986/05/26	1213	52,36	0,6	53.00	?	50	35,19	1,04	50	37.74	5	31,83	0,62	5	31.44	1.21	?	7,37	2,06	?	?
1987/03/20	2315	58,77	0,3	58	?	50	24,47	1,22	50	24.24	3	48,08	1,02	3	48.72	1.59	?	7,13	2,42	6.8	?
1987/03/21	57	37,45	0,46	37	?	50	24,75	1,26	50	24.54	3	47,97	1,16	3	48.66	1.71	?	5,05	3,56	6.8	?
1987/04/01	643	51,63	0,58	51	?	50	23,57	1,48	50	23.82	3	47,21	1,92	3	48.72	2.42	?	6,09	3,08	6.6	?
1987/10/19	1858	55,59	0,5	55	?	50	45,42	2,26	50	45.00	6	2,6	0,72	6	2.76	2.37	?	19,52	3,22	18.8	?
1989/06/22	2202	38,49	0,64	38	?	50	27,15	0,66	50	27.42	5	52,17	1,06	5	51.00	1.25	?	21,4	2,84	21	?
1989/10/20	631	12,62	0,4	12	?	50	27,34	1,76	50	27.3	6	2,39	1,2	6	2.52	2.13	?	8,84	1,96	9.2	?
1989/11/14	1913	20,51	0,42	20	?	50	27,63	1	50	27.66	6	1,99	1	6	1.86	1.43	?	8,2	1,52	8.3	?
1989/11/20	329	40,16	0,48	40	?	50	27,53	0,68	50	27.72	5	48,35	0,58	5	48.3	0.89	?	24,49	2,5	22.8	?
1989/12/04	120	29,59	0,36	29	?	50	31,41	0,38	50	31.38	5	57,42	0,66	5	57.24	0.76	?	7,11	1,38	6.7	?
1989/12/14	727	23,94	0,38	24	?	50	27,86	0,62	50	27.84	6	2,16	0,6	6	2.1	0.70	?	8,49	1,22	8.5	?
1989/12/15	1444	52,47	0,34	52	?	50	27,72	1,04	50	27.6	6	1,72	0,6	6	1.8	1.20	?	7,9	1,1	7.9	?
1989/12/31	2126	11,04	0,4	11	?	50	27,89	0,72	50	27.9	6	1,71	0,8	6	1.62	1.35	?	7,92	1,3	7.9	?
1990/01/04	743	32,37	0,38	32	?	50	27,68	0,62	50	27.66	6	1,85	0,7	6	1.8	0.94	?	8,08	1,3	8.1	?
1990/01/04	1113	20,31	0,4	20	?	50	27,6	1,76	50	27.72	6	1,97	1,44	6	1.74	2.27	?	8,14	1,7	8.1	?
1990/01/06	2121	50,07	0,4	50	?	50	27,72	0,94	50	27.78	6	1,81	1	6	1.68	1.37	?	8,41	1,3	8.5	?
1990/01/07	45	19,12	0,32	18	?	50	27,85	1,28	50	27.66	6	1,34	3,24	6	2.4	3.48	?	7,51	1,48	9.2	?
1990/01/10	906	50,25	0,4	50	?	50	27,76	1,12	50	27.66	6	1,61	0,92	6	1.62	1.45	?	7,56	1,3	7.4	?
1990/01/17	1616	33,77	0,26	33	?	50	27,92	1,4	50	27.72	6	1,59	3,24	6	1.38	3.53	?	7,77	1,32	8.1	?
1990/01/24	2152	17,89	0,36	17	?	50	27,98	0,6	50	27.96	6	1,26	0,62	6	1.26	0.86	?	7,52	1,14	7.5	?
1990/01/28	2315	2,98	0,36	03	?	50	27,91	1,88	50	28.02	6	1,67	1,34	6	1.56	2.31	?	8,17	1,22	8.2	?
1990/01/29	209	9,54	0,4	09	?	50	27,94	0,66	50	28.02	6	1,24	0,66	6	1.2	0.93	?	7,82	1,24	7.7	?
1990/01/29	343	11,61	0,36	11	?	50	28,12	0,62	50	28.02	6	1,19	0,64	6	1.2	0.89	?	7,61	1,18	7.6	?
1990/02/01	1843	42,86	0,36	42	?	50	28,08	0,6	50	27.96	6	1,44	0,48	6	1.38	0.77	?	8,11	1,16	8.3	?
1990/02/07	243	38,26	0,38	38	?	50	28,15	0,94	50	28.08	6	1,35	2,34	6	1.32	2.52	?	7,74	1,28	7.7	?
1990/02/07	324	19,05	0,26	19	?	50	27,97	1,04	50	28.08	6	1,48	0,82	6	1.56	1.32	?	7,74	1,22	8.1	?
1990/02/12	734	4,83	0,24	04	?	50	28,02	1,32	50	28.08	6	1,36	0,76	6	1.44	1.52	?	7,35	1,04	7.5	?
1990/02/14	1836	43,44	0,32	43	?	50	27,81	0,78	50	27.84	6	1,58	0,6	6	1.5	0.98	?	8,39	1,16	8.3	?
1990/02/14	2118	30,34	0,28	03	?	50	28,21	1,32	50	28.38	6	2,41	1,02	6	2.1	1.67	?	8,46	1,46	9.2	?
1990/02/15	446	22,81	0,26	22	?	50	27,94	0,8	50	28.02	6	1,4	0,68	6	1.44	1.05	?	7,35	1	7.4	?
1990/02/15	613	29,4	0,38	29	?	50	28,03	0,82	50	27.96	6	1,59	0,88	6	1.38	1.20	?	8,14	1,28	8.2	?
1990/02/15	1559	37,94	0,32	38	?	50	27,91	0,64	50	28.08	6	1,43	0,92	6	1.2	1.12	?	7,55	1,9	6.6	?
1990/02/21	1233	35,61	0,38	35	?	50	27,82	0,58	50	27.78	6	1,3	3,14	6	1.26	3.19	?	7,95	1,4	7.9	?

date	hour	sec	2σ	Old sec	Old 2σ	latitude (km)		2σ	Old latitude (km)		longitude (km)		2σ	Old longitude (km)		2σ hor	Old 2σ hor	depth (km)	2σ	Old depth (km)	Old 2σ
1990/02/24	940	43,88	0,36	14	?	50	28,12	0,58	50	28.08	6	1,18	2,26	6	1.02	2.33	?	7,37	1,18	7.5	?
1990/02/24	2116	51,13	0,36	51	?	50	28,02	0,6	50	27.96	6	1,17	0,68	6	1.02	0.91	?	7,33	1,18	7.4	?
1990/02/24	2206	49,61	0,38	49	?	50	28,02	0,68	50	27.96	6	1,25	0,82	6	1.02	1.07	?	7,61	1,28	7.6	?
1990/02/25	1758	23,13	0,36	23	?	50	27,92	0,6	50	27.84	6	1,44	0,66	6	1.26	0.89	?	7,67	1,18	7.8	?
1990/02/26	628	25,41	0,38	25	?	50	28,28	0,6	50	28.2	6	1,98	0,88	6	1.74	1.07	?	8,04	1,3	8.1	?
1990/02/27	113	7,85	0,36	07	?	50	28,13	0,64	50	28.08	6	1,14	2,26	6	0.96	2.35	?	7,28	1,18	7.4	?
1990/03/03	2219	39,49	0,32	39	?	50	28,11	0,58	50	28.08	6	0,8	1,64	6	0.84	1.74	?	7,3	1,08	7.4	?
1990/03/06	1240	22,4	0,26	22	?	50	27,97	1,58	50	28.02	6	0,72	1,78	6	0.84	2.38	?	7,47	1,18	7.6	?
1990/03/18	214	32,51	0,22	32	?	50	28,03	0,96	50	28.08	6	1	3,14	6	1.08	3.28	?	7,79	1,08	8	?
1990/07/11	1202	45,39	0,58	45	?	50	28,93	1,14	50	29.46	5	51,67	0,98	5	51.54	1.50	?	17,55	3,44	18.6	?
1990/11/09	1114	12,23	0,44	12	?	50	37,18	1,44	50	37.56	6	13,27	0,7	6	13.08	1.60	?	15,87	1,66	16	?
1991/05/18	952	3,06	0,6	03	?	50	27,71	0,58	50	27.72	5	56,64	0,62	5	57.00	0.85	?	18,55	1,92	18.6	?
1992/04/13	120	2,47	0,34	02	0.3	51	10,41	0,71	51	9.84	5	55,95	0,55	5	57.00	0.90	2.0	17,5	2,56	17.4	2.0
1992/04/13	131	8,04	0,35	08	?	51	9,65	0,39	51	10.44	5	56,2	0,71	5	56.34	0.81	?	15,68	3	14.5	?
1992/04/13	146	42,52	0,43	03	?	51	10,09	1,58	51	10.08	5	56,05	1,17	5	58.02	1.97	?	19,16	3,33	15	?
1992/04/13	153	30,48	0,37	30	?	51	10,81	0,7	51	10.80	5	53,68	1,15	5	56.22	1.35	?	11,95	3,72	14.6	?
1992/04/13	202	23,98	0,39	24	?	51	9,4	0,67	51	10.02	5	55,39	1,13	5	57.18	1.31	?	13,52	3,68	15	?
1992/04/13	205	7,33	0,36	07	?	51	5,8	0,4	51	6.00	5	57,06	0,34	5	58.98	0.52	?	15,45	2,48	16.2	?
1992/04/13	208	20,94	0,34	20	?	51	9	0,69	51	10.08	5	57,89	0,66	5	57.48	0.95	?	17,56	2,52	14.9	?
1992/04/13	238	56,13	0,67	?	?	50	44,34	1,26	50	?	6	23,07	0,87	6	?	1.53	?	14,85	1,1	?	?
1992/04/13	303	26,35	0,34	26	?	51	10,71	0,94	51	10.56	5	54,37	0,68	5	55.68	1.16	?	12,04	3,28	12.5	?
1992/04/13	349	42,2	0,36	42	?	51	9,16	0,61	51	9.6	5	57,8	0,63	5	58.62	0.88	?	13,01	3,4	11.8	?
1992/04/13	432	47,75	0,39	47	?	50	51,19	0,35	50	51.3	6	15,33	0,21	6	15.66	0.41	?	15,35	2,27	14	?
1992/04/13	437	45,92	0,37	46	?	51	3,67	0,44	51	3.72	6	2,23	0,39	6	4.08	0.59	?	15,43	2,59	15.3	?
1992/04/13	520	45,5	0,34	45	?	51	5,68	0,72	51	6.00	5	58,86	0,87	5	59.46	1.13	?	12,78	3	12.0	?
1992/04/13	525	30,04	0,39	30	?	51	8,54	1,35	51	9.48	5	55,44	0,85	5	56.88	1.60	?	20,05	3,47	20.1	?
1992/04/13	601	28,61	0,34	28	?	51	9,11	0,71	51	9.72	5	54,64	1,14	5	56.34	1.34	?	14,73	3,51	14.8	?
1992/04/13	616	35,25	0,34	35	?	51	8,82	0,69	51	9.48	5	58,71	2,72	5	59.7	2.81	?	16,13	2,82	14.4	?
1992/04/13	633	40,13	0,34	40	?	51	8,41	0,56	51	9.12	5	58,59	0,5	6	0.000	0.75	?	16,74	2,86	15.8	?
1992/04/13	832	60,02	30,36	?	?	51	10,16	0,92	51	?	5	55,02	0,93	5	?	1.31	?	8,46	3,51	?	?
1992/04/13	1801	27,21	0,32	26	?	51	9,43	0,66	51	11.34	5	58,38	0,69	5	58.5	0.95	?	20,08	1,52	16.8	?
1992/04/13	1834	39,82	0,28	?	?	50	49,93	1,13	50	?	6	13,72	0,45	6	?	1.22	?	15,28	1,66	?	?
1992/04/13	1946	6,73	0,37	?	?	51	4,9	0,68	51	?	5	58,68	0	5	?	0.68	?	12,8	2,94	?	?
1992/04/13	2259	21,92	0,4	21	?	51	7,96	0,68	51	9.3	6	0,38	3,18	6	0.12	3.25	?	17,15	2,24	13.4	?

date	hour	sec	2σ	Old sec	Old 2σ	latitude (km)		2σ	Old latitude (km)		longitude (km)		2σ	Old longitude (km)		2σ hor	Old 2σ hor	depth (km)	2σ	Old depth (km)	Old 2σ
1992/04/14	136	23,4	0,38	23	?	50	49,7	0,35	50	49.74	6	14,31	0,2	6	14.10	0.40	?	16,06	2,29	15.1	?
1992/04/14	1241	39,6	0,37	39	?	51	9,33	0,35	51	10.5	5	54,93	0,4	5	55.38	0.53	?	18,86	1,73	16.7	?
1992/04/14	1256	32,19	0,4	32	?	51	9,16	0,23	51	10.08	5	59,12	0,32	5	59.34	0.39	?	17,67	1,84	14.6	?
1992/04/14	1733	40,82	0,37	40	?	51	9,4	0,96	51	9.54	6	-0,55	3,24	6	59.88	3.38	?	16,87	2,04	11.8	?
1992/04/15	1534	9,51	0,29	?	?	51	9,63	0,76	51	?	5	56	1,06	5	?	1.30	?	20,31	1,69	?	?
1992/04/16	1407	16,3	0,33	16	?	51	9,52	0,54	51	9.78	5	56,05	0,66	5	54.96	0.85	?	20,42	1,51	16.0	?
1992/04/16	2329	47,98	0,36	47	?	51	12,37	1,4	51	11.46	6	1,53	0,21	6	0.54	1.42	?	21,9	2,26	20.4	?
1992/04/17	527	42,74	0,2	42	?	51	10,37	0,99	51	11.46	5	57,36	1,06	5	56.4	1.45	?	21,09	0,77	16.2	?
1992/04/17	1557	3,76	0,36	03	?	51	10,92	0,68	51	12.0	5	56,02	0,48	5	57.3	0.83	?	16,1	1,99	11.7	?
1992/04/20	111	8,21	0,34	?	?	51	10,37	0,7	51	?	5	55,66	0,72	5	?	1.00	?	17,73	1,87	?	?
1992/04/20	428	28,33	0,35	28	?	51	9,43	0,4	51	10.44	5	58,06	0,35	5	58.2	0.53	?	20,86	1,3	16.6	?
1992/04/20	441	3,21	0,37	03	?	51	9,83	0,56	51	10.44	5	58,03	0,33	5	58.32	0.65	?	21,14	1,4	16.5	?
1992/04/20	1650	8,78	0,37	08	?	50	48,5	0,34	50	48.6	6	13,99	0,32	6	14.28	0.47	?	17,52	1,92	14.8	?
1992/04/20	1952	4,41	0,42	?	?	50	48,57	0,91	50	?	7	3,09	0,66	7	?	1.12	?	13,14	3,75	?	?
1992/04/21	752	20,25	0,36	20	?	51	9,72	0,09	51	10.56	5	56,06	0,4	5	56.88	0.41	?	17,94	1,94	15.0	?
1992/04/23	1619	39,92	0,31	?	?	51	11,45	0,38	51	?	5	56,58	0,66	5	?	0.76	?	21,99	1,65	?	?
1992/04/27	1920	47,36	0,26	?	?	50	50,33	0,97	50	?	6	13,64	0,48	6	?	1.08	?	15,64	1,02	?	?
1992/05/04	38	2,02	0,52	?	?	51	9,15	1,58	51	?	5	58,51	1,2	5	?	1.98	?	18,72	2,9	?	?
1992/05/17	925	57,16	0,72	57	?	50	52,98	0,6	50	52.68	6	13,73	0,74	6	13.68	0.95	?	16,99	3,72	15.0	?
1992/10/22	808	2,24	0,42	02	?	50	23,85	0,82	50	24	5	50,35	1,18	5	50.04	1.44	?	13,93	1,44	14.2	?
1992/10/29	525	27,39	0,24	27	?	50	34,44	0,58	50	34.44	6	5,41	0,86	6	5.46	1.04	?	7,65	1,9	7.8	?
1992/10/30	433	52,83	0,4	52	?	50	34,36	0,74	50	34.44	6	5,54	0,64	6	5.58	0.98	?	6,67	2,44	6.6	?
1994/07/20	2120	38,32	0,38	38	?	50	28,73	2,02	50	28.32	4	2,17	1,3	4	2.64	2.40	?	8,58	2,56	7.9	?
1994/07/21	611	2,68	0,48	02	?	50	27,51	0,76	50	27.42	4	4,04	0,64	4	3.9	0.99	?	6,82	3,32	7.0	?
1995/02/23	1104	19,32	0,3	19	?	50	53,58	1,8	50	53.82	6	5,1	1,26	6	6.72	2.20	?	16,31	2,24	13.1	?
1995/03/10	2258	60,05	56,9	60	?	50	54,84	1,92	50	53.76	6	5,86	1,2	6	6.36	2.26	?	12,37	3,1	11.8	?
1995/03/30	2029	8,18	0,22	08	?	50	50,3	1,58	50	50.58	5	51,33	1,14	5	51.48	1.95	?	20,04	1,78	19.2	?
1995/04/17	1944	24,86	0,4	24	?	50	29,85	0,9	50	29.46	6	9,64	1,56	6	9.00	1.80	?	11,01	1,4	11.1	?
1995/04/23	29	37,25	0,24	37	?	50	54,03	1,2	50	53.64	6	4,93	1,34	6	4.38	1.80	?	16,72	1,02	16.2	?
1995/04/23	445	54,05	0,26	54	?	50	53,86	1,32	50	53.46	6	6,65	1,64	6	6.12	2.11	?	15,99	1,66	15.7	?
1995/04/23	446	19,44	0,26	19	?	50	53,65	1,42	50	53.28	6	6,21	1,86	6	5.64	2.34	?	16,51	1,78	16.1	?
1995/10/30	2316	47,41	0,46	47	?	50	32,21	0,6	50	32.24	5	53,6	0,44	5	53.82	0.74	?	21,48	2,44	21.6	?
1996/07/23	2230	21,79	0,72	21	?	50	28,58	0,4	50	28.56	5	53,23	0,44	5	53.22	0.59	?	16,28	2,86	15.7	?
1997/11/29	1854	50,06	0,58	50	0.82	50	18,69	0,78	50	18.66	7	23,62	1,02	7	23.62	1.28	1.78	12,67	3,2	13.1	2.2

date	hour	sec	2σ	Old sec	Old 2σ	latitude (km)		2σ	Old latitude (km)		longitude (km)		2σ	Old longitude (km)		2σ hor	Old 2σ hor	depth (km)	2σ	Old depth (km)	Old 2σ
1998/02/08	537	57,89	0,6	57	0.42	50	38,84	1,28	50	39.63	6	10,53	0,5	6	9.99	1.37	1.50	0,15	2,04	9.9	2.8
1998/03/09	2346	15,99	0,68	15	0.96	50	24,93	0,58	50	24.90	6	22,36	0,42	6	22.64	0.72	1.02	14,95	2,62	15.5	2.0
1998/03/10	2235	11,65	0,72	11	0.94	50	24,91	0,56	50	25.06	6	22,43	0,3	6	22.55	0.64	1.00	15,4	2,92	15.3	1.6
1998/03/28	650	49,01	0,36	48	0.4	50	39,28	1,26	50	39.22	6	9,64	1,22	6	9.69	1.75	1.62	8,47	2,46	9.00	2.2
1998/04/11	339	1,53	0,46	01	0.32	50	39,4	0,82	50	39.35	6	9,74	0,38	6	9.6	0.90	1.22	9,16	2,08	9.5	2.0
1998/04/21	1454	49,4	0,5	49	0.32	50	39,48	1,04	50	39.40	6	10,06	0,52	6	9.95	1.16	1.48	8,3	2,86	8.6	3.6
1998/06/07	1357	36,73	0,6	36	0.98	50	22,17	1,58	50	22.32	4	20,19	1,14	4	20.23	1.95	6.00	15,49	1,98	15.6	4.5
1998/06/29	1506	31,97	0,48	32	0.44	50	32,71	1	50	32.45	5	51,2	1,02	5	50.97	1.43	2.4	17,63	2,12	16.2	4.7
1998/10/30	1022	34,4	0,5	34	0.38	50	19,39	0,4	50	19.31	5	48,5	0,48	5	48.19	0.62	1.04	20,32	2,14	21.3	3.3
1999/02/01	311	6,44	0,42	05	1.2	50	23,41	0,78	50	22.16	4	25,21	1,14	4	20.67	1.38	6.18	11,62	1,62	16.3	5.2
2001/01/09	1050	59,84	57,92	59	0.42	50	21,77	0,8	50	21.86	5	57,94	0,78	5	57.97	1.12	1.20	16,16	2,52	16.5	2.9
2001/10/03	1100	13,21	0,74	13	?	50	57,46	0,64	50	57.78	6	16,97	0,32	6	17.22	0.72	?	15,33	3,74	14	?
2001/11/12	13	10,83	0,38	11	0.38	50	32,67	1,64	50	33.29	6	6,65	1,76	6	5.47	2.41	2.04	17,15	1,64	17.2	2.4
2001/12/20	830	54,03	0,68	54	0.56	50	31,83	0,6	50	31.75	5	27,08	0,5	5	27.40	0.58	0.96	19,67	2,8	20.2	1.3
2002/04/11	515	56,07	0,5	56	0.32	50	30,37	0,76	50	30.28	5	57,36	1,02	5	57.52	1.27	1.56	13,57	2,36	13.6	3.0
2003/03/23	2220	16,16	0,74	16	0.52	50	28,61	0,44	50	28.45	5	40,33	0,78	5	40.48	0.90	1.50	21,49	2,56	21.1	2.2
2003/03/23	2222	59,27	0,78	59	0.42	50	28,8	0,48	50	28.60	5	40,06	0,44	5	40.32	0.65	1.28	21,95	2,82	21.3	2.0
2003/06/17	2209	46,7	0,48	46	0.52	50	30,09	1,22	50	28.82	5	35,58	1,04	5	36.86	1.60	3.62	21,97	2,3	20.2	4.1
2003/06/29	2126	57,98	0,42	58	0.48	50	32,39	1,96	50	32.08	5	29,59	1,14	5	30.07	2.27	3.30	23,79	2,1	22.4	4.7
2004/02/09	1738	55,21	0,42	55	0.52	50	33,65	1,32	50	33.83	6	4,39	1,5	6	4.40	2.00	3.28	16,12	1,48	16.8	3.7
2004/07/19	140	39,84	0,74	39	1.54	50	26,36	0,7	50	27.26	5	1,86	1,02	5	2.59	1.27	3.50	1,35	1,38	1.4	10.3
2005/05/01	1504	56,37	0,62	56	?	50	53,67	0,66	50	53.64	6	6,51	0,94	6	7.26	1.15	2.20	16,41	3,06	16.1	2.0
2005/09/14	349	16,3	0,38	16	?	50	22,12	1,36	50	22.20	6	17,37	2,92	6	17.76	3.22	2.80	23,03	1,98	23.1	2.2
2005/09/25	1617	50,75	0,5	50	?	50	22,14	0,82	50	22.02	6	15,08	2,46	6	15.06	2.59	2.00	21,84	3	22.2	1.6
2006/06/06	2131	26,08	0,64	26	?	49	57,73	2,6	49	58.44	4	41,21	1,14	4	40.86	2.84	7.40	2,31	2,74	1.1	12
2006/10/15	1	54,91	0,66	54	?	50	53,29	0,78	50	53.28	6	32,98	0,66	6	33.00	1.02	1.20	12,61	2,92	13.1	1.6
2007/02/26	200	32,73	0,7	32	?	50	51,46	0,44	50	51.42	6	11,91	0,4	6	11.70	0.59	1.0	16,03	3,68	15.8	2.4
2007/03/31	646	8,56	0,7	46	?	50	28,45	0,6	50	28.20	5	44,34	0,54	5	44.64	0.81	1.4	19,95	3,02	20.0	2.0

Table 3-3: List of all the well-located earthquakes registered by the Belgian network between 1985 and 2007.
Cells with a ? are not provided in the current data base of the Royal observatory of Belgium.

date	hour	sec	2σ	latitude (km)		2σ	longitude (km)		2σ	depth (km)	2σ
2006/02/17	1751	13,6	0,7	49	23,09	0,7	6	51,582	1,2	1	-
2006/02/07	2222	9,08	0,7	49	21,79	0,62	6	52,08	0,9	1	-
2005/11/26	1447	0,17	0,7	49	21,65	1,3	6	54,27	0,76	1	-
2005/11/15	158	32,5	0,8	49	22,18	0,92	6	52,01	1,45	1	-
2005/09/22	1943	58,6	0,8	49	21,133	0,7	6	52,57	0,95	1	-
2005/08/03	644	40,3	0,9	49	21,51	0,83	6	53,59	1,42	1	-
2006/03/07	2256	55,7	0,8	49	22,16	0,75	6	51,28	0,98	1	-
2005/07/20	127	46,2	0,8	49	21,73	1,08	6	51,23	1,68	1	-
2006/03/29	348	3,25	0,8	49	23,44	2,1	6	53,18	1,5	1	-
2006/03/22	1403	16	0,6	49	22,01	0,62	6	52,33	0,94	1	-
2006/03/16	520	49,8	0,7	49	22,83	0,73	6	52,95	1,2	1	-
2005/06/23	2233	8,36	0,6	49	22,392	0,8	6	54,38	1,25	1	-
2005/11/03	18	7,59	0,4	48	16,45	1,5	7	25,83	1,8	1	-

Table 3-4: List of all the German induced earthquakes used in this study

date	hour	sec	2σ	latitude (km)		2σ	longitude (km)		2σ	depth (km)	2σ
2004/10/07	1950	31,7	0,36	51	29,44	-	2	50,36	-	0,1	-
2005/04/05	1854	8,82	0,48	51	35	-	2	53	-	0,1	-
2005/04/13	1840	37,7	0,67	51	29,2	-	2	50	-	0,1	-
2005/04/25	1727	58,1	0,75	51	9,98	-	2	36,18	-	0,1	-
2005/05/18	1455	2,52	0,79	51	31,74	-	2	58	-	0,1	-
2005/05/25	1420	1,75	0,57	51	38,6	-	2	52,62	-	0,1	-
2005/05/30	910	32,5	0,67	51	32,5	-	2	49,3	-	0,1	-
2005/07/11	1422	17,7	0,67	51	29,3	-	2	55,7	-	0,1	-
2005/07/13	1000	3,47	0,91	51	50,9	-	3	30,8	-	0,1	-
2005/07/14	2047	49,3	0,84	51	32,3	-	3	6,9	-	0,1	-
2005/07/15	124	17,9	0,83	51	50,5	-	3	22,7	-	0,1	-
2005/08/31	2025	2,8	0,91	51	45,13	-	3	34	-	0,1	-
2005/09/06	1932	6,77	0,93	51	52,06	-	3	22,8	-	0,1	-
2005/09/22	1517	2,65	0,62	51	47,2	-	3	19,11	-	0,1	-
2005/10/04	1830	3,36	0,81	51	53	-	3	3	-	0,1	-
2005/10/05	1055	3,15	1,13	51	54	-	3	29	-	0,1	-
2005/11/22	2128	46,4	0,66	52	10,4	-	2	57,29	-	0,1	-
2005/11/30	1126	10,3	1,15	51	27	-	3	25	-	0,1	-
2006/01/18	1450	6,44	0,78	52	3	-	2	59	-	0,1	-
2006/03/03	1610	6,4	0,63	51	49,85	-	3	0,02	-	0,1	-
2006/03/07	1956	37	0,91	52	13,33	-	2	52,83	-	0,1	-
2006/03/08	1319	59,2	0,68	52	2,3	-	2	47,16	-	0,1	-
2006/03/08	1516	2,02	0,59	51	57,75	-	2	51,46	-	0,1	-
2006/03/08	1724	1,88	0,85	51	53,77	-	2	51,07	-	0,1	-

2006/04/12	1909	7,71	0,74	51	55,85	-	2	57,7	-	0,1	-
2006/04/20	1350	56,5	0,87	51	40	-	3	7	-	0,1	-
2006/04/26	1232	0,57	0,59	51	37,54	-	2	54,76	-	0,1	-
2006/04/26	1500	7,59	0,85	51	40,22	-	2	58,6	-	0,1	-
2006/05/04	1705	2,52	0,78	51	49,09	-	3	6,37	-	0,1	-
2006/05/17	1656	58,3	0,76	52	9,5	-	3	7,3	-	0,1	-

Table 3-5:List of all the North Sea Explosions used in this study.

3.4 Relocation evaluation

Looking at the constructed profile for the earthquake of 1992/04/14 at 1h06, the mine-induced earthquake 2006/02/07 22h22 and the North Sea explosion 2006/05/04 17h04 (Figure 3.6), the fit between the recorded arrival time of direct P- and S-waves with the theoretical hodochrone supports the fact that the existing 1D models of the crustal structure in the studied area represents relatively well the average model and also that the locations are reliable. Let us note that Pn- and Sn-phases are also well fitted for larger distance (the Moho depth in the model is 32.5 km). It is of course more delicate to identify later arrivals, like the Moho reflected phases, because they arrive during the arrival of the wave trains of previous arrivals and they are not always the most energetic arrivals, even if on some seismograms a close correlation is also well-established. Even though there is a close correlation, for some seismograms there seems to be a greater difference. This indicates local velocity variations in the earth's crust. A better correlation will be achieved with 3D velocity models deduced from a local seismic tomography.

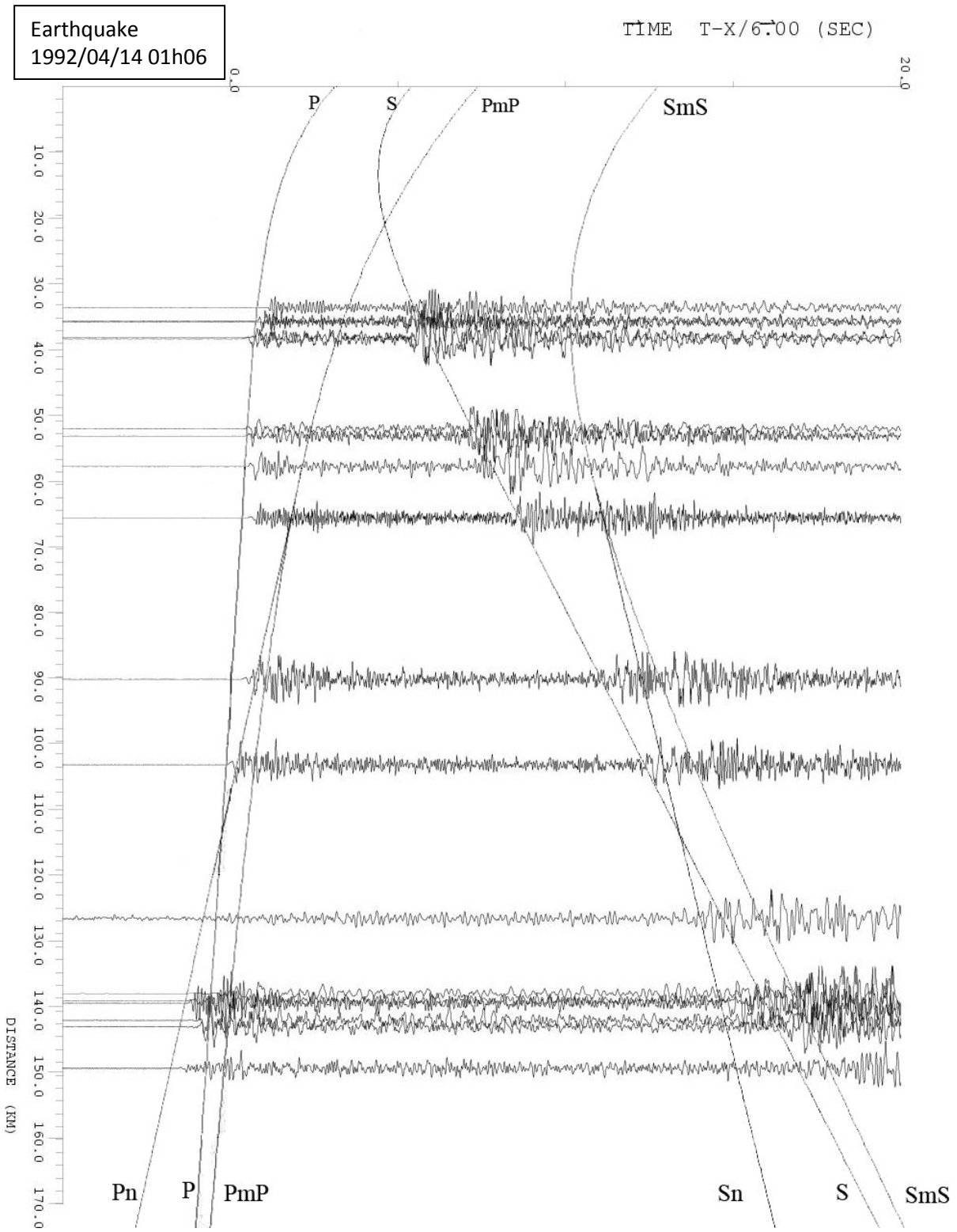
Earthquake
1992/04/14 01h06
TIME T-X/6.00 (SEC)
0.0
20.0
P
S
PmP
SmS
10.0
20.0
30.0
40.0
50.0
60.0
70.0
80.0
90.0
100.0
110.0
120.0
130.0
140.0
150.0
160.0
170.0
DISTANCE (KM)
Pn
P
PmP
Sn
S
SmS

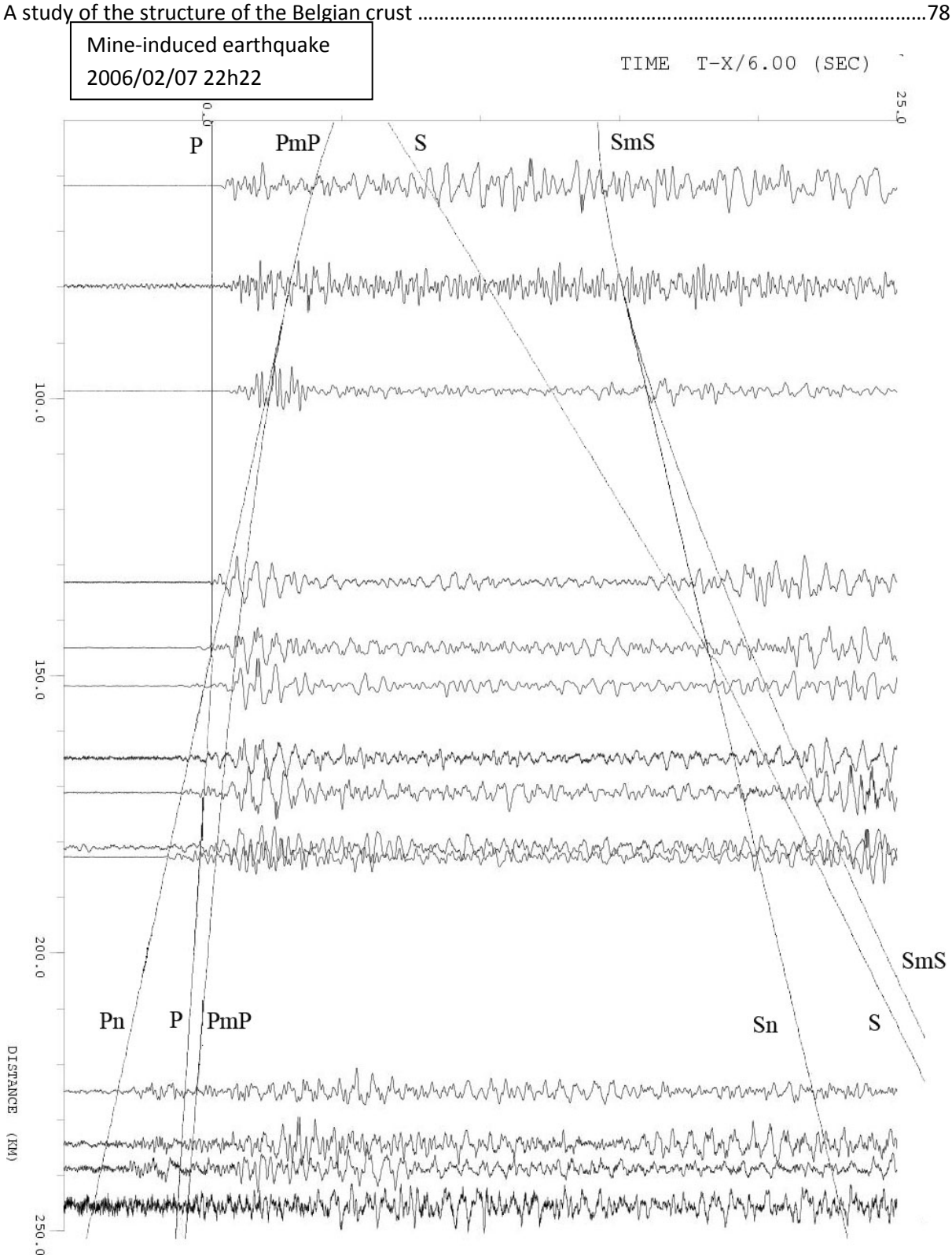
Mine-induced earthquake
2006/02/07 22h22
TIME T-X/6.00 (SEC)
0.0
25.0
P
PmP
S
SmS
100.0
150.0
200.0
250.0
DISTANCE (KM)
Pn
P
PmP
Sn
S
SmS

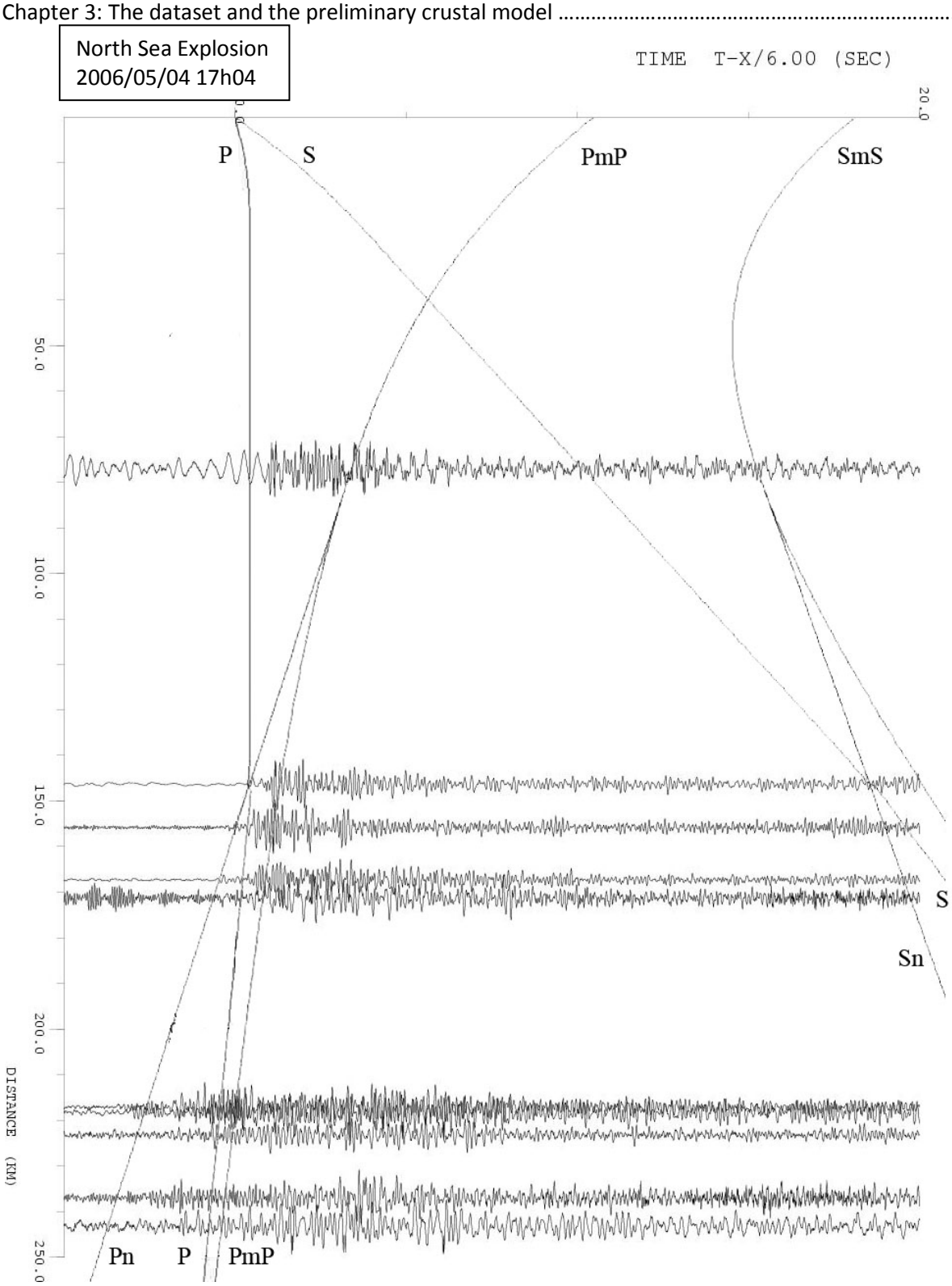

Figure 3.6: Seismograms for different seismic stations.
A. The earthquake 1992/04/14 at 01h06, B. The induced earthquake 2005/08/03 at 06h44 and C. The North Sea explosion 2006/05/04 at 17h04. The Pn, P, PmP, S, Sn and SmS theoretical hodochrones calculated in the CAL model are also represented.

Chapter 4 Moho depth evaluation

4.1 Introduction

The first studies to evaluate the depth of the Moho in Belgium and surrounding regions were the BELCORP (Bouckaert *et al*., 1988), ECORS (Matte and Hirn, 1988) and DEKORP (DEKORP Research group, 1991) seismic reflection profiles (see chapter 1 for more information). As written in chapter 2, on these profiles, the Moho was not visible below the Brabant Massif which constitutes a large part of the Belgian territory. This massif appeared as unreflective for the wavelengths (12-48 Hz) used in these seismic reflection profiles. Profiles in the surrounding areas, however, mostly show a clear Moho-discontinuity. This can be explained if the Moho boundary underneath the Brabant Massif is a gradient zone with anisotropic layers, in which the horizontal velocity is higher than the vertical velocity (Pavlenkova, 2009) and thus impossible to determine on seismic reflection profiles in the considered wavelength range.

This is why the distribution in Moho depth beneath Belgium is estimated, using energetic seismic phases in a different larger frequency band (0.1 - 60 Hz), that corresponds to wide-angle Moho reflected waves (PmP- or SmS-waves) on seismograms from both natural and artificial seismic events recorded by the Belgian seismic network.

In this chapter, the method to determine the Moho depth is explained first, followed by a discussion of the results of the picking of the PmP- and SmS-waves needed. In the following paragraphs, the results of this study will be presented and discussed. Finally, some conclusions will be drawn and some perspectives discussed.

4.2 Moho depth determination method

The crustal thickness in Belgium was evaluated using travel time data of wide-angle PmP- and SmS-waves, taking into account a stratified horizontal velocity model. Based upon the epicentre and station locations, as well as the ray path calculated in the velocity model, the map position of the reflection points of the reflected waves was calculated (points where the PmP-waves reflect on the Moho). The study area was divided into a 20 x 20 km² grid and the reflection points within each of these cells were grouped. For each grid cell, using all the source-station couples from which the reflection point has been located in the cell, the Moho depth for the PmP- and SmS-data was determined separately, by using the procedure described below. The Moho depth that fits the measured arrival times for the PmP- or SmS-waves for each source-station couple was determined by varying the Moho depth in the CAL model between 20 and 41 km in steps of 0.01 km. The Moho depth for a cell is defined as the mean of all these Moho depths.

To determine the reliability of the obtained Moho depth the following procedure was used. The 95% confidence intervals were determined as for a *t*-distribution:

$$\overline{\mathrm{X}}_{\mathrm{n}} - \mathrm{t}_{\mathrm{n}-1}^{-1}(0.975)\sqrt{\frac{\mathrm{S}_{\mathrm{n}}^2}{\mathrm{n}}}, \overline{\mathrm{X}}_{\mathrm{n}} + \mathrm{t}_{\mathrm{n}-1}^{-1}(0.975)\sqrt{\frac{\mathrm{S}_{\mathrm{n}}^2}{\mathrm{n}}}, \tag{4.1}$$

where n is the number of observations (sample size), $\bar{X}_n$ is the sample mean, $t_{n-1}^{-1}(0.975)$ is the inverse at 0.975 of a *t*-distribution with n-1 degrees of freedom and S_n^2 is the sample variance (Student, 1908).

When the length of the 95% confidence interval is greater than 4 km or when not enough reflection points (less than 5) are located in a grid cell, the result was considered as unreliable.

4.3 Picking PmP-arrivals

Before the Moho depth can be calculated, the PmP-waves have to be picked on the different seismograms. To do this, theoretical arrival times were calculated, by a self-developed programme (Appendix 1-3) based on the theory explained in paragraph 1.3 of chapter 1. Using these arrival times, it was not possible to determine the arrival time of the PmP-waves on the real seismograms, because sometimes two energetic phases arrived close to this theoretical arrival. Therefore, synthetic seismograms were calculated. To do this, the programme Axitra developed by Coutant (1990) was used. Because there was no manual available for this programme, it needed to be tested before any synthetic seismograms could be calculated to compare with the real data (see Appendix 4). After testing, synthetic seismograms were calculated for the stations with digital registrations for the best-located earthquakes. These synthetic seismograms were placed in profiles for each earthquake and together with the theoretical arrival times, they were used to determine the arrival of the PmP-waves on the real seismograms. In this paragraph, the programme Axitra is tested before being used on the actual data.

4.3.1 Theory behind Axitra

In this section, the theory on which the programme Axitra is based, using the Green's function and the discrete wavenumber theory, is briefly explained.

4.3.1.1Green's function

One of the solutions of the displacement equation (4.2) in an isotropic, homogeneous, elastic medium is the green's function (Shearer, 1999).

$$\rho \frac{\partial^2 \vec{u}}{\partial t^2} = (\lambda + \mu)\nabla(\nabla \vec{u}) + \mu \nabla^2 \vec{u} + \vec{f} \tag{4.2}$$

where λ and μ are the Lamé constants, $\vec{f}$ represents the force vector and $\vec{u}$ represents the displacement vector.

When a unit force vector $\vec{f}$ is applied at a point r_0 at a time t_0, the displacement u(r,t) at a receiver position r will be a complicated function of the Earth's seismic velocity and density structure, including multiple seismic phases and reverberations. However for every $f(r_0,t_0)$ and r there is a unique function u(t) that describes the earth's response to this force vector. This displacement function could be calculated if the earth's structure would be known accurately. So it might be helpful to develop a notation where the source term (= force vector) is excluded from all the other details of the wave propagation. This is done with a Green's function:

$$u_i(r,t) = G_{ij}(r,t;r_0,t_0) f_j(r_0,t_0) \tag{4.3}$$

where u is the displacement at a point r and a time t, f is the force vector induced at the point r_0 at a time t_0 and G is the elastodynamic Green's function. A Green's function thus represents the displacement in a medium in direction i submitted to a unitary force vector working in direction j infinitely concentrated in time and space.

In the time domain, the solution of the displacement equation for a given force vector is given by the convolution of the Green's function of the medium for the force vector (or source function).

$$u_i(\vec{r},t) = \int_0^t dt \int_{V_0} G_{ij}(\vec{r},t;\vec{r}_0,t_0) f_j(\vec{r}_0,t_0) dV \tag{4.4}$$

where V_0 is the volume on which the force vector works.

In the frequency domain, the relation is given by a simple multiplication:

$$u_i(\vec{r},\omega) = f_j(\omega) G_{ij}(\omega) \tag{4.5}$$

where ω is the circular frequency.

4.3.1.2Discrete Wavenumber theory

The radiation of waves from a line source in an infinite homogeneous medium can be represented by a cylindrical wave or as a continuous superposition of homogeneous and inhomogeneous plane waves (Bouchon and Aki, 1977). Therefore, the displacement and stress along the horizontal x and vertical z axis normal to the source axis can be written in the form:

$$F(x,z;\omega) = e^{i\omega t} \int_{-\infty}^{\infty} f(k,z) e^{-ikz} dk \tag{4.6}$$

where the integration is with respect to the horizontal wave number and where the $e^{i\omega t}$ time dependence is understood.

In order to transform the integral into a summation, an infinite distribution of sources along the x-axis at equal interval L is considered:

$$G(x,z;\omega) = \int_{-\infty}^{\infty} f(k,z)e^{-ikz}dk \sum_{m=-\infty}^{\infty} e^{-ikmL}dk \tag{4.7}$$

The summation factor can be written as when using the results of the distribution theory (Schwartz, 1966):

$$\sum_{m=-\infty}^{\infty} e^{-ikmL} = \frac{2\pi}{L}(\delta(kL))_{\text{modulo } 2\pi} \tag{4.8}$$

where δ is the Dirac delta function.

Equation (4.7) then becomes:

$$G(x,z;\omega) = \frac{2\pi}{L}\sum_{m=-\infty}^{\infty} f(k_n,z)e^{-ik_n x} \tag{4.9}$$

with $k_n = \frac{2\pi}{L}n$

When the series converges, the equation becomes:

$$G(x,z;\omega) = \frac{2\pi}{L}\sum_{n=-N}^{N} f(k_n,z)e^{-ik_n x} \tag{4.10}$$

The impulse response g(t) is obtained from the complex frequency solution G(ω) through the relation:

$$g(t) = e^{\omega_I t}\int_{-\infty}^{\infty} G(\omega)e^{-i\omega_R t}d\omega_R \tag{4.11}$$

4.3.2 The programme Axitra - Identification and picking of the phases

The picking of the phases was done by comparing the seismograms with the synthetic ones calculated by the programme AXITRA and their calculated arrival times. Only the hodochrones of the direct, Moho-reflected and Moho-refracted waves are represented. But one has to stay attentive for other phases, from phase conversion (P waves that change to S-waves when crossing a boundary, etc.), reflections on a boundary that has not been taken into account in the model, ...

For the earthquakes for which focal mechanisms had been calculated, these focal mechanisms were used in the synthetic calculation. When no focal mechanism could be determined for earthquakes due to the low number or similar position of the recordings, the synthetic seismograms are calculated with a normal focal mechanism of ϕ=90°, δ=45°, λ=-90°. For comparison purposes they are calculated for each station in a 3D-environement. This way the directivity of the source is taken into account. Then the calculated seismograms are placed in time-epicentral distance diagrams. The source period was fixed at 0,3 s (3,33 Hz) for verifying the sample condition (tl = 60 s, nfreq = 512). The synthetic seismograms are thus of lower frequencies than the registered ones.

Let us now look at the comparison of the synthetic data with the real ones. The real data are much more complex than the synthetic seismograms and span a longer time-period of shaking, because the velocity model and the source function are simplifications of reality. The longer duration can be explained by lateral reflections on 3D-structures. The direct, refracted and reflected P- and S-waves are very well individualized in a lot of stations. The refracted P-waves at distant stations have very low amplitude, but because they are first arrivals, they are quite visible. Some phases are distinct, but do not correspond to any of the phases in the synthetic seismogram. They probably correspond to unknown local boundaries. Some signals show one or two packets of energy similar to the ones observed in the synthetic seismograms and they are due to a double reflection wave, namely first on the earth's surface and then on the Moho.

For comparison, synthetic seismograms were also determined with a slightly different model, the CAL model (Figure 4.1) (Calbini, 2003), established using the VELEST software (CAL in Table 3-1). The synthetic seismograms of both models are similar, also to the real seismograms, but the Moho reflection waves are better visible on the results calculated with the standard velocity model, therefore this model was preferred to calculate the synthetic seismograms. Subsequently, time-distance profiles per earthquake were constructed with the synthetic seismograms and the arrival of the PmP- or SmS-waves on the synthetic seismograms was determined. Then the synthetic seismograms were compared to the real seismograms and allowed indentifying the arrival times of the PmP- or SmS-waves that are measured on the latter (Figure 4.2). In this way, more than 750 arrival times of PmP- and SmS-waves have been determined. The accuracy of these travel time pickings aided by the synthetic seismograms is estimated to be 0.1-0.2 s. As can be seen in Figure 4.2, the form of the synthetic seismograms often corresponds to the real seismograms, although they have a lower

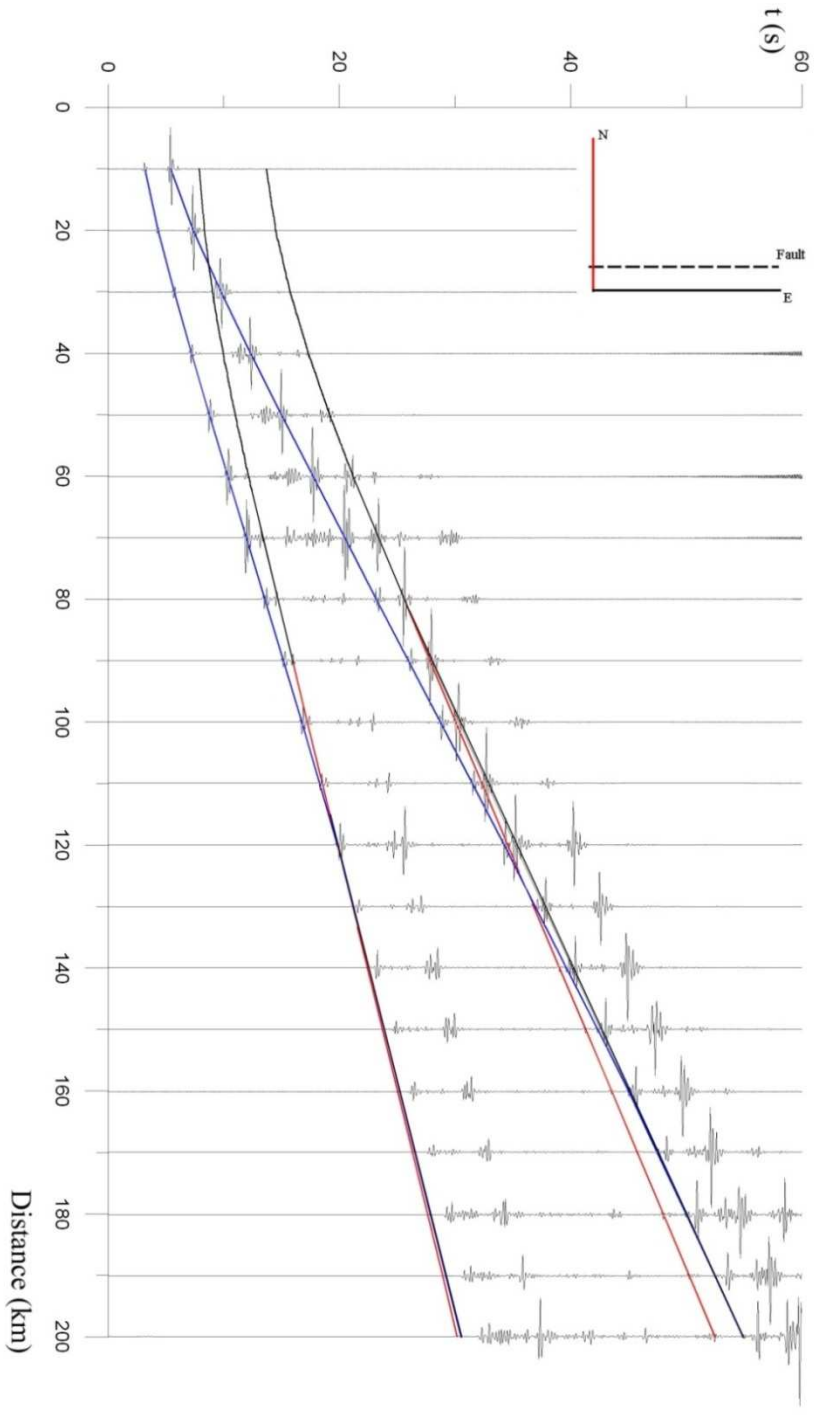

Figure 4.1: Profile 1 Perpendicular to the fault plane: comparison between the arrival times and the synthetic seismograms for the vertical component calculated with the CAL model.
The blue lines represent the arrival of the direct Pg- and Sg-waves, the red line represents the arrivals of the Pn- and Sn-waves refracted on the mantle and the black line represents the arrival of the PmP- and SmS-waves reflected on the Moho

frequency content. In some cases, like seismogram G on Figure 4.2 , the PmP-waves arrive earlier on the synthetic seismograms than on the real seismograms. This is due to differences between the velocity model used to calculate the seismograms and the real 3-D velocity structure of the earth's crust. In these cases the real Moho is probably deeper than the one used in the velocity model for the calculation of the synthetic seismograms. On the seismograms D and E of Figure 4.2, the PmP-wave of the real seismograms arrives before the one in the synthetic seismograms, indicating that the Moho is probably less deep than the one used in the velocity model used to calculate the synthetic one. Only the seismic phase arrival times were modelled and not the waveform. Therefore, the comparison

between the observed and synthetic seismograms is not necessarily valid for the amplitude and sense of motion as can be seen on the seismograms C and D.

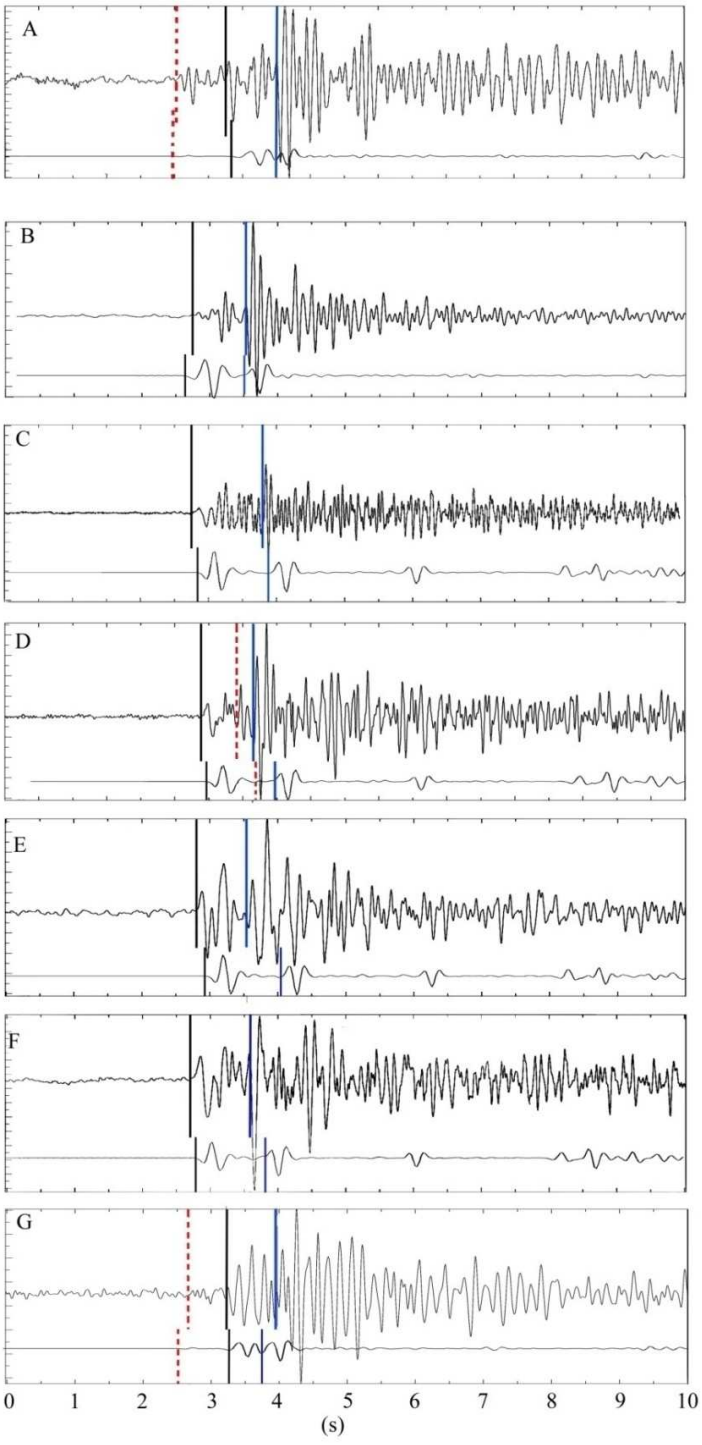

Figure 4.2: Several seismograms (upper trace) compared to their synthetic seismogram (lower trace) in a 10 s time window.
The black line indicates the arrival of the P-wave. the dotted red line the arrival of the Pn-wave and the full blue line. the arrival of the PmP-wave. A. Explosion 2006/01/18 14h50 recorded at Steenkerque (SKQ, Δ=173 km). B. Explosion 2005/08/31 20h24 recorded at SKQ (Δ=147 km). C. Earthquake 1992/04/20 04h28 recorded at Robertville (Rob, Δ=79 km). D. Same earthquake as in C recorded at Meuville (MEU, Δ=86 km). E. Earthquake 1992/04/16 14h07 recorded at Robertville (Rob, Δ=79 km). F. Same earthquake as in E recorded at MEU (Δ=85 km) and G. Explosion 2006/03/08 15h16 recorded at Uccle (UCC , Δ=166 km).

4.4 Results

4.4.1 Influence of the crustal model on the Moho depth evaluation

Before the interpretation of the results, the influence of the used velocity model on the result was evaluated. Therefore, the Moho depth was calculated for 1000 different velocity models, generated by adding a noise with a normal distribution to the original 1-D velocity model in each layer. This distribution corresponds to the one obtained by the inversion of the crustal model in Table 3-1 (Calbini, 2003). The average Moho depth over all the 1000 models differs of some 0.04 km from the one calculated for the original model, whereas the standard deviation of these 1000 Moho depths is 1.06 km.

By analyzing the recordings of quarry blasts, Volon (1989) discovered that the velocity structure of the upper crust under the Brabant Massif and under the Stavelot Inlier is different (Figure 4.3). For the first 4.5 km of depth, the velocity structure of the Brabant Massif is close to the velocity structure modelled by the CAL-model, so the depths calculated underneath the Brabant Massif are most certainly very weakly affected. The velocity structure in the Stavelot Inlier, however, is somewhat different in the first 6 km of depth. Here, the observed velocity is lower than the velocities modelled in the CAL-model. This implies that for grid cells near the Stavelot Inlier, the calculated Moho depths could be overestimations of the real Moho depths. After calculating the Moho depth for several grid cells near the Stavelot Inlier for both the CAL-model and the lower average velocity determined by Volon (1989), the Moho depth varies on average of some 0.3 km between both models, which is lower than the standard deviation of 1.06 km determined in the previous test.

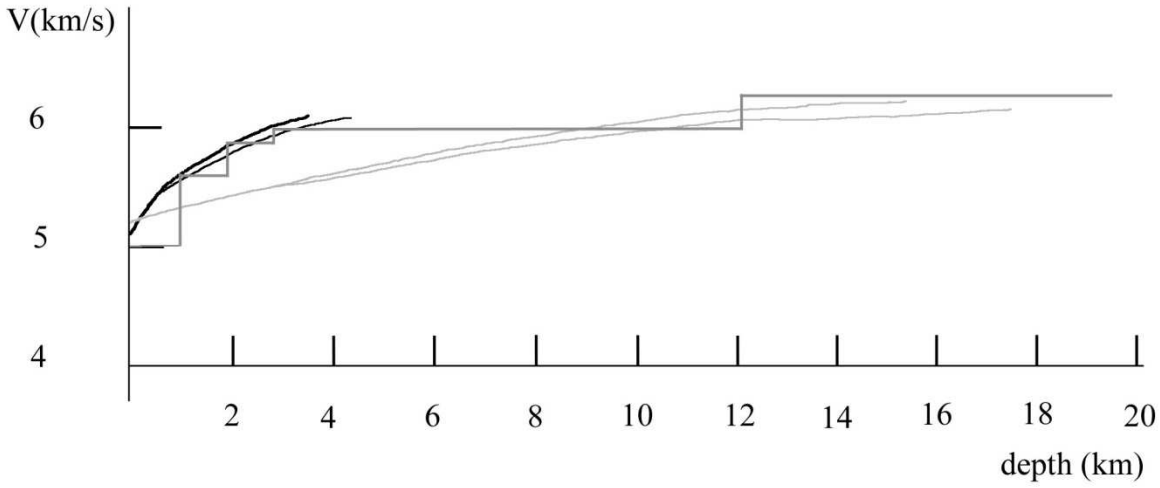

Figure 4.3: Vp-Velocity profiles determined by Volon (1989).
In black, the velocity structure in the Brabant Massif (the two lines represent the lower and upper limit of the model), in light grey, the velocity structure in the Stavelot Inlier (the two lines represent the lower and upper limit of the model) and the step diagram represents the Standard velocity model (Ahorner & Pelzing, 1984).

4.4.2 Stacking of the traces for the German mining-induced earthquakes

To control the determined Moho depth, different seismograms for one grid cell were stacked using Seismic Unix (Stockwell. 1999), an open-source software package for seismic research and seismic processing. A separate module was written (appendix 5) to calculate the normal-move out (this is the correction to the travel times, which are due to their different offset distances) taking into account the depths of the real earthquakes (whereas in reflection seismic studies the source is always at the surface). Unfortunately, the uncertainty on the location of the earthquakes are larger (uncertainty: km-scale) than the uncertainty on the locations of the source and receivers in a seismic reflection study (uncertainty: m-scale). Therefore it was not possible to align the PmP-arrivals for most grid cells to the degree required to enhance them by stacking. For the German induced earthquakes and the North Sea explosions, however, the PmP-arrivals did align to a degree that a zone in which the PmP-wave were expected could be determined (Figure 4.4).

Different band-pass filters on the stacked profile were tried and the PmP-wave is best visible in the low-frequency domain [< 8 Hz]. Hirn *et al.* (1987) found that along the ECORS refraction profile, the Moho depth was best visible in the frequency domain [4-12 Hz], when the data is filtered for this frequency domain, the arrival of the Pn- and PmP-waves is less well visualised. Indicating that very low frequencies are needed to visualise the arrival of Pn- and PmP-waves in the region. The frequency bands in which the Moho depth has been determined, also could explain why on the reflection profiles shot in the region, no Moho depth could be determined. The BELCORP and DEKORP profiles used a vibroseis with a frequency range from 12 to 48 Hz (Bouckaert *et al.*, 1986; DEKORP Research Group, 1991). For the ECORS seismic reflection profile, geophones that could only register frequencies over 10 Hz were used Hirn *et al.* (1987). So all the profiles were shot in frequency bandwidths higher than the frequencies needed to visualise the arrival of the Pn- and PmP-waves. It is only on the wide-angle profiles, where geophones were used that could register waves with frequencies as low as 4Hz, that a Moho was visible Hirn *et al.* (1987). The fact that the Moho is not visible on the MOBIL profiles but can be determined on the MNPI-1901 profile can also be explained by a difference in frequency bandwidth.

Of course, it is not certain that redoing the profiles would give information as it is possible that the Moho depth underneath the Brabant Massif is in fact a zone with anisotropic layers in which the velocity is higher in the horizontal direction than in the vertical direction, as Pavlenkova (2009) has demonstrated underneath the Dnieper Donets Paleorift. In this case, the Moho will only be visible with wide-angle reflection/refraction studies, as is the case for the ECORS reflection profile and the wide-angle PmP and SmS study presented here. It must also be stated that the only two studies that have determined the frequency bandwidths are both studies using wide angle reflections. Whether reflection studies would be able to determine the Moho depth when it is an anisotropic gradient zone, depends on the frequencies used in the study and the thickness of the gradient zone, because seismic waves can only detect structures that are as large or larger than their wavelength. If seismic waves with wavelengths larger than the thickness of the gradient zone can be emitted, a reflection will occur as the seismic wave will see the zone as a simple reflector.

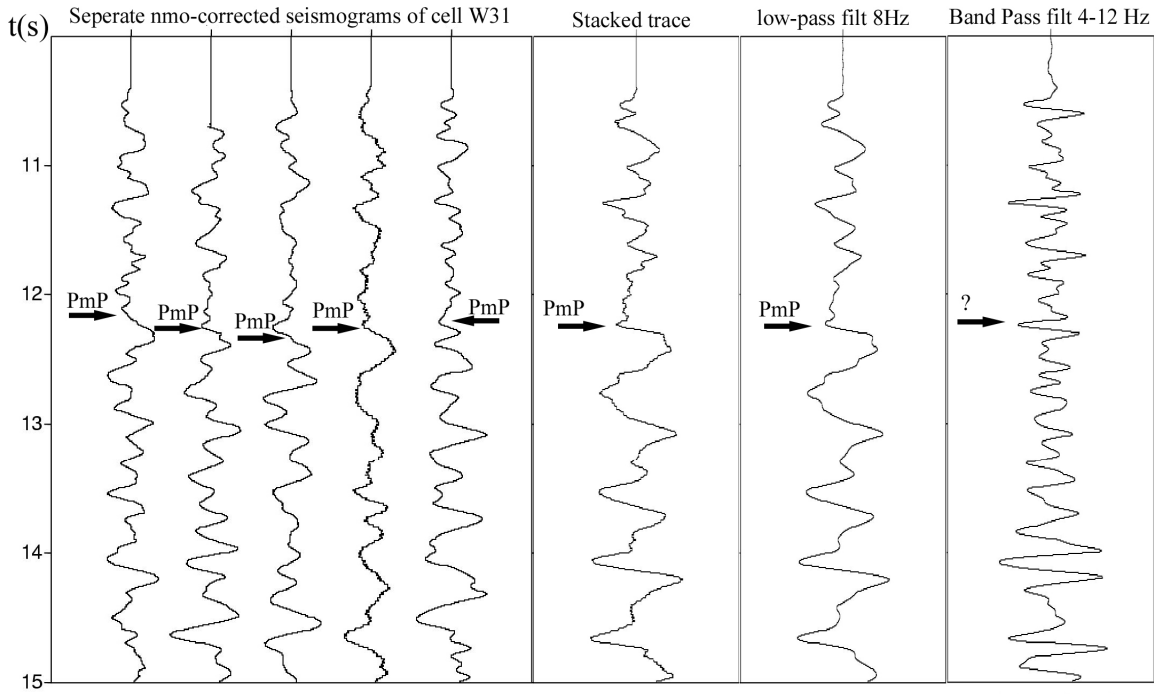

Figure 4.4: Example of stacked seismograms for cell W31.

4.4.3 Trends per grid cell

Some profiles for all the reflection points within the same grid cell (like a common midpoint gather in seismic reflection) were also plotted (Figure 4.5). This step was necessary to verify whether the measured PmP-waves are correct or whether certain earthquake–station couples have anomalous measurements.

The profiles indicate that the cells that do not have very well-constrained Moho depths (standard deviation larger than 2 km) were covered by only a few seismograms (<7), or had PmP-measurements measured at the upper distance limit for easy determination of the PmP-wave (when the arrival of the PmP-wave comes too close to the arrival of the P-wave). The selected cells have a lot of PmP-measurements in the good distance range (50-140 km), and there the Moho depth is very well determined (error below 2 km). The profile of seismograms plotted as a function of increasing distance for the seismograms used in cell M23 (Figure 4.5) shows that the measured arrivals of the PmP-waves stay in between the hodochrones calculated for the standard deviation depths for this cell and therefore follow the expected trends for such a profile. So, it can be concluded that the PmP-waves measured in cell M23 are all in this time window, confirming a reliable Moho depth evaluation.

A

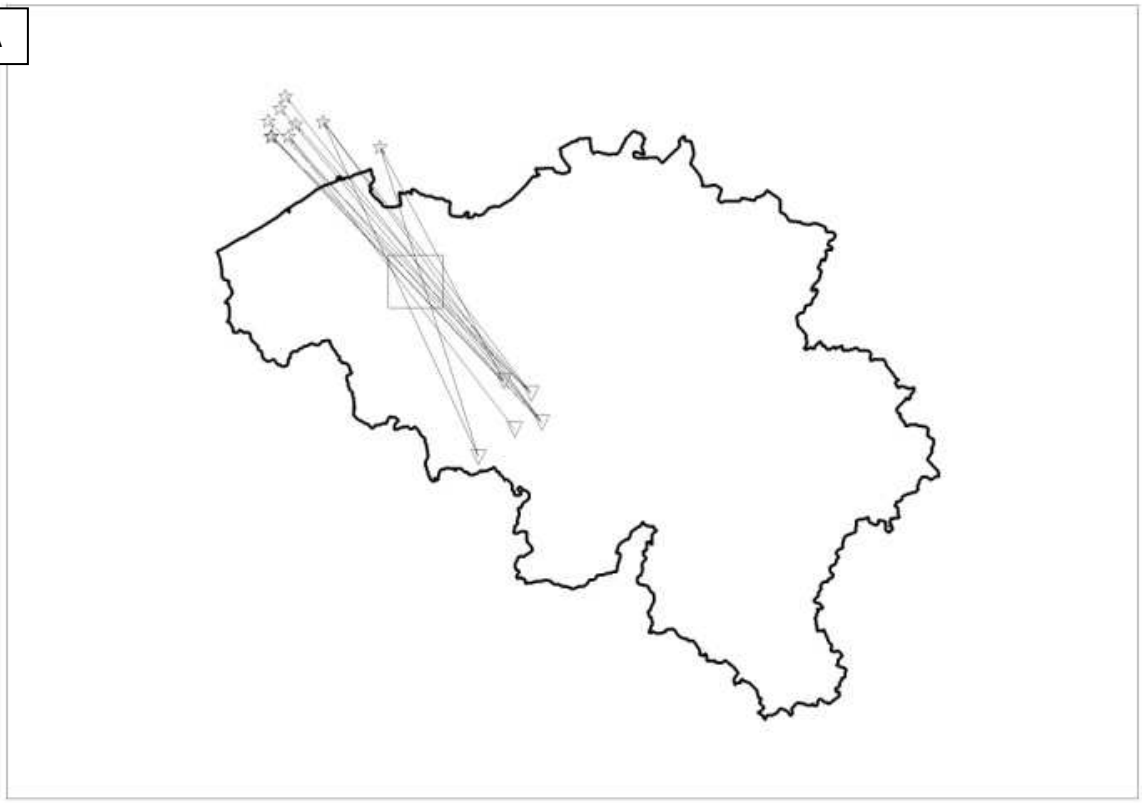

B

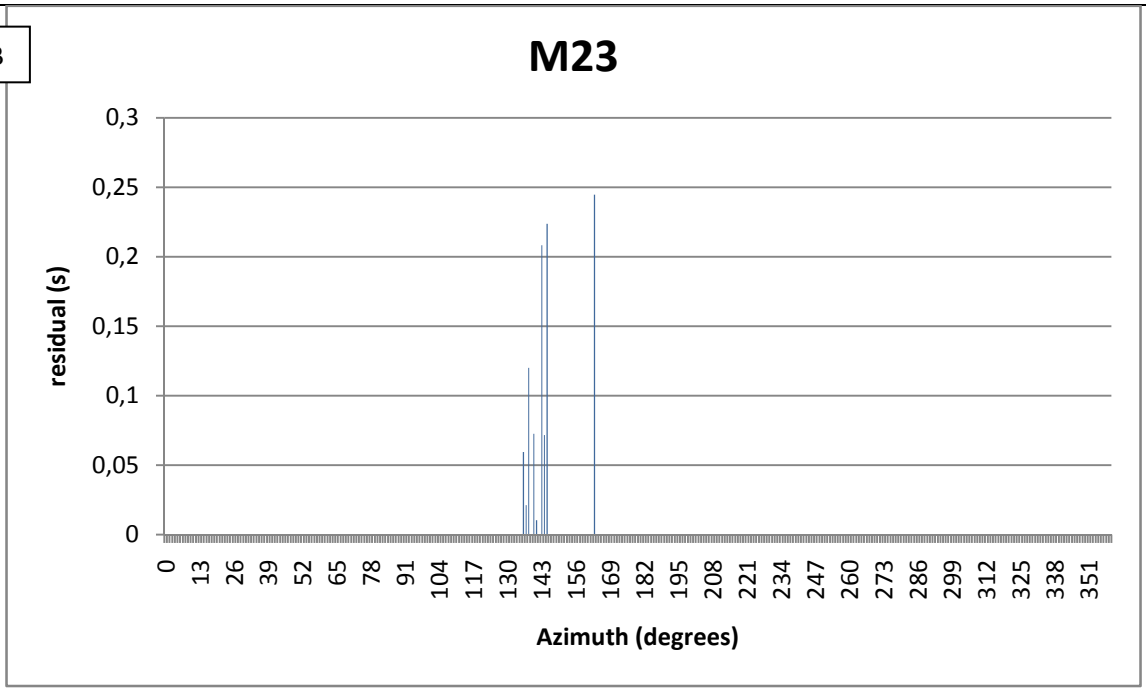
M23
0,3
0,25
0,2
0,15
0,1
0,05
0
residual (s)
0
13
26
39
52
65
78
91
104
117
130
143
156
169
182
195
208
221
234
247
260
273
286
299
312
325
338
351
Azimuth (degrees)

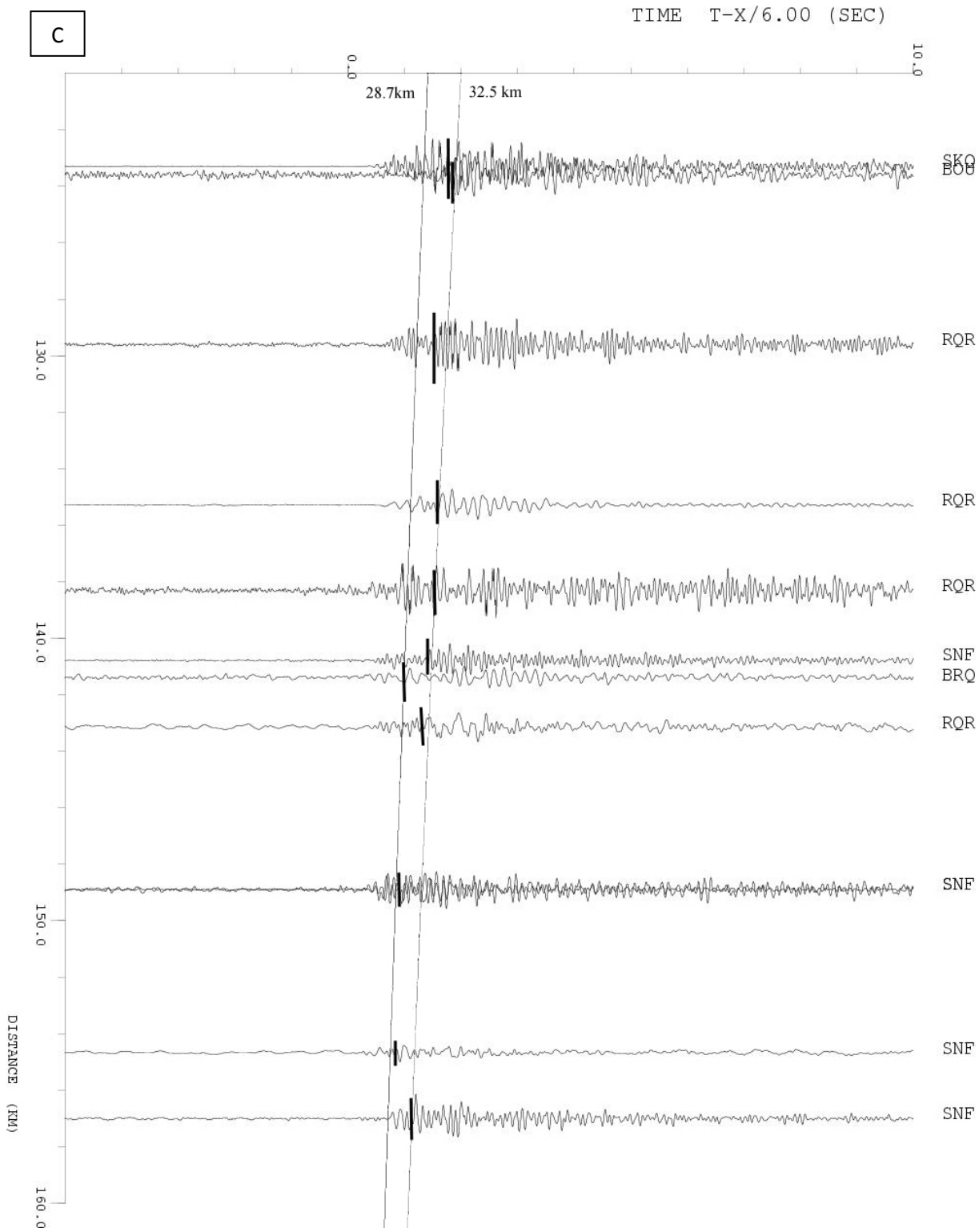

Figure 4.5: Evaluation of the PmP-arrival time measurements and the corresponding Moho depth calculations for cell M23.

A. Map showing the direction of the trajectory between the explosions and the stations for all the reflection points within a specific grid cell M23. B. The azimuth of the uncertainty (s2) for the different Moho depths for cell M23. C. Profile showing the seismograms of the explosion-station couples with a PmP-bounce point in cell M23. The black line represents the measured PmP-wave and the lines indicate the time window limiting the arrival time for the range 2□□range of evaluated Moho depths.

The profiles for the cells W30 and W31 (shown in Figure 4.8) are interesting too, as there is a huge Moho depth difference between both cells. When comparing the real seismograms of the cell W30 to the synthetic seismograms calculated for a Moho depth of 32.5 km (as in the original model), a slight resemblance is seen but it is not perfect. When synthetic seismograms are recalculated for these seismograms, with the Moho depth taken at 28 km (the calculated Moho depth for this cell), a very good fit is obtained, indicating a correct measurement of the PmP-waves.

The cell W31 is much more difficult to interpret due to two possible arrivals on the seismograms. On the profiles of the earthquakes it is not clear whether the PmP-waves are picked correctly. So several profiles with synthetic seismograms were made (with varying Moho depth (37 and 17 km) for this cell (Figure 4.6). When the second arrival, on the real seismograms, is taken as the reflection at the Moho, the synthetic seismograms calculated for a Moho depth of 37 km are more in correspondence with the real seismograms. After measuring these arrivals, the calculated Moho depth is 37 km. In cell W30 a similar second arrival can be observed before the arrival of the PmP-waves. Here, however it corresponds to a reflector at a depth of 24 km. Mooney and Prodehl (1978) have investigated seismic-refraction data in the Rhenish Massif and found that in the profiles closest to the cells W30 and W31 the velocity structure is characterised by an intermediate crustal reflector at about 15 km depth and a Moho discontinuity at about 29-30 km. It is assumed that the first arrival from 17 km depth corresponds to the intermediate crustal reflector as seen by Mooney and Prodehl (1978) and the second arrival from 37 km corresponds to the reflection at the Moho. In cell W30 another arrival can be observed before the arrival of the PmP-waves. This arrival corresponds to a reflector at a depth of 24 km.

It was also evaluated whether the Moho depth depends on the direction of the rays (Figure 4.7), the discrepancy between the measured arrival times to the calculated ones for each source-seismometer couple in function of the direction of the rays was also plotted. In most grid cells, the rays all follow similar directions due to the fact that most of the explosions and some earthquakes are positioned at the edge of the network. This is definitely the case for the grid cells M22 and M23 (see Figure 4.8 and Figure 4.7) because they only contain reflection points from North Sea explosions. The cells W27 to W31 (see Figure 4.8 and Figure 4.7) contain reflection points from mining-induced earthquakes in Germany. Both explosions and mining-induced earthquakes are positioned at the outer edge of the network. On the other hand, the fact that the rays follow similar ray paths minimizes uncertainty in Moho depth evaluation due to anisotropy.

Jongmans & Camelbeeck (1994) suggested a velocity anisotropy in the Stavelot Inlier, located south of the Variscan front, with faster velocities (5.3-6.2 km/s) parallel to the Midi overthrust and slower velocities perpendicular to the thrust (4.7-5.8 km/s) in the first 6 km of the upper crust. Can a similar trend be seen in this study? Combining the results for the cells north and south of the Variscan front (Midi-overthrust), it is not clear if a similar trend can be spotted in the results (Figure 4.7), but it cannot be excluded. Therefore, more data are needed and a more elaborate analysis should be performed.

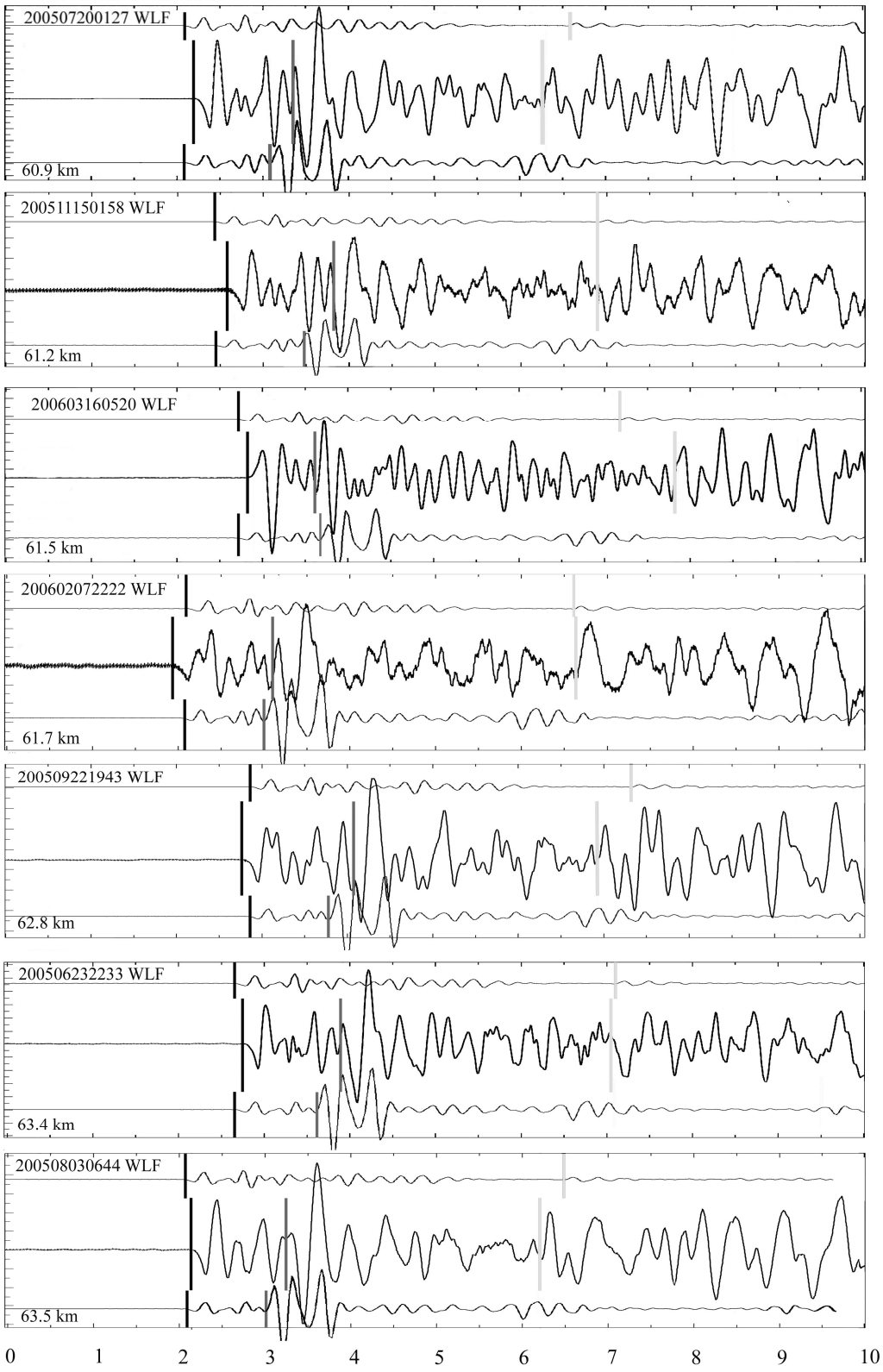

Figure 4.6: Several seismograms (middle trace) from cell W31 compared to their synthetic seismograms calculated for a Moho depth of 20 km (lower trace) and 34 km (upper trace) in a 10 s window.
The black line indicates the arrival of the P-wave. the dark grey line the arrival of the wave reflected at a depth of 20 km and the light grey line, the arrival of the PmP-wave reflected at a depth of 34 km.

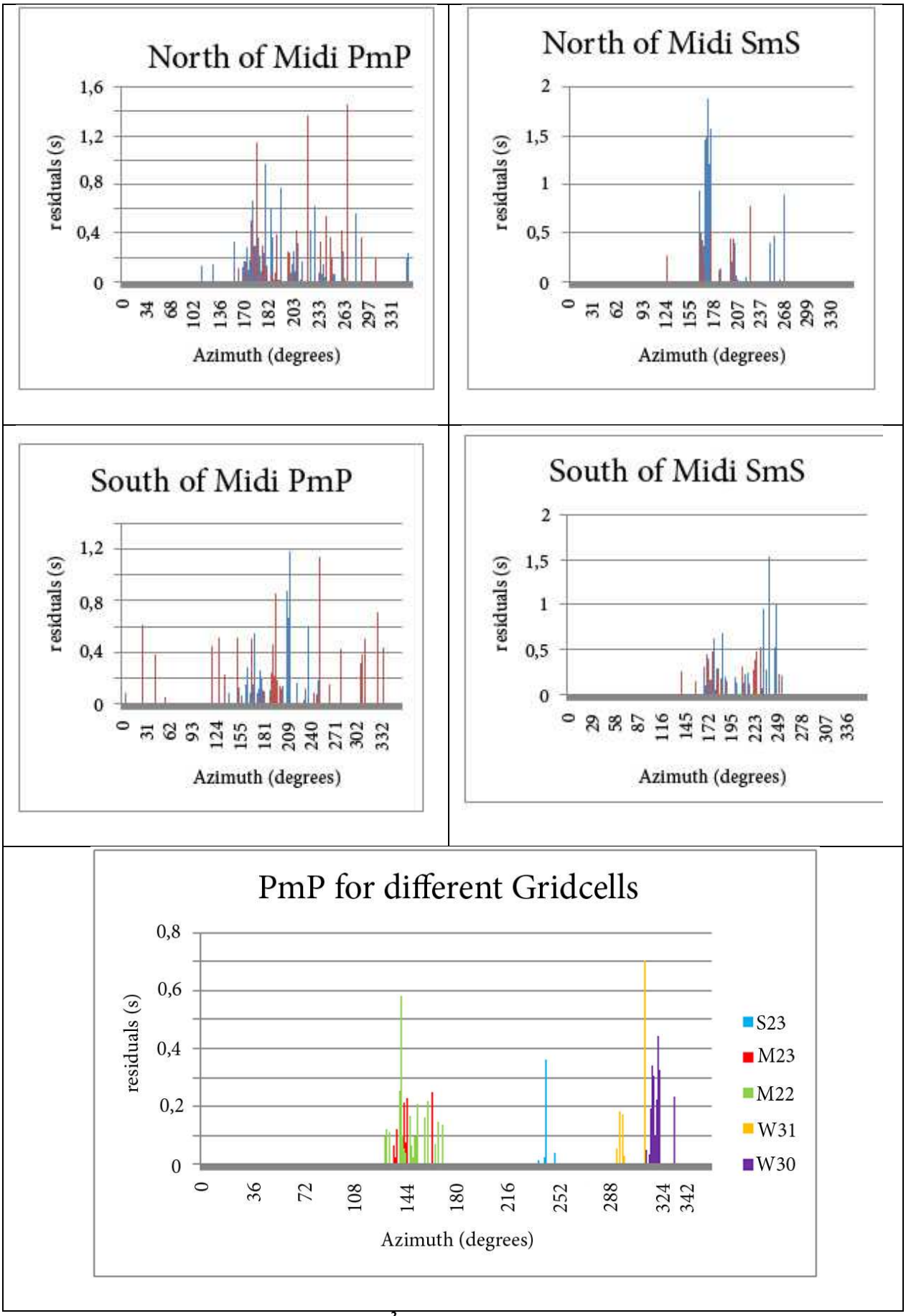

Figure 4.7: The azimuth of the uncertainty (s^2) of the different source-station couples for different cells. Top 4 diagrams: the cells north and south of the Midi overthrust and for both PmP- and SmS-waves. The diagram at the bottom: the cells S23, M23, M22, W31 and W30.

4.4.4 Moho depth underneath Belgium

4.4.4.1PmP-data

Figure 4.8 shows the geographical variation of the crustal thickness evaluated in this study. The map is completed by the results of the DEKORP Research group (1991), Matte and Hirn (1988), Klemperer & Hobbs (1991) and Rijckers *et al.* (1993). Only the grid cells with a 95% confidence interval shorter than 4 km and 5 or more measurements are presented.

The Moho underneath Belgium is rather flat. The thickness of the crust is around 31 km underneath the Brabant Massif and has been evaluated between 31 and 33 km in the east of Belgium. Near the Eifel Volcanic Province, the Moho is shallower than in the other regions (approximately 27 km). In the southeast corner of the map (Saar region in Germany), the Moho depth is only determined in two neighbouring grid cells but their results significantly differ by 7 km ± 4 km. An other anomalous grid cell is S23 to the west of the Roer Valley Graben, which has a depth of 28.7 ± 1.3 km compared to the 30.7 ± 1.1 -31.7 ± 1.3 km of the surrounding grid cells. Nevertheless, this difference is not significant and the depth estimated with the SmS-phases is 32.4 ± 1.8 km.

To confirm the 31 km depth underneath the Brabant Massif, two additional seismic stations were placed in Markegem and Ronse. Unfortunately, due to unfavourable site conditions (both stations were placed at ideal distances from the North Sea explosions but were placed on a rather thick sediment cover resulting in too much noise making it too difficult to clearly measure the PmP-waves), it was impossible to measure sufficient PmP-waves to calculate Moho depths for these stations.

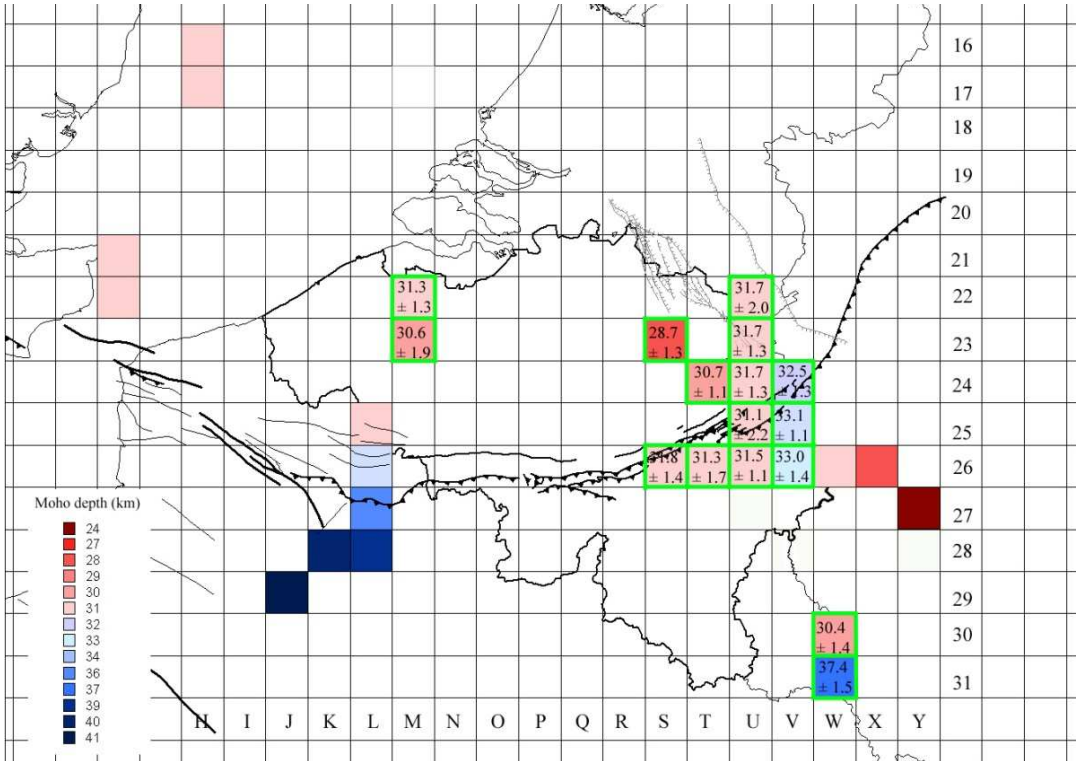

Figure 4.8: Moho depth underneath Belgium calculated from PmP-data in this study. (grid cells surrounded by a green line) and from deep regional seismic reflection profiles ECORS, DEKORP and Birps (grid cells without outline). In black and grey the major fault lines and the political borders.

4.4.4.2SmS-data

Because the S-waves have little energy in the wave train of explosions in the North Sea, no data are available underneath the Brabant Massif (Figure 4.9). Outside this massif, the SmS-data correspond well with the PmP-data, and Moho depth varies between 30.7 ± 1.3 and 32.9 ± 2.0 km underneath the Ardennes Allochthon. Underneath the Eifel Volcanic Province, more SmS-wave arrival times are measured than PmP-arrival times. This is because not all the stations, used to determine the Moho depth in this region, were ideally positioned. So, the signal to background noise ratio is too low to be able to determine the arrival of the P- or PmP-waves accurately. The S- and SmS-waves are more energetic, so they could be better measured, resulting in more data and confirming the PmP-wave trend that the Moho is shallower there than underneath the Ardennes Allochthon (28 km compared to around 31km).

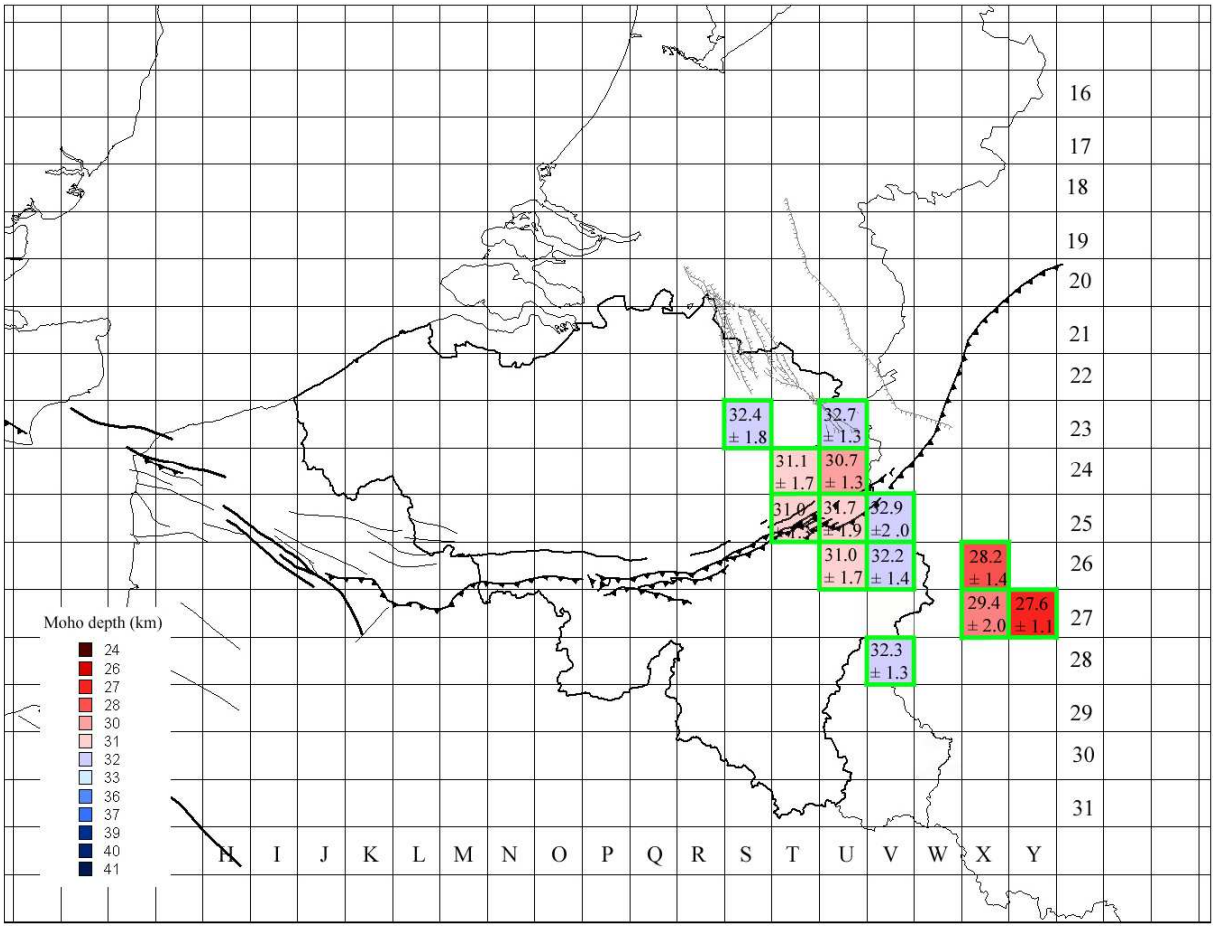

Figure 4.9: Moho depth determination underneath Belgium calculated from SmS-data in this study. In black and grey the major fault lines and the political borders.

4.5 Discussion

For the first time this study has determined that the Moho depth underneath the onshore part of the Brabant Massif is situated at a depth of 31 km ± 1.9 km. South of the investigated region, Matte & Hirn (1988) interpreted the ECORS profile and determined the Moho depth around 31 km near the Belgian border and, dipping southward to a depth of about 40 km (Figure 2.6). This suggests that from the most northward point of the ECORS profile toward the north (this study) the Moho becomes flat at a depth of 30-31 km. In the North Sea, to the west and northwest of the studied region, several seismic profiles have been shot (SNST 93-07, Mobile 6,7 (Figure 2.7) and Shell UK 82-101 (Figure 2.8)). These profiles, particularly the profile Shell UK 82-101, which crosses the Brabant Massif from north to south, show that the Moho both to the north and south of the Brabant Massif is at the same level of about 10 s TWT. The Moho dips to approximately 12 s TWT further north. Converted with the CAL model (Table 3-1, Calbini, 2003), these TWT-times correspond to a Moho depth of about 30 km underneath the Brabant Massif and up to 37 km further north. On the profile MPNI 9101 (Figure 2.9), Rijckers *et al.* (1993) interpreted the base of a band of reflections at 12 s TWT as being the Moho. This corresponds to a depth of 37 km. It is not the objective of this work to question this interpretation, but looking at Figure 2.9, the reflection at 12 s TWT does not seem to be a clear elongated reflection, which would be typical of the Moho as can be seen on Figure 2.6 (ECORS profile) and Figure 2.10 (DEKORP profile). The 12 s TWT reflection on MPNI 1901 might represent an other structure in the crust or upper mantle. However, if the result of Rijckers *et al.* (1993) is correct, it indicates a clear discrepancy with the Moho depth evaluated in this study. Overall, the results presented in this study and the Moho depths found at the edges of the Brabant Massif along several seismic reflection profiles (ECORS, SNST 93-07, Mobile 6,7 and Shell UK 82-101) show that the Moho discontinuity underneath the Brabant Massif is flat at approximately 31 km of depth. This flat Moho is not surprising as the Brabant Massif is an old, cold massif that has not known any deformation for the last 400 Ma.

Underneath the Roer Valley Graben and the Ardennes Allochthon, Moho depths range from about 31 to 33 km (Figure 4.8). These are in accordance with the results of Budweg *et al*. (2006) (Figure 2.25), determined by receiver function analysis. It can be noted that no Moho uplift occurs underneath the Roer Valley Graben as opposed to what one would expect underneath a graben. This could be caused by the fact that the Roer Valley Graben is less wide than the grid cells used in this study and therefore it is possible that an uplift is not visible. To be able to determine the Moho depth more accurately underneath the Roer Valley Graben, more PmP/SmS measures are needed so that smaller grid cells can be used. Smaller grid cells might help to clarify whether the Moho is or is not uplifted beneath the Roer Valley Graben. If not, the flat Moho could be explained by the fact that the Roer Valley Graben is a passive rift in the early stages of opening. This means that the graben is opening as a consequence of pulling forces in the crust and not of a rise of hot mantle underneath it (Sengor & Burke, 1978). In passive rifts, volcanism, the corresponding heat flux and the Moho uplift appear after the initiation of the rift whereas in active rifts these features develop during or before the initiation (Sengor & Burke, 1978). In the Roer Valley Graben there is no active volcanism or high heat flux (Remmelts & Duin, 1990; Geluk *et al.*, 1994). Together with a flat Moho, this would indicate that the Roer Valley Graben is indeed a passive rift in an early phase of opening. In the other case, an uplifted Moho might indicate that the Roer Valley Graben has already passed that early phase.

On the DEKORP profile (Figure 2.10, DEKORP Research group, 1991), the Moho is situated at 8 s TWT or 24 km (converted to depth with the CAL model (Table 3-1, Calbini, 2003)) underneath the Eifel

North-South-zone and dips to the northwest to about 10-10.5 s TWT or 30-32 km. These depths are confirmed by this study. Further to the east, underneath the Eifel Volcanic Province, the Moho becomes shallower, up to 27 km (Figure 4.8). This Moho depth is also similar to that of the DEKORP profile (8 s TWT or 24 km) as well as the depth determined by the receiver function analysis (28 km) (Figure 2.25, Budweg *et al.*, 2006). In the past, this uplift underneath the Eifel Volcanic Province has always been explained as a result of the Eifel Plume, a hot mini-mantle plume (Ritter, 2005; Budweg *et al.*, 2006) that has risen underneath the Eifel Volcanic Region and that originated from a larger European mantle plume risen from the core/mantle boundary, but stuck at the 440 km discontinuity. As it has been discussed in paragraph 2.5.2 of chapter 2, the volcanism in the Eifel Volcanic Province is not necessarily the result of a mini-mantle plume rising to the surface, but rather results from an upwelling branch of the small scale upper mantle convection cell caused by the subduction of the European lithosphere in the Alps (Figure 4.10) (Meyer & Foulger, 2007). In this case, the Moho uplift indicates the position of this upwelling branch.

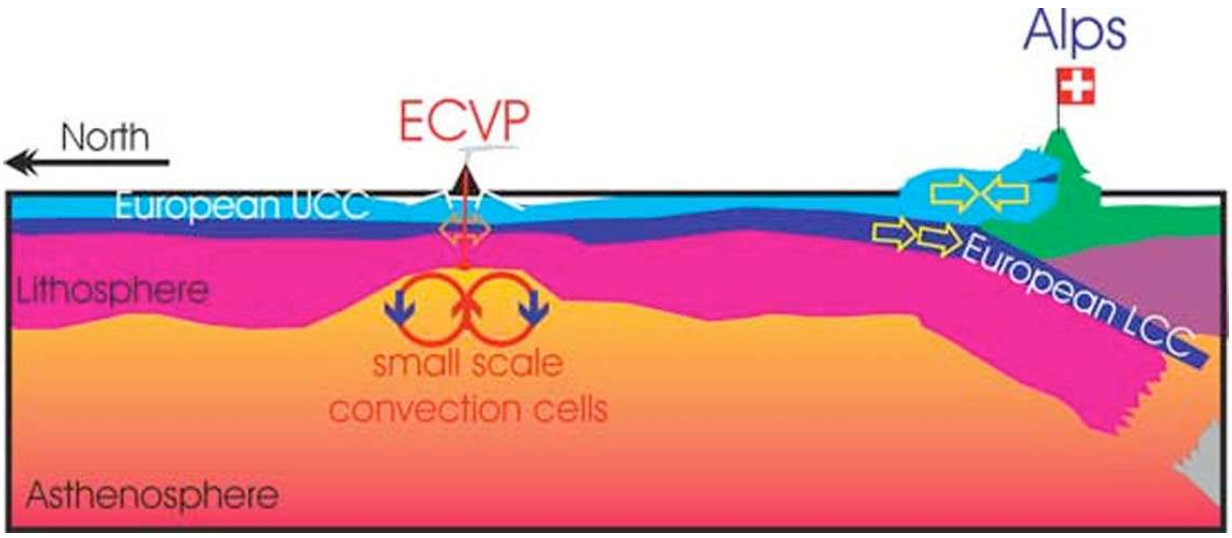

Figure 4.10: Sketch of the geodynamic model proposed here to explain the origin of the Eifel Cenozoic Volcanic Province. Alpine subduction of the European lower continental crust (LCC) thins the crust in the Alpine foreland at Variscan sutures. This thinning allows the upwelling of asthenosphere and the initiation of small-scale convection below Eifel Cenozoic Volcanic Province (ECVP) localities. UCC = upper continental crust. Redrawn from Meyer & Foulger (2007).

Overall, the Moho is quite flat underneath the Belgian territory. This is not surprising considering the low deformation rates in its recent geological history. An exceptional feature is the possible large drop in Moho depth between grid cells W30 and W31 (Figure 4.8). The results suggest a minimum drop of approximately 4 to 7 km over a distance of max 30 km. A similar drop has been observed on the ECORS profile (Figure 2.6) slightly north of Montdidier, France, where two Moho reflections seem to cross (Matte & Hirn, 1988). There the upper Moho is at approximately 35 km and the lower Moho at 41 km. Both Mohos cannot be related to one another, because no clear continuity can be observed. Is a similar effect seen here? Nearby profiles do not show such a structure but instead show a steep Moho. This does not necessarily mean that it does not exist in this region, because these profiles are all shot in a different direction than the ECORS profile. An other explanation might be that the Moho is very steep (as seen in nearby profiles, Figure 4.11) underneath these cells (Mechie *et al.*, 1983). Because a constant Moho depth is assumed underneath the 20x20 km^2 cells, a large jump in Moho depth can be expected between neighbouring cells in such a case.

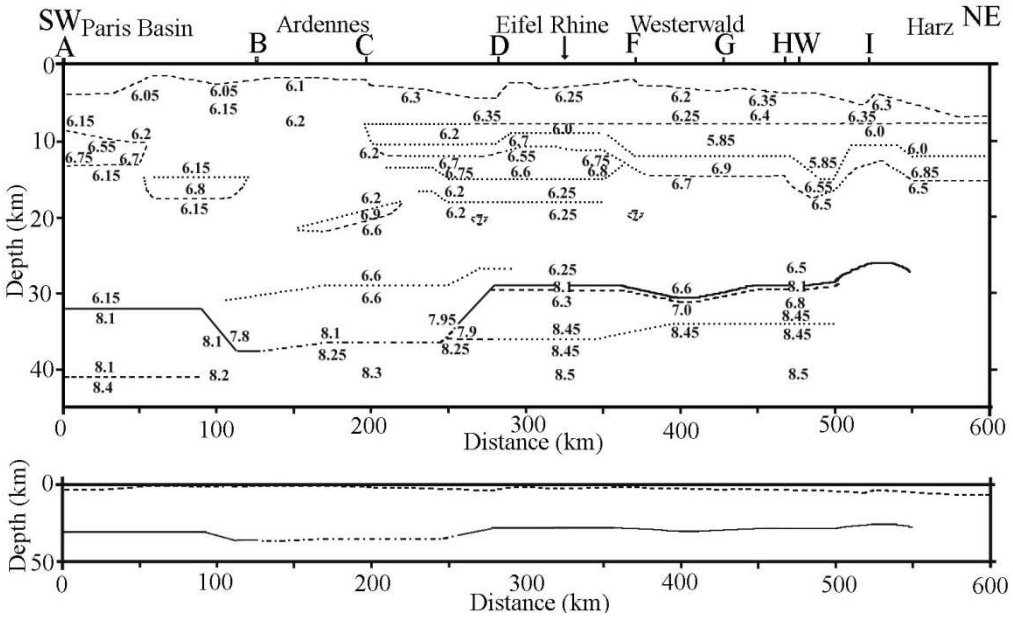

Figure 4.11: Two-dimensional cross-sections (top with vertical exaggeration 5:1; middle without vertical exaggeration) for the P-wave velocity structure beneath the main profile 240-LO-60.
Legend : __ Moho as discontinuity with a velocity contrast of > 0.2 km/s; -.- Moho as discontinuity with a velocity contrast of ≤ 0.2 km/s; ---- other discontinuity with a velocity contrast of > 0.2 km/s; ..... other discontinuity with a velocity contrast of ≤ 0.2 km/s. Redrawn from Mechie *et al*., 1983.

On top of that two reflections can be observed in cell W31 (Figure 4.8). One at 17.1 km depth, the other at 37.4 km. Mechie *et al.* (1982) interpreted these as reflections from respectively the Conrad and Moho discontinuity. Similar double reflections (one at 24 km and the other at 29 km) are also present in cell W30 (Figure 4.8). When the locations where the double reflections have been observed on the old profiles (Mooney & Prodehl, 1978) are plotted on a map, it only appears to be along a small zone (Figure 4.8 and Figure 4.13). It must be stated however that not a lot of information can be retrieved to the south of this zone, as hardly any profiles have been shot there. Two explanations for the double reflections have been offered in the past (Mechie *et al*., 1983; Giese, 1983). Either the first reflection represents the top of a magmatic chamber, or the crust underneath the Rhenish Massif has thickened by stacking of thrusts and crustal slices during the Variscan Orogeny. In the last case, the upper reflection would represent a reflection on an old thrust structure (old Moho, now fault line). It is still under discussion which explanation might be best. Recent insights in the deep structure of the Caledonian microplate Avalonia (Pharaoh *et al.*, 2006) could even offer a third explanation. This explanation suggests that the reflection observed in the middle crust would be a reflection on top of an old Neoproterozoic crust, probably Rondonian, as is seen on a nearby transect (Figure 4.12). Although these three explanations are very different and have very distinct characteristics, no distinction between them can be made at this point as not all the seismic parameters are known, yet. First of all, as the double reflections are only observed in a small zone, the geometry of the plane that causes the reflection cannot be determined. Secondly, no clear information on the seismic velocity underneath this reflection can be determined. This problem was resolved by the results of a local seismic tomography, see next chapter, as this approach determines the 3D velocity structure of the crust.

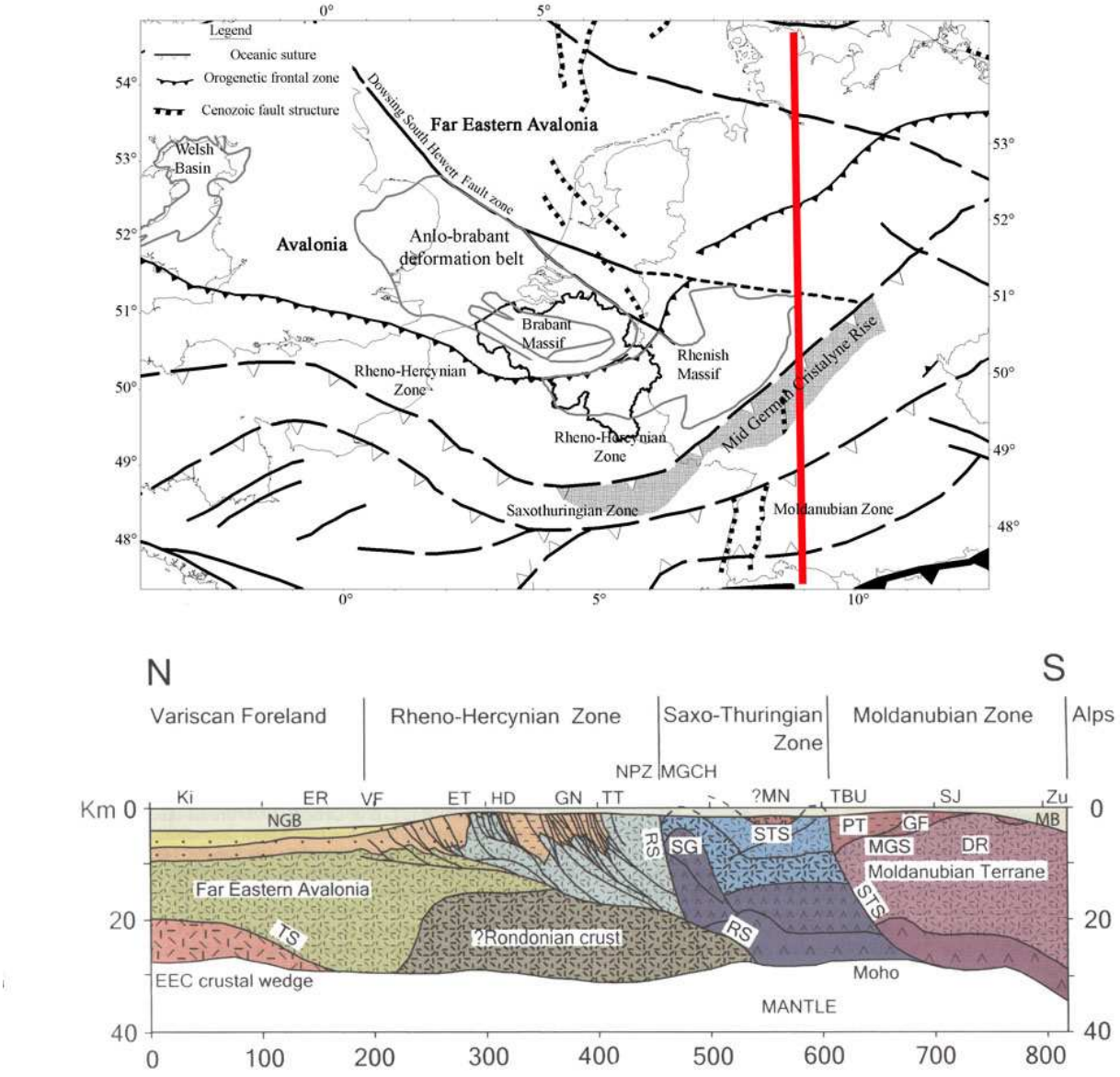

Figure 4.12: Transect to illustrate inferred structure of the "Variscide" accreted crust in the central German region (Pharaoh *et al.*, 2006).

Top: Basement tectonic sketch map of NW Europe with position of the transect shown in the bottom part of the figure (redrawn from Verniers et al., 2002). Political borders are indicated in light grey, Belgian borders in black.

Bottom: Transect : 5x vertical exaggeration. Interpretation of full crustal structure from the EGT deep seismic refraction experiment (Aichroth & Prodehl, 1990; Prodehl & Aichroth, 1992). Detail of shallow crustal structure in central part of transect is after interpretation of DEKORP deep seismic reflection profiles by Giese (1995) and Oncken et al. (2000). Post-Palaeozoic basins and platforms: HD, Hessen Depression; MB, Molasse Basin; NGB, North German Basin;. Postulated Palaeozoic terranes and possible terrane and sub-terrane boundaries: MGCH, Mid-German Crystaline Rise; NPZ, Northern Phyllite Zone; PT, Perunica (Bohemia) Terrane; MGS, Moldanubian-Gföhl Suture; MT, Moldanubia Terrane; RS, Rheic Suture; STS, Saxo-Thuringian Suture; TS, Thor Suture. Proterozoic-Paleozoic tectonic elements: BM, Bohemian Massif; DR, Drosendorf Unit (of BM); ET, Ebbe Thrust; GF, Geföhl Unit (of BM); GN, Giessen Nappe; MN, Münchbergh Nappe (of BM); SG, Saxonian Granulites; TBZ, Tepla-Barrandian Basin (of BM); TT, Taunus Thrust. Other Geographical Locations: Ki, Kiel; ER, Elbe River; SJ, Swabian Jura; Zu, Zurich.

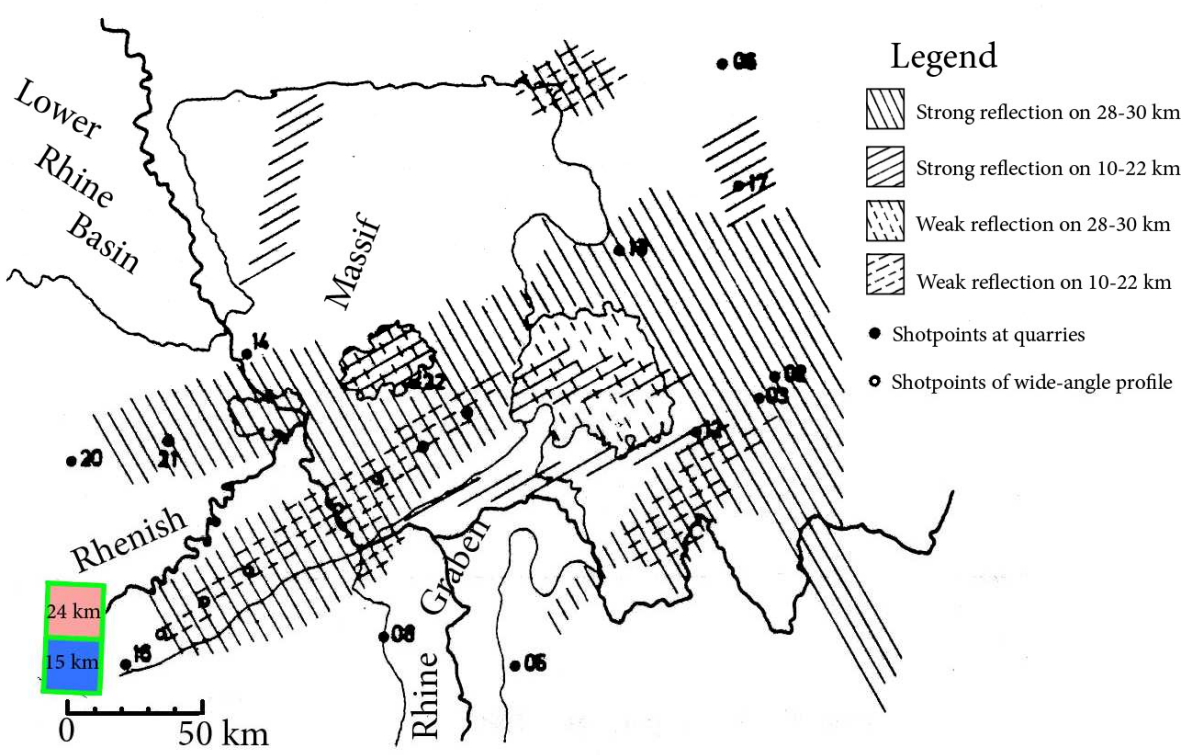

Figure 4.13: Map of the area of the Rhenohercynian zone showing main features of crustal structure deduced from seismic reflection profiles. (Mooney & Prodehl, 1978).
The cells with intra crustal reflections of Figure 4.8 (pink and blue square) are also indicated.

Finally, the results presented in this work are compared to the Moho map of Dèzes & Ziegler (2001), which is seen as the reference for Moho depth maps in Western Europe. No resemblance can be seen however between the results of this study (Figure 4.8 and Figure 4.9) and the Moho map of Dèzes & Ziegler (2001)(Figure 4.14). Dèzes & Ziegler's (2001) map differs not only from the results presented here, but also from those of several seismic reflection profiles shot in the region (Figure 4.8) and from other Moho maps in Belgium and its surroundings, like the Moho map of the UK (Chadwick *et al.*, 1996) (Figure 4.15) or the older Moho map of Europe (Meissner, 1987) (Figure 4.16). All these maps match the results presented in this work more than with the map provided by Dèzes & Ziegler (2001). Why there is such a difference between Dèzes & Ziegler's (2001) map and the results presented in this and other works cannot be clarified with certainty, because it is very difficult to know the exact studies Ziegler (1990) (on which the Dèzes & Ziegler map is based) used to determine the Moho depth in the Belgian region. The differences might be due to "interpolation problems" in the Dèzes & Ziegler Moho map. As it is a map for the entire European continent, the node spacing used to determine the map is most certainly greater than for the study presented in this work and those of the other Moho maps. In that case, the Moho depth is interpolated over larger distances between the nodes and its final result will largly depend on the interpolation technique used.

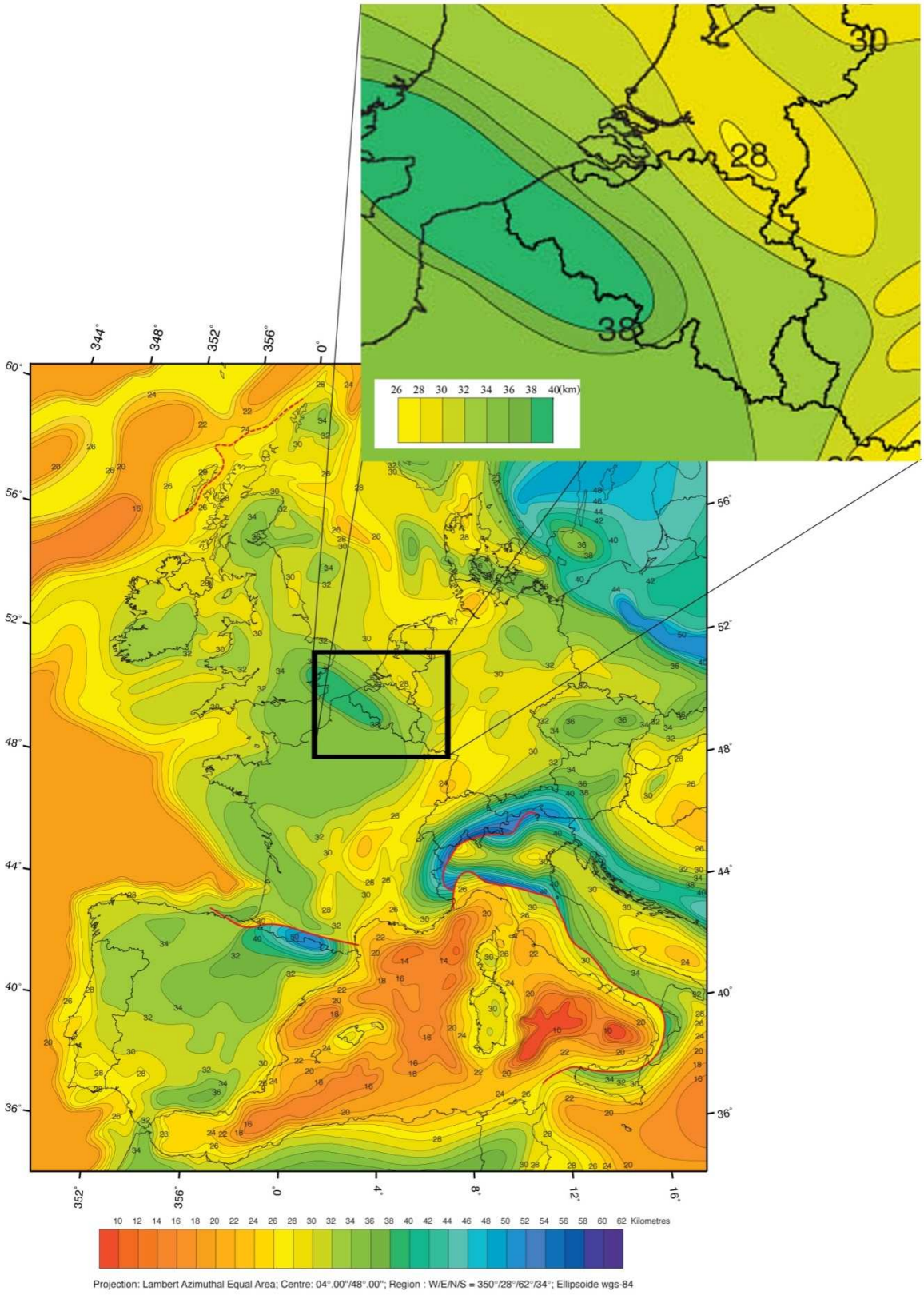

Figure 4.14: Map of the European Mohorovicic discontinuity (Dèzes & Ziegler, 2001) and zoom on the studied region in this work.

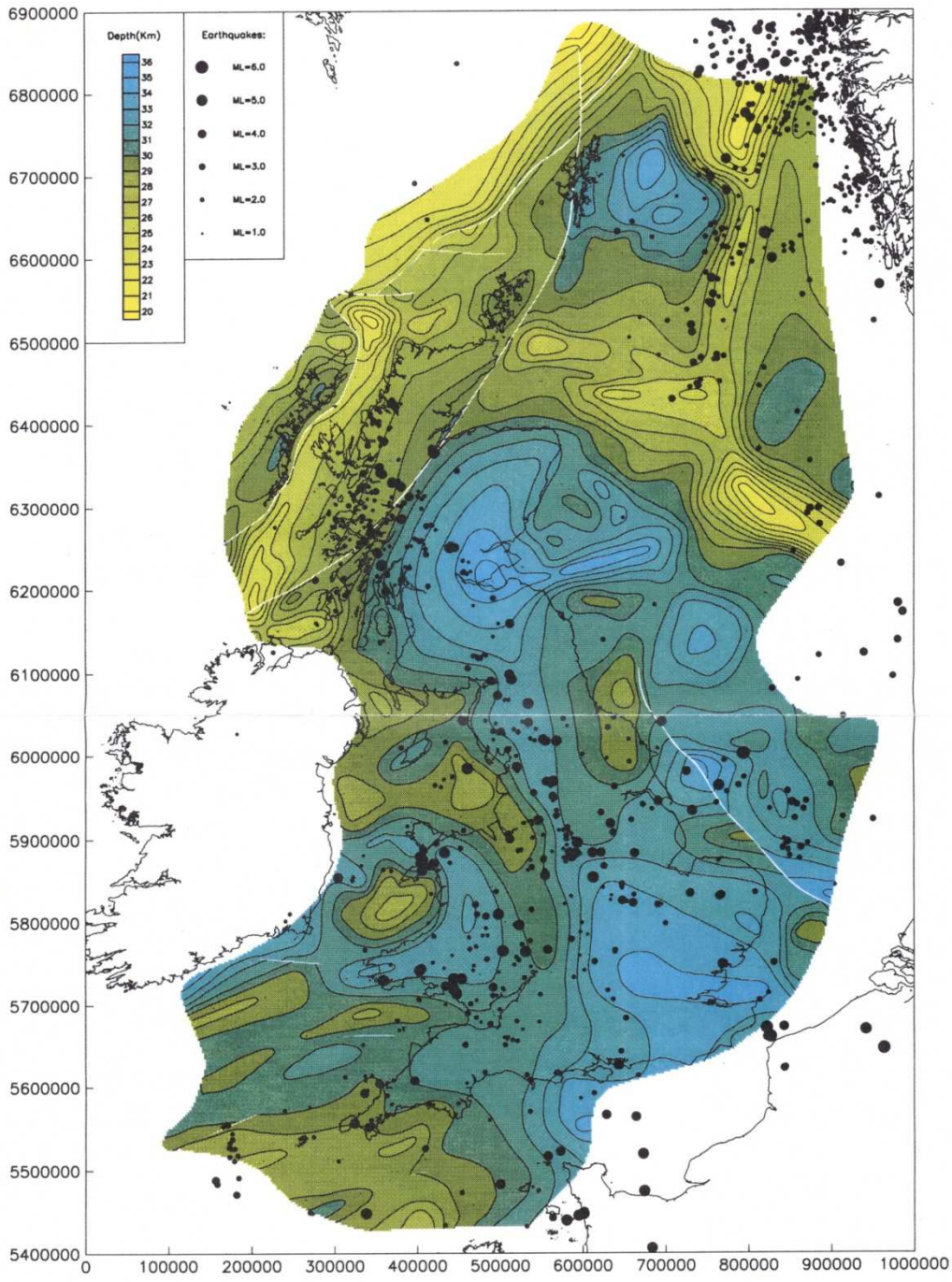

Figure 4.15: Moho depth map of the UK and earthquakes (1/5000000). (Chadwick *et al.*, 1996).

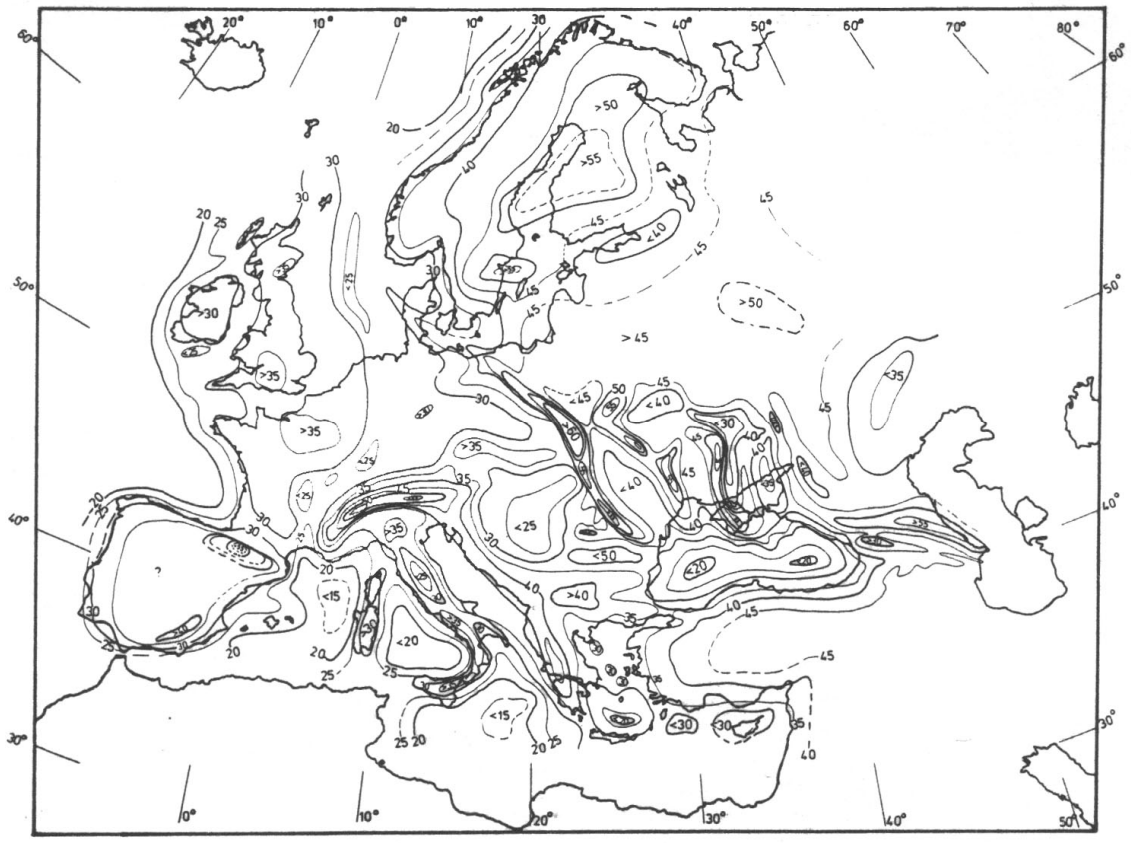

Figure 4.16: The Moho depth in Europe (Meissner, 1987), contour interval 5km.

4.6 Conclusions

This study demonstrates that the Moho reflected PmP-wave is best visible in the low frequency domain (< 8 Hz). This can help to improve the recognition and determination of PmP-arrival times in comparable studies in the future.

Using arrival times of PmP-phases of local seismic events recorded by the stations of the Belgian seismic network, the Moho depth underneath the Belgian onshore part of the Brabant Massif was evaluated at 31 ± 1.9 km. Such a degree of precision has not been reached before. This result is comparable to the values obtained offshore by seismic reflection profiles (Klemperer & Hobbs, 1991). The fact that the Moho can be visualized by wide-angle seismology and not by reflection seismology may indicate the nature of the Moho boundary underneath the Brabant Massif: it could be a gradient zone with anisotropic layers in which the horizontal velocity is higher than the vertical velocity as Pavlenkova (2009) has observed underneath the Pannonian Basin. The Moho underneath the Brabant Massif is very flat as can be expected from an old, cold massif, where no deformation occurred at for the last 400 Ma.

More to the east, the Moho depth has been evaluated by combining the analysis of PmP- and SmS-seismic phases. Similar values of about 31 km for the Campine region to the west of the Roer Valley Graben and the northern part of the Ardennes Allochthon were obtained. No Moho uplift appears underneath the Roer Valley Graben, but this depth should be re-evaluated when more PmP- and SmS-

arrivals are available so that smaller grid sizes can be used. The absence of a Moho uplift underneath the Roer Valley Graben indicate that it is a passive rift in an early stage of opening. With the recordings of SmS-phases reflected underneath the Eifel Volcanic Province, a value of 28 km has been obtained. This thinning of the crust is in agreement with the results obtained by Budweg *et al.* (2006) using receiver function analysis and with the uplift observed on the (DEKORP Research group, 1991). It is however better explained by the upwelling branch of an upper mantle convection cell caused by the subduction of European lithosphere in the Alps then by the rise and presence of a hot mantle plume.

At the southeast of Grand-Duchy of Luxemburg, two seismic reflection phases have been observed on the seismograms. The first can be interpreted as a result of the presence of a strong intracrustal reflector at depths ranging from 15 to 24 km. This first reflection is interpreted by Mechie *et al.* (1982) as a reflection on the top of an old magmatic chamber or as a reflection on an old Moho that was thrusted into the crust during the Variscan Orogeny. According to more recent insights it could also be a reflection on an old Neoproterozoic crust of Rondonian origin (Pharaoh *et al.*, 2006). To determine which explanation for the double reflection is correct, the velocity structure between both reflectors should be determined. This can be done by performing a local seismic tomography. The results of such a tomography are discussed in the following chapter. The second reflection is interpreted as the current Moho interface. Due to the huge difference in Moho depth (37 and 29 km), a very steep Moho seems to be present here.

The results in this work do not correspond to the Moho map of Dèzes & Ziegler (2001). They can however improve this Moho map.

Chapter 5 Seismic Tomography

5.1 Introduction

In the previous chapter the thickness of the crust has been determined. Although this is important information, it does not provide any knowledge on the structure or composition of the crust. As mentioned in the introduction, when one really wants to understand the upper crustal geology, one needs to have some understanding of the geology in the middle and lower crust. Because these regions cannot be attained by drilling (only to 5.6 km depth in Belgium), they cannot be studied directly, and therefore other techniques have to be used. Several of these techniques, like the deep seismic profiling, gravimetric and magnetic data, have been discussed in chapter 2. Another technique that is often used to study the lower and middle crust is a local seismic tomography. In a local seismic tomography, the three-dimensional velocity structure of the crust is determined. The velocity at which seismic waves travel through the crust is determined by the composition, pressure and temperature of this crust. The S-wave velocity is even sensitive to the presence of fluids. So, when one is able to determine the velocity structure of the P- and S-waves, one can determine the composition, structure, pressure and temperature of the crust and even the presence of fluids in the crust. Because S-waves are more difficult to measure accurately, instead of simply determining the S-velocity structure in the same way as the P-wave velocity structure, the Vp/Vs-ratio is determined as is explained further in paragraph 5.2.6 of this chapter. The combination of the P-wave velocity structure and the Vp/Vs-ratio allows to determine the composition and structure of the crust better than separately. So, to study the lower and middle crust underneath Belgium, a local seismic tomography was performed. The initial idea was to use the programme INVER3D, a tomographic inversion programme developed by Collin (1998) at the Royal Observatory of Belgium. It was tested first to see how and if it works for a 3D-tomography, because it had not been used to perform a 3D-tomography yet. The local seismic tomography of the Belgian crust would simultaneously be performed with SIMULPS (Evans *et al.*, 1994), a tomographic inversion programme that has been used worldwide for seismic tomographies and that has proven its reliability.

In this chapter, the theory behind tomographic inversion as well as the difference between the programmes INVER3D and SIMULPS will be discussed, followed by the interpretation of the results of the INVER3D inversion and the tomographic inversion of the Belgian dataset with the SIMULPS programme.

5.2 Velocity Tomography: Theory

Virtually all local tomography methods begin with equation (1.40) or (1.43) and then diversify to some extent, based on different treatments of some or all of the following aspects of the problem:

- the representation of the velocity structure
- the travel time and ray-path calculations
- the method of inversion
- the treatment of the hypocenter-velocity structure coupling
- the assessment of the solution quality
- the use of S-waves

The following sections cover each of these topics in detail.

It is important to note that the ray theoretical approach used in nearly all local earthquake tomographies has its limitations. The method uses the arrival times of observed first arriving waves. It is implicitly assumed that these observed waves are the "direct" waves. Unfortunately, it is possible that what is seen as a first arrival on a seismogram is not the direct arrival in reality. In some cases, the direct arrival is so low in energy that it is not distinguishable from the noise and so an arrival of a later wave is taken as direct arrival. It is also possible that the waves are reflected on a low velocity zone and that the reflections arrive before the direct waves that go through the low velocity layer (Wielandt,1987). Furthermore, the energy that travels with a wave is not pin-pointed to the infinitesimal line (representing the ray), but the structure that is sampled by an observed arrival corresponds roughly to the Fresnel volume around the ray (Chou and Booker, 1979). One must be aware of these limitations when assessing the results of an inversion.

5.2.1 Velocity structure representation

There are many ways to represent the three-dimensional velocity structure of the Earth's crust and upper mantle in local earthquake tomography. None of these can completely represent the Earth's structure because the earth's crust is composed of several heterogeneous structures of various scales, like discontinuities, layers, faults, intrusions and other random geological heterogeneities. Furthermore, some degree of anisotropy can also exist. The scale of the structures that can be studied with a local seismic tomography depends on the ray density with a lower limit proportional to the minimum wavelength of the recorded seismic energy.

Two main approaches (both with a range of varieties) are used in the present day tomographic methods. The first one is the constant-velocity block approach (Aki and Lee, 1976), which treats the earth's crust as blocks in which the velocity is constant. A disadvantage of this method is the fact that heterogeneities cannot be represented correctly, even very simple structures like velocity discontinuities and velocity gradients. Variants of this method are the constant velocity-layer approach (Crosson, 1976), laterally varying layers (Hawley *et al.*, 1981) and a 3D-grid of nodes (Thurber, 1983). They all suffer from the same disadvantages, to variable degrees.

In the laterally varying layers approach, the model is divided into layers with a constant velocity in the vertical direction. The spacing between the lines can vary from layer to layer and the velocity is determined by interpolating between the vertical velocity lines. In the 3D-grid of nodes, the velocity can vary between the nodes in every direction, with a linear B-spline interpolation amongst the nodes.

The second main approach is where every set of four neighbouring nodes are seen as the vertices of a tetrahedron (Lin and Roecker, 1990; Collin, 1998). The velocities of the four nodes are used to determine a unique linear velocity gradient in each tetrahedron; the velocity gradient can thus point in any direction. The advantage of this approach is that an analytical ray-tracing procedure can be used, as rays-paths are circular segments in a medium with constant velocity gradient.

The two programmes t used to perform the local tomography, SIMULPS (Thurber, 1983) and INVER3D (Collin, 1998) use a different main approach to represent the velocity structure. SIMULPS uses a three-dimensional grid of nodes, where the velocity is interpolated with a B-spline linear interpolation. INVER3D, however, uses a tetrahedron approach to represent the earth's velocity structure.

5.2.2 Travel time and ray-path calculations

Because a travel time tomography compares the calculated arrival times with the observed arrival times, it is important that the ray path of the seismic wave between each source and receiver is correctly calculated. The ray path does not only affect the calculated arrival time and thus the arrival time residual, it also determines the hypocenter and velocity model partial derivatives. There are as many techniques to determine the ray path as there are ways to represent the earth's crust. The way to represent the earth's crust determines the best way the rays-paths are calculated and vice-versa.

Ray-tracing is a two-point boundary problem, where the end points (source and receiver positions) are known, but where the propagation time and path have to be determined. The two most-used methods are bending and shooting. In the bending method, the source and receiver are connected with each other (mostly along a straight line or a circle arc), and then the path is modified by an iterative method to find the best solution, by respecting the ray equations or by satisfying the principle of the stationary travel time (principle of Fermat). The general method is described in the annexes of Wesson (1971). In the shooting method, the ray-path is calculated by integrating numerically, analytically or semi-analytically the equations of the ray, starting from initial arbitrary conditions (problem of ray tracing) and iterating the processes on the initial conditions in a way to arrive with the ray at the receiver.

Both methods suffer some disadvantages. With the bending method, the number of calculations is very high, which makes the method rather demanding in computer power and time consuming when numerous calculations are necessary (Thurber & Ellsworth, 1980) . Furthermore, the convergence is slow and not guaranteed and the method does not guarantee that the obtained ray-path is the one that gives the fastest travel time. For the shooting method, the convergence is also slow because no efficient correction strategy can be determined. Furthermore, it is also not sure that the ray-path found is the one corresponding to the minimal travel time. The shooting method is also sensible to shadow zones.

Not only do the programmes SIMULPS and INVER3D use different ways to represent the earth's structure, they also use different ways to calculate the ray-path and the travel time. SIMULPS uses the bending method and INVER3D uses a shooting method.

5.2.3 Inversion method

Because of the non-linear nature of the local earthquake tomography problem, an iterative approach is essential in finding the solution. There are only a few different schemes that have been employed for this iterative procedure.

One of these schemes combines parameter separation with the construction of normal equations and the incorporation of damping using:

$$\Delta m = [(M')^T M' + \varepsilon^2 I]^{-1} (M')^T r' \qquad (5.1)$$

where M and Δm are the matrix and vector of the velocity partial derivatives and perturbations, respectively; r is the residual vector and ε^2 represents the damping factor.

This results in a matrix size fixed by the number of velocity model parameters (Spencer & Gubbins, 1980; Thurber, 1983). Therefore, the matrix size does not increase when the number of earthquakes included in the inversion increases. The costs of this normal equation shortcut are: the loss of singular values information, the sensitivity of the solution to the choice of the damping value and the squaring condition number of the matrix to be inverted.

In an attempt to diminish the storage and manipulation of large matrices, Kissling (1988) used parameter separation and applied an Algebraic Reconstruction Technique (ART) type approximation of the equation (1.43):

$$\Delta m_j = [(M')^T r']_j / [(M')^T M' + \varepsilon^2 I]_{jj} \qquad (5.2)$$

where j and jj indicate the jth vector element and the jjth diagonal element of the corresponding vectors and matrix. The conjugate gradient method, in particular the algorithm LSQR (Paige & Saunders, 1982), is an effective alternative for reconstruction techniques. In this method, conjugated gradients introduced by Hestenes and Stiefel (1952) for resolving systems of squared equations are implemented. Both LSQR and the conjugate gradient method are analytically equivalent, but LSQR shows better numerical behaviour when the matrix is poorly determined. It has been used by different authors in different tomographic studies (Spakman, 1988,1991,...).

SIMULPS uses the approach where the damping value is added to the equations, whereas INVER3D uses the LSQR approach to carry out the iterative procedure.

5.2.4 Treatment of hypocenter-velocity structure coupling

In the previous paragraphs, the tomography only considered the three-dimensional velocity structure. In order to perform a local tomography, suitable earthquakes are required. These are earthquakes that are very well located in a 2D velocity structure. In some tomographic inversions, these hypocenters are kept fixed during the entire inversion. In other inversions, the hypocenter is coupled to the velocity structure and is thus re-determined with every iterative step.

The main reason why not all tomographies take into account the hypocenter velocity structure is the growth of the matrix representing equation (1.43). For a dataset and model of L stations, N earthquakes and M velocity parameters, a matrix of approximately (L x N) by (4N+M) is needed. Even for modest-sized problems this matrix becomes huge. There is however a set of equations that only depend on the velocity parameters but that do not discard the hypocenter–velocity coupling. Equation (1.43) can be written as:

$$r = H\Delta h + M\Delta m \tag{5.3}$$

where r is the residual vector; H and Δh are the matrix and vector of hypocenter parameter partial derivatives and perturbations and M and Δm are the matrix and vector of velocity parameter partial derivatives and perturbations. If the QR decomposition of H (Lawson and Hanson, 1974) is considered

$$QH = \begin{pmatrix} r_{11} & r_{12} & r_{13} & r_{14} \\ 0 & r_{22} & r_{23} & r_{24} \\ 0 & 0 & r_{33} & r_{34} \\ 0 & 0 & 0 & r_{44} \\ \vdots & \vdots & \vdots & \vdots \\ 0 & 0 & 0 & 0 \end{pmatrix} \tag{5.4}$$

the partition of Q below row 4, known as Q_0, can be used to form the equation

$$Q_0 r_i \equiv r_i' = Q_0 H\Delta h + Q_0 M\Delta m \equiv M'\Delta m \tag{5.5}$$

where the property $Q_0H=0$ is used. This leads to a smaller set of equations containing only the velocity model parameters as unknowns

$$r' = M'\,\Delta m \tag{5.6}$$

When the hypocenters of the earthquakes are kept fixed in an inversion, the inversion only gives reliable results where the geological structure is very simple. In regions with complex geology, the fact that the hypocenters stay fixed during the tomographic iteration leads to a bias in the results and therefore, results of these methods have to be treated with great care. The methods that use a hypocenter-velocity structure coupling are less biased.

The programme SIMULPS uses this hypocenter-velocity structure coupling to determine the velocity structure and re-determines the hypocenter location. The programme INVER3D does not have this option yet. So in this programme the hypocentres are kept fixed at all times, therefore it is very important to use only very well located earthquakes in INVER3D and its results have to be viewed with a cautious eye.

5.2.5 Solution quality assessment: checkerboard and "feature" test

After a local earthquake tomography, the resulting complex three-dimensional velocity model can only be interpreted meaningfully if the model's quality is known. Some ways to assess the model's quality are data variance, model resolution and model covariance. Data variance is the difference between the observed and predicted data. Model resolution measures the interdependence of the predicted model parameters. Covariance represents the mapping of the data errors onto the model parameter errors.

When calculating the solution to the problem Gm=d following the "standard" discrete inverse theory approach, an inverse G^{-1} is computed. From this matrix one can directly determine the matrices of model resolution R and covariance C_m when the data covariance matrix C_d is known in some (assumed) form (Menke,1989).

$$R=G^{-1}G \tag{5.7}$$

$$C_m=(G^{-1})^T C_d G^{-1} \tag{5.8}$$

R represents the "filter" through which the model estimate is derived from the "true" model, while C contains the estimated variance of individual parameters (diagonal elements) and the covariance between pairs of parameters (non-diagonal elements).

Misfit, model resolution and covariance are related to one another. It is well known that increasing the number of model parameters will diminish the misfit. On the other hand, a model with a finer scale will be able to represent structure at a higher spatial resolution, but the resolution of the individual model parameters will diminish when using the same dataset. The influence of the covariance depends on the way it is calculated, but it can be stated that improved resolution comes at the cost of increased model variance.

The spread function is an easier way to represent the model resolution for each parameter (node or cell). A spread function (Menke, 1989) is a single value, instead of a matrix, and determines the way the result of a node is smoothed over neighbouring nodes. High spread values mean that the result is smoothed over a lot of nodes, low spread values means that the result is restricted to the node itself.

Because it is not easy to calculate the resolution and covariance matrices due to the unavailability of a full matrix, it is easier to perform synthetic tests that reproduce isolated anomalies in the model. This provides a sense of model fuzziness at selected points. In a synthetic test, a synthetic dataset is

calculated in a velocity model with a predetermined anomaly. The stations and hypocentres of the real tomography are used as base for calculating the new ray distribution and new travel times. Afterwards, this synthetic dataset is used in a local earthquake tomography starting with an initial velocity model. In the end, the result of the velocity tomography is compared to the model the synthetic dataset was calculated from, to see in what way the original model was found. Two kinds of synthetic tests often used in local tomographies are the checkerboard test and the "feature" test (Figure 5.1).

In a checkerboard test, a checkerboard like anomaly (first node + 10% of the average velocity; second node -10% of the average velocity; third node + 10% of the average velocity; ...) is placed over the resulting model of the real tomography, followed by the method described above, and afterwards one compares how well the checkerboard is found by substracting the original result from the synthetic one (one should obtain the checkerboard pattern).

In a "feature" test, an anomaly or anomalies like the one(s) to be investigated, are placed in a velocity model. Then the method described above is followed and afterwards, the way this feature is resolved determines the solution quality.

The quality of the solution will be assessed in similar ways for both SIMULPS and INVER3D by performing several synthetic tests.

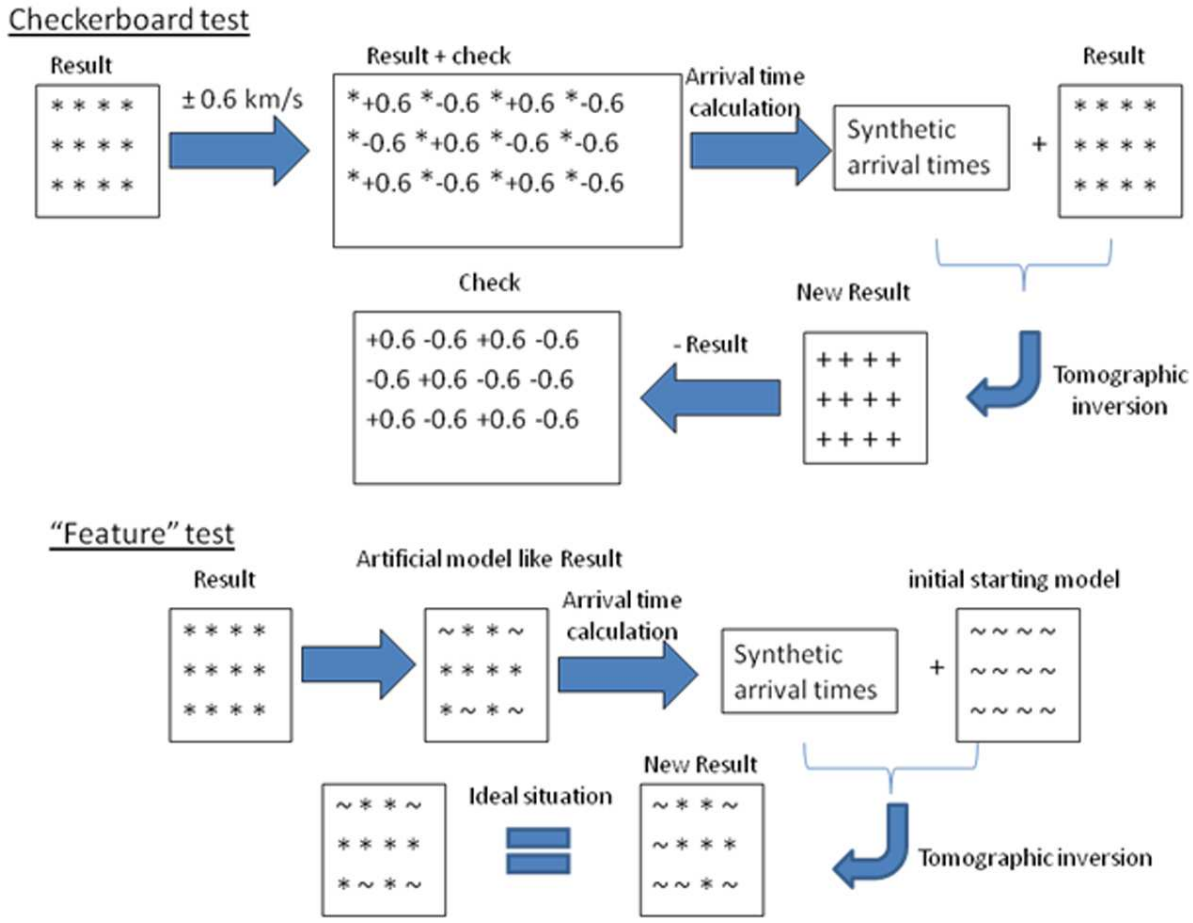

Figure 5.1: Schematic view on how a feature test and a checkerboard test is performed.
*** represents the value in the result of the tomographic inversion, + represent the values in the result of the checkerboard test and ~ represent the values from the initial model.**

5.2.6 The use of S-waves

A more complete characterization of the geological structure of the earth's crust and mantle can be obtained by knowledge about the combination of the P- and S-wave velocity structures. The use of S-waves also helps to further decouple the hypocenter-velocity problem, because more constraints are put on the earthquake source depth and location. The treatment of S-waves in a local earthquake tomography is similar to that of P-wave tomography. In principle it needs a separate but similar set of parameters modelling the S-wave velocity structure. In the ideal case, every P-wave arrival time measurement should be accompanied by an S-wave arrival time measurement with the same uncertainty. In this case both datasets should be of similar quality. In practice, this is not the case because the S-waves arrive during the arrival of the P-wave train. Therefore the S-waves are much more difficult to pick and almost always have a larger uncertainty. So the S-velocity models tend to have lower resolution and higher uncertainty than the P-velocity models, making it difficult to make a direct comparison between both models and to determine the spatial Vp/Vs-variations.

It is also possible to carry out a direct tomographic study of the three dimensional variations of the Vp/Vs-ratio. Because Vp/Vs is usually better known and varies less than Vs, a better constrained three dimensional S-velocity model can be deduced from an inversion of the Vp/Vs-ratio with a three dimensional Vp-model.

Derivation of Vp/Vs from S-wave arrival times minus P-wave arrival times as data is equivalent to the treatment of P-wave arrival times as described in Chapter 1 paragraph 1.5.4, except for the forward problem stated in equation (1.40), which is now expressed as:

$$t_{ij}^{S-P} = \int_{path} \left[\frac{1}{v_s} - \frac{1}{v_p}\right] ds = \int_{path} \left[\frac{v_p}{v_s} - 1\right] \frac{1}{v_p} ds \qquad (5.9)$$

S-P time residuals can be calculated based on the P-wave velocities and an initial Vp/Vs-model. They can be related to Vp/Vs-model perturbations just as for the P-wave.

The programme SIMULPS is able to calculate the variation of the Vp/Vs-ratio at the same time of the variation of Vp. For the programme INVER3D, this is not yet possible.

5.3 Comparing INVER3D with SIMULPS

In this paragraph, the results of a similar inversion performed by the programme INVER3D and SIMULPS will be compared to one another. As mentioned in the previous paragraph 2, there are several differences between the programme INVER3D and SIMULPS (Table 5-1).

Parameter	INVER3D	SIMULPS
Velocity structure representation	Tetrahedron approach	3D grid of nodes
Travel time and ray path calculation	Shooting method	Bending method
Method of inversion	LSQR approach	Damping value added to equations
Hypocenter-velocity structure coupling	No coupling	Coupling
Solution Qualtity assessment	Feature tests	Checkerboard and Feature tests
The use of S-waves	Not possible	Possible

Table 5-1 : Summary of the differences between INVER3D and SIMULPS.

INVER3D uses five input files (see appendix 6): *sou.dat* (coordinates of the earthquakes to a predetermined origin point), *rec.dat* (coordinates of the stations to the same origin point), *tobs.dat* (the arrival time observations for the different couples earthquake-station), *para.dat* (containing several parameters f.i. the number of stations, number of earthquakes, number of observations, the dimension of the model and whether only the ray trajectories, the arrival times or the full inversion have to be accomplished, …) and *velocity.dat* (gives the velocity model for the different blocks).

When the programme is launched, the arrival times are calculated in the velocity model. When these calculated arrival times are mostly lower or higher than the observed arrival times, the entire model is re-evaluated by adding a certain correction factor before the actual iterative procedure is started. When the programme finishes an iterative step, the velocity model is saved as well as an *output* file. This gives the different calculated arrival times for the different iterative steps. In the *verify.doc* file, all the problematic earthquake-station couples are stored (f.i. the shadow zones, etc.) (for more information on the output files see Appendix 7).

The SIMULPS programme uses several input files (see appendix 8): *EQKS, BLAS* and *SHOT* files containing the arrival times and locations of the earthquakes, blasts and shots respectively; the *STNS* file containing the coordinates of the stations; the *MOD* file containing the velocity model and the *CNTL* file containing several parameters needed for the inversion, like the damping factor. The programme constructs several files as output (see appendix 9). The *velomod.out* file gives the resulting velocity model that can be re-used as input file, the *results.for_plot* file gives the same result but in a format so that it can be used in plots. In the ”output” file, different steps of the inversion are written. The *fort.47* file gives the DWS (derivative weight sum) values whereas the *resol.out* file gives the resolution matrix for every grid point.

5.3.1 Adapting the programme INVER3D to the present studies requirements

In the past, the programme INVER3D has only been used to calculate the velocity variations along several 2D-profiles (Collin, 1998) that where only a few km in length and a few meters in depth. In this study, the programme was used in a three-dimensional setting of several tens of km in width and several km in depth. It soon became obvious that several problems had to be solved before the programme could be used in such a larger setting. To be sure that some problems were not caused by the small amount of data in the Belgian dataset, the tomography was first performed on a Chilean dataset with more than 12,000 P-wave measurements, that has been used before in an attenuation tomography study (Sichien, 2002).

5.3.1.1Problems with the tomographic inversion component

First the programme had to run on one of the servers. No problems in calculation have been encountered with this dataset, except that if the original grid size of 20 km by 20 km in length and 10 km in depth is used, the programme takes two weeks to calculate 2 iterative steps and is far from finished at that point. Because it is very difficult and time consuming to rewrite the programme so that it calculates faster, it was decided to do the test with a higher grid cell size namely 40x40 km in the x- and y-direction and 10 km in depth. After this test, the results were compared with the result of the SIMULPS programme (see paragraph 5.3.3). In the future, this part of the programme should be rewritten, so that it calculates faster and finer grid sizes can be used.

5.3.1.2Problems with the arrival time calculation component

When the programme ran with the Belgian dataset, several arrival times could not be calculated although the input velocity model was a simple layered model with increasing velocity with depth. Even when the input model was taken as one cell with a small vertical velocity gradient, not all the arrival times could be calculated. This problem was due to several bugs (or conditions that work for small-scale nearby problems but not for large-scale problems) in the programme.

5.3.1.2.1 Shadow zone problem

To diminish the time for calculating the ray paths in the original programme, a condition to abort calculation when a shadow zone was encountered has been added. Although it was a good idea, the condition in the original programme was not determined correctly (it worked for small-scaled cases, but not for large-scaled cases), so that some arrival times were left out of the iteration although they were not positioned in a shadow zone. In the abort condition, the ratio of the previous and last receiver location error had to be lower than a maximum value. If this was not the case, the programme stopped calculating for that couple earthquake-station. The original value was so low, it

worked for short distances and thus small errors, but not for the larger errors encountered in large-scale problems. Moreover, the condition did not verify if the suspected shadow zone was real. This can be done by calculating the rays for all the angles in between the last correct angle and the one determining the shadow zone. In the end, the condition was altered so that it works for large-scale cases and only filters out real shadow zones.

5.3.1.2.2 The ray-tetrahedron intersection problem

For some rays no solution was found and a "min3=0" comment occurred on the screen and in the verify.doc file. This comment means that the real solutions of a quadratic equation were not found, when calculating the intersection of the ray and the tetrahedron. Because in a simple velocity model, the ray follows a simple arc, this equation had real solutions. It took a thorough study of the programme code to find the problem. When the results of different iterative steps (with and without the "min3=0" condition) were plotted in a three-dimensional graph, it became obvious that they did not intersect the tetrahedrons in the same places (Figure 5.2). For the problematic iterative steps, the intersection was positioned well outside of the tetrahedron. The quadratic equation that calculates the intersection was wrongly resolved. The programme first determined whether the quadratic equation was in fact a linear equation. This is the case when the factor at the quadratic term is zero or very low in comparison to the other terms. If this condition was not fulfilled, it computed the results for the quadratic equation. In fact the first condition, that determined whether the equation was linear or not, was not correct. It forced the equation to be linear even when it was not. After changing this condition, the problem was solved, and it still worked for the small-scale cases.

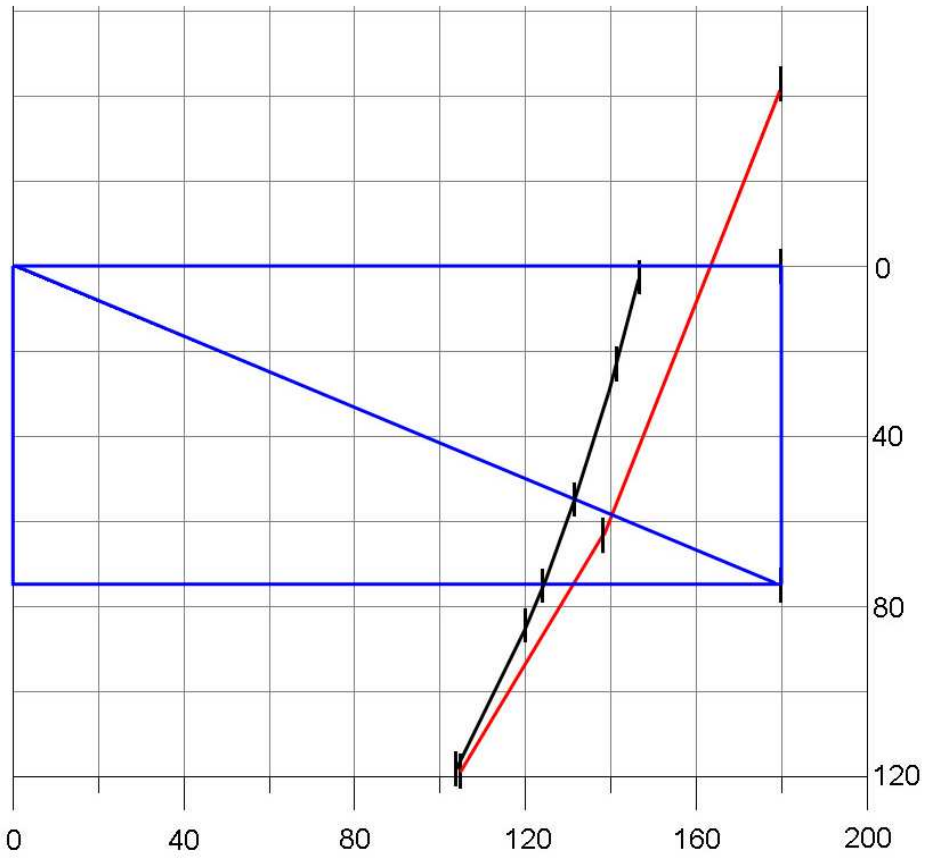

Figure 5.2: Ray paths calculated for one couple earthquake-station for two iterative steps in the zy-plane. The black line represents a ray path arriving at the surface. The red line represents a ray path giving rise to the min3=0 comment. The blue lines represent the intersections of the tetrahedrons with the zy plane.

5.3.1.2.3 The correction determination problem

Some ray paths could not be calculated because the correction added to the first incident angle after each iterative step never arrived at the other side of the receiver or suddenly appeared at the wrong side of the source (Figure 5.3). Therefore, the complicated calculation to determine this angle was erased and replaced by a simple correction of the angle by 10 degrees every step, until the bisection calculation could be used.

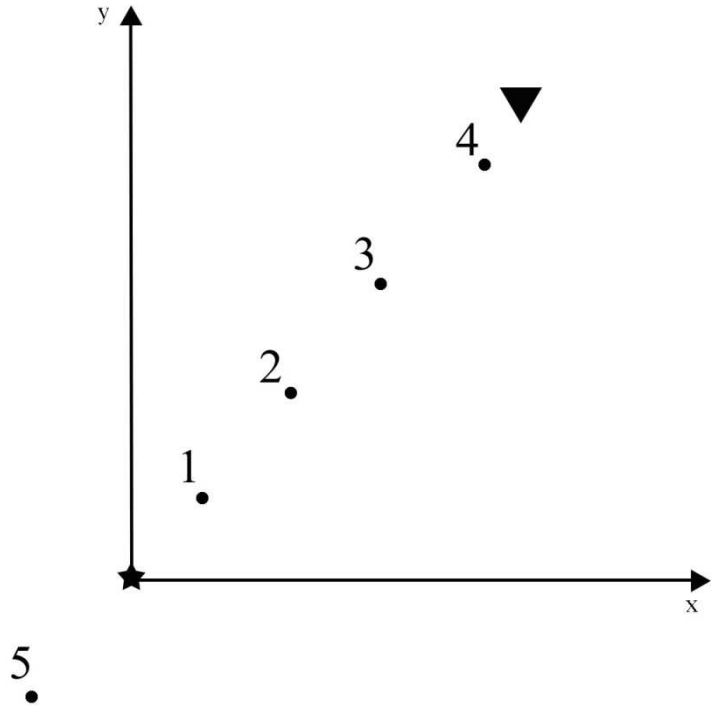

Figure 5.3: Representation at the surface of the endpoints of the ray tracing for different iterative steps. The source is represented by the black star whereas the receiver that needs to be reached is represented by the black triangle. The iterative procedure of ray tracing often stopped at step 4 or continued to step 5.

5.3.1.2.4 The problem of rays hitting the edges of the model

The programme also aborted the ray path calculation when one of the rays hits the edges of the model before it reaches the receiver. This problem was easily overcome by adding an extra condition so that when this happens, instead of aborting the ray tracing component, the programmes uses the bisection part of the ray tracing component.

5.3.1.2.5 The bottom layer problem

For the Belgian and Chilean data it soon occurred that for some ray paths, the source-receiver distance became so large that the measured wave might be a refracted wave, that enters lower layers not included in the velocity model of the inversion. In the SIMULPS programme this problem is resolved by

adding very large cells at the edges of the model. This is not possible in the programme INVER3D because, the cells have to be of the same size. When adding more grid cells at the edges, making sure that the ray stays in the model, the amount of cells in the iteration is increased and therefore the calculation time increases and the solution quality lowers. After carefully examining the problem, a layer at the bottom of the grid with a very high velocity gradient was added, so that ray paths that pass through this layer are forced back up very fast and therefore resemble the ray trajectory of reflected or head waves as much as possible.

It is obvious that sometimes, when a condition resolving any of the above mentioned problems worked for one of the datasets, it generated problems in other datasets. In the end, the conditions solving the problems where fine-tuned enough to work for all the datasets, and the ray paths and arrival time along these paths could be calculated for all types of simple velocity models.

5.3.2 Testing the tomographic inversion component of INVER3D

Before the local tomography with the Chilean data was performed with the programme INVER3D and its result compared to that of SIMULPS, several tests were carried out with the programme INVER3D. For these tests, the anomalies were calculated in the same velocity model that is used to perform the local tomography and with the same dataset (same earthquakes and same stations).

5.3.2.1Test 1: Columnar anomaly

In this test, a column of higher velocities (+ 0.6 km/s) was added in the middle of the region over all the depths. On the depth slices in Figure 5.4, it can be seen that around the anomaly, no abnormal perturbations can be observed, due to an extensive smearing of the result. Most differences in the surrounding layers are lower than 0.10 km/s. The anomaly itself is very well resolved in the upper 80 km (difference between the result and the original model is max 0.5 km/s for the top layer, 0.12 km/s for the following layers, the average difference for the anomaly from 0 to 80 km of depth is 0.08 km/s). At greater depths, the anomaly is less well resolved. This is not caused by the programme, but is due to the data distribution. Not many rays cross the model at greater depths. Nevertheless, the programme seems to solve this simple model very well in the zones with an adapted ray density.

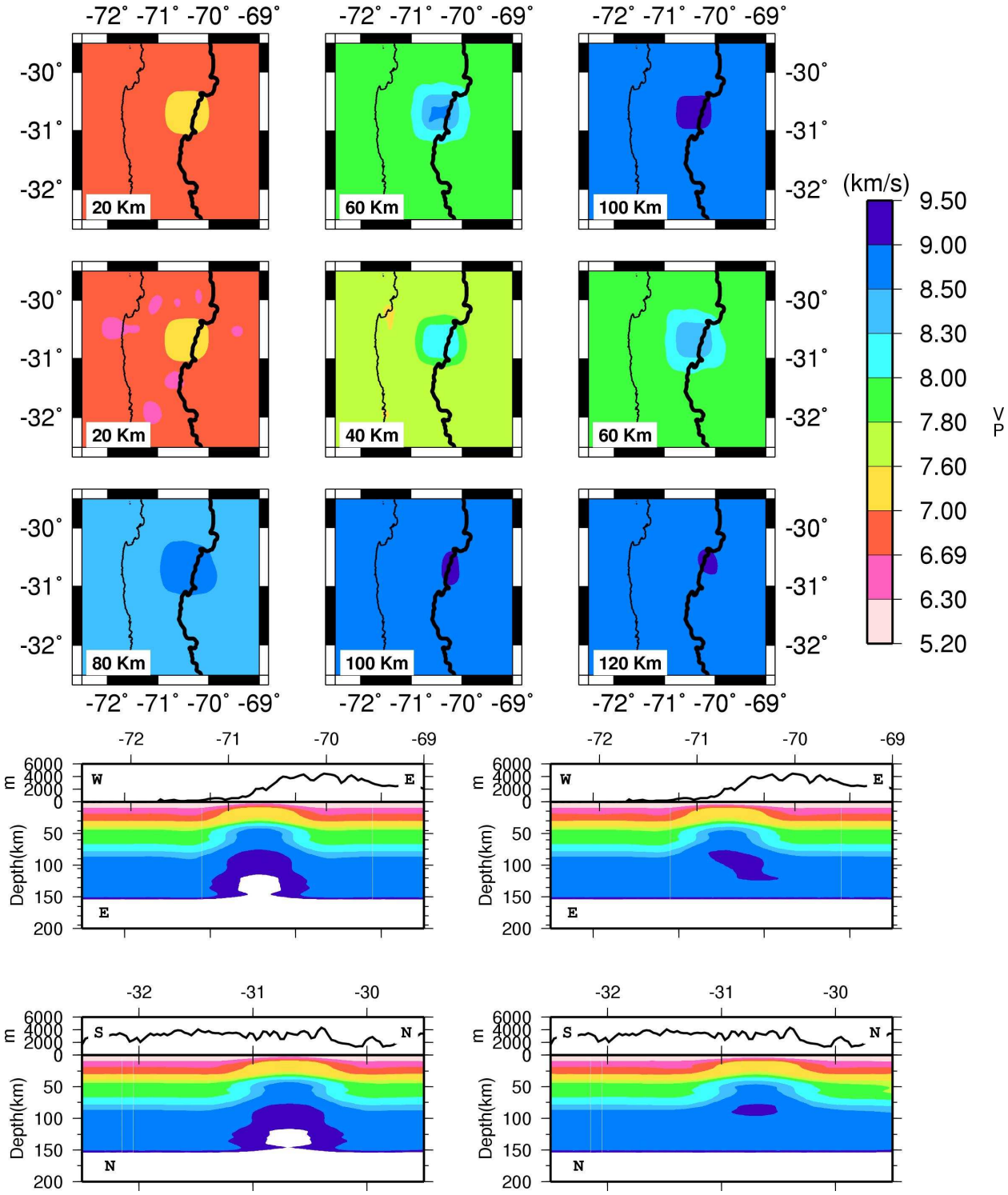

Figure 5.4: The Initial model used in the spike test with the columnar anomaly and the results. The top three depth slices represent the initial model, the following 6 depth slices, the results of the test. The black lines represent the coastline and the political border between Chile and Argentina. The bottom left two profiles (at 30.7° S and 70.5 ° W) represent the initial model, whereas the two profiles on the right represent the result. The black line on top represents the topography along the profile.

5.3.2.2Test 2: "Checkerboard" anomaly

First, this test was performed with a normal checkerboard test including all the nodes, but INVER3D was not capable to calculate all synthetic arrival times. So the test was repeated with, a checkerboard pattern added to the middle 2 columns in the x-direction of the model. This means that a higher velocity was applied in alternation for the different depths. So for 0 km, the velocity was kept, for the following depth (10 km), the velocity was risen by about 10%, then the velocity was kept to its original value again (20 km), to be risen by 10% for the following depth (30 km), etc... This was only done for the even slices in the y-direction. This model was not resolved at all, as can be seen in Figure 5.5 . The reason why this model was not resolved is that a lot of rays could not be traced to their receiving stations. Apparently, the problems with the ray tracing component of the programme are not completely solved yet. Due to the time limit of this study, the ray tracing component was not further adapted. Instead a third synthetic test was performed.

5.3.2.3Test 3: Result of SIMULPS

In this third test, synthetic arrival times were calculated with the resulting model of the programme SIMULPS. Figure 5.6 shows that the model is quite well resolved. The maximum difference between the result and the original velocity model is 0.3 km/s. In most nodes, the velocity difference is even less than 0.1 km/s which is normal for such a test. In case the difference between the result and the original model is significant, the velocity anomaly is however in the same direction (this means that in both cases the velocity is higher or lower than the starting model). Therefore, it was decided that the real data should normally also be resolved.

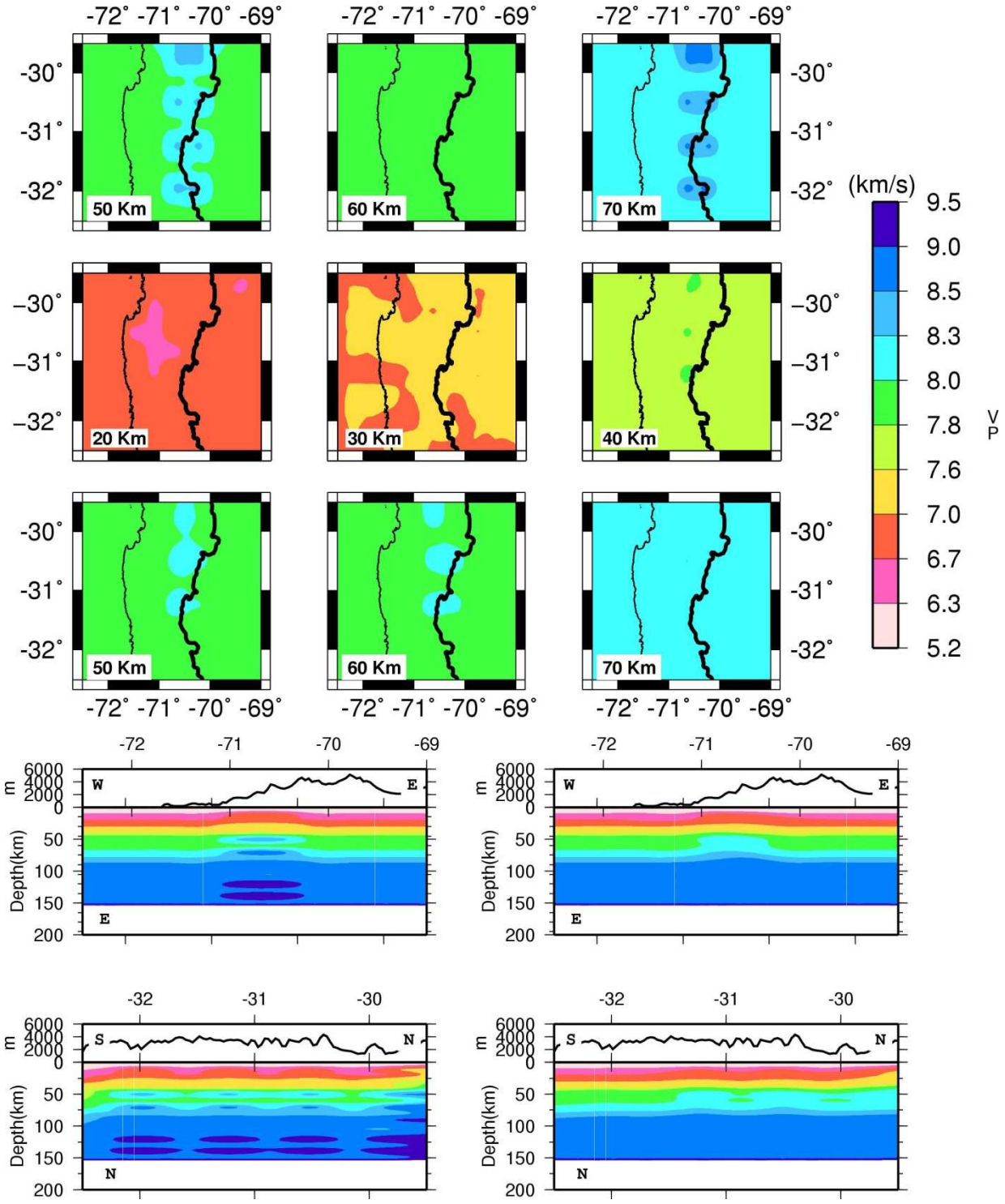

Figure 5.5: The Initial model used in the spike test with the checkerboard anomaly and the results. The top three depth slices represent the initial model, the following 6 depth slices, the results of the test. black lines represent the coastline and the political border between Chile and Argentina. The bottom left two profiles (at 30.5° S and 70.5 ° W) represent the initial model, whereas the two profiles on the right represent the result. The black line on top represents the topography along the profile.

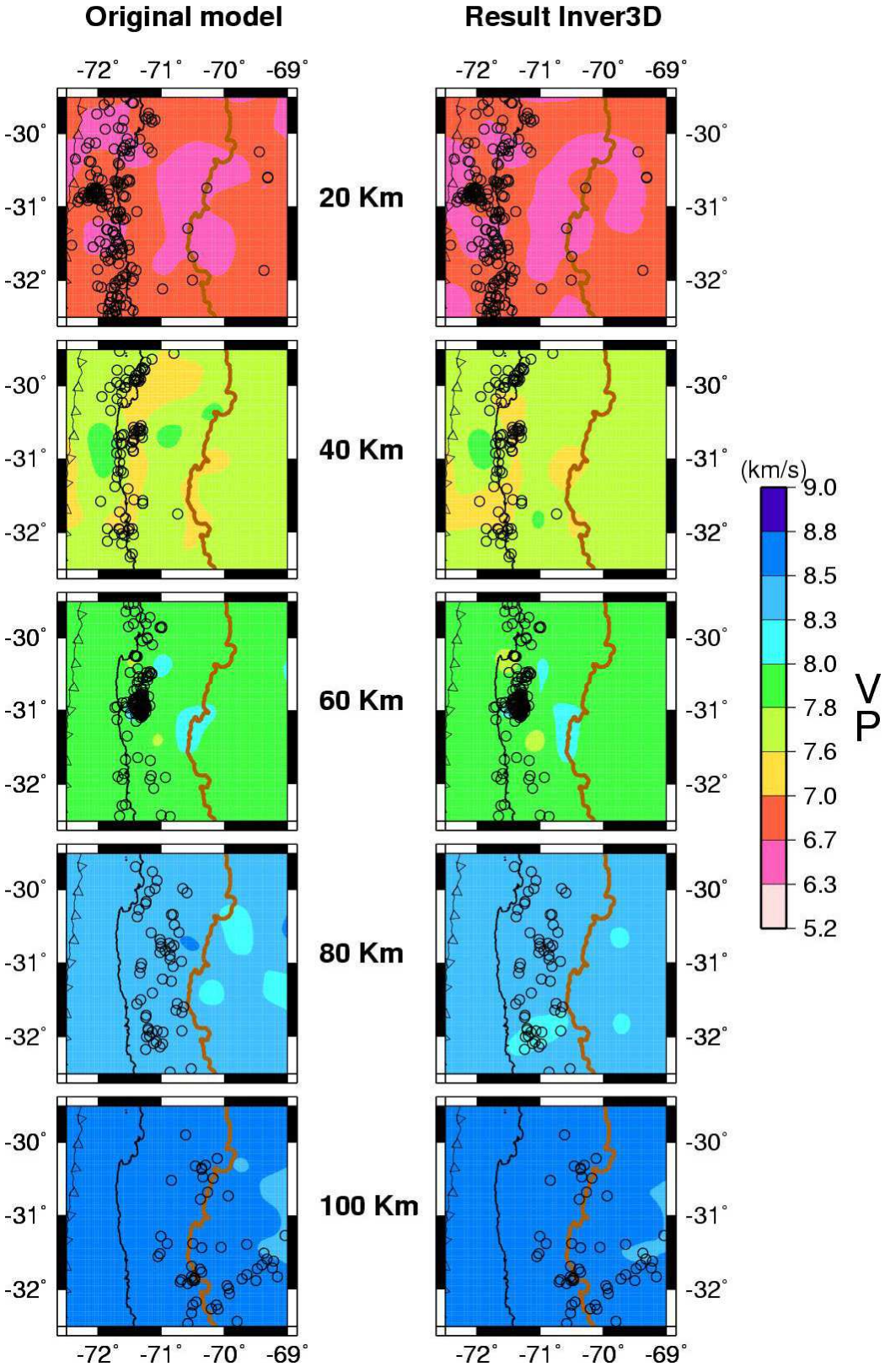

Figure 5.6: The results of the spike test where the result of the SIMULPS programme is used as initial model (shown on the left) and the result of the INVER3D programme (shown on the right).

The black line represents the coastline, the brown line the political border between Chile and Argentina. The subduction zone is also represented. The black circles indicate the seismicity registered by the network.

5.3.3 Results of INVER3D and comparison with SIMULPS

In this paragraph, the results of the programme INVER3D are compared with the results of the SIMULPS programme. First the data used for these inversions in Chile will be discussed as well as the result of the SIMULPS programme.

5.3.3.1Data and station setting in Chile

To gain further insight into the subduction of aseismic ridges and to study the aftershocks of the Punitaqui mainshock, a temporary seismological network was installed in central Chile between 30°S and 32°S (Figure 5.7), in the framework of the French-Chilean project OVA99. Local earthquakes of magnitudes between 1 and 5 were recorded over a two month period (mid-November 1999 to mid-January 2000) by thirty-two stations equiped with three-component, short-period sensors of 2 Hz and 4.5 Hz. Each station recorded in a continuous mode, at a sampling rate of 125 samples/sec. The stations were approximately 30 km apart (Figure 5.7).

Of all the registered events, only 1041 of the best-located earthquakes were selected for this tomography, representing 13,295 P-phase and 13,476 S-phase time readings. The distribution of these earthquakes is shown in Figure 5.7. Two groups of earthquakes can be distinguished: a first group with lowest magnitude is situated along the coastline between the trench and the deepest part of the seismic zone (~50 km in depth) or to the coupling between the two plates. Because the angle of subduction is more important in between 60 to 100 km of depth a lower number of earthquakes take place between these depths. The second group is located at a depth of approximately 100 km along the horizontal part of the subducting plate.

5.3.3.2Result of the SIMULPS programme

In the study of Pardo *et al.* (2002) the tomography was performed with the SIMULPS programme which used a velocity node spacing of 20 km along the north-south direction and 10 km at depth. In the east-west direction, the distance between nodes was a function of the ray coverage, and ranges from 15 km over 20 to 40 km (Figure 5.7). Pardo *et al.* (2002) used an extrapolation of the best one-dimensional layered velocity model determined with the VELEST software (Kissling *et al.*, 1994) as the initial three-dimensional Vp-velocity model.

Because for the programme INVER3D, it is not possible to calculate a velocity model with varying grid cell sizes in one direction, the local seismic tomography has been repeated with the programme SIMULPS, using the same grid cell distribution as for the INVER3D programme (Figure 5.9). Therefore, the different parameters needed in the SIMULPS programme had to be re-evaluated and a checkerboard test (Figure 5.8) to evaluate the way the new node spacing is capable of resolving the velocity structure had to be applied again.

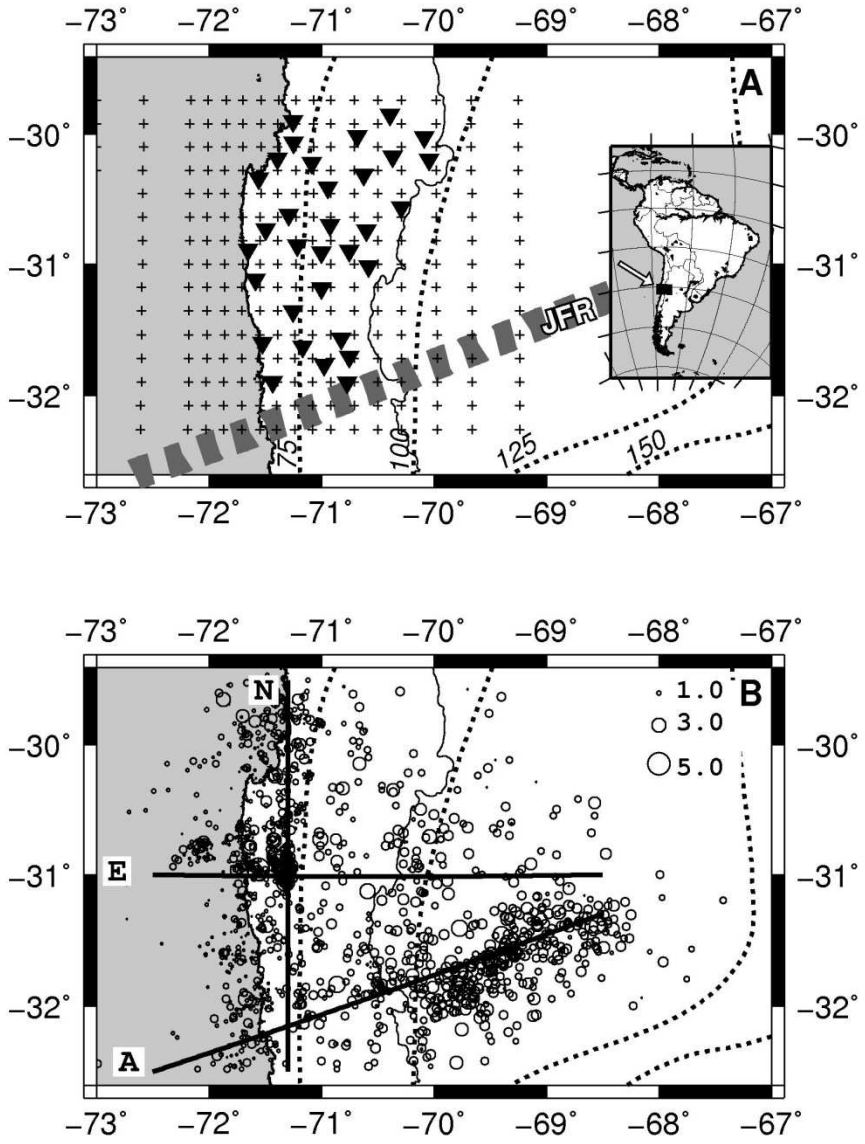

Figure 5.7: Maps showing the position of the temporary stations used in the OVA99 project in Chile and the locations of the earthquakes used in the local tomography.
(A) The temporary seismic network OVA99 with its 32 stations (reversed triangles) and grid nodes used in the attenuation tomography (crosses). The aligned grey blocks represent the subducted part of the Juan Fernandez ridge (JFR). (B) The local earthquakes (open circles) detected by the OVA99 network. The size of the circles is proportional to their magnitude. The contours of Cahill and Isacks (1992) in dashed lines represent the depth of the subduction zone at 75, 100, 125 and 150 km depth.

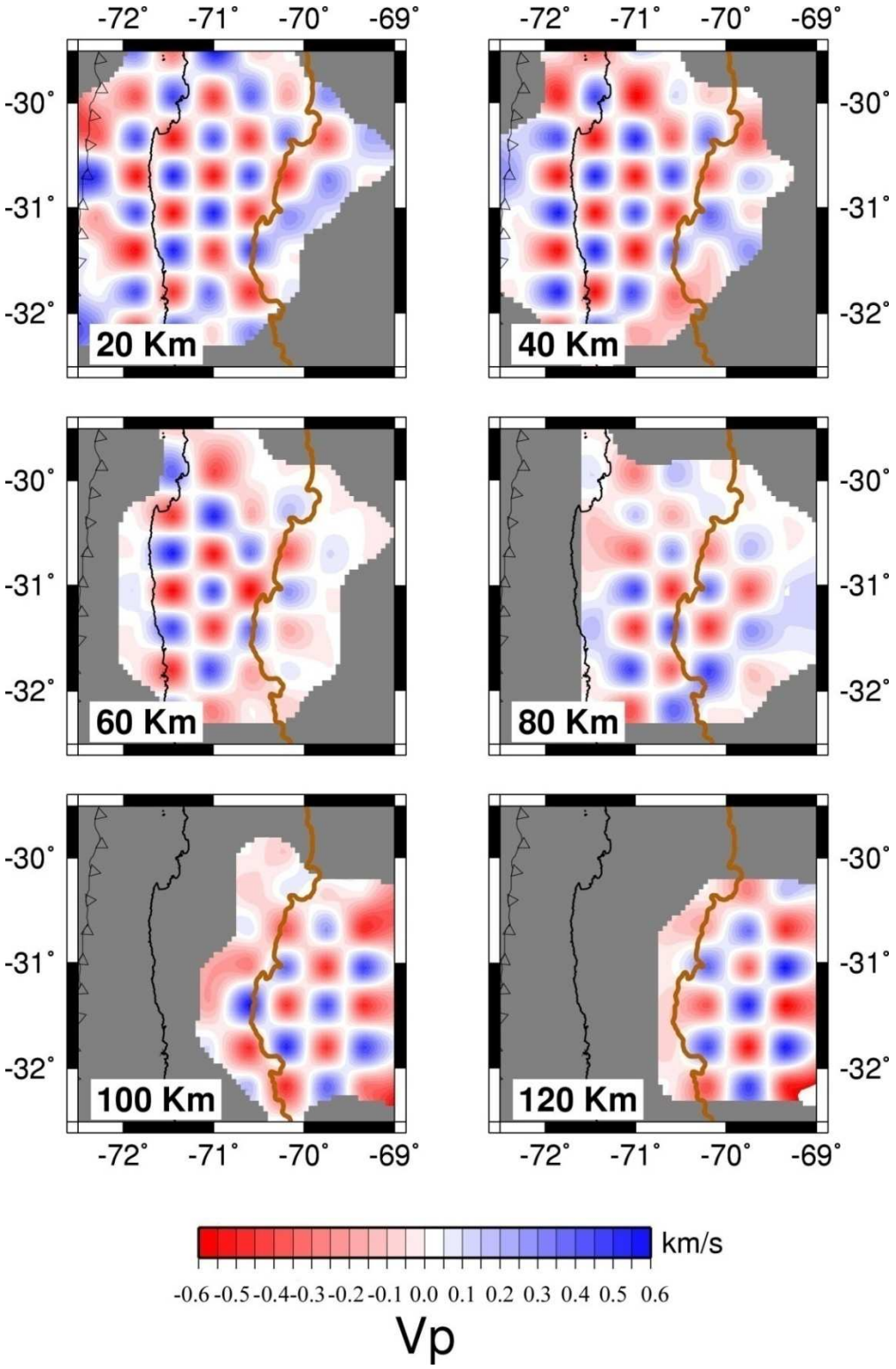

Figure 5.8: Checkerboard test result of the tomographic inversion with SIMULPS using the node spacing of the INVER3D programme.
The The black line represents the coastline, the brown line the political border between Chile and Argentina. The subduction zone is also represented.

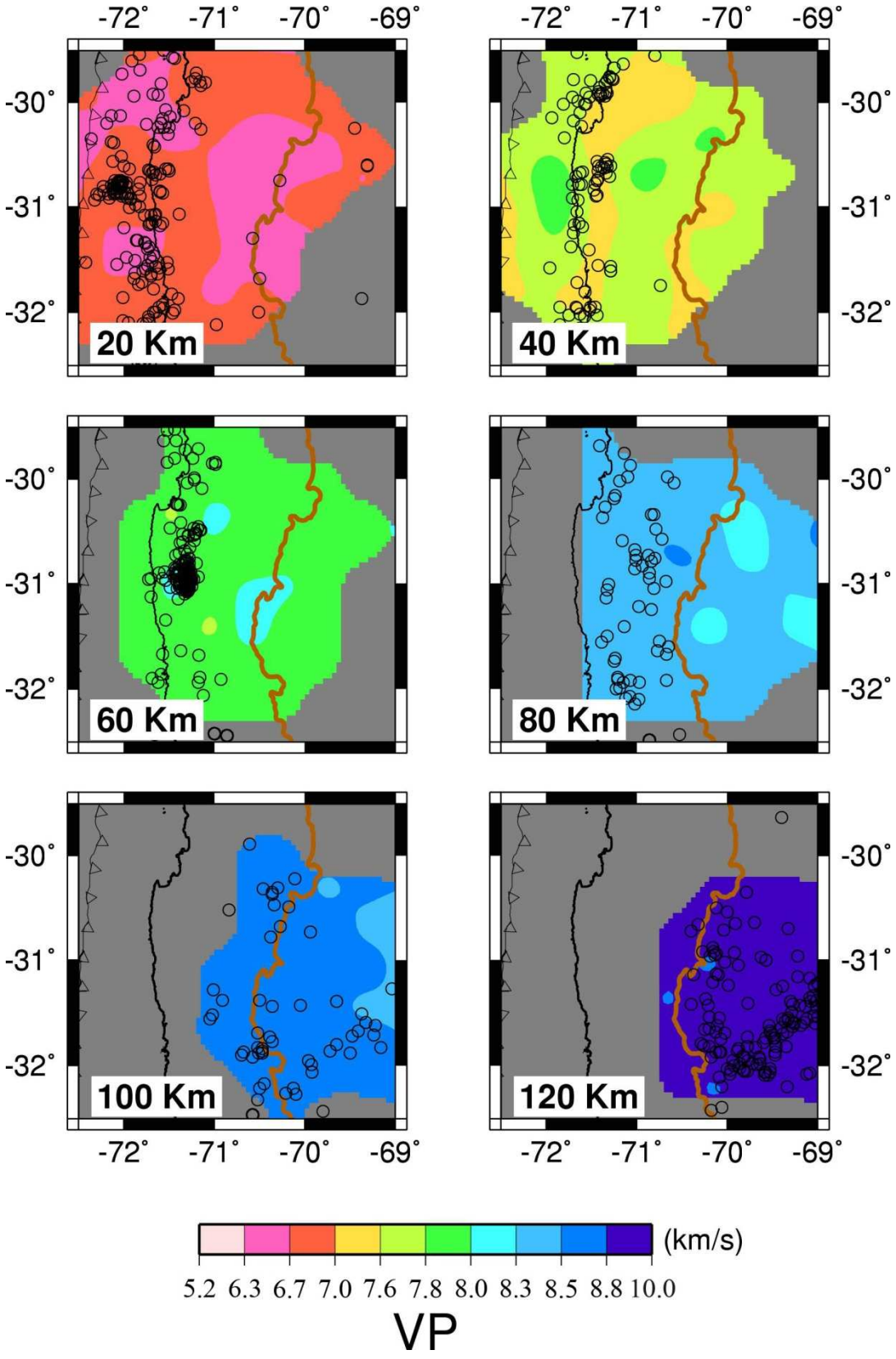

Figure 5.9: Result of the tomographic inversion with SIMULPS using the node spacing of the INVER3D programme. The black line represents the coastline, the brown line the political border between Chile and Argentina. The subduction zone is also represented. The black circles indicate the seismicity registered by the network.

5.3.3.3Results of INVER3D in comparison to that of the SIMULPS programme.

In a first step, the same dataset and velocity model as the programme SIMULPS was used with the original INVER3D programme, where the option to recalculate the entire model at the beginning of the inversion is not excluded. In this case, the result was not very realistic as mantle velocities were already attained at 20-30 km of depth (Figure 5.10). Because this tomography models the crustal and upper mantle structure underneath the Andes, a crustal root is expected with crustal velocities to depths of 40-60 km. The fact that lower-mantle/core boundary velocities are already attained at 160 km of depth is not very realistic either. To further investigate the result of the INVER3D programme, the option of removing errors by averaging over the entire model was excluded at first. The option where the velocity is averaged is useful for small-scale tomographies; it does not seem to be applicable to large scale model.

In the second step, the same dataset and velocity model as for the programme SIMULPS was used with the programme INVER3D without the option to average the velocity model. In this case, the result appeared to be more realistic attaining mantle velocities at 50-60 km of depth. When the INVER3D result is compared to the SIMULPS result, however it is completely different (Figure 5.11 and Figure 5.9). It is not even possible to see similar tendencies. This huge difference is most certainly caused by the fact that in the SIMULPS programme the hypocenters are relocated with every iterative step whereas in the INVER3D inversion, they stay fixed (as was already mentioned in paragraph 5.2.4). So, to test whether this is truly the case, the inversion was repeated with INVER3D, this time using the final earthquake locations from the SIMULPS programme as dataset.

The result of this third iteration is composed of realistic velocities for the first 40-50 km depth, then velocities seem to skyrocket to velocities over 9 km/s in the upper mantle. It is clear that the result does not correspond to the SIMULPS result at all. The main reason for the discrepancy between the SIMULPS and INVER3D result is probably the fact that when in INVER3D the ray tracing component is not capable of reaching the receiver, that ray is discarded from the iteration. This means that in the INVER3D inversion, a different dataset is used for the first and the final iteration. In a final test, the inversion with the SIMULPS programme is repeated, using the dataset from the final iteration of the INVER3D programme as input file.

In a last test, the same dataset as is used in the last iteration with the INVER3D programme is used to perform the tomographic inversion with the SIMULPS programme. The result of this inversion does not correspond to the result of the INVER3D programme at all. The result does show realistic values, but it corresponds more to the result of the SIMULPS programme with the original dataset than to the INVER3D results with the same dataset.

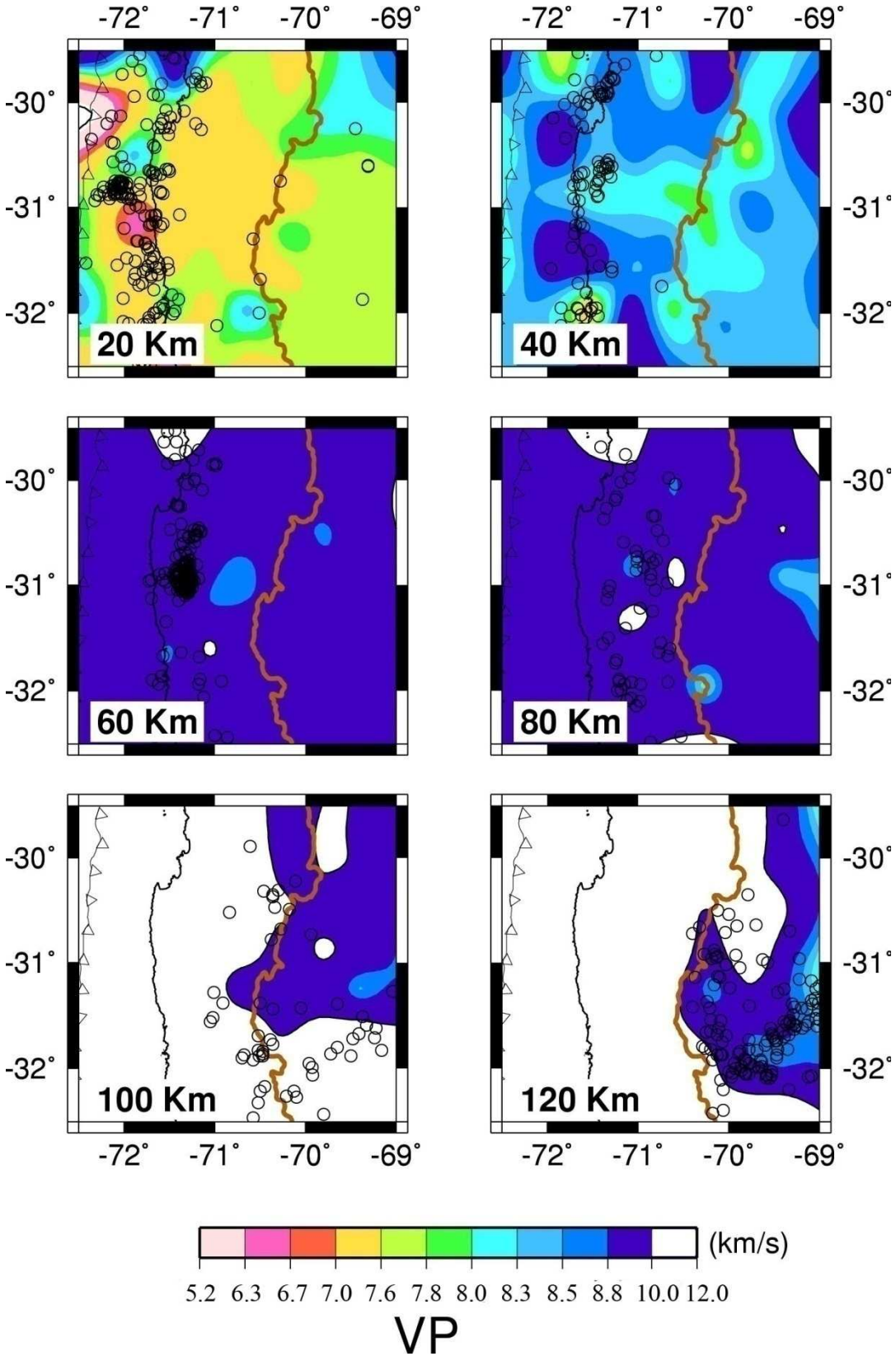

Figure 5.10: Result of the tomographic inversion by INVER3D including the option that the travel time errors are removed by averaging.
The black line represents the coastline, the brown line the political border between Chile and Argentina. The subduction zone is also represented. The black circles indicate the seismicity registered by the network.

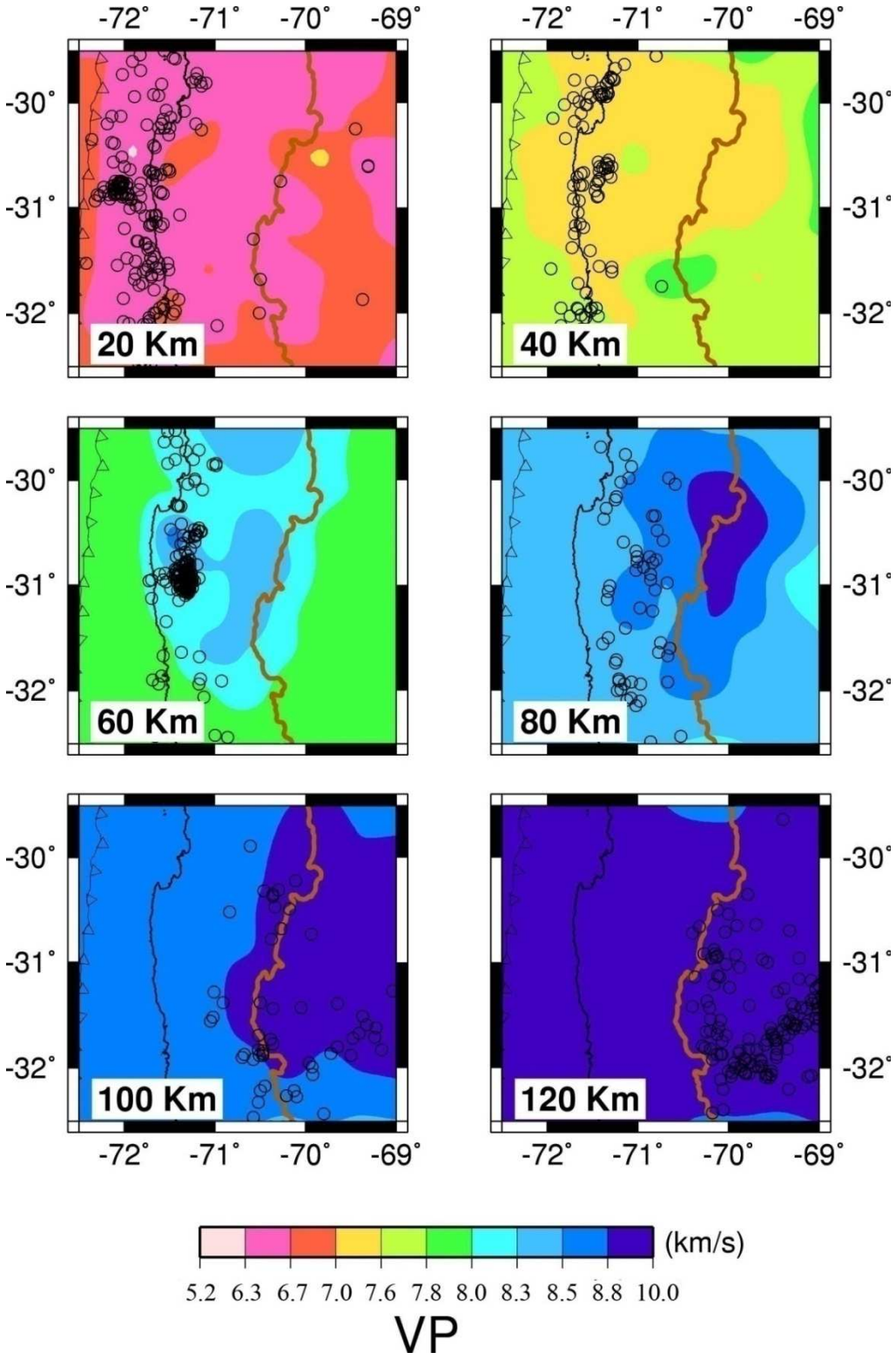

Figure 5.11: Result of the tomographic inversion by INVER3D excluding the option that the travel time errors are averaged. The black line represents the coastline, the brown line the political border between Chile and Argentina. The subduction zone is also represented. The black circles indicate the seismicity registered by the network.

5.3.4 Conclusions

The synthetic tests performed with the programme INVER3D show that the programme is capable of performing a 3D tomography and it is able to get good results. However, some problems still have to be solved. In a first stage, the ray tracing component of the programme should be tested carefully in a number of more complicated models, so that rays are only excluded when they really are positioned in a shadow zone. Secondly, some parts of the programme should be re-programmed so that certain calculations might be performed in parallel, to reduce calculation time and allow the use of smaller grid node spacings.

The results of the SIMULPS and the INVER3D programmes do not correspond at all at this stage. This might be due to deficiencies in ray tracing in the INVER3D programme, but it is also possible (as in tomography there are several solutions) that the programme and thus the approach used influence the final result of the inversion. To confirm this, the tomographic inversion should be repeated with a third programme for the Chilean dataset, and its result should be compared to the results of the INVER3D and the SIMULPS programme.

In the future, it might also be useful to add a hypocentre-inversion coupling in the programme, because, as was mentioned in paragraph 5.2.4 resulting models should be more correct. Until now, it is only possible to calculate the P- and S-wave velocity structures separately with the programme INVER3D. As was discussed in paragraph 5.2.6, one gets a better result when the inversion for the S-waves can be done simultaneously with the P-wave velocity inversion, using the Vp-model as a base for the Vs-model. So, it might also be useful to add a simultaneous inversion option for both Vp- and Vp/Vs-models.

Overall, the INVER3D programme has the potential to be a good inversion programme for local seismic tomographies, but some big changes still have to be done.

5.4 Local tomography with Belgian Data

In view of the limits of INVER3D, brought to light in the comparison with the SIMULPS programme with the Chilean dataset performed in paragraph 5.3, only SIMULPS was used to perform the tomography for the Belgian dataset. The approach and results will be discussed here.

5.4.1 Data and starting model

As original dataset for the local tomography, the very well located earthquakes, explosions and mine-induced events from chapter 3 were used (For their parameters see table 3-4; 3-5;3-6). Because it is very important to have a homogeneous distribution of the rays, it soon became obvious that the mine-induced events and the North Sea explosions should be withdrawn from the dataset. Not only these events but some stations like Zevekote, WIT0, see Figure 5.12 and some earthquakes like 19940722 at 05:09 are also withdrawn from the date set for similar reasons. In the end, 178 earthquakes were kept

for the local earthquake tomography, resulting in more than 2100 P- and 1500 S-wave arrival times and a fairly homogeneous ray distribution as can be seen in Figure 5.12.

As it is shown in chapter 3 that the 1-D crustal model CAL (table 3-1) represents well the average crustal structure for this part of Europe. it was used as the starting velocity model for the 3-D tomography. The results of the Moho depth determination of the previous chapter would have been taken into account in the initial velocity model of the seismic tomography, but because these results indicate a rather flat Moho and because the node spacing in depth in the tomography will be greater than the maximum difference between the Moho depths, they are not added to the initial velocity model. The initial three-dimensional Vp/Vs-ratio model is a homogeneous medium of constant value of 1.74. This is the average Vp/Vs-ratio found in the Wadati plots of the earthquakes of the dataset.

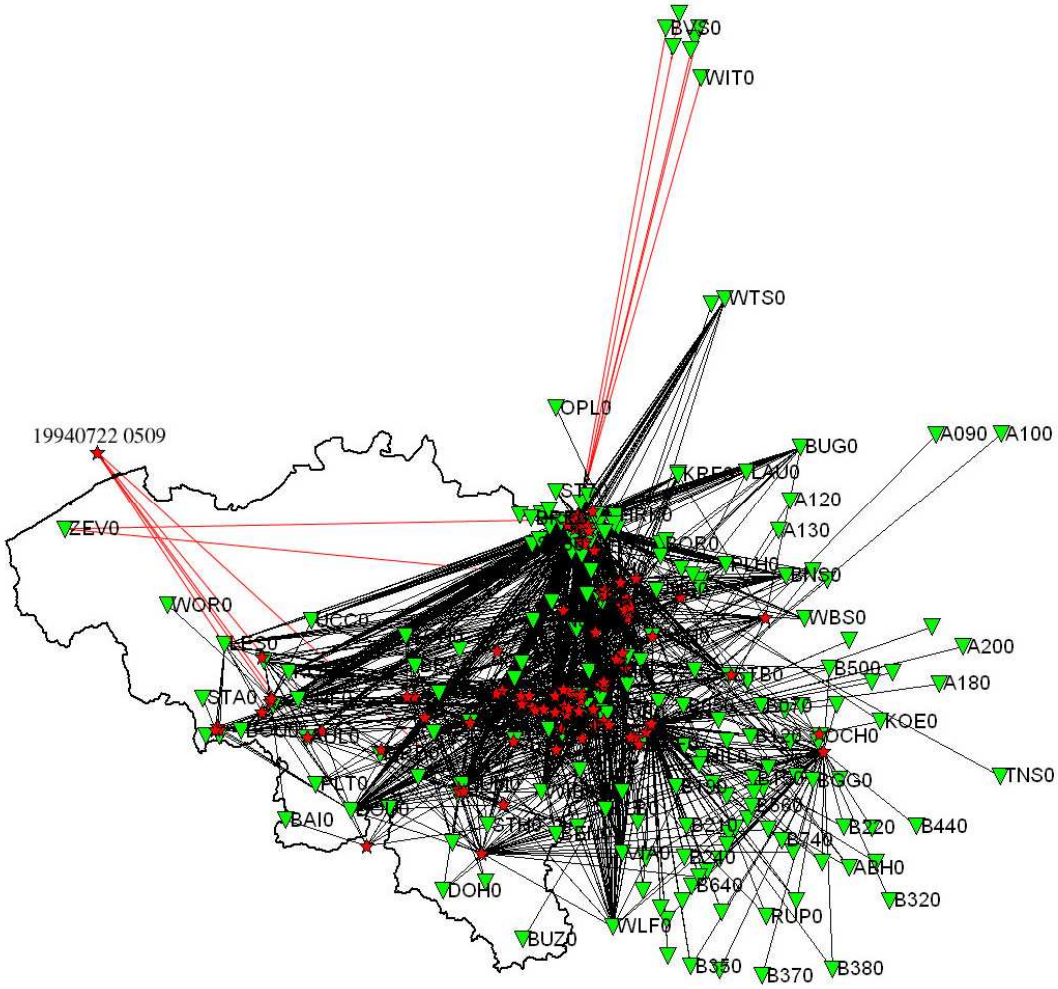

Figure 5.12: Rays used for the tomography.
The stations ZEV, A090, A100, WIT0 (and surrounding stations) and the earthquake 19940722 at 05:09 were not used in the tomographic inversion.

5.4.2 Resolution

5.4.2.1Grid size

As mentioned in paragraph 5.2, it is important to determine a correct grid size, which depends on the ray density and distribution and on the geological structure to investigate. A fine grid allows investigating fine geological structures, at the same time it limits the number of rays that determine the velocity in a node and as such limits the solution quality. A coarser grid will only allow investigating coarser structures, but the solution quality will be better. To determine the optimum grid size for the Belgian dataset, checkerboard tests (with perturbations of ± 10 %) were performed for different grid sizes and finally the grid resolving the checkerboard test best for the finest grid, was selected. In Figure 5.15 to Figure 5.15, all the checkerboard tests performed for all the different grid sizes are shown. In the beginning, checkerboard tests were performed with the same node spacing along both axes. As can be observed here, the checkerboard tests are solved for all the node spacings higher than 70 km. When the node spacing in the grid is lower than 35 km, the checkerboard test is not resolved any more. For the grid with a node spacing of 35 km, the checkerboard test is well resolved in the center of the model, but not at the edges, while the model with slightly higher node spacing resolves the edges as well. Therefore, the final grid was taken as a combination of both node spacings: a higher distance between the nodes at the edges of the grid and a lower distance between the nodes in the center. This grid has a node separation of 45–90 km in the x- and of 35-70 km in the y-direction and of 4.5 to 9 km in depth as can be seen in Figure 5.16.

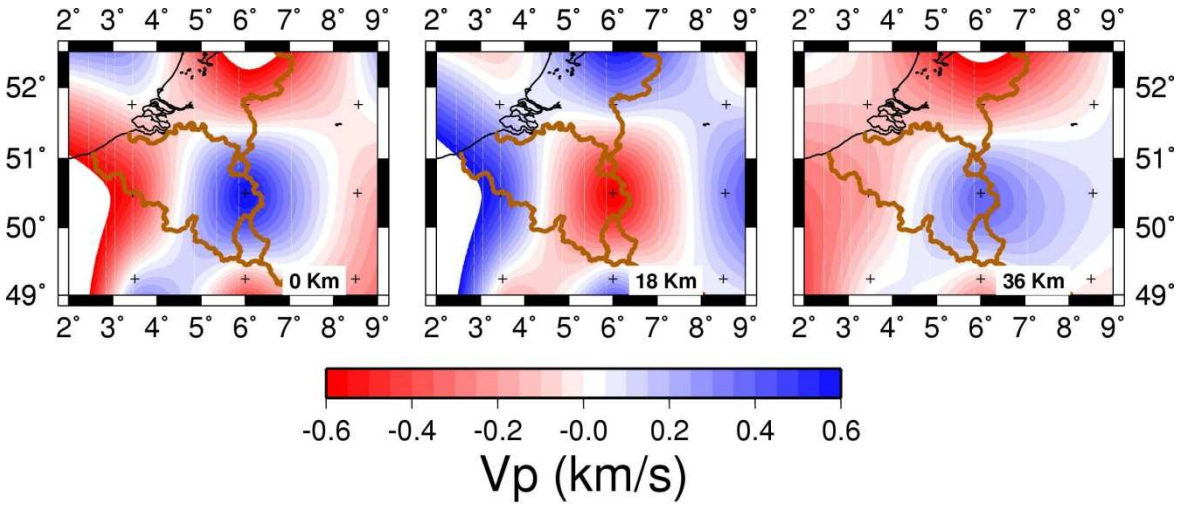

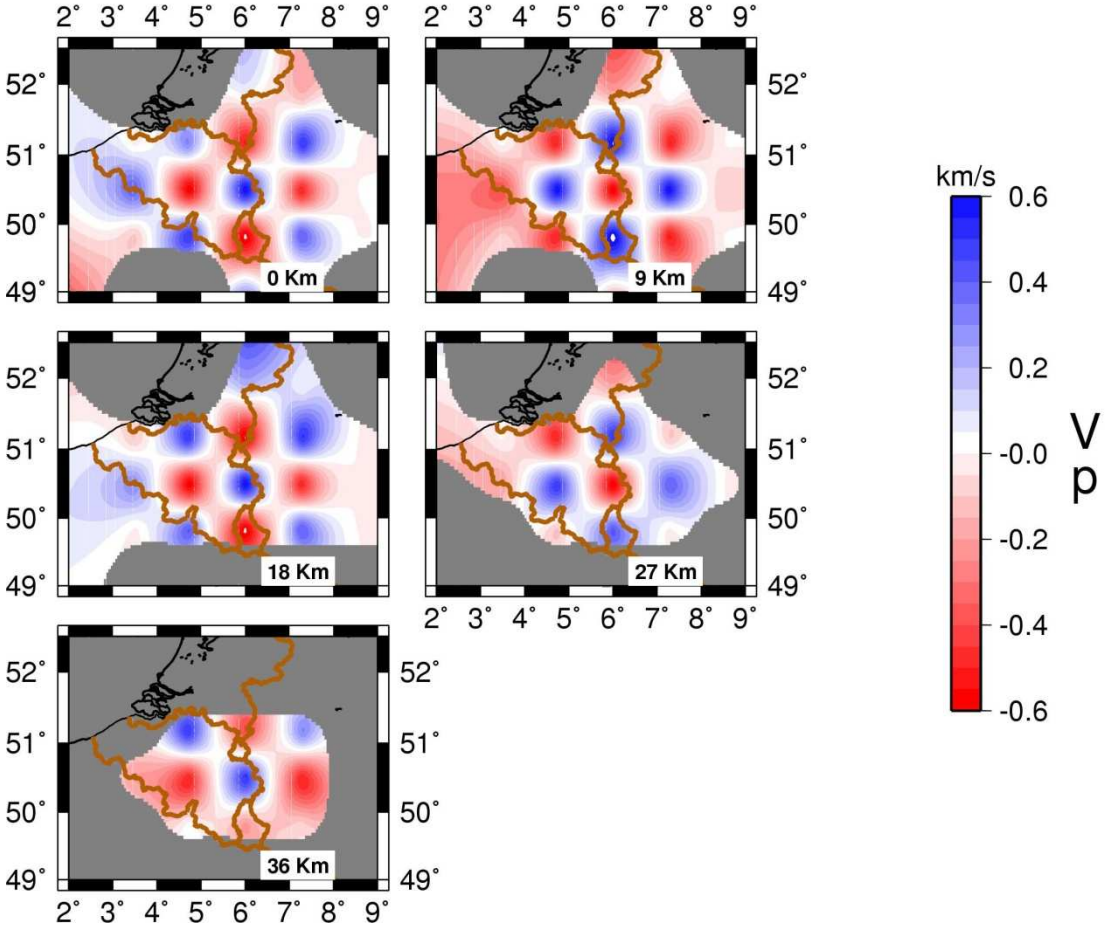

Figure 5.13: Results in depth slices for the same source-receiver geometry as in the real datasets for different grid spacings.
Checkerboard resolution test for the same source-receiver geometry as in the real datasets for a grid spacing (Top) 180 km in the x-direction, 140 km in the y-direction and 18 km in depth. (Bottom) 90 km in the x-direction, 70 km in the y-direction and 9 km in depth. The black line represents the coastline, the brown line the political borders.

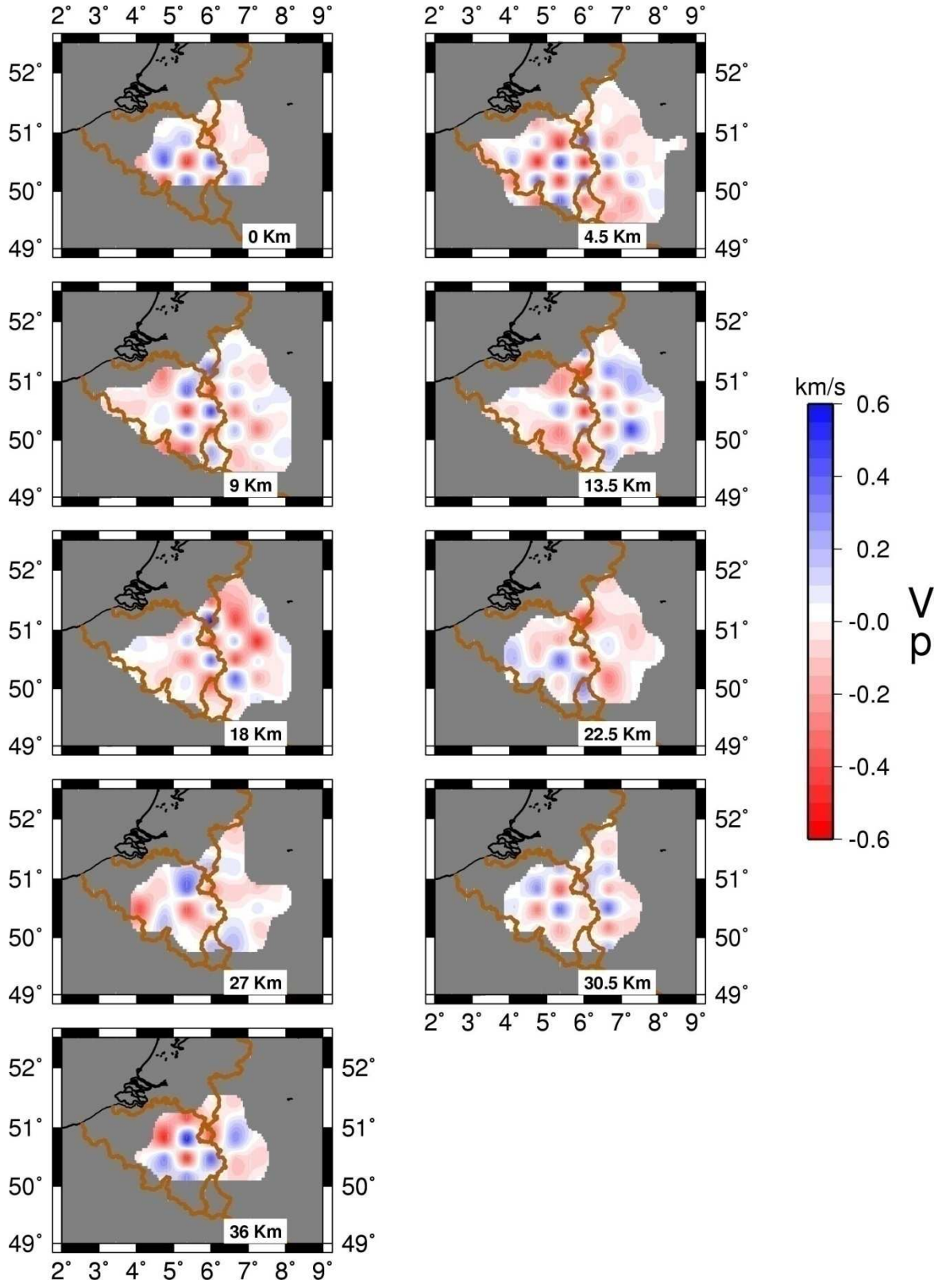

Figure 5.14: Results in depth slices for the same source-receiver geometry as in the real datasets for a grid spacing of 45 km in the x-direction, 35 km in the y-direction and 4.5 km in depth.
The black line represents the coastline, the brown lines the political borders.

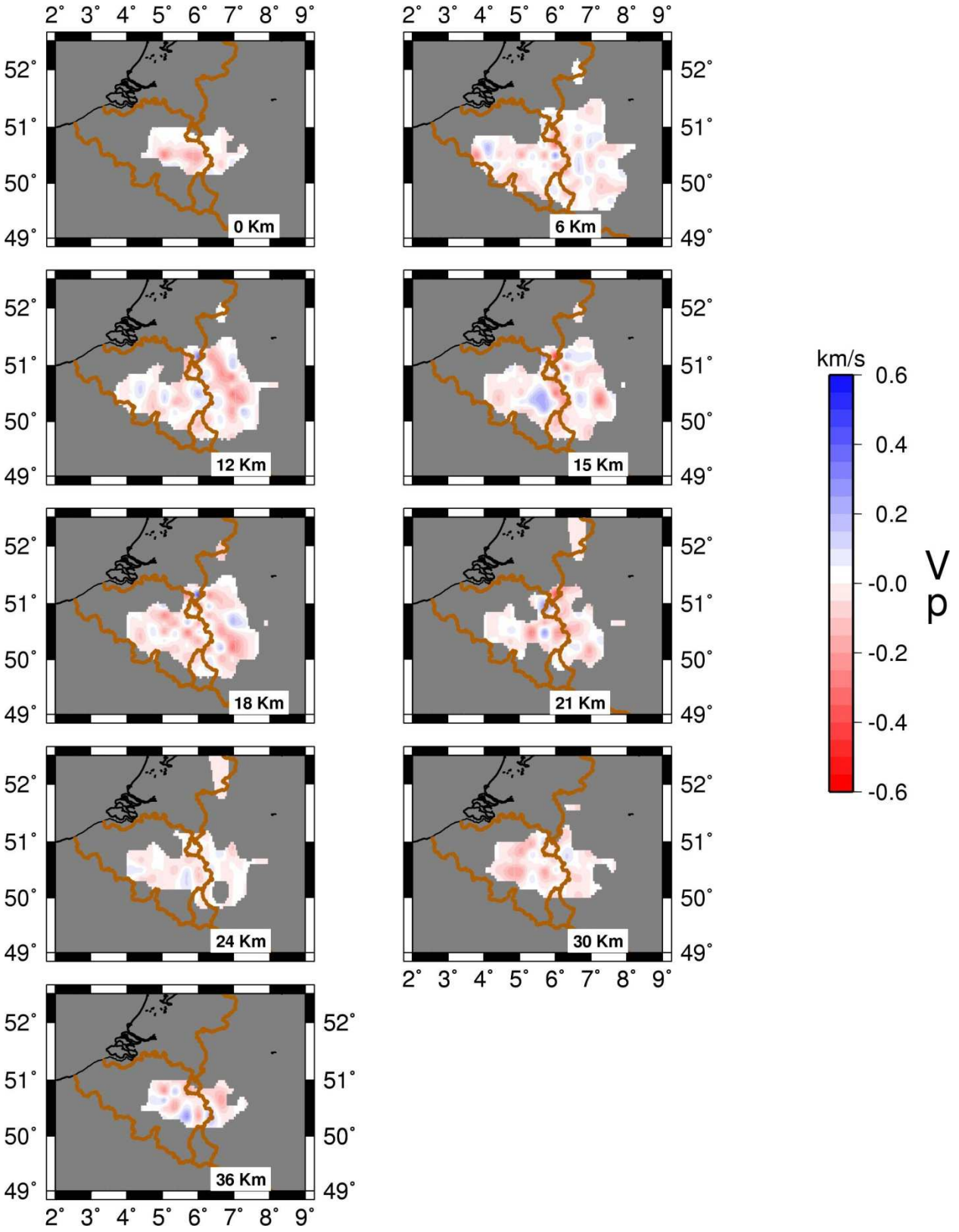

Figure 5.15: Results in depth slices for the same source-receiver geometry as in the real datasets for a grid spacing of 22.3 km in the x-direction, 17.3 km in the y-direction and 3 km in depth.
The black line represents the coastline, the brown lines the political border.

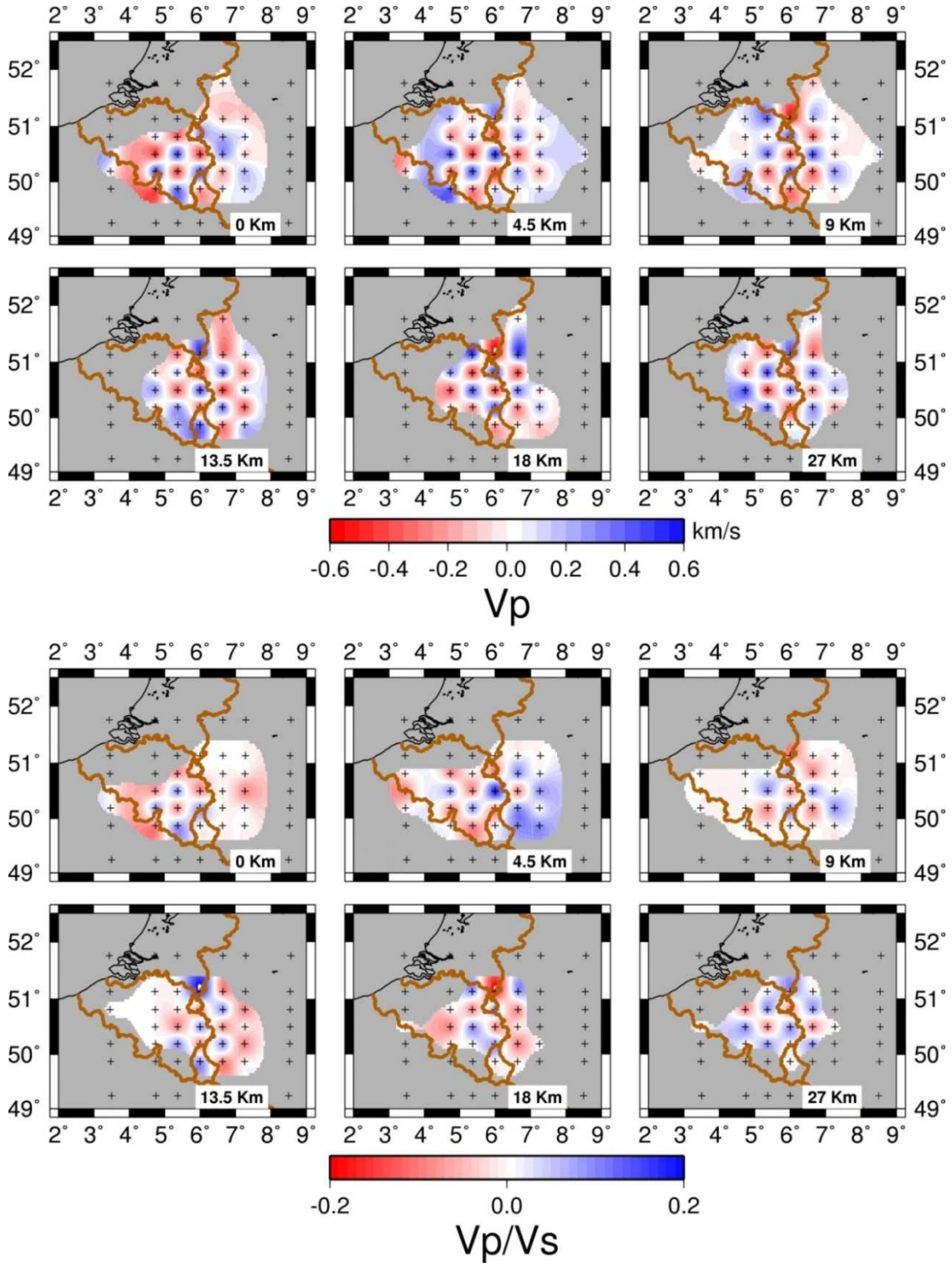

Figure 5.16: Result for the checkerboard resolution test for depth slices of 0, 4, 9, 13.5, 18 and 27 km. (Top) Checkerboard resolution test for the same source-receiver geometry as in the real datasets for the Vp-model. In grey, regions with no resolution. (bottom) Checkerboard resolution test for the same source-receiver geometry as in the real datasets for the Vp/Vs-model. In grey, regions with no resolution. The black line represents the coastline, the brown lines the political border. The node points of the grid used to perform the inversion are indicated with + .

5.4.2.2Damping value

The damping value is a parameter that optimizes the inversion as mentioned in paragraph 5.2.3 and therefore has to be selected carefully. The best way to determine the damping value is to perform a series of single-iteration inversions changing the damping value every time, and plotting the data misfit versus the model variance for these iterations. If a logarithmic series of damping values is chosen, a hyperbolic curve should appear (Figure 5.17) (Eberhart-Phillips, 1986). The damping has to be chosen so that there is a good compromise between data misfit and a large model variance. A damping value of 20 was chosen for the Vp- and the Vp/Vs-iteration, i.e. a value close to the minimum data-variance, yet it desirably yields only moderate model-variance.

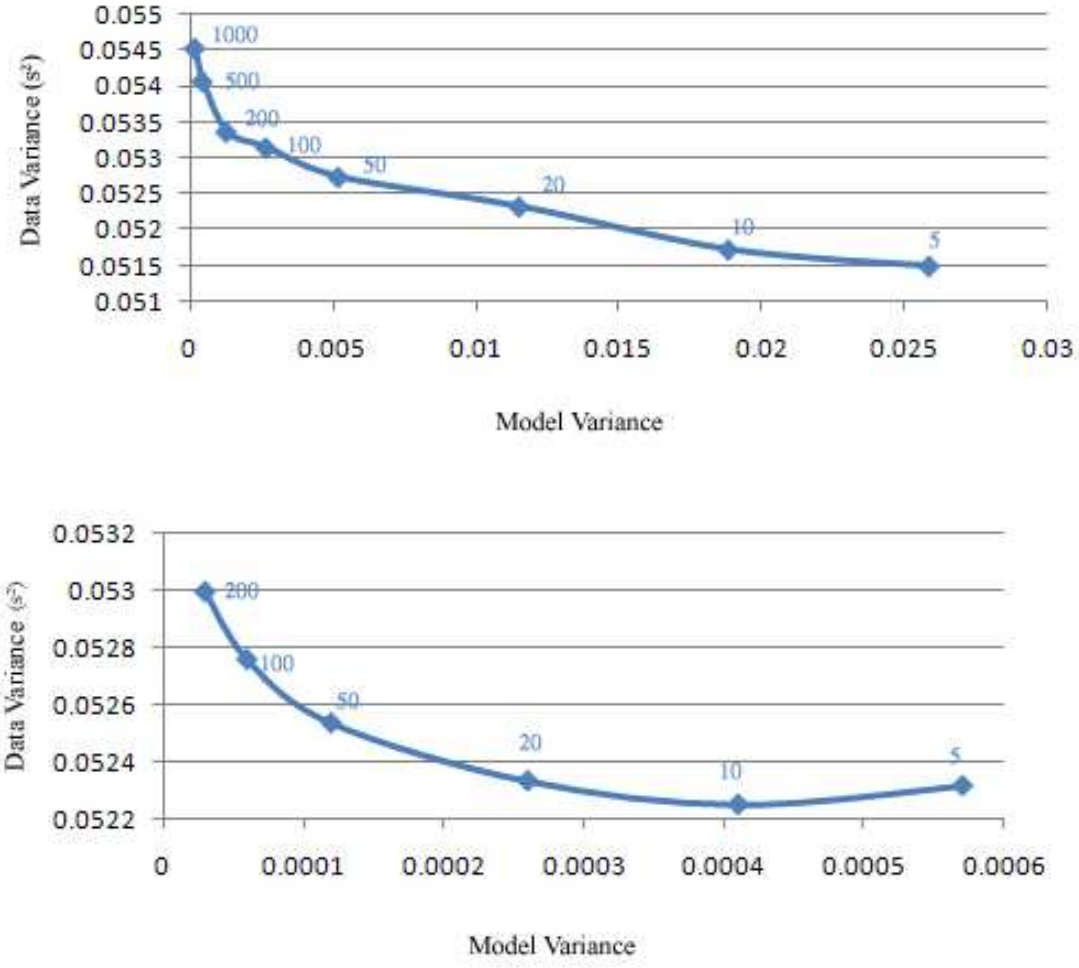

Figure 5.17: Data misfit versus model length for Vp-(top) and Vp/Vs-(bottom) data for different value of the damping parameter.

5.4.2.3Spread value

On the other hand, the model resolution is determined by the resolution matrix. Each row of this matrix describes the dependence of one model parameter of all the other parameters constituting the model. For a perfectly resolved dataset, the diagonal elements of the matrix should be surrounded by

zeros. Because it is difficult to evaluate an entire matrix, to take the "quality" of the resolution into account, the spread function was calculated of the resolution matrix (Michelini and Mac Evilly, 1991; Haberland and Rietbrock, 2001) which takes into account the influence of diagonal and off-diagonal elements. If the smearing is important for a node, then the corresponding spread function is large. On the contrary (Figure 5.18), a small spread function means a small smearing and a good resolution value. Analyzing the relation between the spread function and the derivative weight sum (DWS), it is observed that when the spread is low, the DWS is high and vice versa. To determine the best spread value, the DWS has to be as low as possible, as well as the spread value. So, the value 2.5 was chosen as the threshold of spread function to delineate poorly resolved regions for Vp- and 2.0 for Vp/Vs. In the following (Figure 5.22 to Figure 5.25), only regions with values of the spread function lower than 2.5 are plotted. After all these tests, the tomographic inversion can be performed and the results described. Before they can be discussed, feature tests have to be performed as will be seen in the following paragraphs.

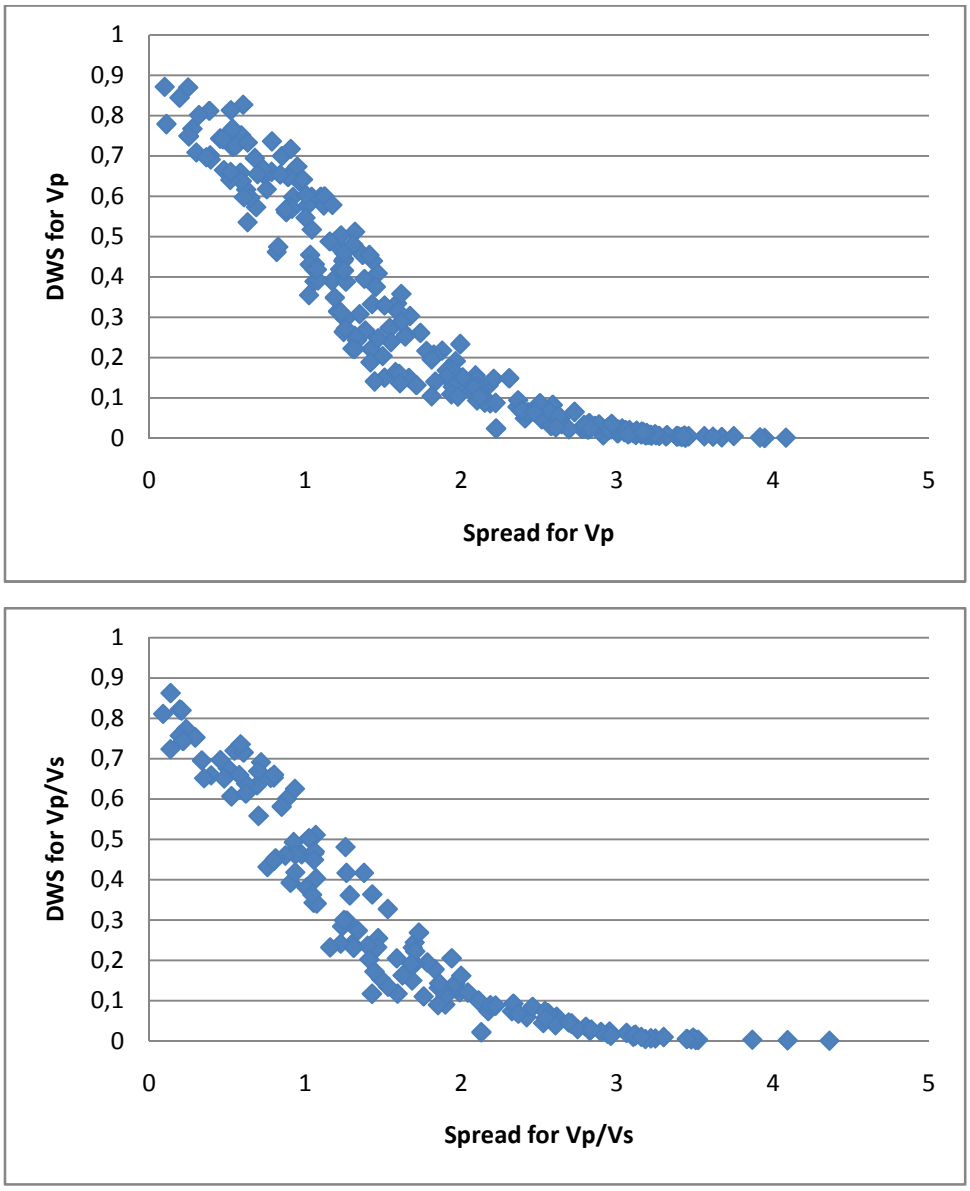

Figure 5.18: Diagonal value of the resolution matrix (DRM) versus spread function value for Vp-model. The threshold of spread function to delineate poorly resolved regions is chosen at 2.5.

5.4.3 Results

Several anomalies can be seen in the tomographic result. The results are presented in Figure 5.19 to Figure 5.23. They are discussed following the different geological regions. Not much information can be obtained for the Brabant Massif because it is situated at the edges of the resolved region. In fact, no Vp/Vs-ratio information is obtained here, so only the Vp-anomalies will be discussed for this region. Overall, the surface P-wave velocities are higher than expected for this region (+7%) (0-4.5 km). Also a sharp transition (from +7% to -7%) in the seismic P-wave velocity can be seen at the southern edge of the Brabant Massif at a depth of 4.5 km. The middle crust however is characterised by velocities (-4%) lower than expected. Underneath the Campine region, the velocity is higher than expected at 27 km of depth.

Another important geological feature is the Eifel Volcanic Province. Here, both Vp- as Vp/Vs-models are solved. The P-wave velocity shows low velocities (< -9%) at the surface, whereas at 27 km of depth, the P-wave velocity is higher than what would be expected at this depth (+5%). Another remarkable anomaly here is the high velocity (+8%) at 13.5 km of depth. Absolute velocity values of 7.20 to 7.5km/s here seem to correspond to values for a lower-crust setting. The Eifel Volcanic Province is characterised by lower Vp/Vs-values (< 1.65) at a depth of 9 km, whereas at the surface, a high Vp/Vs-ratio can be seen (1.85).

The Roer Valley Graben region is characterised by slightly lower Vp-anomalies (-6%) throughout the entire crust. At the surface, the graben is characterised by high Vp/Vs-values (1.80 – 1.85), whereas at depth an intermediate to low ratio (1.65-1.70) appears. At 27 km high Vp/Vs-values reappear (> 1.85).

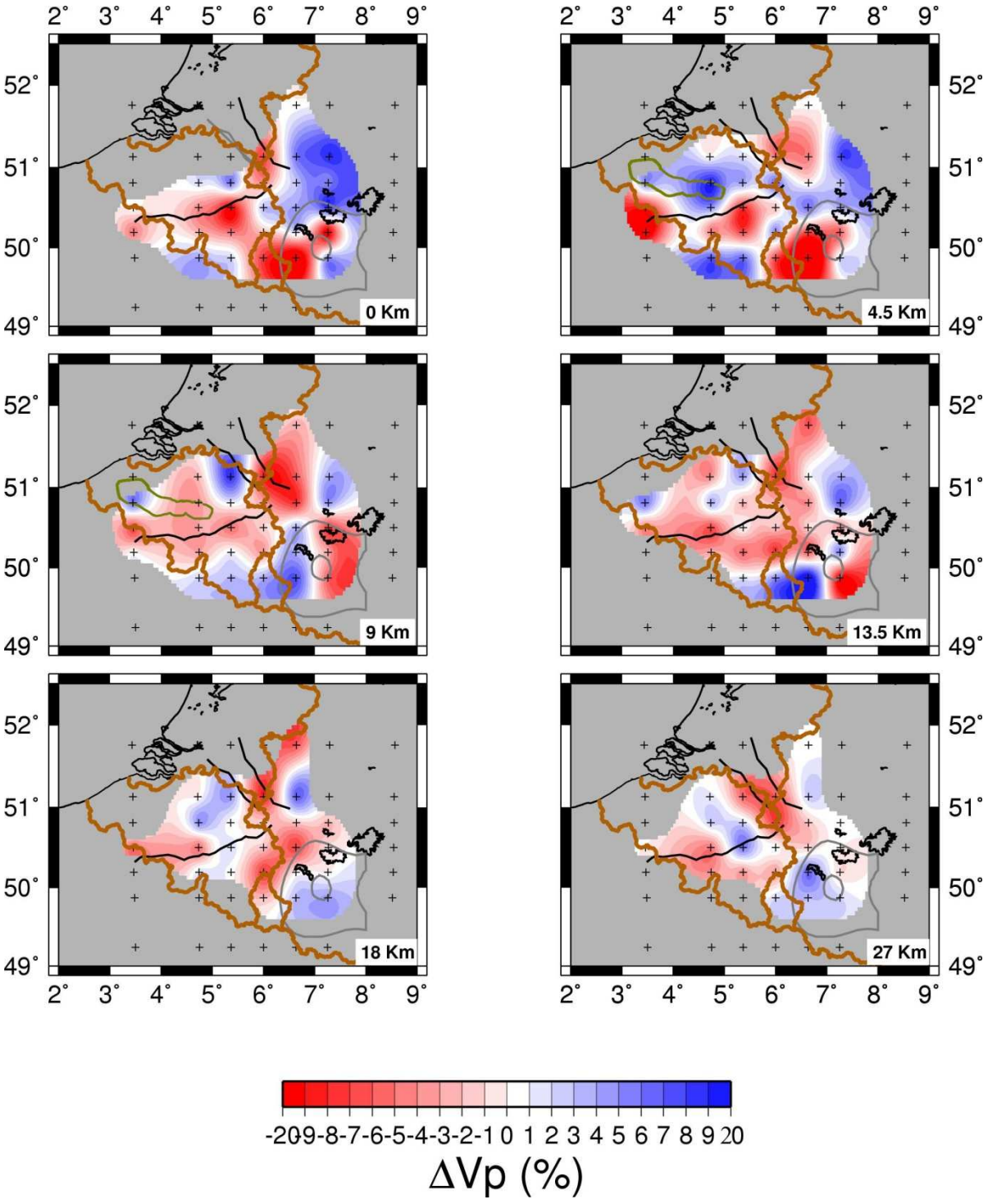

Figure 5.19: Depth slices (0, 4.5, 9, 13.5, 18 and 27 km) through the 3D Vp-model.
The black crosses are the locations of the nodes of the iteration. The black line represents the coastline, the thick brown line the borders of the different countries. The black lines represent major fault lines, whereas the grey lines indicate the position of the Eifel Plume (estimated by Budweg *et al.*, 2006). The black irregular shapes represent the position of the Eifel volcanism. Regions with poor resolution are grey. The khaki shape in the Brabant Massif at 4.5 and 9 km of depth represents the outline of the gravimetric low underneath the Brabant Massif.

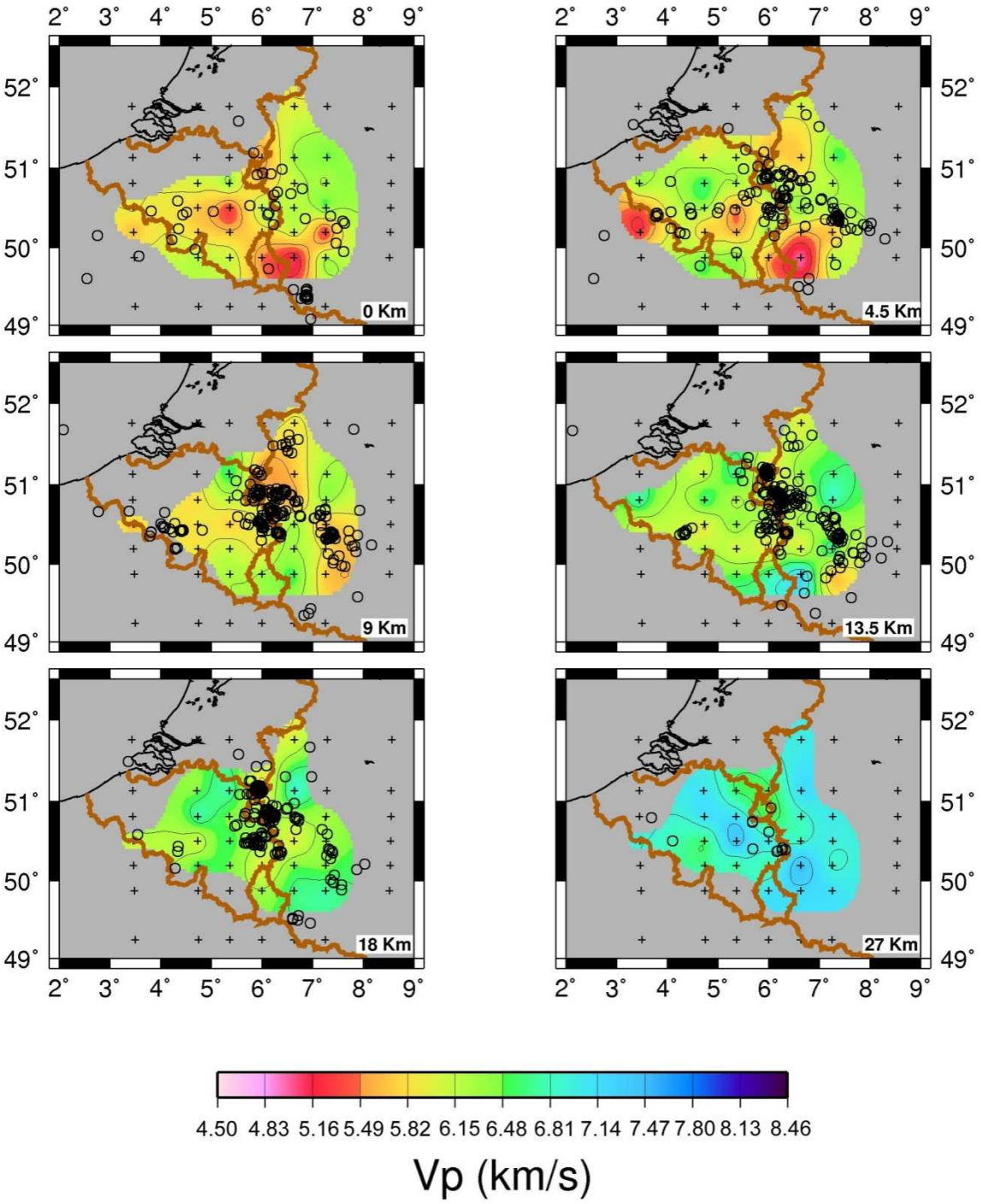

Figure 5.20: Depth slices (0, 4.5, 9, 13.5, 18 and 27 km) through the 3D Vp-model.
The black crosses are the locations of the nodes of the iteration used. The black line represents the coastline, the thick brown line the borders of the different countries. The black circles represent the seismicity registered by the seismic network.

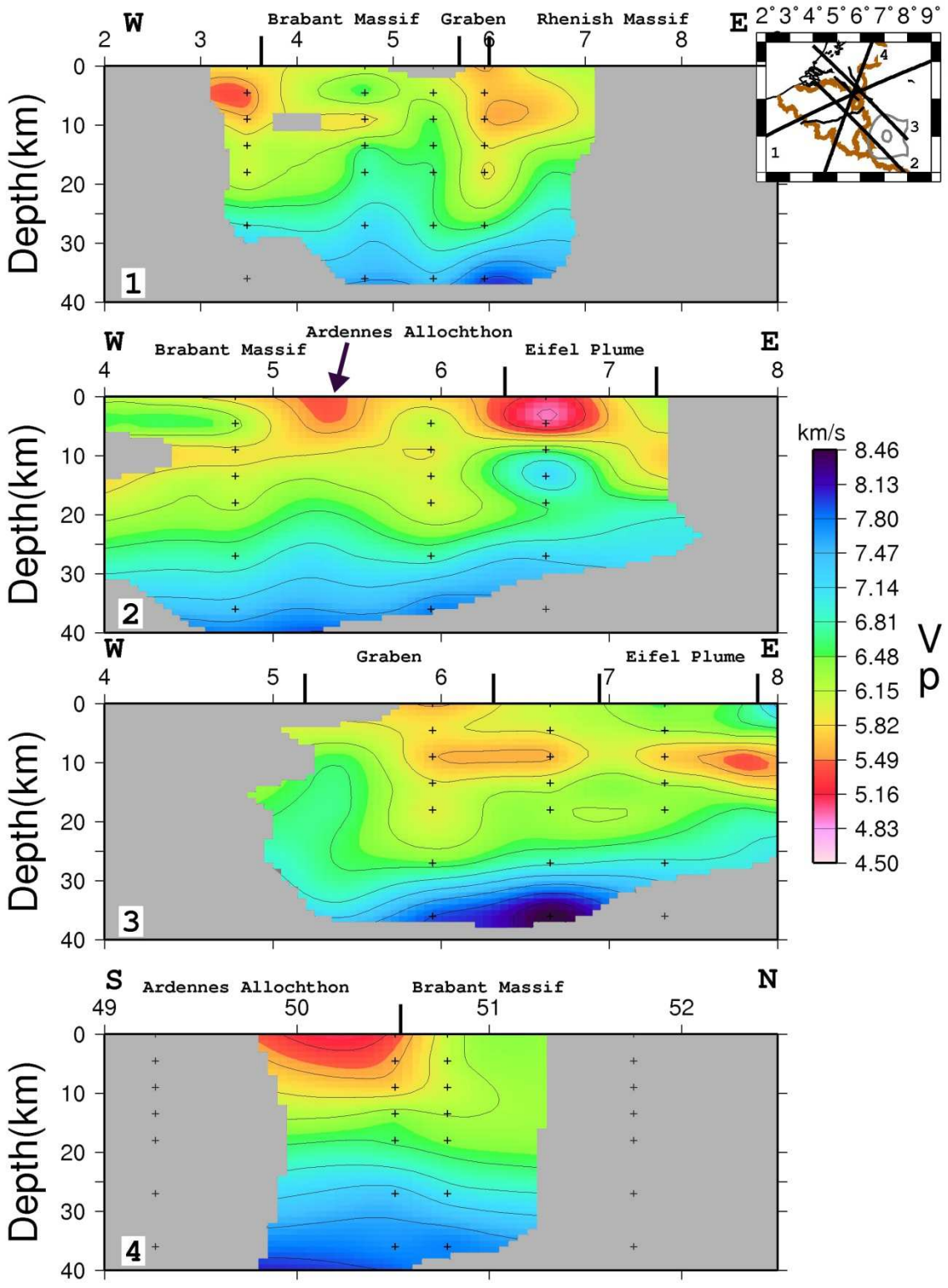

Figure 5.21: Profiles through the 3D Vp-model.
The position of the different profiles is shown on the map in the upper right corner. On this map, the main geological features of the region are shown (the Roer Valley Graben in the north-eastern corner of Belgium, the Midi overthrust, the other black line and the Eifel plume outline in grey (after Budweg *et al*., 2006)).

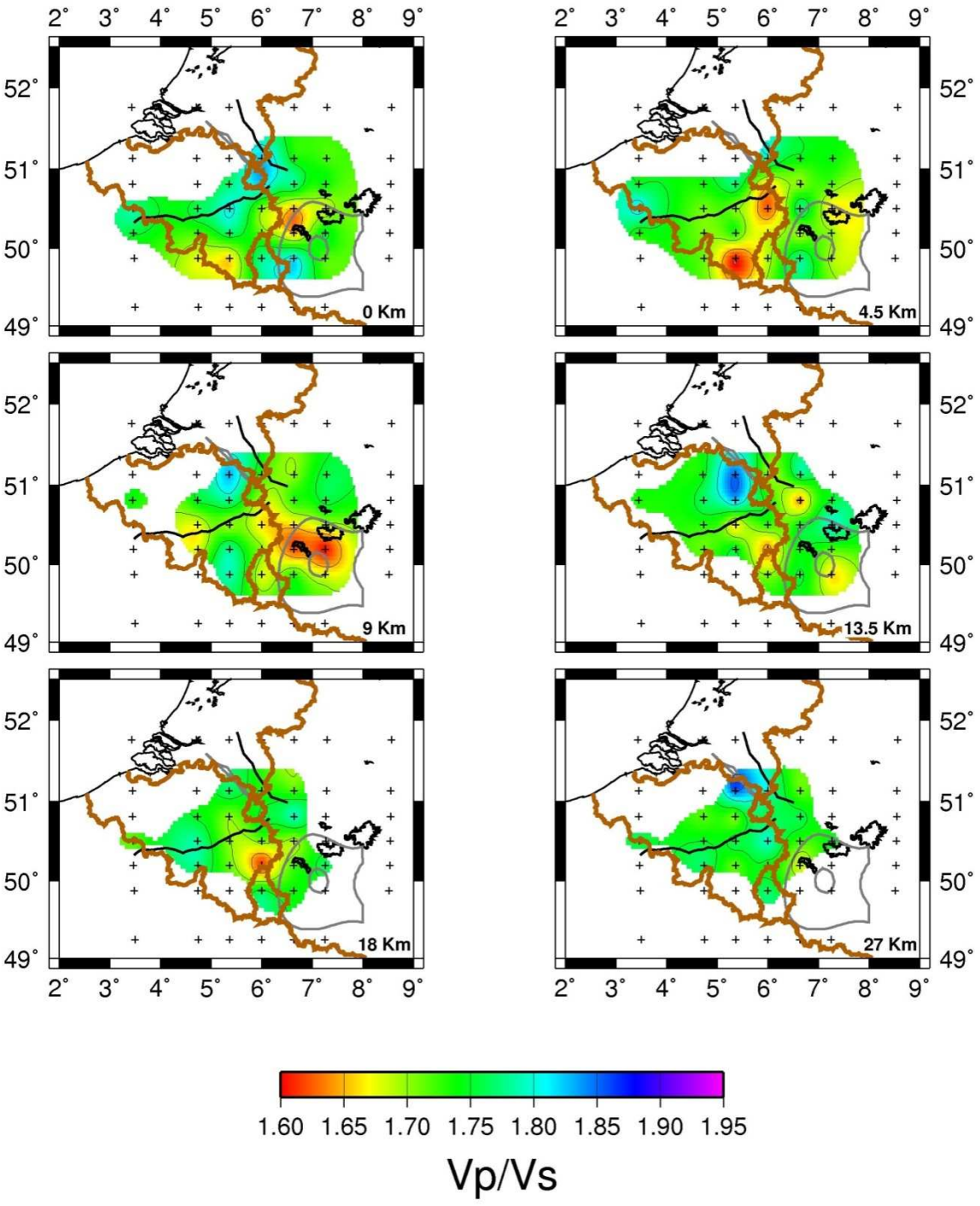

Figure 5.22: Depth slices (0, 4.5, 9, 13.5, 18 and 27 km) through the 3D Vp/Vs-model. See Figure 5.19 for more details. Regions with poor resolution are grey

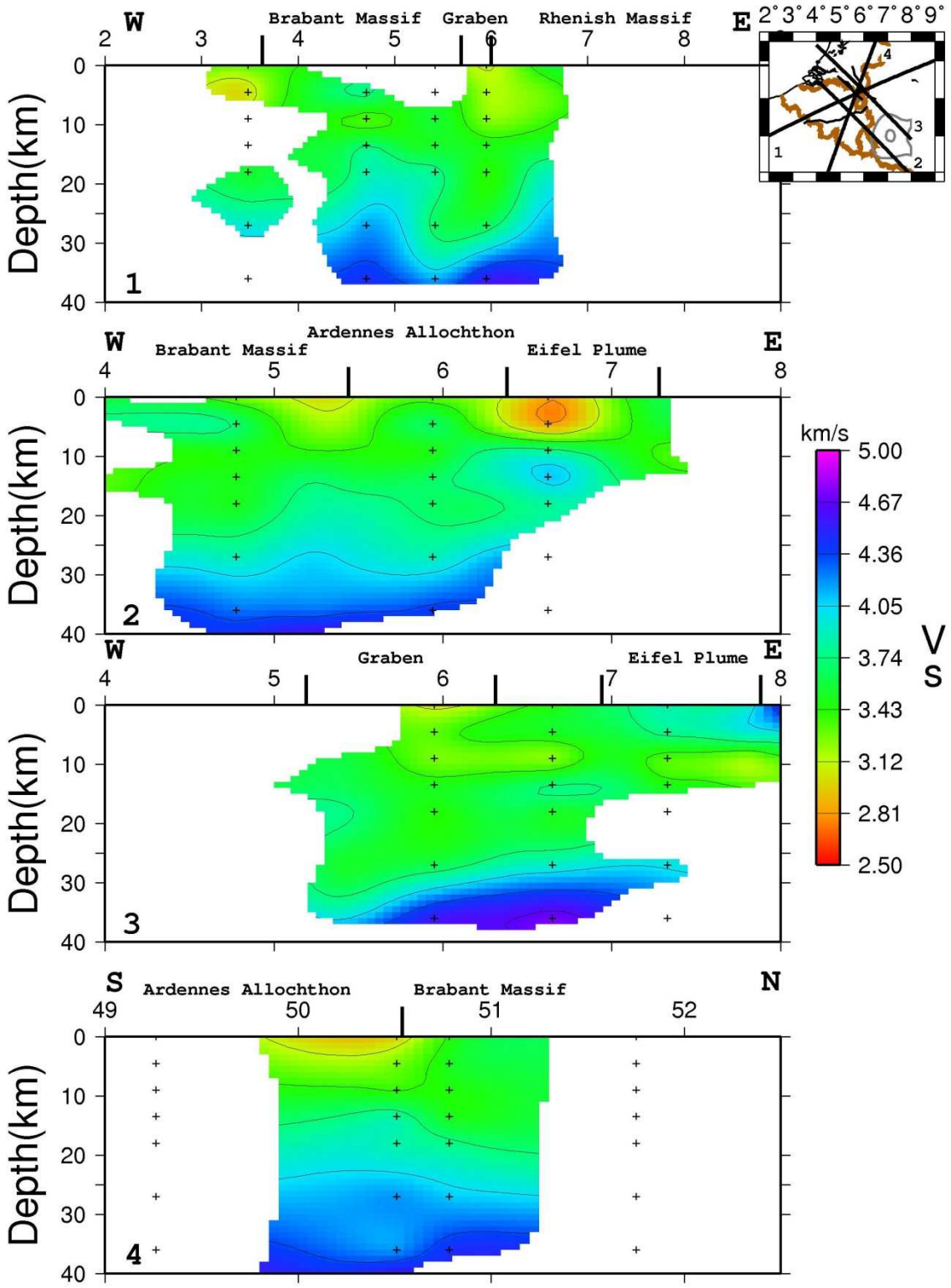

Figure 5.23: Profiles through the 3D Vs-model.

The position of the different profiles is shown on the map in the upper right corner. On this map, the main geological features of the region are shown (the Roer Valley Graben in the north-eastern corner of Belgium, the Midi overthrust, the other black line and the Eifel plume outline in grey (after Budweg *et al.*, 2006)). The position of the nodes closest to the profiles are indicated by the black crosses.

5.4.4 Feature tests

To interpret the anomalies in the final velocity model, they have to be evaluated on their "real"existence. This is done with a feature test. Similar anomalies as the ones obtained in the final result are included in an artificial velocity model. Synthetic arrival times are calculated in this model. Afterwards, the tomography is performed using the same initial model as the original tomography, but with a synthetic dataset, to see in what way the anomalies are resolved (Figure 5.24 and Figure 5.25).

First, the different anomalies were tested separately, so that interferences between different anomalies could be avoided. Because the results are similar to the second test, no figure is provided for these tests. Overall, the anomalies are recovered very well, although small differences between the input values and the calculated values occur due to some smearing in the model. The sharp transition in velocity along the Midi-overthrust is very well resolved in the feature test. The low velocities are almost entirely recovered whereas the higher velocities are recovered less well (6.17-6.33 km/s instead of 6.30 km/s and 6.60 km/s). The high velocity underneath the Campine basin is only found in one node instead of the two nodes shown in the original result (7.11 km/s instead of 7.12 km/s).

In the Eifel Volcanic Province, both the velocity low at the surface as the velocity high at depth are found, although they are somewhat lower in amplitude than the anomalies in the original model (synthetic velocity of 5.25 km/s is at 5.00-5.10 km/s after inversion for the superficial anomaly; synthetic velocity of 7.50 km/s is at 7.33 km/s after inversion). The Vp/Vs-anomaly found in this region at 9 km of depth is also very well resolved (1.62-1.63 instead of 1.60). The very low Vp/Vs-ratio at the surface (1.60) is only at 1.64 after the inversion. The velocity high (7.50 km/s) at 13.5 km of depth underneath the Eifel Volcanic Province is only partially recovered at 7.02 km/s.

The high Vp/Vs-value (1.80) found at the top and the bottom of the Roer Valley Graben is recovered with the synthetic test (1.76-1.77).

In a second test, all the anomalies were grouped to see whether some anomalies are the result of interferences between different anomalies (Figure 5.24 for Vp- and Figure 5.25 for Vp/Vs). In this test, the superficial low anomalies in the Eifel Volcanic Province are determined to the same degree as when they were tested alone. The high velocity contrast at the Midi-overthrust is also visible and shows similar velocity trends as when the anomaly was inverted alone. The high velocity near the Eifel Volcanic Province at a depth of 13.5 km is now better recovered than when it was tested alone (7.36 km/s instead of 7. 02 km/s for an original value of 7.50 km/s). This means that other anomalies in the model enhance this anomaly, indicating an overestimation of the real values. However the anomaly is still underestimated so higher starting velocities are required to explain the anomaly. The velocity highs at 27 km underneath the Campine basin and the Eifel Volcanic Province are also very well recovered.

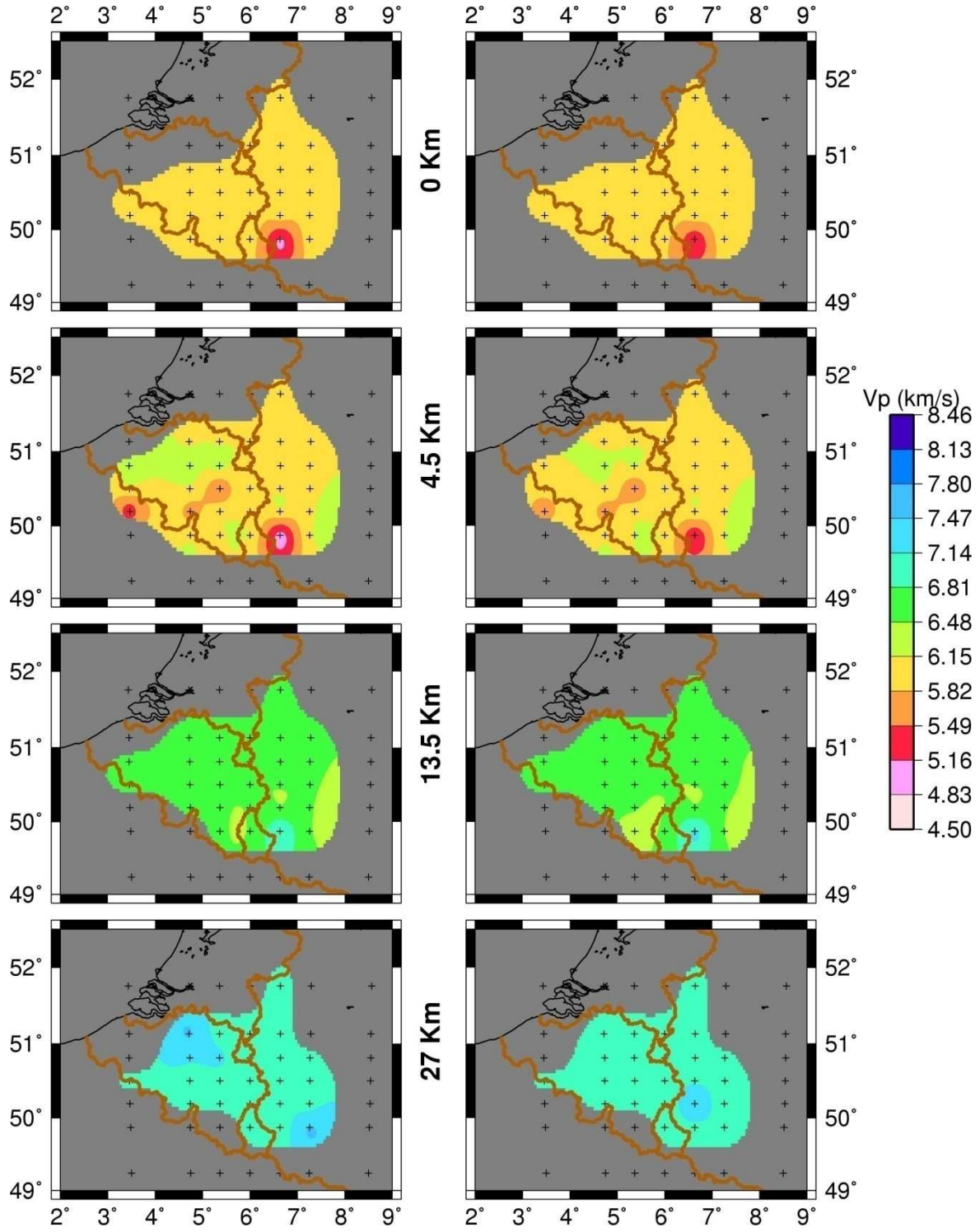

Figure 5.24: Results of the feature test for Vp, where all the anomalies are inverted at once. The left four depth slices represent the model for which the synthetic dataset is calculated. The right four depth slices show the result of the feature test and thus how well the different anomalies are resolved. Regions that are not resolved are shown in grey. The black line represents the coastline, the brown lines the political border. The node points of the grid used to perform the inversion are indicated with + .

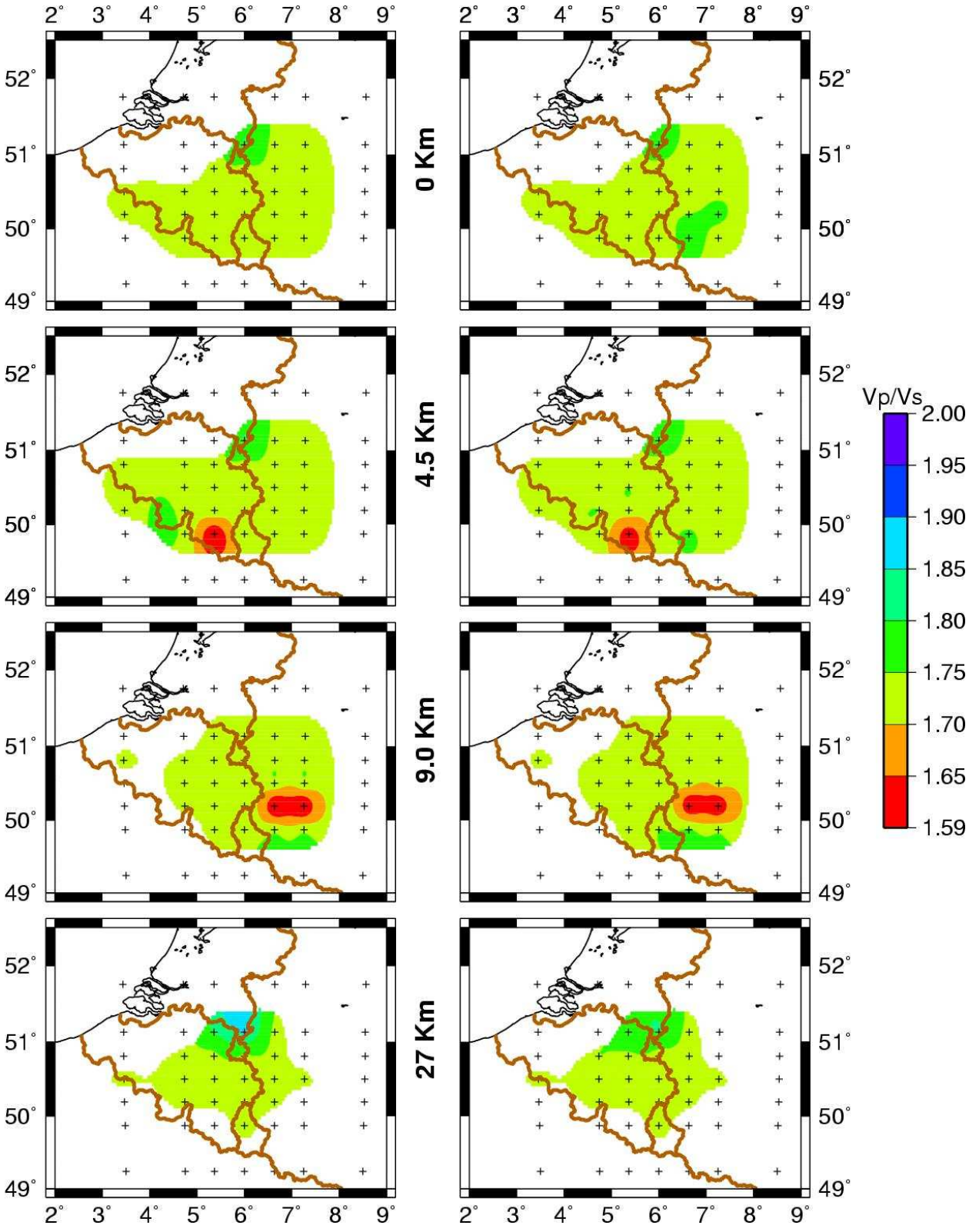

Figure 5.25: Result of the second feature test for Vp/Vs, where all the anomalies are inverted at once. The four depth slices on the left represent the model for which the synthetic dataset is calculated. The four depth slices on the right represent the result of the feature test with the low vp/Vs-anomalies. Regions that are not resolved are shown in white. The black line represents the coastline, the brown lines the political border. The node points of the grid used to perform the inversion are indicated with + .

5.4.5 Discussion

Every superficial tectonic structure is characterised by its own velocity structure as is evidenced on the profiles on Figure 5.21. For the convenience of the reader profile 1, 2 and 4 of this Figure are repeated in Figure 5.26. Profile 2 and 4 of Figure 5.26 show that the Ardennes Allochthon is characterised by lower velocities near the surface than the Brabant Massif. Both the velocities of 5.1 to 5.5 km/s in the Ardennes Allochthon as the velocity of 6.1 and 6.4 km/s in the Brabant Massif are similar to those found by Volon (1989). In depth, the difference in velocity beneath both structures seems to disappear and a similar velocity structure can be observed. This also corresponds to the velocity models determined by Volon (1989). The fact that in the tomographic results the same trends as previously determined velocity models are observed, indicates that the result is close to reality and is an independent proof of the quality of the solution.

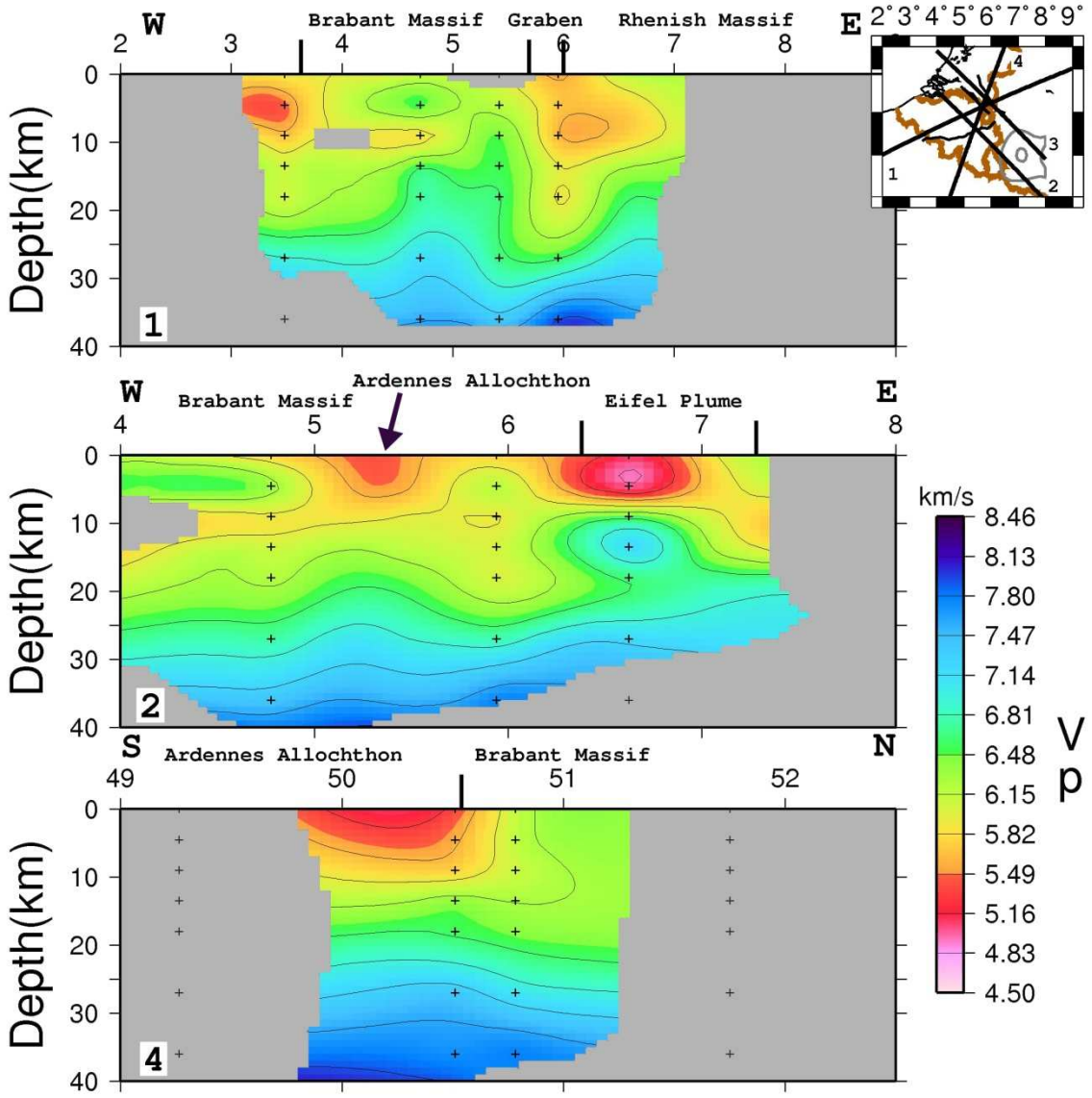

Figure 5.26: Profiles through the 3D Vp-model.
The position of the different profiles is shown on the map in the upper right corner. On this map, the main geological features of the region are shown (the Roer Valley Graben in the northeastern corner of Belgium, the Midi overthrust, the other black line and the Eifel plume outline in grey (after Budweg *et al.*, 2006)).

The Roer Valley Graben and the Eifel Volcanic Province are also characterised by their own velocity structure. In the Roer Valley Graben very low velocities are observed down to a depth of 13.5 km. Even at depth, the Roer Valley Graben is characterised by lower velocities than the surrounding Brabant and Rhenish Massifs (Profile 1 of Figure 5.26). In the Eifel Volcanic Province, low velocities are observed at the surface, whereas very high velocities can be determined in both the middle and lower crust (Profile 1 of Figure 5.26). All these observations indicate that the "superficial" tectonic structures have roots in the middle and lower crust. Several velocity anomalies observable on Figure 5.19 to Figure 5.23 will be discussed in a more elaborate way in the following paragraphs.

The Brabant Massif is characterised by relatively high velocities at the surface, which could be expected for an old, cold massif that has not known important deformation in the last 400 Ma. The Ardennes Allochthon however is characterised by lower velocities, except for the location of the Stavelot and Rocroi Inliers. At 4.5 km depth, a sharp transition between the Brabant Massif and the Ardennes Allochthon can be seen. It corresponds to the location of the Bordière fault and the Midi-overthrust. On the Bouguer gravimetric anomaly map (Figure 2.26 (for the convenience of the reader this figure is repeated in Figure 5.27, Everaerts, 2000), a similar sharp transition is present at this location. Everaerts (2000) proposed two explanations: either a rapid plunge of the Brabant Massif or a structural separation of the entire crust (the latter was also proposed by Chacksfield *et al.* (1993)), but was also able to model this sharp transition with only superficial features, namely, the presence of the Mons Basin in combination with a gradual plunge of the Brabant Massif.

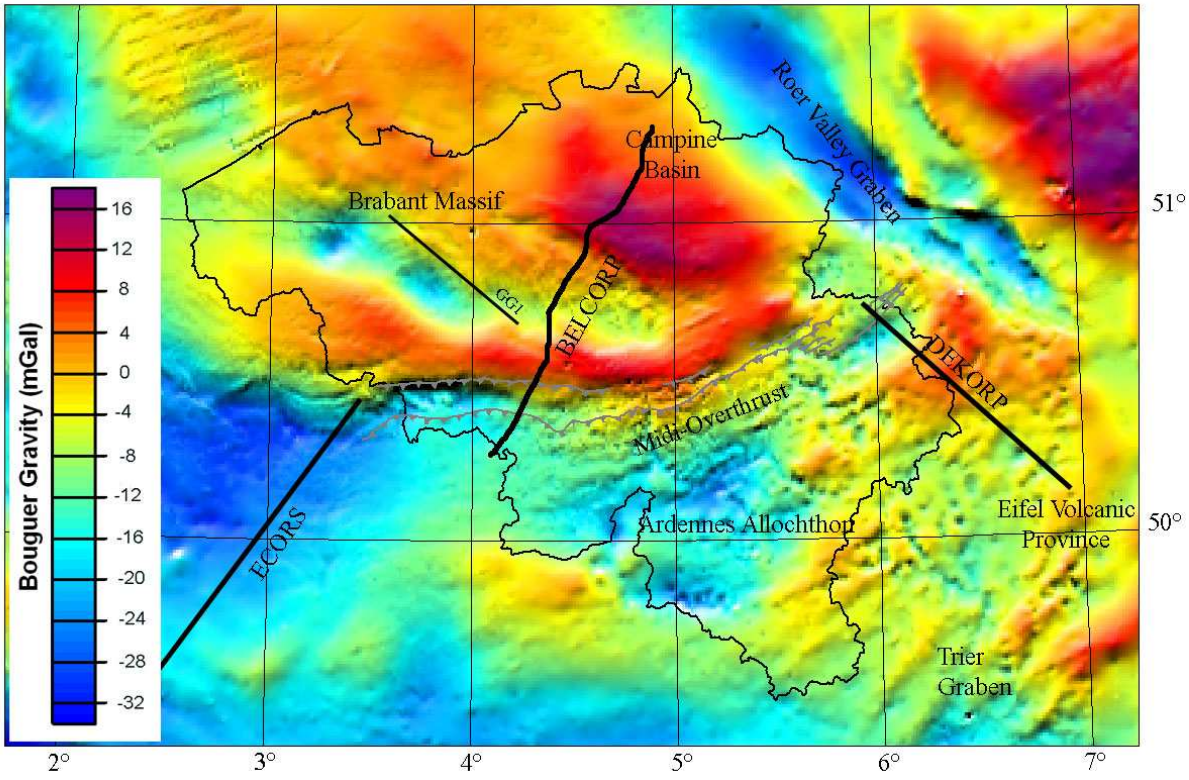

Figure 5.27: The Gravity Bouguer Anomaly map of the Region with the location of the most important tectonic structures and positions of important seismic reflection profiles. The back line represents the Belgian border. Bouguer gravity anomaly data: Royal Observatory of Belgium

The results of this study show a higher velocity in the Brabant Massif and a sharp velocity contrast at the edge of this massif, approximately at the location of the gravimetric contrast (Figure 5.27). When the results of the seismic tomography are plotted together with the gravimetric profile along the same line, crossing the sharp gravimetric contrast (Figure 5.28), a difference in velocity can be observed between both sides of the gravimetric contrast. This difference in velocity is very clear in the first 5 km of depth which is evidenced by the depth slices (Figure 5.19) and the profiles (Figure 5.21) and which is supported by the previous results of Volon (1989). At depth there is also a difference in velocity, however, less pronounced and abrupt. Feature tests (Figure 5.24) indicate that this difference is real and not caused by smearing of the high velocity contrast near the surface. At the position of the gravimetric contrast there is thus a difference in velocity crossing the entire crust, indicating some form of crustal separation.

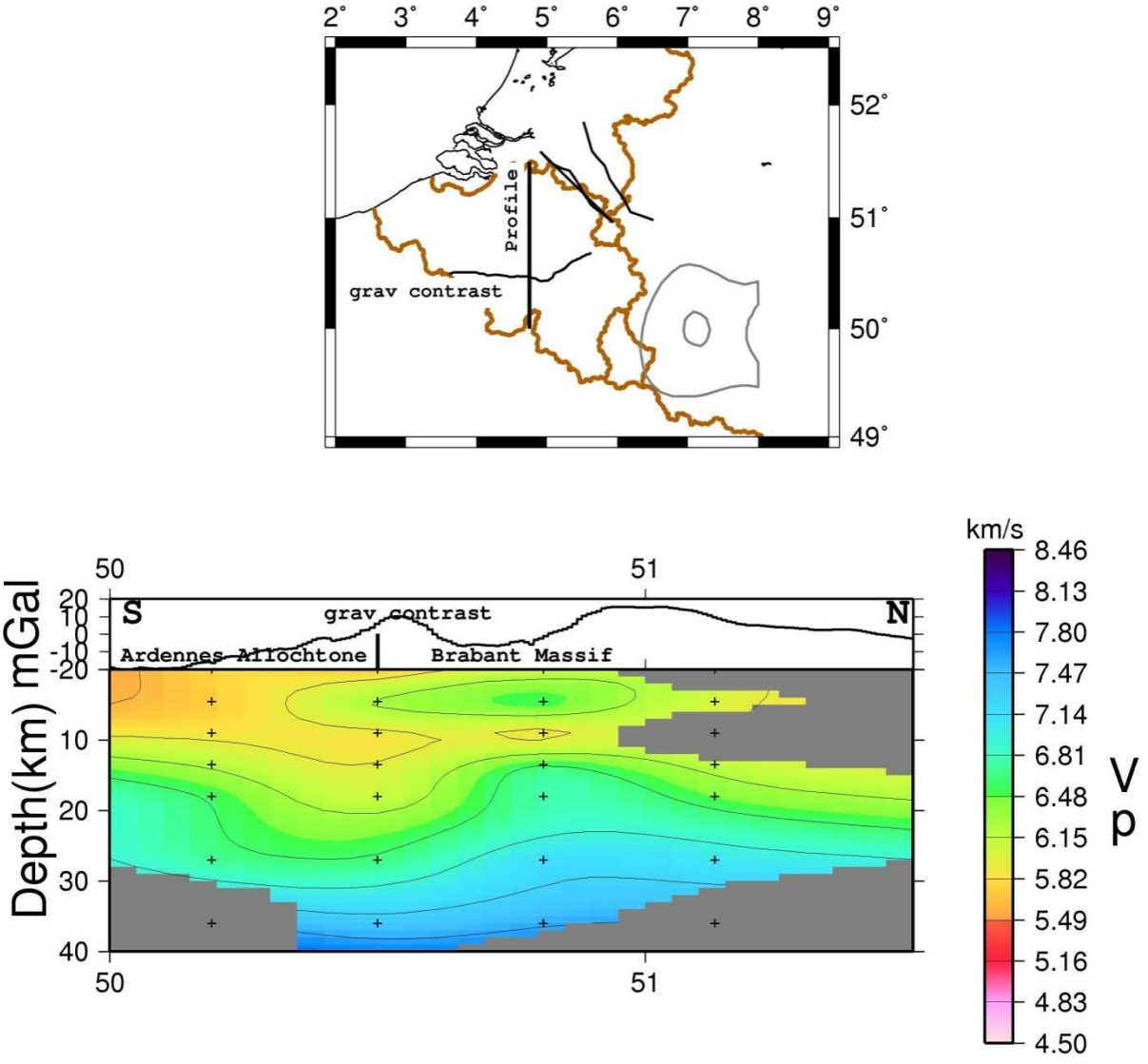

Figure 5.28: Result along a profile crossing the sharp gravimetric contrast.
The map at the top shows the position of the profile, the position of the gravimetric contrast and the main geological features (Roer Valley Graben in the northeast and the Eifel Plume region in the southeast (after Budweg *et al.*, 2006)). The profile at the bottom of the figure shows the result of the local seismic tomography along the profile. Above, the Bouguer gravity measurements are shown along the same profile.

Two possible explanations can be put forward. Either, the lower crust underneath the Ardennes Allochthon is different from the one underneath the Brabant Massif or alternatively, deformation in the middle crust probably caused by the northward displacement of the Ardennes Allochthon during the Variscan Orogeny. From seismic profiles in the region, the Brabant Massif is known to plunge gradually underneath the Midi overthrust, so a clear crustal separation with different types of rocks to the left and right of the contrast can be excluded in the upper crust. It is however possible that at depth, a crustal separation exists, as can be deduced from the magnetic data (Figure 2.27; for the convenience of the reader this Figure is repeated in Figure 5.29). Pharoah *et al.* (2006) modelled the presence of Rondonian crust in a transect northeast of Belgium (Figure 4.13 or the convenience of the reader the Figure is repeated in

Figure 5.30). Could this kind of crust (or another type) be present underneath the Ardennes Allochthon? If this were the case, the difference in seismic velocity in depth would be observed everywhere underneath the Ardennes Allochthon. This is not the case as can be seen on profiles 2 and 4 of Figure 5.26. The difference in velocity seems to be restricted to the position of the sharp gravimetric contrast.

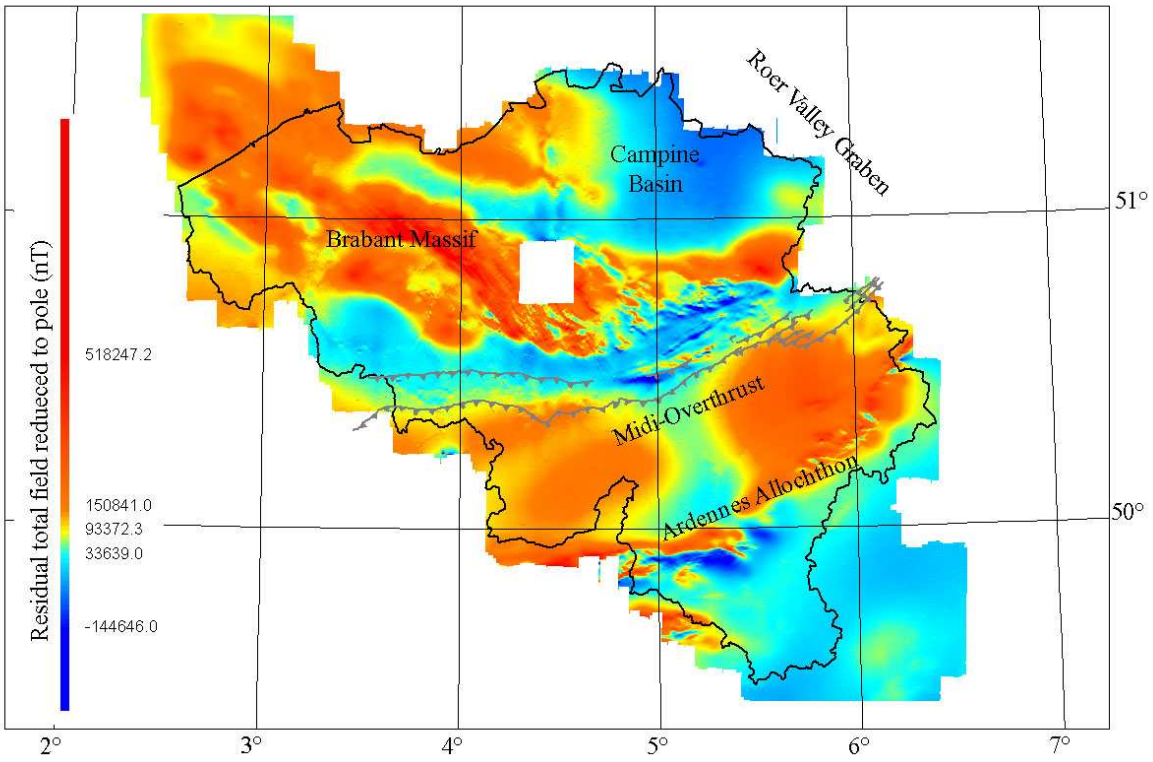

Figure 5.29: Aeromagnetic anomaly map reduced to the pole with the location of the most important tectonic structures. The black line represents the Belgian border.

Magnetic field reduced to the pole data: Royal Belgian Institute of Natural Sciences, Belgian Geological Survey.

It could therefore be equally possible that the crustal structure underneath the Brabant Massif and the Ardennes Allochthon is the same, as can be seen on seismic profiles (like the ECORS-profile). The profile in Figure 5.28 crosses the eastern part of the negative gravimetric anomaly, which has been modelled as a gravimetric granitic body (Everaerts, 2000). This granitic body has shielded the southern parts of the Silurian sediments from deformation during the Caledonian Orogeny. Could this granitic body have played a role in the deformation of the Belgian crust during the Variscan Orogeny? Then, the northward overriding Ardennes Allochthon also deformed and displaced some of the underlying

Brabant Massif toward the north in such a way that it got squeezed in between the Ardennes Allochthon and the "unmovable" granitic body, resulting in a deformed middle crust.

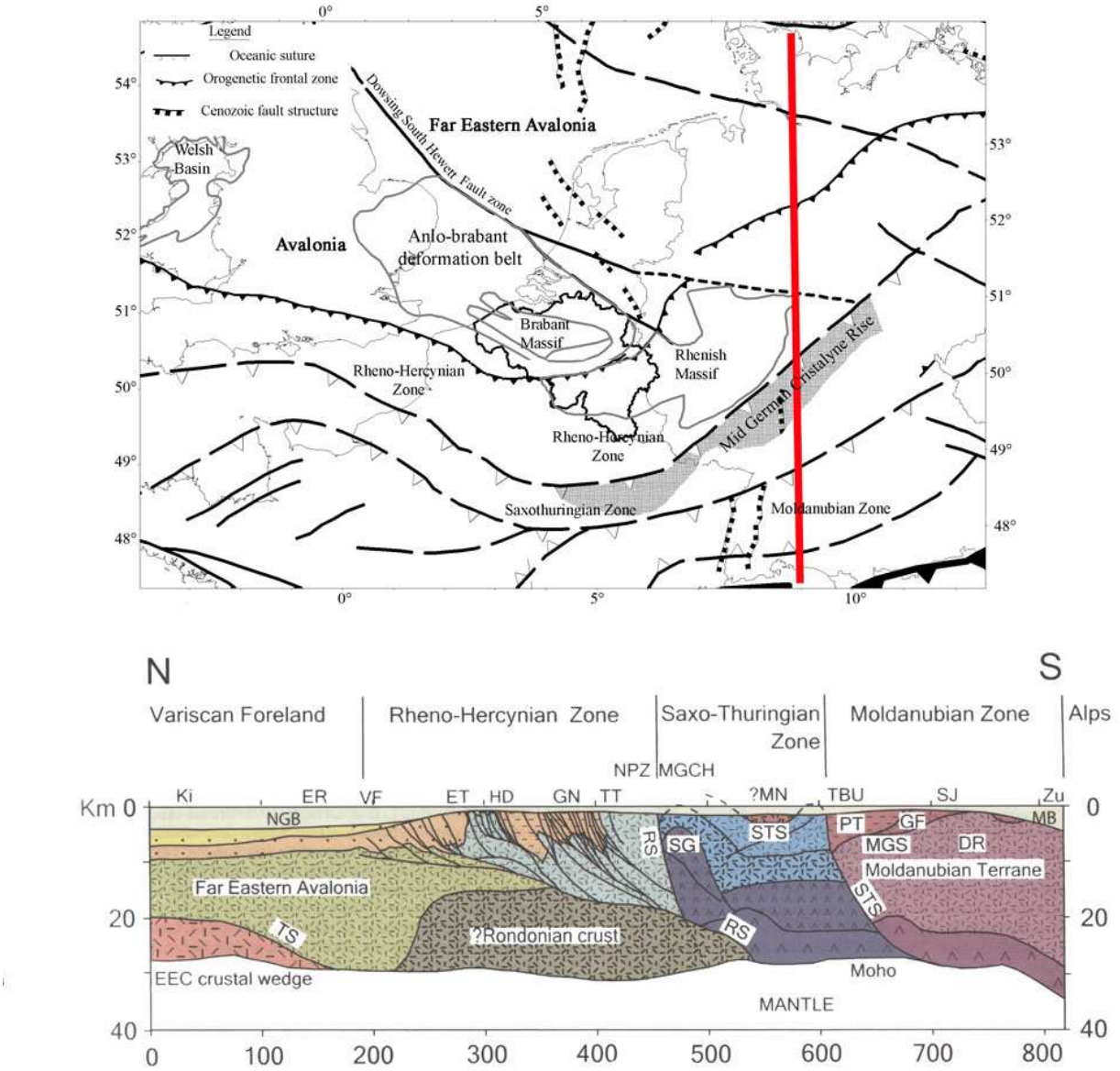

Figure 5.30: Transect to illustrate inferred structure of the "Variscide" accreted crust in the central German region (Pharaoh *et al.*, 2006).

Top: Basement tectonic sketch map of NW Europe with position of the transect shown in the bottom part of the figure (redrawn from Verniers et al., 2002). Political borders are indicated in light grey, Belgian borders in black.

Bottom: Transect : 5x vertical exaggeration. Interpretation of full crustal structure from the EGT deep seismic refraction experiment (Aichroth & Prodehl, 1990; Prodehl & Aichroth, 1992). Detail of shallow crustal structure in central part of transect is after interpretation of DEKORP deep seismic reflection profiles by Giese (1995) and Oncken et al. (2000). Post-Palaeozoic basins and platforms: HD, Hessen Depression; MB, Molasse Basin; NGB, North German Basin;. Postulated Palaeozoic terranes and possible terrane and sub-terrane boundaries: MGCH, Mid-German Crystaline Rise; NPZ, Northern Phyllite Zone; PT, Perunica (Bohemia) Terrane; MGS, Moldanubian-Gföhl Suture; MT, Moldanubia Terrane; RS, Rheic Suture; STS, Saxo-Thuringian Suture; TS, Thor Suture. Proterozoic-Paleozoic tectonic elements: BM, Bohemian Massif; DR, Drosendorf Unit (of BM); ET, Ebbe Thrust; GF, Geföhl Unit (of BM); GN, Giessen Nappe; MN, Münchbergh Nappe (of BM); SG, Saxonian Granulites; TBZ, Tepla-Barrandian Basin (of BM); TT, Taunus Thrust. Other Geographical Locations: Ki, Kiel; ER, Elbe River; SJ, Swabian Jura; Zu, Zurich.

Which of the two explanations can be favoured over the other could maybe be found in the gravimetric data. As mentioned before, Everaerts (2000) was able to explain the gravimetric contrast seen at this location by superficial origins only, but he never modelled the presence of the Mons Basin with a gradual plunge of the massif and the presence of a structural "difference" at depth. Gravimetric data highlight superficial origins over deep origins and therefore a crustal "difference" at depth does not have a large effect on gravimetry measured at the surface. With this in mind the possibility of a crustal "difference" cannot be excluded based on Everaerts previous modelling (Everaerts, pers. comm.). To be able to distinguish between both explanations, it is useful to re-model the gravimetric data in combination with the gravimetric data and the results of the seismic velocity tomography.

Underneath the Campine Basin a higher velocity (+5% or 7,50 km/s) is found at 27 km of depth (see Figure 5.20). Although the anomaly is located at the edges of the resolved region, feature tests were able to partially recover it (Figure 5.24). Oulidi (1998) modelled a gravimetric high found at this location and proposed an uplift of the Moho up to 28km at this location. The results of the Moho depth determination using PmP-waves in the previous chapter, confirm this uplift of the Moho, the SmS-results however do not. The observed higher velocities at 27 km depth represent lower crust velocities, which can be expected if the Moho is at 28 km depth and so it confirms the Moho uplift.

A pronounced gravimetric low (Figure 5.27) in the Brabant Massif has been interpreted as a granitic body at minimum 2.5 km of depth (Everaerts, 2000). When the outline of this gravimetric low is placed on the tomographic result at a depth of 4.5 km and 9 km (Figure 5.19), no velocity contrast corresponding to this shape can be seen at this depth. It is impossible to further constrain the position or existence of this granitic body with the local seismic tomography. It has to be stated however that the fact that the granitic body is not visible can be due to its position at the edge of the resolved region of the seismic tomography, indicating that not a lot of rays cross this structure. One way to resolve this problem in the future would be to add several stations on top and around this structure to record future seismic events that pass through the structure and then redo the local seismic tomography.

In the Eifel Volcanic Province a high velocity anomaly (+8% or 7,50 km/s) is observed at 13.5 km depth. This anomaly has to be interpreted with caution because it is positioned at the edges of the resolved region of the local tomography and because the results of the feature test shows that the obtained velocity value is a slight overestimation of the real velocity (see previous paragraph). This high velocity is situated at approximately the same position as the two cells from the previous chapter where a double reflection was observed (Figure 4.8 and Figure 5.31). These double reflections have also been observed on several seismic profiles in the region (Mechie *et al.*, 1983; Giese, 1983). The lower one is interpreted as the Moho, whereas the origin of the other is not clear. As was discussed in the previous chapter, several explanations have been put forward for these double reflections:

- Some authors argue it to be a reflection on top of a magmatic chamber;
- others assume a lower crust thrusted in between middle crust during the Variscan Orogeny.
- Recent insights in the structure of the Avalonian microplate suggest that it can also be a reflection on a Neoproterozoic crust.

The tomographic result can be distinguished between these explanations as all three propositions are characterised by different seismic velocities. The seismic velocity observed in a magmatic chamber depends not only on the composition of the magma, but also on its temperature and whether the magma is still "fluent" or already crystallised. The seismic velocity can easily range from 3.5 to 6.0 km/s. As this does not correspond to the observed velocities, this theory can be excluded. It is more difficult to distinguish between the other two explanations, as not much is known on the composition of the Rondonian crust. Therefore, the magnitude of the anomaly cannot help us, but its form might. As can be perceived on Figure 5.20, the high velocity of 7.50 km/s is only observed at a depth 13.5 km, at 18 km, middle crust velocities are observed again. If the reflection would have appeared on a Rondonian crust, one would expect a single velocity (or at least an increase) underneath the reflection. This is not the case. **Therefore, the preferred interpretation is that of a mantle wedge which has been thrusted into the crust at 13.5 km depth (Figure 5.32).** It is difficult to model the exact position of this surface, because the double reflections are only visible in a small zone and no information is available more to the south of the studied region (Figure 5.31). This lower crust is probably thrusted into the middle crust along the Midi overthrust and thus it may represent the Midi-overthrust at this location.

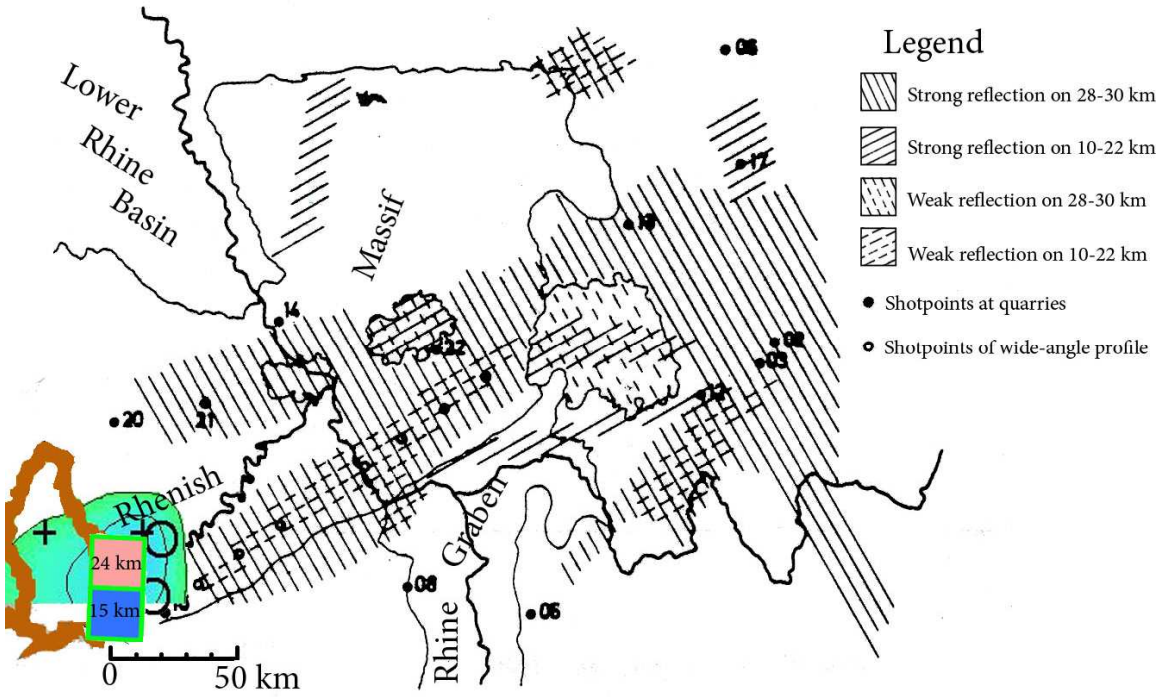

Figure 5.31: Map of the area of the Rhenohercynian zone showing main features of crustal structure deduced from seismic reflection profiles (Mooney & Prodehl, 1978) and the results with intracrustal reflections of the Moho determination (pink and blue square).
In the squares a second reflection can be seen at 37 km for the blue square and at 29 km for the pink square. The outline of the high velocity anomaly (bright blue/green) derived of the local seismic tomography is also indicated.

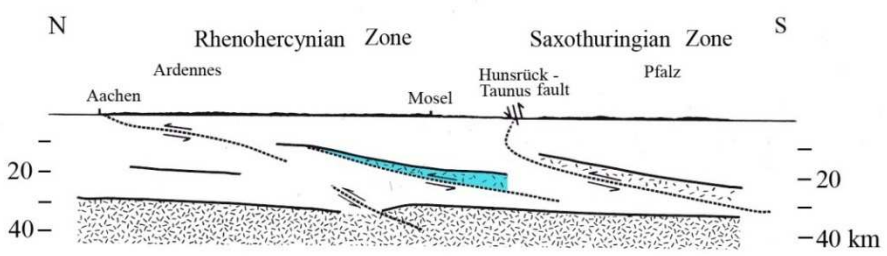

Figure 5.32: Interpretation of the double reflection and high seismic velocity at 13.5 km of depth. The blue zone represents the lowercrust/upper mantle that has been thrusted into the crust along the possible prolongation of the Midi overthrust and that causes the high seismic velocities at 13.5 km of depth in the seismic tomography and the double reflection. Redrawn from Giese, 1983.

Underneath the Eifel Volcanic Province, the Moho has been determined at a depth of 28 km by several authors (Budweg *et al.*, 2006; DEKORP Research Group, 1991; this study). In this tomography, the velocities (7.44 km/s) found at a depth of 27 km (Figure 5.19 and Figure 5.20) are already close to values expected for the mantle (> 7.71 km/s). Thus the high velocity found at 27 km depth is another indication of this Moho uplift. Unfortunately, the Vp/Vs-model is not resolved at 27 km of depth in the area, so no further information can be obtained. At shallow depths (0-4 km), the low velocities obtained for the Eifel Volcanic Province correspond with the position of the Trier Graben (Figure 2.1). This graben has been filled with Triassic and Jurassic sediments (Boulvain *et al.*, 2001). The deposited formations are a mixture of sand, clay and marl. This marl has lower velocities than the terrigene sediments found in the Ardennes Allochthon (Kearey and Brooks, 1991).

The low velocity anomaly found at the location of the Dinant Synclinorium cannot be explained by the presence of the Devonian and Carboniferous limestones in this synclinorium as they are characterised by higher velocities than the surrounding terrigene sediments (Kearey and Brooks, 1991). An alternative explanation for these low velocities comes from the fact that this region is strongly fractured due to the important deformation of the synclinorium of Dinant during the Variscan Orogeny. O'Connel and Budansky (1974) determined that the higher the crack density in a rock, the lower its Vp-velocity. The Synclinorium of Dinant is situated just south of the Midi-overthrust (which crops out in the Condroz region). On deep seismic profiles just to the east (DEKORP Research Group, 1991) and boreholes (Everaerts, 2000) to the south, the Midi-overthrust is situated at a depth of approximately 4 km. So, one can assume that the fault can be found at about the same depth underneath the Synclinorium of Dinant. This is exactly the depth at which the node that shows the lower velocity is located in this region and thus the low velocities can be explained by higher crack density of this fault zone.

The low velocity obtained at 9 and 13.5 km depth underneath the Roer Valley Graben corresponds to the location of several earthquake swarms that have occurred in the past. Because of the number of earthquakes at this depth (243), a strongly faulted zone can be expected (0'Connell & Budiansky, 1974). As highly faulted zones lower the Vp-velocity more in comparison to the S-wave velocity and can thus explain the observed low Vp/Vs values.

5.5 Conclusions and perspectives

On the results of the local earthquake tomography, the large tectonic structures like the Brabant Massif, the Ardennes Allochthon, the Roer Valley Graben and the Eifel Volcanic Province are recognisable by their own velocity structure, indicating that they have middle/lower crustal roots. it is also possible to recognise the superficial geological structures like the sediment infill of the Roer Valley Graben and the Trier Graben.

The local seismic tomography of the Belgian crust confirmed several trends that have been determined in the previous chapter on the Moho depth, like the Moho uplift to 28 km of depth underneath the Campine region and the Eifel Volcanic Province. Furthermore, the tomographic

inversion enables us to discriminate between the three theories on the origin of the double reflections oberved in cells W30 and W31 in the Moho depth determination. Because velocities typical of the lower crust are measured at 13.5 km of depth at this location, the theory of the lower crust/upper mantle being upthrusted in the middle crust during the Variscan Orogeny can be favoured over the theories of a reflection on the top of a magmatic chamber or on a Neoproterozoic crust.

The sharp gravimetric contrast between the north and south of Belgium is also a velocity contrast even at depth. Two possible explanations can be put forward at this point. It could be caused by a difference in composition of the middle/lower crust or by deformation of the middle crust during the Variscan Orogeny. More information on its origin may be retrieved by a future combined modelling of the gravimetric, magnetic and seismic data.

Major faulted regions like the Midi overthrust and the Roer Valley Graben also show up on the Vp/Vs-results of the tomographic inversion. The granitic body in the Brabant Massif modelled by the gravimetric data cannot be distinguished however on the results of the tomographic inversion. This is probably due to the fact that it is positioned at the edges of the resolved region.

To further improve the tomographic inversion, the same measures as for the Moho depth are proposed. First of all one can increase the number of earthquakes used in the study by ameliorating the location of the now insufficiently located older earthquakes or by waiting several years so that more earthquakes become available, maybe even at other locations as is the case for the 2008-2009 earthquake swarm near Court Saint Etienne. Secondly, one could add new stations to increase the number of rays. With these new ray trajectories, it might be possible to resolve more regions and/or use a finer grid

.

Conclusions

As we have seen in the introduction, the crust is constantly deforming under the influence of a stress field induced by the tectonic plate movements. This deformation is evidenced by intraplate earthquakes and mainly greatly on the geological evolution of the area and the pre-existing structural trends in the basement of this area. In the TOPO-Europe project (Cloetingh *et al.*, 2007), in which the influence of the lithospheric and lower crustal structure on the topography and other superficial structures is studied. Its influence on human life is also evaluated. Before such a study can be performed in Belgium, the lower crustal and upper mantle structures have to be very well known. This is not the case, yet. Therefore, the Moho depth has been determined using wide-angle PmP- and SmS-waves registered by the Belgian seismic network and a local seismic tomography was performed using arrivals of the direct P- and S-waves registered by the Belgian seismic network in this study.

The results of the Moho depth determination allow improving the current maps of Moho depth in Europe as published by Ziegler (1990) and Dèzes and Ziegler (2001) with whom no correspondence is observed at this point. The Moho depth underneath the Belgian onshore part of the Brabant Massif was evaluated as 31 ± 1.9 km. Such a degree of precision has not been reached before. The fact that the Moho can be visualized by wide-angle seismology and not by reflection seismology might give an indication of the nature of the Moho boundary underneath the Brabant Massif. It suggests a gradient zone with anisotropic layers in which the horizontal velocity is higher than the vertical velocity.

More to the east, the Moho depth has been evaluated at about 28 km for PmP-waves and 32 km for the SmS-waves for the Campine region to the west of the Roer Valley Graben. Underneath the northern part of the Ardennes and the Roer Valley Graben the Moho is at 31-33 km of depth. The absence of a Moho uplift underneath the Roer Valley Graben indicates that it is a passive rift in an early stage of opening, although the Moho depth needs to be re-evaluated when more data are available.

Underneath the Eifel Volcanic Province, a value of 28 km has been obtained. This Moho depth is in agreement with the uplift observed on the DEKORP profile (DEKORP Research group, 1991) and with the results obtained by receiver function analysis (Budweg *et al.,* 2006). The thinning of the crust is more in agreement with the presence of the upwelling branch of an upper mantle convection cell caused by the subduction of European lithosphere in the Alps then by the presence of an hot mantle plume (Budweg *et al.,* 2006).

At the southeast of Grand-Duchy of Luxemburg, two seismic reflection phases are observed on the seismograms. The first can be interpreted as resulting from the presence of a reflector at depths ranging from 15 to 24 km. The second reflection is interpreted as the current Moho interface at a depth of 37-30 km of depth. The origin of the first reflector could only be determined by the local tomography results. Two possible explanations have been provided in the past (Mechie *et al*., 1983; Giese, 1983): either it represents a reflection on the top of a magmatic chamber, or the crust has thickened by stacking of thrusts and crustal slices during the Variscan Orogeny. According to recent insights, it could also be a reflection on an old Neoproterozoic crust.

The PmP-wave is best visible in the low frequency domain (< 8 Hz). This can help to improve the recognition and determination of PmP-arrival times in comparable studies in the future.

The results of the local seismic tomography seem to indicate an uplift of the Moho underneath the Campine region, as was modelled by Oulidi (1998) and the Moho depth modelled by the PmP-waves in this study. Also underneath the Eifel Volcanic Province, a Moho uplift to 28 km of depth can be expected.

Low crustal velocities can be modelled at 13.5 km of depth at the location of the double reflection at the south east of the Grand Duchy of Luxembourg. This allows us to determine the origin of the reflection seen at 15 to 24 km in this region when the Moho depth was determined. It is probably a reflection on a lower crust/upper mantle that was thrusted into the crust during the Variscan Orogeny (Mechie *et al*., 1983; Giese, 1983).

It is also possible to recognise the major tectonic structures by their own velocity structure like the Brabant Massif, the Ardennes Allochthon, the Roer Valley Graben and the Eifel Volcanic Province and some superficial geological structures like the sediment infill of the Roer Valley Graben and the Trier Graben.

The sharp gravimetric contrast separating the north and the south of the country also corresponds to a velocity contrast (6.50 to 5.85 km/s) even at depth, indicating a possible crustal separation over the entire crust. Two explanations can be put forward. It could be a difference in crustal composition in the middle and lower crust or it is a deformation zone in the middle/lower crust due to the Variscan Orogeny. This should be further evaluated by remodelling the gravimetric data combined with magnetic and seismic data.

Fractured regions like the Midi overthrust and the Roer Valley Graben show up on the Vp/Vs-results of the tomographic inversion, because they are characterised by low Vp/Vs-values, low Vp-values and normal Vs-values. The granitic body modelled by the gravimetric data cannot be identified on the results of the tomographic inversion. This is probably due to the fact that it is positioned at the edges of the resolved region.

Outlook

To be able to determine the Moho depth at more places and to have a finer node spacing in the tomographic inversion grid than in this study, several approaches can be followed. First of all one can increase the number of earthquakes used in the study. Simply by waiting several years so that more earthquakes, maybe even at other locations as is seen with the 2008-2009 earthquake swarm near Court Saint Etienne become available, so that more cells will have 5 or more PmP- or SmS-reflection points or more rays would cross the region. Secondly, one could add new stations to increase the number of traces and therefore the number of cells. In this case, the distance between the sources and the stations has to be taken into account (preferably between 90-120 km) and the conditions for placing the stations need to be perfect, as is not the case for the Zevekote, Markegem and Ronse stations. The three latter stations were placed on a considerable sediment cover and therefore the level of noise is very high, making it difficult to determine the different phases. New information will be obtained when the first data arrive from the station in Ostend that is placed on the basement.

More information on the structure of the Belgian crust could also be obtained from a combined inversion of the seismic, gravimetric and magnetic data.

As for the Inver3D programme, it has the potential to be a useful inversion programme for local seismic tomographies, but some large changes still have to be done, like debugging the ray tracing

component and some parallel programming. In the future, it might also be useful to add a hypocenter-inversion coupling in the programme and to add a simultaneous inversion option for both Vp/Vs-models.

Nederlandse Samenvatting

De complexiteit van de korst

Het Belgische territorium, dat zich situeert aan de noordelijke rand van het deformatiefront van de Variskische Orogenese, heeft een complexe vervormingsgeschiedenis gekend. Het is opgebouwd uit verschillende structuren zoals de Caledonische Massieven (het Brabant Massief en de Ardeense Inliers (Rocroi en Stavelot)), de Condroz regio en het Variskische Allochtoon. De Ardeense Inliers en het Brabant Massief werden vervormd door de Caledonische Orogenese, wanneer Avalonia met Baltica en Laurentia botste. De eersten werden vervormd tijdens de Ardeense fase, de laatste tijdens de Brabant fase. Na een episode van extensie en afzetting werden de Ardeense Devoon- en Carboonafzettingen vervomd tijdens de Variskische Orogenese, wanneer Laurussia botste met Gondwana om Pangeae te vormen. De Rhenohercynische zone van het Variskisch vervormingsfront, tot welke de Ardeense sedimentaire bekkens behoren, gedroeg zich als een “thin-skinned fold and thrust belt”. Het werd verschillende kilometers naar het noorden verplaatst langsheen de Midi-overschuiving en zodoende over de zuidoostelijke rand van het Brabant Massief geduwd. Gedurende de Alpijnse Orogenese was het Belgische territorium vrij stabiel en heeft het niet veel vervorming gekend, behalve in zijn meest noordoostelijke hoek, waar de Roervalleislenk opende tijdens het Oligoceen als een deel van het Europese Cenozoïsche Riftsysteem. Deze ingewikkelde vervormingsgeschiedenis wordt weerspiegeld in de complexiteit van de Europese korst. Wanneer de snelheid waaraan de verschillende seismische golven zich voortplanten in de korst bepaald wordt, dan worden verschillende blokken zichtbaar, met elk een eigen interne seismische snelheidsstructuur, die kunnen worden toegekend aan geologisch verschillende terreinen van de Caledonische en Variskische Orogenese. De gemiddelde dikte van de korst is 28 tot 30 km, behalve onder de Rijnslenk waar de korst verdunt tot 25-26 km en onder het Rhenisch Massief waar de Moho tot 37 km diep gaat. Onder de Alpen verdikt de korst zelfs progressief tot een 60 km onder de Centrale Alpen.

Zelfs nu vervormt de korst nog steeds onder een geodynamisch spanningsveld ten gevolge van de opening van de Atlantische Oceaan en de noordwaartse beweging van Afrika. Een indicatie hiervoor zijn de intraplaataardbevingen die Europa treffen, vooral in de Rijnslenk (die ook de Roervalleislenk bevat), Zuid-Noorwegen, West-Frankrijk, enz. Hoe de verschilllende Europese regios reageren op dit spanningsveld hangt af van hun vroegere geologische geschiedenis. Heterogeniteiten worden veelal overgeërfd van vroegere bekkengeometriën, die zelf beïnvloed worden door al bestaande sokkelstructuren. Bijvoorbeeld de positie van het Europese Cenozoïsche Riftsysteem dat zich uitstrekt van de Nederlandse Noordzee tot de westelijke Middellandse Zee, wordt bepaald door de reactivatie van Perm-Carboon schuifsystemen. Het is dus belangrijk om te weten welke structuren kunnen worden gereactiveerd tijdens het huidige spanningsveld en welke niet, zodat hun invloed op het menselijke leven kan bestudeerd worden. Dit is één van de objectieven van het TOPO-Europe project (Cloetingh *et al.*, 2007), waarin de invloed van de lithosfeer en de onderkorststructuur op de topografie en andere oppervlakkige structuren kan bestudeerd worden. Vooraleer zo’n studie in België kan gebeuren, moet de structuur van de midden- en onderkorst zeer goed gekend zijn. Omdat dit nog niet het geval is, zal de huidige kennis met deze studie worden vergroot door de diepte van de Moho onder België te bepalen en een lokale seismische tomografie uit te voeren.

De huidige kennis van de structuur van de korst

In België is er niet veel bekend over de extensie van de verschillende oppervlakkige korststructuren in de diepte, vooral in de midden- en onderkorst. Geofysische methoden zijn een belangrijk hulpmiddel om de geologische structuur van de Belgische korst te bestuderen omdat, behalve een paar dagzomen, de meeste structuren bedekt zijn door een dikke laag Tertiaire en Quartaire sedimenten. Tot nu toe konden alleen seismische profielen, gravimetrische en magnetische data een idee geven over de geologische structuur. Al deze methoden hebben een aantal beperkingen, zo geven de seismische reflectie- en refractiestudies niet veel informatie over de midden- en onderkorst omdat er geen reflecterende of refracterende horizons zichtbaar zijn op deze dieptes. Verder geven ze ook alleen een 2D-zicht op de aanwezige structuren. Gravimetrische gegevens vertonen dan weer een tendens om meer te focussen op oppervlakkige structuren dan op diepe structuren, wat het dus niet het beste hulpmiddel maakt om de diepe korst te bestuderen. Magnetische gegevens zijn even gevoelig voor diepe als ondiepe structuren, maar kunnen alleen de structuur tonen van magnetische objecten. Waar significante magnetische contrasten ontbreken, kan geen informatie bekomen worden.

In de jaren 70 en 80 werden verschillende seismische reflectie- en refractieprofielen geschoten in België en omringende landen. Op deze profielen wordt het Brabant Massief gekarakteriseerd door een niet-reflectieve midden- en onderkorst onder de welke geen Moho kon worden waargenomen. Alleen de sedimentbedekking op het massief en de Midi-overschuiving zijn zichtbaar. Verder weg van het Brabant Massief worden verschillende korststructuren zichtbaar en kan de Moho-diepte worden bepaald. In het oosten verdiept de Moho van 8 s TWT tot 10 s TWT bij het Brabant Massief langsheen het DEKORP profiel. In het zuiden verdiept de Moho van ongeveer 10 s TWT bij de Belgische-Franse grens tot 13 s TWT net ten noorden van de Bray breukzone langs het ECORS profiel. In de Noordzee kon de Moho-diepte bepaald worden ten noorden en ten zuiden van het Brabant Massief maar niet er onder. De Moho komt hier overeen met een diepte van 10 s TWT langs beide zijden van het massief. Ook in de regio van de Eifel Vulkanische Provincie werden verschillende refractieprofielen geschoten. Langsheen sommige van deze profielen is er een dubbele refractie zichtbaar. Eén in de middenkorst op een diepte variërend tussen 10 km en 20 km en een Moho-reflectie rond 30 km. De oorsprong van deze dubbele reflectie is niet duidelijk. Ze wordt ofwel verklaard als een reflectie op de rand van een oude magmakamer of als een reflectie op een oude onderkorst/bovenmantel die in de korst is geschoven gedurende de Variskische Orogenese. De Moho-diepte is ook bepaald geweest onder de Eifel Vulkanische Provincie door een Receiverfunctie-analyse. Bij deze studie werd de diepte van de Moho bepaald op een 28 km onder het centrum van de Eifel Vulkanische Provincie en rond een 32 km in het oosten van België.

Gravimetrische en magnetische gegevens tonen aan dat er een groot verschil is in de korst in het noorden en het zuiden van België. In het noorden wordt de korst gekenmerkt door hoge gravimetriewaarden, verklaard door de hogere dichtheid ($\rho > 2.70$) van de Cambrium- en Siluursedimenten van het Brabant Massief. In het zuiden worden de lage gravimetriewaarden dan weer verklaard door de aanwezigheid van lichte ($2.64 < \rho < 2.70$) Devoon- en Carboonsedimenten. Eigenlijk moet de hele onderkorst uit lichte sedimenten zijn opgebouwd om deze anomalie te verklaren. Deze scherpe transitie wordt ofwel verklaard door een snel zuidwaarts wegduiken van het Brabant Massief of door een structurele scheiding in de volledige korst tussen de Ardennen en het Massief van Brabant (Everaerts, 2000). Everaerts(2000) slaagde er echter ook in de gradiënt te

modelleren met alleen oppervlakkige structuren, namelijk de aanwezigheid van het bekken van Mons en het zachtjes wegzinken van het Brabant Massief naar het zuiden. Verder wordt de noordelijke positieve anomalie onderbroken door een negatieve anomalie die wordt geïnterpreteerd als een Ordovicische batholiet of een Precambrisch intrusief lichaam dat de vervorming van het Brabant Massief blokkeerde gedurende de Brabant fase. Onder de Kempen bereikt de positieve anomalie haar maximum. Deze waarden kunnen niet verklaard worden door de lichte sedimenten die het Kempens bekken vullen, maar worden waarschijnlijk verklaard door de opheffing van de grens tussen de midden- en onderkorst of door een opheffing van de Moho-discontinuïteit. Niet alleen gravimetrische data zien een scheiding in de korst tussen het noorden en zuiden van België. Magnetische gegevens tonen een magnetische diepe korst onder de Ardennen en een niet-magnetische korst onder het Brabant Massief. Deze diep zittende magnetische korst wordt geïnterpreteerd als Neoproterozoïsche korst. De oppervlakkige magnetische anomalieën komen overeen met de magnetische Paleozoïsche sedimenten van de verschillende Caledonische Massieven.

De objectieven van de studie en de gebruikte dataset

Het algemene doel van deze thesis is om het inzicht in de structuur, meer specifiek van de Belgische midden- en onderkorst te verbeteren. Dit zal worden bereikt door de diepte van de Moho te bepalen en een lokale seismische tomografie uit te voeren. Beide mehodes maken gebruik van de aankomsttijden van de verschillende seismische golven. Dit zijn golven die ontstaan bij aardbevingen en explosies en die zich door de aarde voortplanten. Na een aardbeving ontstaan verschillende types van lichaams- en oppervlaktegolven. De twee belangrijkste lichaamsgolven zijn de P- en S-golven of respectievelijk de primaire of longitudinale golven en de secundaire of transversale golven. De P-golven worden primaire golven genoemd omdat ze zich met een hogere snelheid voortplanten dan de S-golven en dus eerst in een seismisch station aankomen. Wanneer deze lichaamsgolven het aardoppervlak bereiken, dan kunnen ze zich langsheen dit oppervlak voortplanten als oppervlaktegolven. In de aardkorst wordt elk gesteente gekenmerkt door een eigen seismische voortplantingssnelheid. Wanneer de seismische golven een groot snelheidscontrast bereiken, dan zullen deze golven gereflecteerd, gerefracteerd of kritisch gerefracteerd (hierbij plant de golf zich langsheen het oppervlak van het snelheidscontrast voort en wordt ook wel kopgolf genoemd) worden. Wanneer dit op de Moho gebeurt, dan krijgen deze verschillende golven een specifiek symbool. Zo wordt een op de Moho-gereflecteerde golf voorgesteld als PmP of SmS. Een kopgolf langsheen de Moho wordt voorgesteld als Pn of Sn naargelang het type lichaamsgolf. Gewoon gerefracteerde golven worden op een onderliggend snelheidscontrast gereflecteerd of gerefracteerd en worden dan ook naar dit snelheidscontrast genoemd. Om de diepte van de Moho te bepalen zal gebruik gemaakt worden van de aankomsttijden van de op de Moho gereflecteerde golven, voor het uitvoeren van de seismische tomografie wordt gebruik gemaakt van de aankomsttijden van de rechtstreekse seismische golven (dus golven die zich enkel in de korst voortplanten). Aangezien seismische golven de basis zijn om de Moho-diepte te bepalen en de seismische tomografie uit te voeren, zijn er dus aardbevingen en explosies nodig als bron van deze seismische golven. Om precieze Moho-dieptes te kunnen bepalen en tomografische resultaten te kunnen bekomen, moeten de gebruikte aardbevingen zeer goed bepaald zijn zowel in de tijd als in de ruimte.

Aardbevingen worden niet alleen gelokaliseerd met gegevens afkomstig van het Belgische seismische netwerk, maar ook met gegevens afkomstig van naburige netwerken zoals het Bennsberg seismisch netwerk. De gegevens van dit netwerk zullen ook gebruikt worden om de lokale seismische tomogafie

uit te voeren, maar niet om de diepte van de Moho te bepalen. Omdat de seismogrammen geregistreerd door de verschillende seismometers van dit netwerk niet ter beschikking werden gesteld, konden de aankomsttijden van de PmP- en SmS-golven niet worden bepaald, alleen de aankomsttijden van de P- en S-golven werden ter beschikking gesteld. Uiteindelijk werden drie soorten bronnen gebruikt om de Moho-diepte te bepalen en de lokale seismische tomografie uit te voeren: lokale aardbevingen in België en omliggende regio's, mijn-geïnduceerde aardbevingen in Duitsland en artificiële explosies in de Noordzee. Ten gevolge van homogeniteitsredenen (zie verder) zullen alleen de lokale aardbevingen gebruikt worden voor de lokale seismische tomografie. Voor de bepaling van de diepte van de Moho zullen de drie verschilllende bronnen worden gebruikt. Omdat de lokale aardbevingen vooral gebeuren in het oosten en noordoosten van België en de meeste stations in het zuiden van het land geplaatst zijn, zou alleen de diepte van de Moho kunnen worden bepaald onder de Ardennen, daarom werden zowel de Duitse mijn-geïnduceerde aardbevingen als de Noordzee-explosies aan de dataset toegevoegd.

De mijn-geïnduceerde aardbevingen zouden informatie moeten leveren over het zuidoosten van het Belgisch territorium en het Groothertogdom Luxemburg. Deze mijn-geïnduceerde aardbevingen waren oorspronkelijk alleen gelokaliseerd met de gegevens van het Bennsberg netwerk, wat geen goed gelokaliseerde aardbevingen oplevert. Daarom werden ze geherlokaliseerd met zowel de gegevens van het Bennsberg netwerk als deze van de Belgische stations. Bij de herlokalisatie kan hun diepte worden vastgesteld op 1 km omdat de mijnen die deze aardbevingen induceren niet dieper zijn dan 1 km.

De Noordzee-explosies werden aan de dataset toegevoegd om informatie over het Massief van Brabant te bekomen. Deze explosies werden uitgevoerd door de marine van zowel het Belgische als het Nederlandse leger om bommen die in de Noordzee zijn achtergelaten tijdens de Tweede Wereldoorlog te ontmijnen. Beide legers verspreiden de locatie en de tijd van ontmijning. Omdat ze zich op de rand van het Belgische seismisch netwerk bevinden, is het zeer moeilijk om hen beter te lokaliseren met de aankomsttijden van de seismische golven. Daarom worden de coördinaten die verpreid werden door het leger gebruikt voor de plaatsbepaling en moet alleen de exacte tijd (seconden) van de ontploffingen bepaald worden door gebruik te maken van de aankomsttijden van de verschillende golven in de verschillende stations. De lokale aardbevingen werden geherlokaliseerd omdat de aardbevingsdatabase van de Koninklijke Sterrenwacht van België een classificatie mist die toelaat goed-gelokaliseerde aardbevingen te selecteren en omdat sommige aardbevingen verschillende locaties hebben in de database.

Omdat alleen goed gelokaliseerde aardbevingen kunnen gebruikt worden om de Moho-diepte en de lokale seismische tomografie uit te voeren, werd beslist om alle aardbevingen te herlokaliseren vooraleer de Moho-diepte te bepalen en de lokale seismische tomografie uit te voeren. Voor deze herlokalisatie werd het programma mknorm2000 gebruikt, een programma dat ontwikkeld werd door H. Martin aan de Koninklijke Sterrenwacht van België en gebaseerd op het programma Hypo71 (Lee & Lahr, 1975). In vergelijking met Hypo71 kunnen er in dit programma twee verschillende modellen voor P- en S-golven gebruikt worden. De Vp/Vs-verhouding kan dus verschillen van laag tot laag, waar bij Hypo71 een constante Vp/Vs-verhouding wordt gebruikt. De dikte van de verschillende lagen moet wel steeds dezelfde zijn bij zowel de Vp- als Vs-snelheidsmodellen. Om de gevoeligheid van de berekende locaties aan de geometrie van het netwerk te evalueren, berekent het programma mknorm2000 500 verschillende locaties voor elke aardbeving door aan de aankomsttijd van de P- en S-golf een ruis met een normaaldistributie met een standaarddeviatie van 0.05 s voor P-golven en één

van 0.1 s voor S-golven toe te voegen. De uiteindelijke locatie van de aardbeving is het gemiddelde van de 500 mogelijke oplossingen. De spatiale distributie van de gehele oplossingenset wordt gebruikt om het 95%-confidentie-interval van de oplossing te berekenen. Uiteindelijk werden 140 aardbevingen, 13 mijn-geïnduceerde aardbevingen en 30 Noordzee-explosies goed gelokaliseerd en gebruikt in de verdere studie.

De diepte van de Moho onder België

De dikte van de korst onder België werd geëvalueerd door gebruik te maken van aankomsttijden van PmP- en SmS-golven en een horizontaal gelaagd snelheidsmodel. De positie van de reflectiepunten van de gereflecteerde golven werd berekend gebaseerd op zowel de epicentrumlocatie, de locatie van de stations als de berekening van het golftraject in het snelheidmodel. Het studiegebied werd onderverdeeld in een grid van 20 bij 20 km^2 en de reflectiepunten in elke cel werden gegroepeerd. Voor elke gridcel werd, door gebruik te maken van de hieronder beschreven procedure, een afzonderlijke Moho-diepte berekend voor de PmP- en SmS-gegevens die in de cel gelegen zijn. De Moho-diepte waarvoor de in het CAL-snelheidmodel berekende aankomsttijden de gemeten aankomsttijden van de PmP- of SmS-golven het best benaderen, werd bepaald door de Moho-diepte te variëren tussen 20 en 41 km met een stap van 0,01 km. De Moho-diepte van een cel was dan het gemiddelde van al deze Moho-dieptes. Om de betrouwbaarheid van de verkregen Moho-diepte te bepalen werden de 95%-confidentie-intervallen via een student t-verdeling berekend. Wanneer de lengte van de 95%-confidentie-intervallen groter is dan 4 km of wanneer er minder dan 5 relfectiepunten in een cel gelokaliseerd zijn, werd het resultaat als onbetrouwbaar aanzien. Vooraleer de resultaten besproken kunnen worden, wordt de invloed van het gebruikte snelheidsmodel geëvalueerd. Daarvoor werd de Moho-diepte berekend in 1000 verschillende snelheidsmodellen die gegenereerd werden door ruis met een normaaldistributie toe te voegen aan elke laag van het originele 1D-snelheidsmodel. Deze distributie komt overeen met diegene die verkregen werd bij de modellisatie van het CAL-snelheidsmodel. De gemiddelde Moho-diepte verschilt 0,04 km van deze berekend in het originele model en de standaarddeviatie over deze 1000 verschillende modellen bedraagt 1,06 km.

De Moho-diepte onder het Belgische gedeelte van het Massief van Brabant werd bepaald op een diepte van 31 ± 1.9 km . Deze graad van precisie werd nog nooit gehaald. Dit resultaat is vergelijkbaar met de dieptes bepaald op seismische reflectieprofielen geschoten op zee. Het feit dat de Moho diepte alleen kan bepaald worden met bredehoeks seismologie en niet door reflectie seismologie kan een idicatie zijn voor de natuur van de Moho-discontinuïteit onder het Brabant Massief. Het wijst op een zone met anisotrope lagen waarin de horizontale snelheid hoger is dan deze in de verticale.

Meer naar het oosten werd de Moho-diepte geëvalueerd met een gecombineerde analyse van PmP- en SmS-seismische fases. Onder het Kempens Bekken ten westen van de Roervalleislenk werd de Mohodiepte geëvalueerd op een diepte van 28 km voor PmP-golven en 32 km voor SmS-golven. Onder het noordelijk gedeelte van de Ardennen en onder de Roervalleislenk bevindt de Moho zich tussen 31 en 33 km diepte. De afwezigheid van een Moho opheffing onder de Roervalleislenk wijst erop dat deze slenk een pasieve rift is in een initiële fase van opening. De diepte onder de Roervalleislenk zou wel moeten worden geherevalueerd wanneer meer gegevens beschikbaar zijn. Met de geregistreerde

SmS-gereflecteerde fases onder de Eifel Vulkanische Provincie werd de Moho-diepte hier bepaald op ongeveer 28 km. Deze diepte komt overeen met de opheffing waargenomen op het DEKORP reflectie profiel en de resultaten bekomen met ontvangerfunctie-analyse . Deze verdunning in de korst kan beter worden verklaard door de aanwezigheid van een omhoogkomende tak van een kleine bovenmantel convectiecel dan door de aanwezigheid van een mantelplume.

Ten zuidoosten van het Groothertogdom Luxemburg werden twee seismische reflecties gezien op de seismogrammen. De eerste kan geïnterpreteerd worden als de aanwezigheid van een sterke intercrustale reflector op dieptes tussen de 15 en 24 km. Deze reflectie kan worden geïnterpreteerd als de reflectie op de top van een oude magmakamer of als een reflectie op een oude Moho die in de korst is geschoven tijdens de Variskische Orogenese of als de reflectie op een oude Neoproterozoïsche korst van Rondonische ouderdom. De tweede reflectie wordt dan geïnterpreteerd als de huidige Moho-discontinuïteit.

De lokale seismische tomografie

In de vorige paragraaf werd de dikte van de korst bepaald. Alhoewel dit belangrijk is, geeft het geen informatie over de structuur en de compositie van de korst. Wanneer men de oppervlakkige geologie echter goed wil begrijpen, moet men ook de geologie in de midden- en onderkorst begrijpen. Omdat deze regio's niet bereikt kunnen worden met boringen (slechts tot 5,6 km in België), kunnen ze niet direct bestudeerd worden en moeten andere technieken worden gebruikt. Bepaalde technieken zoals seismische reflectie- en refractieprofielen, gravimetrische en magnetische gegevens hebben al bepaalde informatie opgeleverd. Een andere techniek die veel gebruikt wordt om de midden- en onderkorst te bestuderen, is de lokale seismische tomografie. Bij een lokale seismische tomografie wordt een driedimensionele snelheidsstructuur van de korst bepaald. De snelheid waarmee seismische golven zich doorheen de korst verplaatsen, hangt af van de compositie ervan en de druk en temperatuur in die korst. De snelheid van de S-golven is daarnaast ook gevoelig voor de aanwezigheid van gassen en vloeistoffen in de korst. Omdat S-golven veel moeilijker te meten zijn, wordt de snelheidsstrucutuur van de S-golven niet bepaald zoals deze van de P-golven maar wordt de Vp/Vs-verhouding berekend. De combinatie van de Vp-snelheidsstructuur en de Vp/Vs-verhouding maakt het mogelijk de compositie en structuur van de korst beter te bepalen dan met elk van deze gegevens afzonderlijk. Dus zal om de midden- en onderkorst onder België te bestuderen een lokale seismische tomografie worden uitgevoerd. Oorspronkelijk was het de bedoeling om het programma INVER3D (Collin, 1998), een tomografisch inversieprogramma ontwikkeld aan de Koninklijke Sterrenwacht van België, te gebruiken. Omdat dit programma nog nooit gebruikt is geweest om een lokale seismische tomografie uit te voeren, werd het eerst uitvoerig getest. De lokale seismische tomografie zou dan ook simultaan worden uitgevoerd met het programma SIMULPS (Evans *et al.*, 1994), een tomografisch inversieprogramma dat wereldwijd wordt gebruikt om seismische tomografieën uit te voeren en dat dus zijn betrouwbaarheid heeft bewezen.

Een seismische tomografie gebruikt dezelfde theorie als een X-stralen CT-scan in de medische wereld. Waar een CT-scan de demping van de röntgenstralen meet op verschillende punten rondom een menselijk lichaam en zo een doorsnede doorheen dit lichaam creëert, zal een seismische tomografie gebruik maken van de aankomsttijden van lichaamsgolven van aardbevingen geregistreerd in een

homogeen netwerk van seismometers. Doordat verschillende gesteenten een andere seismische snelheid hebben, kan door modellisatie de structuur van de korst worden bepaald. Bij een lokale seismische tomografie worden de schattingen van de modelparameters (hypocenters en snelheidsstuctuur) verbeterd door hen te veranderen tot het verschil tussen de berekende en geobserveerde aankomsttijden minimaal is. Hiervoor is in het algemeen een iteratieve procedure nodig, omdat de hypocenterlocatie en de snelheidsstructuur onherroepelijk aan elkaar gekoppeld zijn en dit leidt tot een significante non-lineariteit van de vergelijkingen. Ook zijn verschillende evaluaties van de kwaliteit van de gevonden oplossing noodzakelijk door zowel de resolutie-matrix, de onzekerheid, de verbetering van de datafit als de uniekheid van de finale oplossing te evalueren via verschillende procedures.

Twee programma's werden dus gebruikt om de lokale seismische tomografie uit te voeren: SIMULPS (een programma dat al wereldwijd wordt gebruikt) en INVER3D (een programma ontwikkeld aan de ROB en dat nog nooit werd gebruikt voor zo'n grote tomografie). Alhoewel INVER3D het potentieel heeft om een goed inversieprogramma te worden, moeten nog een aantal problemen opgelost worden.

De lokale seismische tomografie bevestigt verschillende reultaten die in de vorige paragraaf werden bepaald, zoals de Moho-diepte van 28 km onder het Kempens bekken en de Eifel Vulkanische Provincie. Verder maakt de inversie het mogelijk een onderscheid te maken tussen de drie theorieën over de dubbele reflectie zoals waargenomen ten zuidoosten van het Groothertogdom Luxemburg. De theorie over de onderkorst/bovenmantel die in de korst werd geschoven tijdens de Variskische Orogenese kan verkozen worden boven de theorieën van de magmakamer en de reflectie op een oude Neoproterozoïsche korst omdat onderkorstsnelheden gemodelleerd werden op 13.5 km diepte.

Het is ook mogelijk om de verschillende tektonische structuren zoals het Massief van Brabant, het Ardeens Allchtoon, de Roervalleislenk en de Eifel Vulkanische Provincie te herkennen aan hun eigen snelheidsmodel doorheen de korst. Ook verschillende oppervlakkige structuren zoals de sedimenten van de Roervalleislenk en de Trierslenk zijn te herkennen.

Het scherpe gravimetrische contrast dat een scheding tussen het noorden en het zuiden van het land weergeeft, is ook een snelheidscontrast (6.50 tot 8.85 km/s) dat waarschijnlijk een opdeling van de gehele korst voorstelt. Twee mogelijke verkaring kunnen worden naar voor geschoven. Enerzijds kan het verklaard worden door een verschil in samenstelling van de midden en/of onder korst of door een zone van vervorming veroorzaakt door de Variskische Orogenese. Meer informatie over de juiste oorzaak van deze opdeling zou kunnen worden verkregen door het gecombineerd hermodeliseren van de gravimetrische data met de magnetische en seismische gegevens.

Gebroken regios zoals de Midi–overschuiving en de Roervalleislenk zijn zichtbaar op de resultaten van de Vp/Vs-verhouding van de tomografische inversie. De granitische batholiet gemodelleerd door de gravimetrische data kan niet worden waargenomen in de resultaten. Dit komt waarschijnlijk door het feit dat de batholiet gepositioneerd is op de rand van de door de tomografie opgeloste regio.

Toekomstperspectieven

Om de diepte van de Moho op meer plaatsen te kunnen bepalen en om een fijnere grid bij de tomografische inversie te verkrijgen kunnen verschillende manieren van aanpakken gevolgd worden. Ten eerste kan men het aantal aardbevingen dat gebruikt werd in deze studie verhogen door simpelweg een aantal jaren te wachten. Dan zullen er meer aardbevingen beschikbaar worden, zelfs op andere locaties zoals de aardbevingszwerm uit 2008-2009 die in de buurt van Court Saint Etienne heeft plaatsgehad. Op die manier zullen meer cellen 5 of meer PmP- en SmS-reflectiepunten bevatten en zullen meer trajecten de regio doorkruisen zodat een fijner grid kan worden gebruikt bij de tomografische inversie. Ten tweede kan men ook het aantal trajecten verhogen door nieuwe seismische stations te plaatsen. In dit geval moet rekening gehouden worden met het feit dat de afstand tussen de aardbevingen en de stations ideaal is tussen de 90 en 120 km. Verder moet ook de plaatsingsconditie ideaal zijn, zoals wordt aangetoond met de stations van Zevekote, Marke en Ronse. Deze seismische stations werden op een redelijk dik sedimentpakket geplaatst waardoor het ruisniveau vrij hoog is en dit bemoeilijkt het meten van de verschillende aankomsten van de verschillende seismische golven. Nieuwe informatie zal kunnen worden verkregen wanneer de eerste gegevens van het nieuw op de sokkel geplaatste station in Oostende beschikbaar zijn.

Meer informatie over de structuur van de Belgische korst kan ook worden verkregen door een gecombineerde modellisatie uit te voeren van zowel seismische, gravimetrische en magnetische gegevens.

Wat het INVER3D programma betreft, het heeft zeker het potentieel om een goed tomografisch inversieprogramma te worden, maar er moeten nog een aantal grote verbeteringen gebeuren. Zo moet de component die de golftrajecten berekent nog verder gedebugged worden en moeten bepaalde berekeningen parallel geherprogrammeerd worden. In de toekomst kan het ook interessant zijn om een hypocentrum-snelheidsmodelkoppeling toe te voegen aan het programma alsook de mogelijkheid aan te bieden om een simultane inversie van zowel Vp als Vp/Vs-modellen mogelijk te maken.

References:

Adams, R. & Vandenberghe, N. (1999). The Meuse Valley section across the Condroz-Ardennes (Belgium) based on a predeformational sediment wedge, *Tectonophysics*, **304**, 179-195.

Ahorner, L. & Pelzing, R. (1984). The source characteristics of the Liège earthquake of November 8 1983, from digital recordings in West Germany. In: Melchior P. (ed.): *Seismic Activity in Western Europe*, Reidel Publishing Company, 263-289.

Aichroth, B & Prodehl, C. (1990). EGT Central Segment refraction seismic. In: Freeman, R. & Mueller, S. (eds): *Sixth EGT Workshop: Data Compilations and Synoptic Interpretation,* European Science Foundation, France*,* 187-197.

Aki, K. & Lee, W.H.K. (1976). Determination of three-dimensional velocity anomalies under a seismic array using First P arrival times from local earthquakes, I, A homogeneous initial model, *J. Geophys. Res.*, **81**, 4381-99

Aki, K. & Richards, P.G. (1980). In: Freeman W.H. (ed): *Quantitative Seismology: Theory and Methods*, W.H. Freeman and Compagny, San Francisco.

Alexandre, P. (1985). Catalogue des séismes survenus au Moyen-Âge en Belgique et dans les régions voisines. In: Melchior, P (ed), *Seismic activity in Western Europe*, Reidel Publishing company, 189-203.

André, L., Deutsch, S. & Michot, J. (1981). Données géochronologiques concernant le développement tetono-métamorphique du segment Calédonien Brabaçon, *Ann. Soc. Géol. Bel.*, **104**, 241-253.

André, L., Hertogen, J. & Deutsch, S. (1986). Ordovician – Silurian magmatic provinces in Belgium and the Caledonian Orogeny in middle Europe, *Geol.*, **14**, 879-882.

André, L. & Deutsch, S. (1986). Magmatic $^{87}Sr/^{86}Sr$ relicts in hydrothermally altered quartz diorites (Brabant Massif, Belgium) and the role of epidote as a Sr filter, *Contr. Min. and Petr.,* **104**, 241-253.

André, L. (1991). The concealed crystalline basement in Belgium and the « Brabantia » microplate concept: constraints from the Caledonian magmatic and sedimentary rocks. In: André, L., Herbosch, A., Vanguestaine, M. & Verviers, J. (eds.): Proceedings of the international meeting on the Caledonides of the Midlands and the Brabant Massif, 1989. *Ann. Soc. Geol. Bel,* **114**, 117-139.

Burov, E. & Guillou-Frottier, L. (2005). The plume head-continental lithosphere interaction using a tectonically realistic formulation for the lithosphere, *Geophys. J. Int.*, **161**, 469-490.

Blundell, D.J. (1990). Relationships between deep crustal structure and sedimentary basins around Britain. In: Pinet B., Bois C. (eds.): *'The Potential of Deep Seismic Profiling for Hydrocarbon Exploration'*, Editions Technip, Paris, 317-333.

Blundell, D.J., Hobbs, R.W., Klemperer, S.L., Scott-Robinson, R., Long, R., West, T. & Duin, E. (1991). Crustal structure beneath the central and southern North Sea from BIRPS deep seismic reflection profiling, *J. Geol. Soc. London,* **148**, 445-458.

Bouchon, M., and Aki, K. (1977). Discrete wave-number representation of seismic-source wave fields, *Bull. Seis. Soc. Am*., **67**,259-277.

Bouckaert, J., Fock, W. & Vandenberghe, N. (1988). First results of the Belgian Geotraverse 1986 (BELCORP), *Ann. Soc. Géol. Bel.*, **111**, 279-290.

Boulvain, F., Belanger, I., Delsate, D., Dosquet, D., Ghysel, P., Godefroit, P., Laloux, M., Roche, M., Teerlynck, H. & Thorez, J. (2001). New lithostratigraphical, sedimentological, mineralogical and palaeontological data on the Mesozoic of Belgian Lorraine: a progress report, *Geologica Belgica*, **3**, 3-33.

Brauer, A., Endes, C., Günter, C., Litt, T., Stebich, M. & Negendank, J.F.W. (1999). High resolution sediment and vegetation responses to Younger Dryas climate change in varved lake sediments from Meerfelder Maar Germany, *Quaternary Science Reviews*, **18**, 321-329.

Brousse, R. & Bellon, H. (1983). Réflexions chronologiques et pétrologiques sur le volcanism associé au développement des rifts de France, *Bull. Cent. Rech. Explor.-Prod. Elf-Aquitaine*,**7**, 409-424.

Budweg, M., Bock, G. & Weber, M. (2006). The Eifel plume, imaged with converted seismic waves, *Geophys. J. Int.*, **166**, 579-589.

Cahill, T. & Isacks, B. (1992). Seismicity and Shape of the Subducted Nazca Plate, *J. Geophys. Res.*, **97**, 4997-5009.

Calbini, V. (2003). *La structure de la croûte en Belgique par inversion en deux dimensions de données sismiques*, Mst. Sci thesis, Université Catholique de Louvain, 70pp.

Camelbeeck, T. (1994). *Mécanisme au foyer des tremblements de terre et contraintes tectoniques: le cas de la zone intraplaque belge*, Phd thesis, Université Catholique de Louvain, 295pp.

Camelbeeck, T., van Eck, T., Pelzing, R., Ahorner, L., Loohuis, L., Haak, H.W., Hoang-Trong, P. & Hollnack, T. (1994). The 1992 Roermond earthquake, the Netherlands, and its aftershocks, *Geologie en Mijnbouw*, **73**, 181-197.

Chadwick, R.A.; Pharaoh, T.C.; Williamson, J.P.; Musson, R.M.W..(1996). *Seismotectonics of the UK. Final report.* Nottingham, UK, British Geological Survey, 172pp. (WA/96/003)

Chacksfield, C., De Vos, W., D'hooge, L., Dusar, M., Lee, M.K., Poitevin, C., Royles, C.P. & Verniers, J. (1993). A new look at Belgian aeromagnetic and gravity data through image-based display and integrated modelling techniques, *Geol. Mag*., 130, 583-591.

Chou, C.W. & Booker, J.R. (1979). A Backus-Gilbert approach to the inversion of travel time data for three dimensional velocity structure, *Geophys. J.R. Astron. Soc.*, **59**, 325-44

Cloetingh, S.A.P.L., Ziegler, P.A., Bogaard, P.J.F., Andriessen, P.A.M., Artemieva, I.M., Bada, G., van Balen, R.T., Ben-Avraham, Z., Brun, J.-P., Bunge, H.P., Burov, E.B., Carbonell, R., Facenna, C., Friedrich, A., Gallart, J., Green, A.G., Heidbach, O., Jones, A.G., Matenco, L., Mosar, J., Oncken, O., Pascal, C., Peters, G., Sliaupa, S., Soesoo, A., Spakman, W., Stephenson, R.A., Thybo, H., Thorsvik, T., de Vicente,

G., Wenzel, F., Wortel, M.J.R., & TOPO-EUROPE Working Group (2007). TOPO-EUROPE: the geosciences of coupled Deep Reath-surface Processes, *Global and Paletary Change*, **58**, pp 1-118.

Collin, F. (1998). Tomographie sismique en 3 dimensions, Ph. D. Thesis, Université Catholique de Louvain, pp. 113.

Coulon, M. (1992). La distension oligocène dans le nord-est du bassin de Paris (perturbation des directions d'extension et distribution des stylolites, *Bull. Soc. Géol. France,* **162**, 531-540.

Coutant, O. (1990). Programme de Simulation Numérique AXITRA*, Rapport LGIT*, Université Joseph Fourier, Grenoble, France.

Crosson, R.S. (1976). Crustal structure modeling of earthquake data 1. Simultaneous least squares estimation of hypocenter and velocity parameters, *J. Geophys. Res.*, **81**, 3036-46

Debacker, T.N., Sintubin, M. & Verniers, J. (1999). Cleavage/fold relationships in the Silurian metapelites, southeastern Anglo-Brabant fold belt (Ronquières, Belgium), *Geologie &* Mijnbouw, **78**, 47-56.

Debacker, T.N. (2001). *Paleozoic deformation of the Brabant Massif within eastern Avalonia : how, when and why?* Unpublished Ph. D. thesis, Ghent University.

DEKORP Research group (1991). Results of the DEKORP 1 (BELCORP-DEKORP) deep seismic reflection studies in the western part of the Rhenish Massif, *Geophys. J. Int.*, **106**, 203-227.

Delmer, A. (1963). Mijnkaart van het Kempens kolenbekken, *Ann. der mijnen van België*, 739-754.

Demyttenaere, R. (1989). The post-Paleozoic geological history of north-eastern Belgium, *Meded. Kon. Akad. Wetensch. Lett. Schone Kunsten België*, **51**, 51-81.

De Vos, W., Poot, B., Hus, J. & El Khayati, M. (1992). Geophysical characterization of lithologie from the Brabant Massif as a contribution to gravimetric and magnetic modelling, *Bull. Soc. Bel. Géol.*, **101**, 173-180.

De Vos, W., Verniers, J., Herbosch, A. & Vanguestaine, M. (1993). A new geological map of the Brabant Massif, *Geol. Mag.*, **130**, 605-611.

De Vuyst, A. (1967). De verdeling, de op- en neerwaartse voortzetting en de statistische behandeling van de magnetische anomalies van de vertikale intensiteit van België, *Verhandelingen van de Koninlijke Vlaamse Academie voor Wetenschappen*, *Letteren en Schone Kunsten van België, Klasse der Wetenschappen*, **29 (98)**, p 67.

Dèzes, P. and Ziegler, P. A., 2001: *European Map of the Mohorovicic discontinuity*. 2nd EUCOR-URGENT Workshop (Upper Rhine Graben Evolution and Neotectonics), Mt. St. Odile, France.

Duncan, R.A., Petersen, N. & Hargraves, R.B. (1972). Mantle plume, movement of the European plate, and polar wandering, *Nature*, **239**, 82-85.

Eberhart-Phillips, D. (1986). Three-dimensional velocity structure in the northern California Coast Ranges from inversion of local earthquake arrival times, *Bul. Seis. Soc. Am.*, **76**, 1025-1052.

Evans, J.R., Eberhart-Phillips, D. & Thurber, C.H., 1994. User's manual for SIMULPS 12 for imaging Vp and Vp/Vs: a derivative of the "Thurber" inversion SIMUL3 for local earthquakes and explosion, *U.S. Geol. Surv. Open File Rep*., 94-431.

Everaerts, M., Poitevin, C., De Vos, W. & Sterpin, M. (1996). Integrated geophysical/ geological modelling of the western Brabant Massif and structural implications, *Bull. Soc. Belge Géol.*, **105**, 41-59.

Everaerts, M. (2000). L'interprétation structurale de la Manche au Rhin: apport du filtrage des champs de potentiel, Ph. D. Thesis, Université Catholique de Louvain, pp 167.

Fielitz, W. (1992). Variscan transpressive inversion in the northwestern central Rhenohercynian belt of western Germany, *J. Struct. Geol.*, **14**, 547-564.

Fielitz, W. & Mansy, J.-L. (1999). Pre- and synorogenic burial metamorphism in the Ardenne and neighbouring areas (Rhenohercynian zone, central Europe Variscides), *Tectonophysics*, **309**, 227-256.

Fowler, C. M. R. (2005). *The Solid Earth: An introduction to Global Geophysics*, Cambridge University press, Cambridge, pp. 685.

Geluk, M.C. (1990). The Cenozoic Roer Valley Graben, southern Netherlands, *Mededel. Rijks. Geol. Dienst*, **44**, 65-72.

Geluk, M.C., Thuin, E.J.th., Dusar, M., Rijkers, R.H.B., van den Berg, M.W. & van Rooijen, P. (1994). Stratigraphy and tectonics of the Roer Valley Graben, *Geologie en Mijnbouw,* **73**, 129-141.

Geukens, F. (1999). Notes accompagnant une révision de la carte structurale du Massif de Stavelot, *Aardkundige Mededelingen*, **9**, 183-190.

Giese, P., Prodehl, C. & Stein, A. (eds)(1976). Explosion seismology in central Europe-data and results, Springer, Berlin, pp 429.

Giese, P. (1983). The Evolution of the Hercynian Crust-Some Implications to the Uplift Problem of the Rhenish Massif. In: Fuchs, K., von Gehlen, K., Mälzer, H., Murawski, H., & Semmel, A. (eds.): *Plateau Uplift The Rhenish Shield-A case History*, Springer-Verlag, 303-314.

Giese, P. (1995). Main Features of geophysical structures in Central Europe. In: Dallmeyer, R.D., Franke, W. & Weber, K. (eds):*Pre-Permian Geology of Central and Eastern Europe*, Springer, Berlin, 7-25.

Goemare, E. & Dejonghe, L. (2005). Paleoenvironmental reconstruction of the Mirwart Formation (Pragian) in the Lambert quarry (Flamierege, Ardenne Belgium), *Geologica Belgica*, **8/3**, 37-52.

Goemare, E., Geeninckx, S. & Vanbrabant, Y. (2006). Les coupes de Tihange et de Huy: Etude paléoenvironnemental des Formations de Marteau et de Bois d'Ausse (Dévonien Inférieur) au bord nord du Synclinorium de Dinant, Belgique, *Géol. De la France*, **1-2**, 35-39.

Griesshaber, E., O'Nions, R.K. & Oxburgh, E.R. (1992). Helium and carbon isotope systematics in crustal fluids from the Eifel, the Rhine Graben and Black Forest, F.R.G., *Chemical Geology*, **99**, 213-235.

Haberland, C. & Rietbrock, A., 2001. Attenuation tomography in the western central Andes: A detailed insight into the structure of a magmatic arc, *J. Geophys. Res.*, **106**,11151-11167.

Hawley, B.W., Zandt, G. & Smith, R.B. (1981). Simultaneous inversion for hypocenters and lateral velocity variations: an iterative solution with a layered model, *J. Geophys. Res.*, **86**, 7073-76.

Hestenes, M.R. & Stiefel, E. (1952). Methods of conjugate gradients for solving linear systems, *J. Research of the National Bureau of Standards*, **49**, 409-436.

Hirn, A., Damotte, B., Torreilles, G. & ECORS (1987). Crustal reflection seismics : the contibutions of oblique, low frequency and shear wave illuminations, *Geophys. J. R. astr. Soc.*, **89**, 287-296.

Husen, S., Kissling, E., & Flueh, E.R. (2000). Local earthquake tomography of shallow subduction in north Chile: a combined onshore and offshore study, *J. Geophys. Res*., **105**, 28,183-28,198.

Illies, J.H., Prodehl, C., Schmincke, H.U. & Semmel, A. (1979). The Quaternary uplift of the Rhenish Shield in Germany, **61**, 197-225.

International Commission on Stratigraphy (2009). *International Stratigraphic Chart*, www.stratigraphy.org.

Jongmans & Camelbeeck (1994). Structure superficielle de la croûte en Ardenne Belge obtenue à partir des enregistrements de tirs de carrière : méthodologie et premiers résultats, *Ann. Soc. Géol. Bel.*, **116**, 119-127.

Kearey, P. & Brooks, M. (eds.) (1991): *An Introduction to Geophysical Exploration*, Blackwell Scientific Publications, pp 272.

Kissling, E. (1988). Geotomography with local earthquake data, *Rev. Geophys.*, **26**, 659-698.

Kissling, E., Ellsworth, W.L., Eberhart-Phillips, D. & Kradolfer, U. (1994). Initial reference models in local earthquake tomography, *J. Geophys. Res.*, **99**, 19, 635-19, 646.

Klemperer, S. & Hobbs, R. (eds.) (1991): *The BIRPS Atlas: Deep seismic reflection profiles around the British Isles*, Cambridge university press, Cambridge, 107-116.

Lawson, C.L. & Hanson, R.J. (eds.) (1974). *Solving Least Squares Problems*, Prentice-Hall, Englewood Cliffs, NJ.

Lee, W.H.K. & Lahr, J.C. (eds.) (1975): « *HYPO71 » a computer program for determining hypocentral location, magnitude and first motion pattern of local earthquakes,* US. GEOL. SURV., open file rept, **114**, 75-363.

Lee, W. H. K. & Pereyra, V. (1993). Mathematical introduction to seismic tomography. In: Iyer, H.M. & Hirahana, K. (eds): *'Seismic Tomography'*, Chapman and Hall, London, p. 9-22.

Lee, W. H. K. & Stewart, S. W. (1989). Large-Scale processing and analysis of digital waveform data from the USGS Central California Microearthquake Network. In: Litehiser, J.J (ed): *'Observatory Seismology'*, University of California Press, p. 86-98.

Legrand, R. (1967). Ronquières. Documents géologiques, *Mémoires pour servir à l'Explication des Cartes Géologiques et Minières de la Belgique,* Mémoire, **6**, 1-60.

Lin, C.H. & Roecker, S.W. (1990). Determination of earthquake hypocenters, focal mechanisms, and velocity structure in the Morgan Hill area through 3-D circular ray tracing, *Eos. Trans. Am. Geophys. Union*, **71**, 1445.

Lippolt, H.J. (1983). Distribution of volcanic activity in space and time. In: Fuchs, K., von Gehlen, K., Mälzer H., Murawski, H. & Semmel, A. (eds.): *Plateau Uplift The Rhenish Shield-A case History*, Springer-Verlag, 112-120.

Lutgens, F.K. & Tarbuck, E.J. (1989). *Essentials of Geology*, Merrill publishing company, Colombus, Ohio, pp 378.

Mansy, J.-L., Everaerts, M. & De Vos W. (1999). Structural analysis of the adjecent Acadian and Variscan fold belts in Belgium and northern France from geophysical and geological evidence, *Tectonophysics*, **309**, 99-116.

Matte, P. & Hirn, A. (1988). Seismic signature and tectonic cross section of the Variscan crust in western France, *Tectonics*, **7**, 141-155.

Mechie, J., Prodehl, C., Fuchs, K., Kaminski, W., Flick, J., Hirn, A., Ansorge, J., & King, R. (1982). Progress report on Rhenish Massif seismic experiment, *Tectonophysics*, **90**, 215-230.

Mechie, J., Prodehl, C. & Fuchs, K. (1983). The Longe-Range Seismic Refraction Experiment in the Rhenish Massif. In: Fuchs, K., von Gehlen, K., Mälzer H., Murawski, H., & Semmel, A. (eds.): *Plateau Uplift The Rhenish Shield-A case History*, Springer-Verlag, 260-275.

Meissner, R., Bartelsen, H., Glocke, A. & Kainski, W. (1976). An interpretation of Wide-Angle Measurements in the Rhenish Massif. In: Giese, P., Prodehl, C. & Stein, A. (eds.): *Explosion Seismology in Central Europe*, Springer-Verlag, 245-256.

Meissner, R., Wever, Th. & Flüh E.R. (1987). The Moho in Europe-Implications for crustal development, *Annales Geophysicae*, **5B**, 357-364.

Menke, W. (1989): *Geophysical Data Analysis: Discrete Inverse Theory*, Academic Press, San Diego, California.

Meyer, R. & Foulger, G.R. (2007). The European Province is not caused by mantle plumes, www.mantleplumes.org.

Michelini, A. & Mac Evilly, T.V., 1991. Seismological studies at Parkfield, I, Simultaneous inversion for velocity structure and hypocenters using cubic B-splines parameterization, *Bull. Seismol. Soc. Am.*, **81**, 524-552.

Michot, P. (1980). Le segment tectogenic calédonien belge, *Mémoires de l'Académie Royal de Belgique, Classe de Sciences*, Collection in – 8°, 2ème série, **43**, 1-61.

Mooney, W.D. & Prodehl, C. (1978). Crustal Structure of the Rhenish Massif and Adjacent Areas; a Reinterpretation of Existing Seismic-Refraction Data, *J. Geophys.*, **44**, 573-601.

Morgan, W.J. (1971). Convection plume in the lower mantle, *Nature*, **230**, 42-43.

Murphy, J.B., Keppie, J.D. Dostal, J. & Nance, R.D. (1999). Neoproterozoic-early Paleozoic evolution of Avalonia. In: Ramos, V.A. & Keppie, J.D. (eds.): *Laurentia-Gondwana Connections before Pangea,* Geological society of America Special Papers, **336**, 253-266.

O'Connell, R.J., Budiansky, B. (1974) : Seismic velocities in Dry and Saturated Cracked Solids, *J. Geophys. Res.*, **79**,5412-5426.

Officer, C.B. (1974). *Introduction to Theoretical Geophysics*, Springer-Verlag, Berlin.

Oncken, O., Plesch, A., Weber, J., Ricken, W., Schrader, S. (2000). Passive margin detachment during arc-continent collision (Central Europe Variscides). In: Franke, W., Haak, V., Oncken, O. & Tanner, D. (eds.) : *Orogenic Processes : Quantification and Modelling in the Variscan Belt*, Geological society of London, 199-216.

Oulidi H. (1998): Modèle géophysique de la croûte dans le nord de la France et en Belgique- étude de la limite sud du massif du Brabant, Ph D. Thesis, Université Catholique de Louvain, pp. 258.

Paige, C.C. & Saunders, M.A. (1982). An algorithm for sparse linear equations and sparse least squares. *ACM Trans. Math. Software*, **8**, 43-71

Pardo, M., Monfret, T., Vera, E., Eisenberg , E., Gaffet, S., Lorca, E., and Perez, A. (2002). Seismotectonic and Body-wave Tomography of Central Chile-NW Argentina Flat-slab Subduction Zone Using Local Earthquakes, 27th European Geophysical Society, Nice, EGS02-A-01454.

Pavlenkova, (2009). Mohorovichich discontinuity: handredth anniversary of the discovery, European Geosciences Union General Assembly 2009, Vienna, EGU2009-1749.

Pharaoh, T.C., Winchester, J.A., Verniers, J., Lassen, A. & Seghedi, A. (2006). The Western Accretionary Margin of the East European Craton: an overview. In: Gee, D.G & Stephenson, R.A. (eds): *European Lithosphere Dynamics*, Geoligical Society London, Memoirs, **32**, 291-312.

Prodehl, C. & Aichroth, B. (1992). Seismic investigations along the European Geotraverse and its surroundings in Central Europe, *Terra Nova*, **4**, 14-24.

Remmelts, G. & Duin, E.J.T. (1990). Results of a regional deep seismic survey in the Netherlands. In: Pinet, B. & Bios, C. (eds.): *The Potential of Deep Seismic Profiling for Hydrocarbon Exploration*, Editions Technip, Paris, 335-343.

Reston, T.J. & Blundell, D.J. (1987). Possible mid-crustal shears at the edge of the London Platform, *Geophys. J. Roy. Astr. Soc.*, **89**, 251-258.

Rijckers, R., Duin, E., Dusar, M. & Langenaeker, V. (1993). Crustal structure of the London-Brabant Massif southern North Sea, *Geol. Mag.*, **130**, 569-574.

Ritter, J.R.R. (2005). Small-scale mantle plumes: Imaging and geodynamic aspects. In: Wenzel, F. (ed.): *Perspectives in modern seismology, Lecture Notes in Seismology*, **105**, Springer-Verlag, 69-91.

Schwartz, L. (1966). *Théory des distributions*, Herman, Paris.

Seck, H.A. & Wedepohl, K.H. (1983). Mantle Xenoliths from the tertiary basalts of the northern Hessian Depression. In: Fuchs, K., von Gehlen, K., Mälzer H., Murawski, H. & Semmel, A. (eds.): *Plateau Uplift The Rhenish Shield-A case History*, Springer-Verlag, 153-162.

Sengor, A.M.C. & Burke, K. (1978). Relative timing of rifting and volcanism on Earth and its tectonic applications, *Geophys. Res. Lett.*, **5**, 419-421.

Shearer, J.M. (1999). *Introduction to seismology*, Cambridge university press, Cambridge, pp 260.

Sichien, (2002). Image tomographique de l'atténuation des ondes P et S au Chili Central, à partir de séismes locaux, Mem. DEA, Université Nice-Sophia Antipolis, pp 24.

Sintubin, M. (1994). Phyllosilicate preferred orientation in relation to strain path determination in the Lower Paleozoic Stavelot-Venn Massif (Ardennes, Belgium), *Tectonophysics*, **237**, 215-231.

Sintubin, M. & Everaerts, M.A. (2002). A compressional wedge model for the Lower Palaeozoic Anglo-Brabant Belt (Belgium), based on the potential field data. In: Winchester, J.A., Pharaoh, T.C. & Verniers, J. (eds), *Palaeozoic Amalgamation of Central Europe*, Geological Society, London, Special Publications, **201**, 327-344.

Sourriau, A. (1979). Upper mantle beneath the Paris basin and Benelux, including possible volcanic anomalies in Belgium, *Tectonophysics*, **57**, 167-188.

Spakman, W. (1988). *Upper mantle delay time tomography*. PhD Thesis, Rijksuniversiteit te Utrecht.

Spakman, W. (1991). Delay-time tomography of the upper mantle below central Europe, the meditaranean, and asia minor, *Geophys. J. Int.*, **107**, 309-332.

Spencer, C. & Gubbins, D. (1980). Travel-time inversion for simultaneous earthquake location and velocity structure determination in lateral varying media. *Geophys. J.R. Astron. Soc.*, **63**, 95-116.

Stein, S. & Wysession, M. (2002). *An introduction to seismology, earthquakes and Earth structure*, Blackwell Publishings, Oxford, UK, pp 498.

Stockwell, J.W., Jr. (1999). The CWP/SU: Seismic Un*x package, *Computers and Geosciences,* **25,** 415-419

Student, 1908. The probable error of a mean, *Biometrica*, **6**, 1-25.

Thurber, C.H. & Ellsworth, W.L. (1980). Rapid solution of ray tracing problems in heterogeneous media. *Bull. Seismol. Soc. Am.*, **70**, 1137-48

Thurber, C.H. (1983). Earthquake locations and three-dimensional crustal structure in the Coyote Lake area, central California, *J. Geophys. Res.*, **88**, 8226-36.

Thurber C.H. (1986). Analysis methods for kinematic data from local earthquakes, *Rev. Geophys.*, **24**, 793-805

Thurber, C.H. (1993): Local earthquake tomography. In: Iyer, H.M. & Hirahara, K. (eds.): *Seismic tomography: theory and practice*, Chapman and Hall, London, pp 563-583.

Vander Auwera, J. & André, L. (1985). Sur le milieu de dépôt, l'origine des matériaux et le faciès métamorphique de l' Assise de Tubize (Massif du Brabant, Belgique), *Bull. Soc. belge Géol.,* **94**, 171-184.

Van Grootel, G., Verniers, J., Geerkens, B., Laduron, D., Verhaeren, M., Hertogen, J. & De Vos, W. (1997). Timing of magmatism, foreland basin development, metamorphism and inversion in the Anglo-Brabant fold belt, *Geol. Mag.,* **134**, 607-616.

Vanguestaine, M. (1992). Biostratigraphie par acritarches du Cambro-Ordovicien de Belgique et des regions limitrophes: synthèse et perspectives d'avenir, *Ann. Soc. Geol. Bel.,* **155**, 1-18.

Verniers, J., Herbosch, A., Van Guestaine, M., Geukens, F., Delcambre, B., Pingot, J. L., Belanger, I., Hennebert, M., Debacker, T., Sintubin, M. & De Vos, W. (2001). Cambrian-Ordovician-Silurian lithostratigraphical units (Belgium). In: Bultynck, P. & Dejonghe, L. (eds.): *Guide to revised lithostratigraphic scale of Belgium*, Geologica Belgica, **4**, 5-38.

Verniers, J., Pharaoh, T., André, A., Debacker, T.N., De Vos, W., Everaerts, M., Herbosch, A., Samuelson, J., Sintubin, M. & Vecoli, M. (2002). The Cambrian to mid Devonian basin development and deformation history of Eastern Avalonia, east of the Midlands Microcraton: new data and a review. In: Winchester, J.A., Pharao, T.C. & Verniers, J. (eds.): *Palaeozoic Amalgamation of Central Europe*, Geological society of London.

Volon, C., 1989. Etude préliminaire de la structure des Massifs du Brabant et de Stavelot par sismique refraction, *Ma. Sci. Thesis*, Université Libre de Bruxelles, Brussels, Belgium, pp. 100.

Von Hoegen, J., Lemme, B., Zielinski, J. & Walter, R. (1985). Cambrian and Lower Ordovician in the Stavelot-Venn Massif. A model for depositional history, *Neues Jahrbuch für Geologie und Paläontologie, Abhandlungen*, **171**, 217-235.

Von Hoegen, J., Kramm, U. & Walter, R. (1990). The Brabant Massif as part of Armorica/Gondwana: U-Pb isotopic evidence from detrital zircons, *Tectophysics,* **185**, 37-50

Wadati (1933). On the travel time of earthquake waves. Part II, *Geophys. Mag.*, **7**, 101-111.

Wesson, R.L. (1971). Travel-time inversion for laterally inhomogeneous crustal velocity models, *Bull. Seismol. Soc. Am.*, **61**, 729-46

Wielandt, E. (1987). On the validity of the ray approximation for interpreting delay times. In: G. Nolet (ed.), *Seismic tomography*, Hingham, MA, pp 85-98

Wolters (1999). *Wolters' Algemene Wereldatlas*, Wolters Plantyn, Gronigen.

Zhu, L. & Kanamori, H. (2000). Moho depth variation in southern California from teleseismic receiver functions, *J. Geophys. Res.*, **105**, 2969-2980.

Ziegler, P.A. (1990): *Geological Atlas of Western and Central Europe*, Shell International Petroleum Maatschappij BV, The Hague/Geological Society Publishing House, Bath/Elsevier, Amsterdam.

List of Appendixes:

Appendix 1: Computer code to calculate the arrival time of direct P- or S-waves.

See included CD-rom

Appendix 2: Computer code to calculate the arrival time of refracted P- or S-waves.

See included CD-rom

Appendix 3: Computer code to calculate the arrival time of reflected P- or S-waves.

See included CD-rom

Appendix 4: Testing the programme Axitra A-1 A-11

Appendix 5: Computer code to calculate the nmo-correction for earthquakes at depth.

See included CD-rom

Appendix 6: Examples of the Input-files of the INVER3D programme

See included CD-rom

Appendix 7: Examples of the Output-files of the INVER3D programme

See included CD-rom

Appendix 8: Examples of the Input-files of the SIMULPS programme

See included CD-rom

Appendix 9: Examples of the more important Output-files of the SIMULPS programme

See included CD-rom

Appendix 4: Testing the programme Axitra

O. Coutant (1990) of the University of Grenoble developed the programme AXITRA, a programme to calculate synthetic seismograms, based on the theory of discrete wavenumbers. It permits to generate synthetic seismograms, with a possible complex source, defined by its Fourier spectrum and its focal mechanism. The programme is limited to one-dimension: it can account for horizontally-structured layers only. Unfortunately, no manual of this program exists, so it had to be tested extensively before it could be used to calculate the synthetic seismograms for the data of this study. Enabling to pick the arrivals of the PmP- and SmS-waves more accurately. In this appendix, all the tests that were performed to understand how the programme AXITRA works and their results are explained and shown.

The programme needs four input files: one that contains the coordinates of the station location in x, y and z. (Station, The x-axis is oriented N-S), one that contains de coordinates and depth of the location of the source (Source), one that contains the magnitude of the earthquake, strike and dip of the fault plane and rake of the mouvement (axi.hist) and one that contains the parameters needed for calculation and the velocity model (axi.data).

The parameters needed for calculation are: the number of layers (nc), the number of stations (nr), the number of sources (ns), the number of frequencies in the signal (nfreq), the time over which the signal is calculated (tl), the distance between fictive sources (xl, this must be high enough so there is no overlap on the required registration time), a parameter that fixes the imaginary frequency (aw, introduced to avoid the phenomenon of aliasing induced by the cutoff of the signal. In general it equals 2), the precision level at wich the iteration process stops (uconv, here taken 10^{-4}) and the maximum number of iterations, if the precision level is not reached (ikmax).

The parameter aw is defined by the formula:

$$F_{imag} = tl/aw \qquad (4.1)$$

Because of the relation between the spectral and time domain, the imposition of the number of frequencies and the registration time fixes the number (nt) and the interval (dt) of the time steps and the sampling frequency (f_{samp}) and the interval frequency (df).

$$df = 1/tl \qquad tl = nt*dt$$
$$dt = 1/f_{samp} \qquad f_{samp} = nfreq*df \qquad (4.2)$$

If all the frequencies of the signal have to be represented (theorem of sampling), the maximal source frequency has to be so, that:

$$F_{max} \leq f_{nyquist} \qquad \text{with } f_{nyquist} = f_{samp}/2 \tag{4.3}$$

So, the source frequency has to be approximately 2 to 3 times smaller than the maximal frequency.

The velocity model is defined as a succession of layers with fixed depths, P-wave velocity, S-wave velocity and a factor of quality for both P- and S-waves.

From these 4 files, AXITRA calculates the Green's functions of the environment in the frequency domain in an iterative way. These Green's functions are then convoluted with the source (a Ricker function defined by its predominant frequency). The calculation of the inverse Fourier transform gives the displacement along the x, y and z components.

Tests on the parameters that define the fault plane

A series of tests have been performed to verify the validity of the programme and to clarify the convention of the fault plane parameters adopted by the author of the programme.

A fault plane is defined by three angles (Figure A-4. 1):

ϕ [0,2π] Strike or azimuth of the horizontal trace counted positive in clockwise direction from the north.

δ[0, π/2] Dip, this is the highest angle to the horizontal

λ[π,-π] Rake of the vector of slip to the horizontal trace in the fault plane.

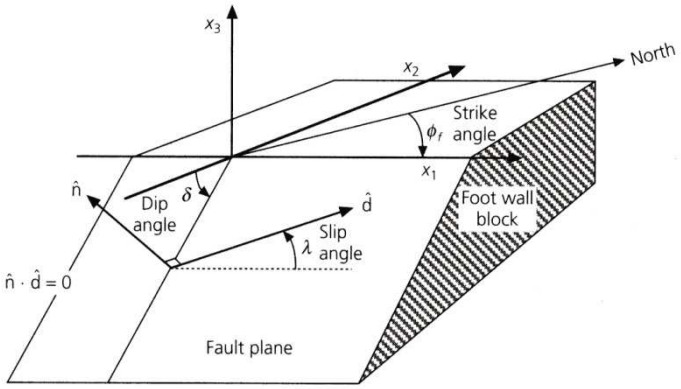

Figure A-4. 1: Fault geometry used in this study: strike, dip and rake.

For different parameters of ϕ, δ and λ, synthetic seismograms are calculated in points situated around the source. The spatial distribution of the polarities of the first arrivals will allow us to reconstitute the focal mechanism defined by its parameters (Figure A-4. 2,Figure A-4. 3 and Figure A-4. 4).

The velocity model is very simple and consists of a homogeneous environment with a P-wave velocity of 5.0 km/s and an S-wave velocity of 2.890 km/s. The source period is 0.5 s and is situated at a depth of 12 km and x,y = 0. The parameters of the axi.data file are: nfreq = 256 Hz, tl = 8 s, xl = 55001. 45 km, ikmax = 5000, uconv = 10^{-4}

A fault has two gliding surfaces: one that is part of the footwall and the other belonging to the hanging wall. By convention the rake is defined as the gliding of the hanging wall over the surface of the foot wall.

If $\delta \neq 0$ and $\pi/2$ and if $\lambda^* \in [0,\pi]$, it is a normal fault;

If $\delta \neq 0$ and $\pi/2$ and if $\lambda^* \in [-\pi,0]$, it is a reverse fault;

If $\delta = \pi/2$ and if $\lambda^* = 0$, it is a pure dextral movement;

If $\delta = \pi/2$ and if $\lambda^* = \pi$, it is a pure sinistral movement;

The rake convention of AXITRA (λ^*) does not correspond to the rake convention defined by Aki and Richards (1980). Their convention:

If $\delta \neq 0$ and $\pi/2$ and if $\lambda \in [0,\pi]$, it is a reverse fault;

If $\delta \neq 0$ and $\pi/2$ and if $\lambda \in [-\pi,0]$, it is a normal fault;

If $\delta = \pi/2$ and if $\lambda = 0$, it is a pure sinistral movement;

If $\delta = \pi/2$ and if $\lambda = \pi$, it is a pure dextral movement;

The case of a normal fault with dextral component is explained in detail in Figure A-4. 2. The parameters that characterize the geometry of the fault are the following:

$\phi = 0°$ the fault plane represented by its surface trace (----) is oriented N-S. The first pulses of the seismograms situated at one or the other site of the plane are opposed.

$\delta = 60°$ the trace of the fault plane is situated between y = –5 and –10 km. In fact, for a source situated at a depth of 12 km and inclined by 60° in comparison to the horizontal, intersects the surface at y = -6,9 km.

$\lambda = 90°$ in the upper hemisphere of the Schmidt diagram, the distribution of the signs indicates a mechanism of a normal fault with a dextral component along the fault plane. This validates the convention for $\lambda \in [0, \pi]$.

When comparing the Figure A-4. 2 and Figure A-4. 3, it can be seen that the movement along two nodal planes of a focal mechanism is identical. From Figure A-4. 2 and Figure A-4. 4 can be concluded that a normal and inverse fault with the same geometry produce approximately the same movement in the opposite sense.

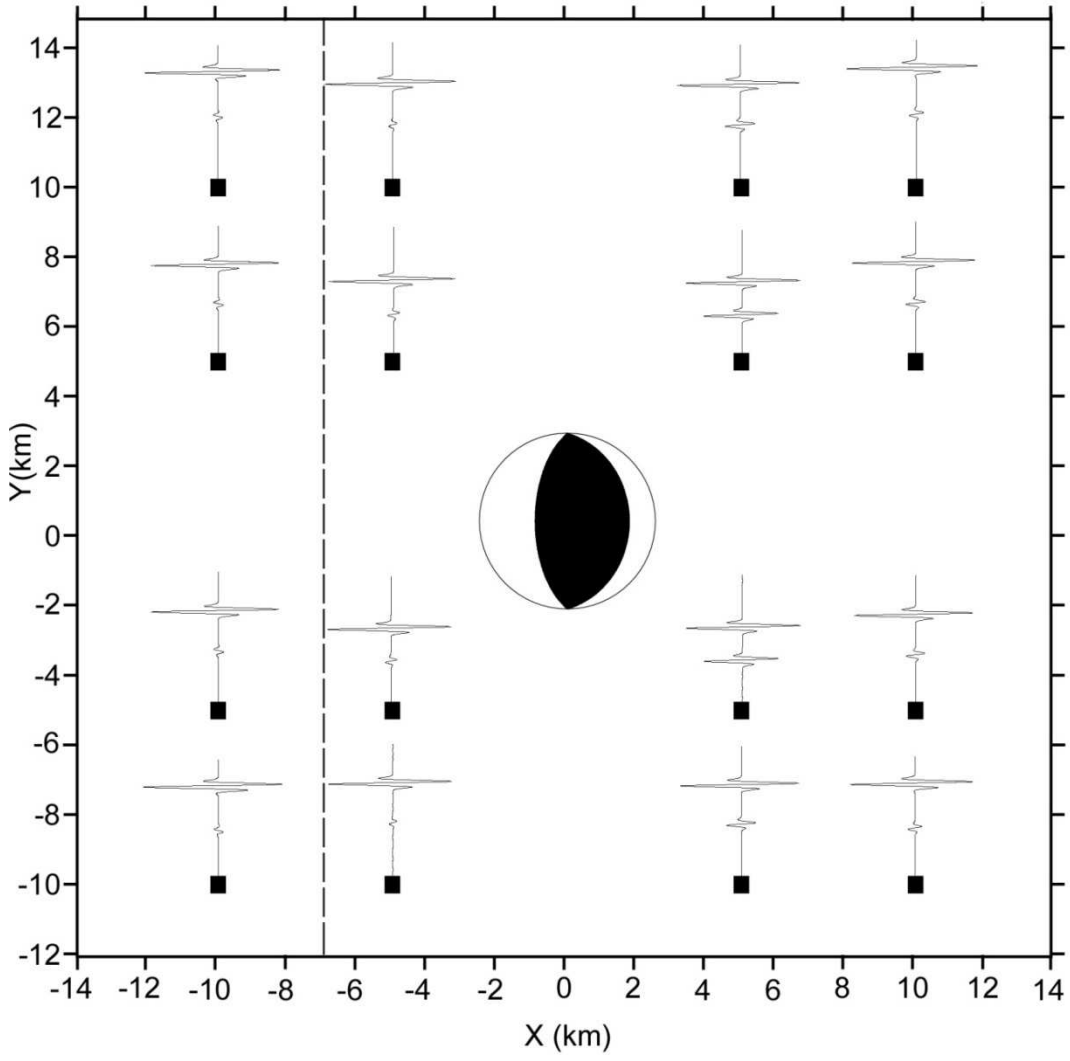

Figure A-4. 2: Non-normalized synthetic seismograms for a normal fault movement ($\phi = 0°$; $\delta = 60°$; $\lambda = 90°$).

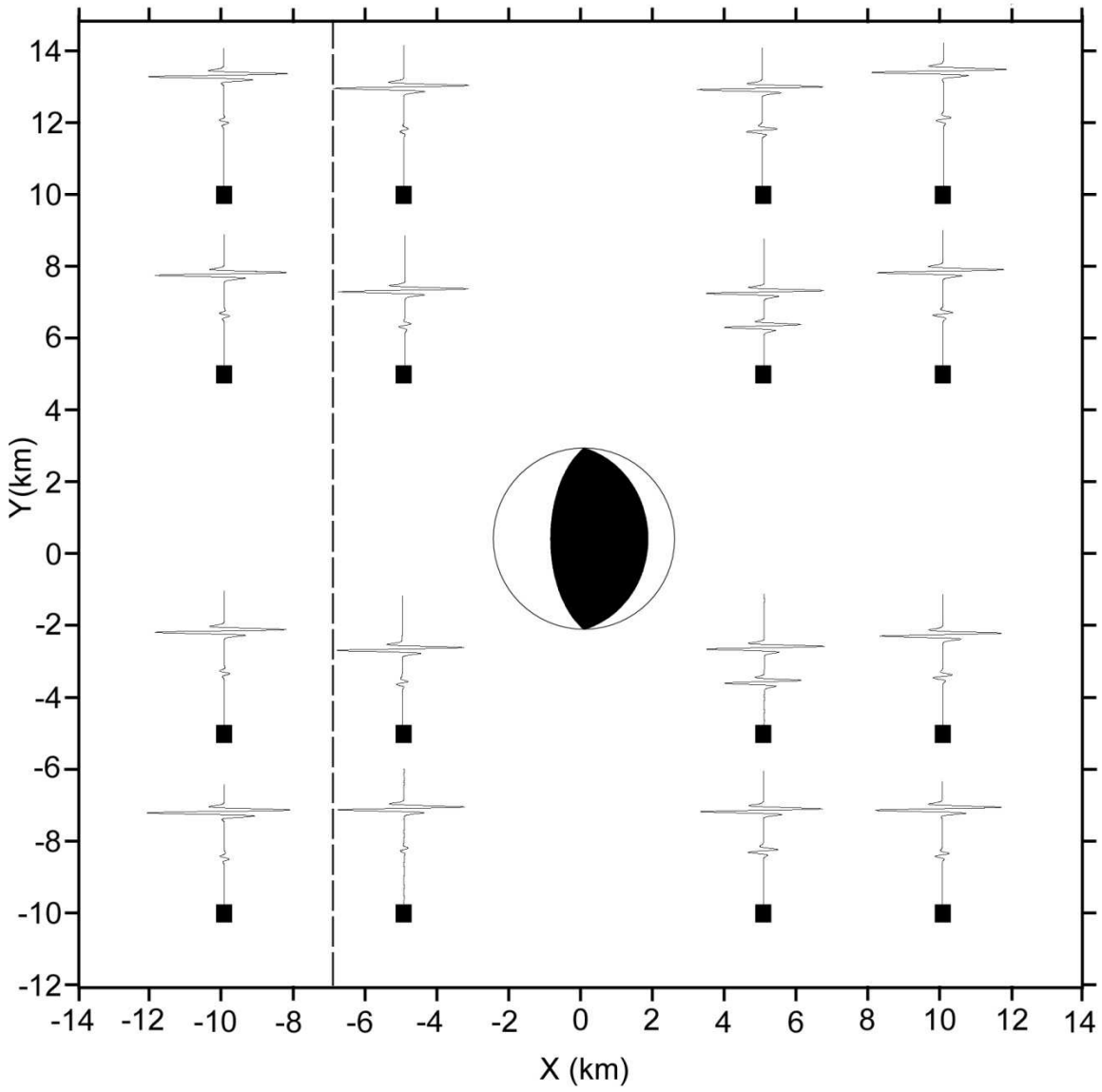

Figure A-4. 3: Non-normalized synthetic seismograms for a normal fault movement (ϕ= 180°; δ= 30°; λ= 90°).

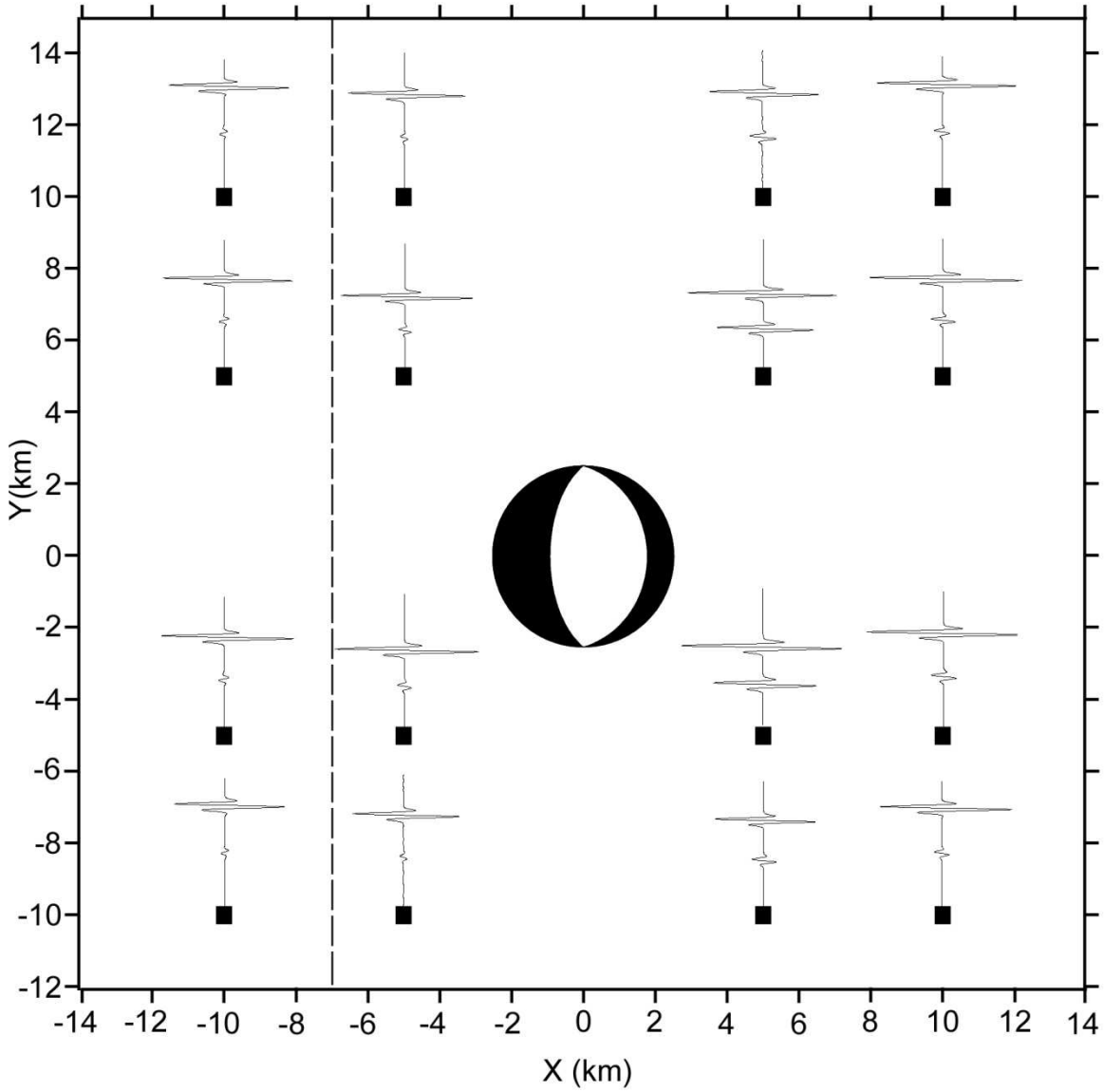

Figure A-4. 4: Non-normalized synthetic seismograms for an inverse fault movement (ϕ= 0°; δ= 60°; λ= –90°).

Recognizing the phases

For this test, synthetic seismograms are simulated using a normal focal mechanism (ϕ=90°, δ=45°, λ=90°). The inverse case was not tested here. It would give the same results but with opposite sign.

The stations are aligned over 200 km along a radial profile to the epicenter. To take the influence of the radiation diagram of the source into account, three profiles are treated (Figure A-4. 5).

1. Alignment of stations perpendicular to the orientation of the fault
2. Alignment of stations along a 45° angle with the orientation of the fault
3. Alignment of stations parallel with the orientation of the fault.

Only one quadrant is analyzed because of symmetry reasons. The seismograms are calculated along the three component axes x (N-S), y (E-W) and z (vertical).

Along Profile 1 (Figure A-4. 5), the direct P- and S-waves are very energetic the first 200 km. The refracted P- and S-waves however are not energetic (almost 0) at the critical angle and become first arrivals at a distance of 120 km. The Moho-reflected P-waves become visible at a distance of 70 km, The S-waves at 40 km. The direct, reflected and refracted waves are undistinguishable between 110 and 130 km. A package of energy arriving after the P- and S-waves and converted waves starts to develop at a distance of 100 km. Along profile 2 (Figure A-4. 6), the most important feature is the faint visibility of the Moho reflected P-waves. Along profile 3 (Figure A-4. 7) the direct P-waves are only very well distinguishable for the first 30 km. Further away they are very low-energetic. The Moho-reflected waves appear at 40 km. At 70 km, this wave is very energetic in comparison to the other waves. On every profile, two packets of energy are observed one behind the P-wave train and one behind the S-wave train that develop at a distance of 100 km. It probably corresponds to a double reflection of waves first on the roof of a covering layer and then on the Moho. A test has been performed to check their origin Figure A-4. 8. The seven-layer model is reduced to a two-layer model where the first layer has an average velocity of 6.25 km/s. In the synthetic signals the two packages are still visible for this new configuration. Their form is less complex because of the simplicity of the new model. These double reflections are thus caused by a reflection first on the free surface and then on the Moho.

This simulation shows the phases that can be recognized in the real signals. The direct P- andS-waves are very energetic (no matter what the epicentral distance is). The Moho-reflected waves may be visible for stations at a distance of 40 km. On the contrary, the Moho-refracted waves are of very low amplitude at the critical angle but also at greater distances, where they are first arrivals.

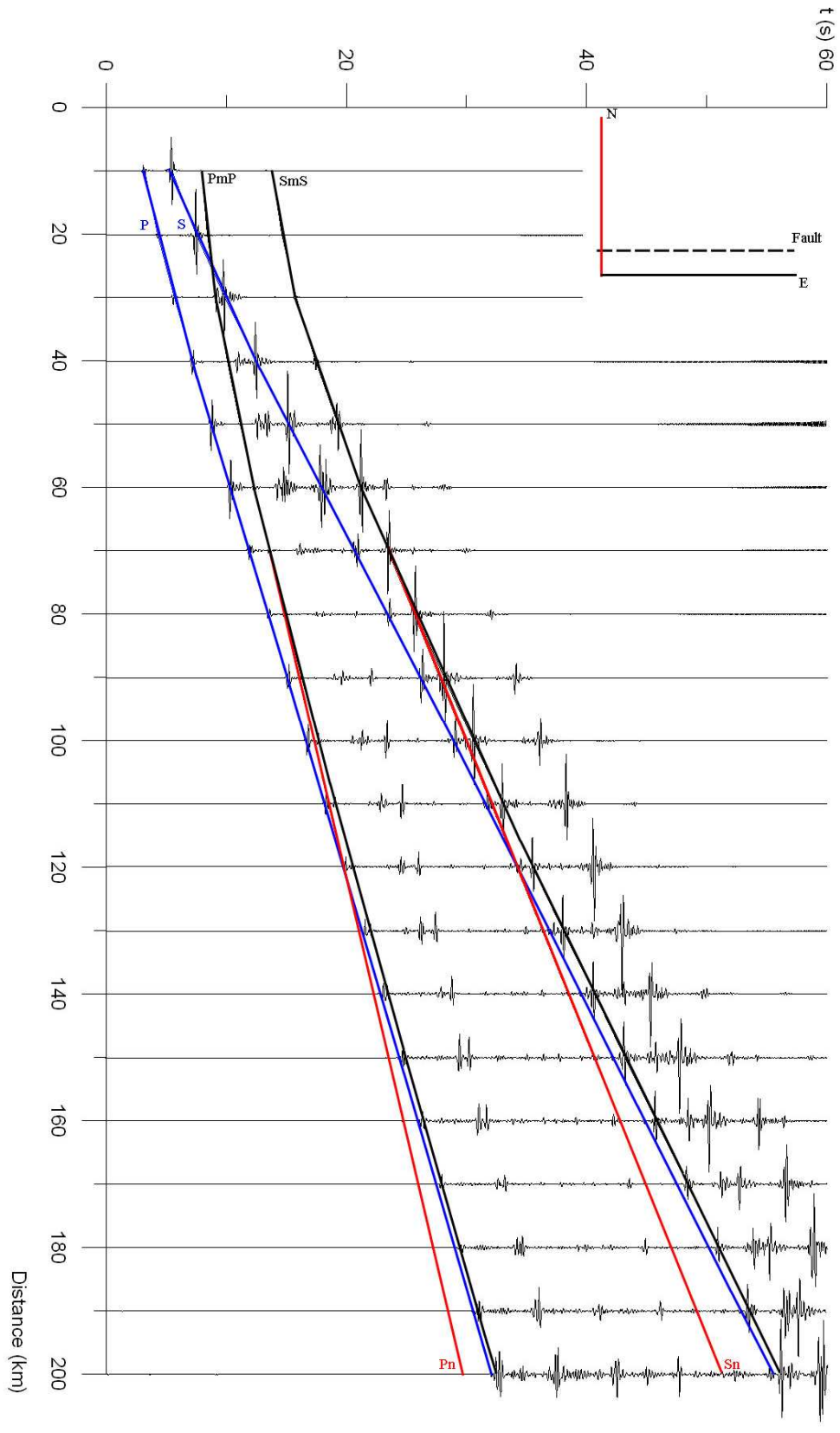

Figure A-4. 5: Profile 1 perpendicular to the fault plane: comparison between the arrival times and the synthetic seismograms for the vertical component.
The blue lines represent the arrival of the direct Pg- and Sg-waves, the red line represents the arrivals of the on the mantle refracted Pn- and Sn-waves and the black line represents the arrival of the on the Moho reflected PmP- and SmS-waves

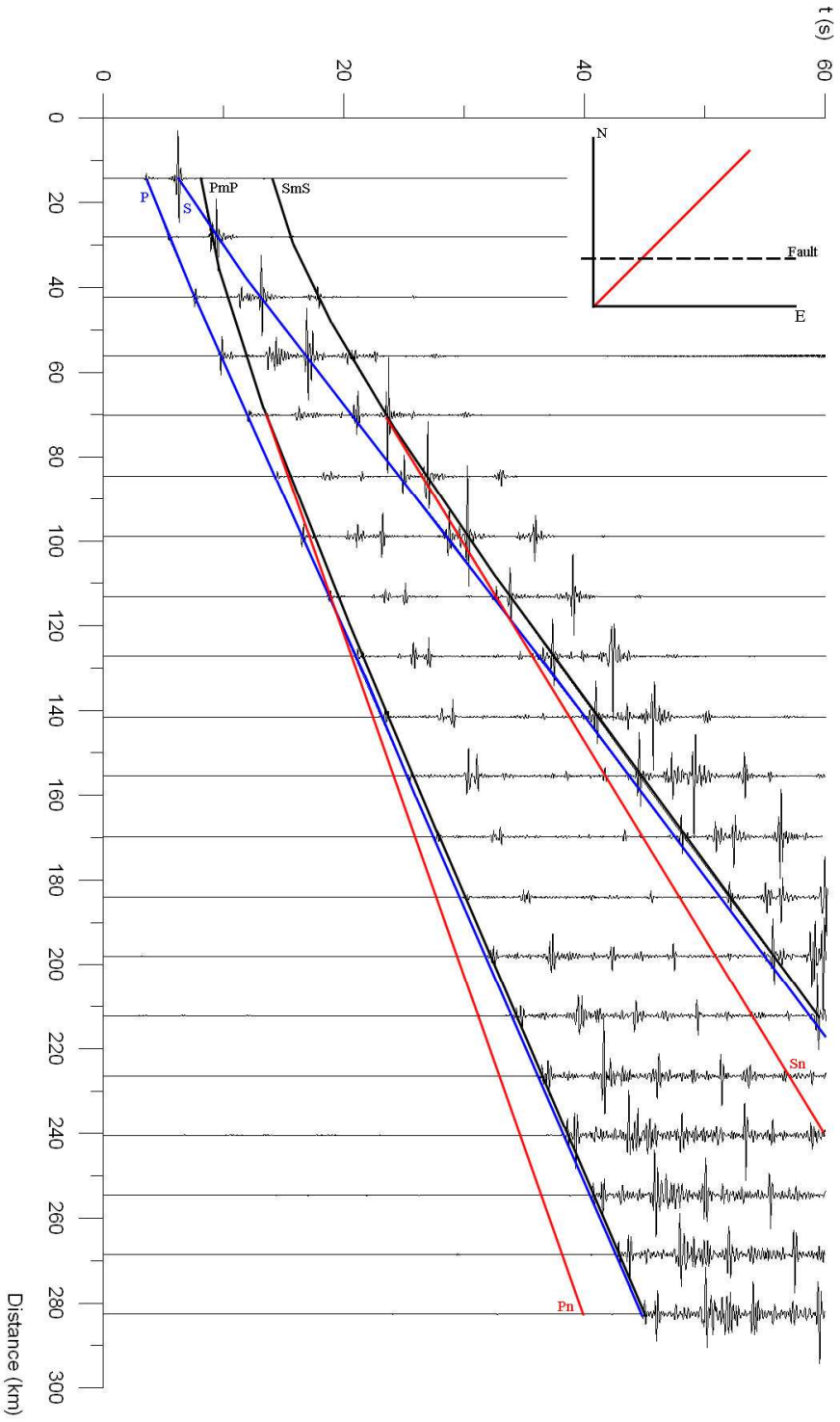

Figure A-4. 6: Profile 2 making a 45° angle with the fault plane : comparison between the arrival times and the synthetic seismograms for the vertical component.
The blue lines represent the arrival of the direct Pg- and Sg-waves, the red line represents the arrivals of the Pn- and Sn-waves refracted on the mantle and the black line represents the arrival of the PmP- and SmS-waves reflected on the Moho

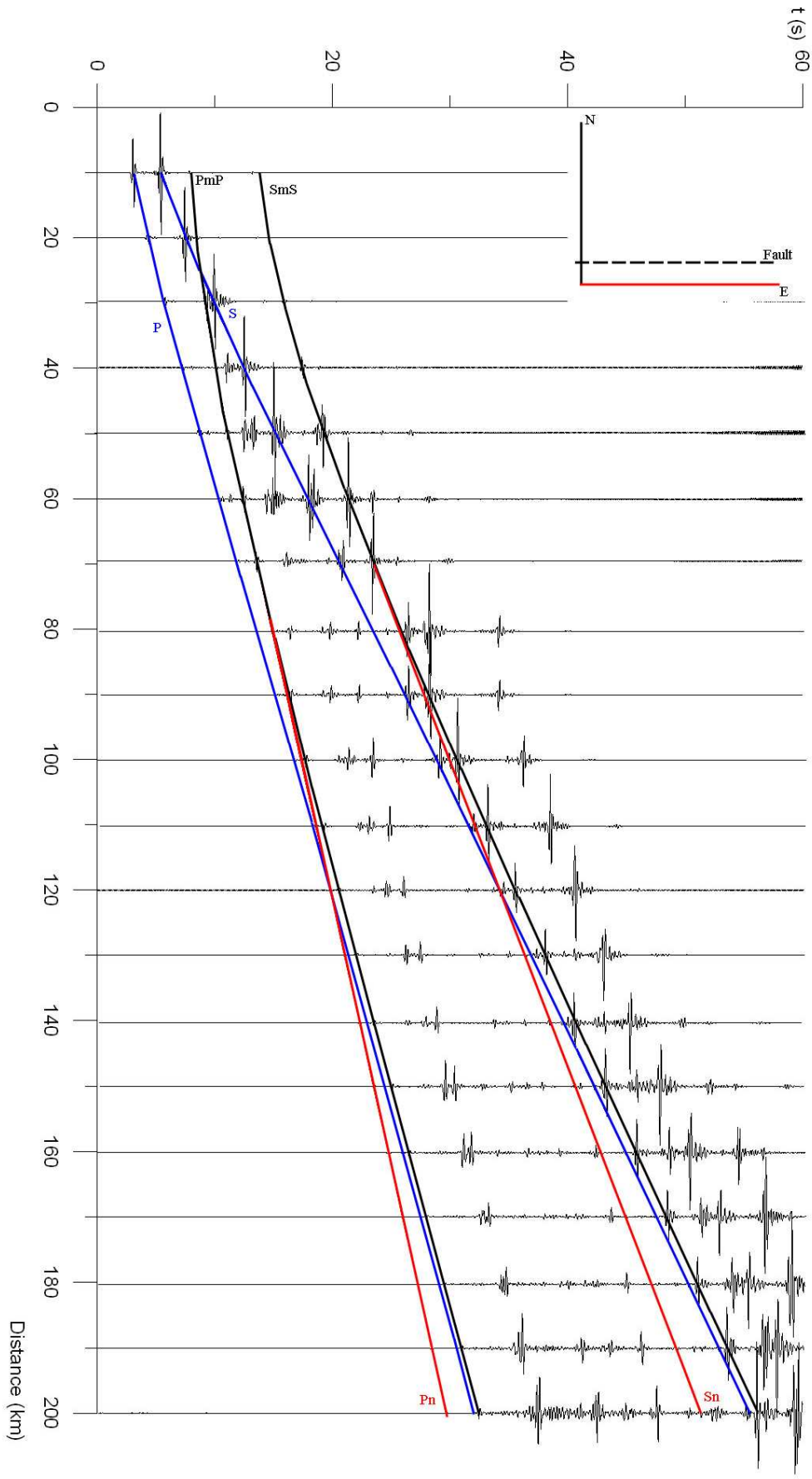

Figure A-4. 7: Profile 3 parallel to the fault plane: comparison between the arrival times and the synthetic seismograms for the vertical component. For more information see Figure A-4. 6. Error! Reference source not found.

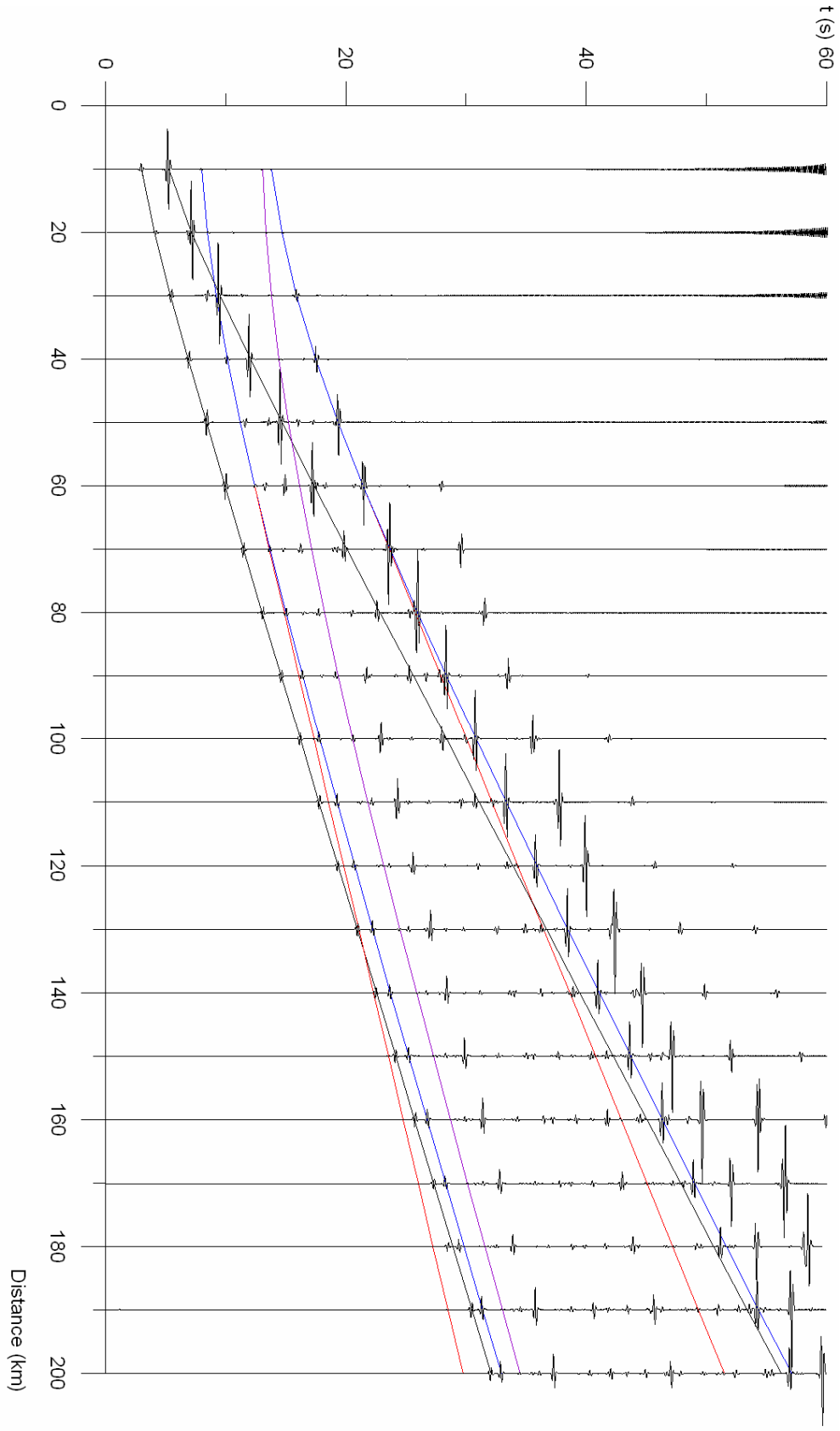

Figure A-4. 8: Profile 1: comparison between the arrival times and the synthetic seismograms for the vertical component calculated for the COL-model. See Figure A-4. 5 for more information.